Alexandre Sadurní Caballol

DOCTORAL THESIS

UPC – july 2012

UPC **CTTC**

Numerical Analysis and Experimental Studies of Vapour Compression Refrigerating Systems. Special Emphasis on Different Cycle Configurations.

Centre Tecnològic de Transferència de Calor
Departament de Màquines i Motors Tèrmics
Universitat Politècnica de Catalunya

Alexandre Sadurní Caballol
Doctoral Thesis

Numerical Analysis and Experimental Studies of Vapour Compression Refrigerating Systems. Special Emphasis on Different Cycle Configurations.

Alexandre Sadurní Caballol

TESI DOCTORAL

presentada al

Departament de Màquines i Motors Tèrmics
E.T.S.E.I.A.T.
Universitat Politècnica de Catalunya

per a l'obtenció del grau de

Doctor Enginyer Industrial

Terrassa, july 2012

Numerical Analysis and Experimental Studies of Vapour Compression Refrigerating Systems. Special Emphasis on Different Cycle Configurations.

Alexandre Sadurní Caballol

Director de la tesi

Dr. Carlos David Pérez-Segarra
Dr. Carles Oliet Casasayas
Dr. Joaquim Rigola Serrano

Tribunal Qualificador

Dr. José Fernández Seara
Universidad de Vigo

Dra. Maria Manuela Prieto González
Universidad de Oviedo

Dr. Jesús Castro González
Universitat Politècnica de Catalunya

Acknowledgements

Als meus pares, per tot l'esforç que han fet per formar-nos a mi i a tots els meus germans. En gran part aquesta tesis recull tot els valors que m'han transmès (cultura del treball, interès per el coneixement, esperit de superació, etc.).
Als meus germans Carles, Judith i Marc, tots vosaltres que cadascú a la seva manera m'heu servit de suport i exemple.
A la meva cunyada i amiga Raquel, i a les meves nebodes Nastia i la recent nascuda Laura.
Als meus amics Dani, Monica, Magda (que malgrat la distància) sempre heu estat al meu costat en els moments bons i els dolents al llarg d'aquesta tesis.
Al Jordi, a la Mireia, a l'Eva, al Ruben, als Tonis, a la Patri, a la Laia, a l'Albert, a la Gina, al Jose ... que heu estat una via d'escapada aquests últims mesos de tot l'estrès que he anat acumulant.
Vull agrair a l'Assensi Oliva i al David Pérez-Segarra la oportunitat i el suport que m'han proporcionat.
Vull agrair especialment al Carles Oliet tot el seu suport, la seva orientació i ajudes varies i inestimables, si aquesta tesis ha acabat tenint cara i ulls ha estat gràcies a tu.
No puc oblidar tampoc al Quim, qui ha estat part molt activa en plasmar en el document tota la feina feta. El teus comentaris, orientació, etc. ha estat clau perquè el document final hagi adquirit un mínim de qualitat.
No menys importants heu estat els companys de sala (Joan Farnós, Santi, Lluís, Nico, etc.), d'altres sales (Roser, Rash, Joan Lopez, Joan Calafell, Guillem, Lalo etc.) amb qui he compartit cafès i molt més. Tots vosaltres també heu contribuït a que aquest treball arribes a bon port.
Al Dani que vas ser el suport informàtic infatigable que en moments de desesperació em calia.
A l'Octavi que va prendre el rol del Dani en la última fase de la tesis.
I al Manolo, veritable pilar de la part experimental. Sense tu no haguéssim pogut portar a terme cap dels experiments que hem realitzat.
Finalment agrair al Ministerio de Educación y Ciencia pel suport econòmic durant els anys de beca FPI.

Abstract

The main objective of this thesis is the develpment of a numerical infrastructure to simulate Vapour-Compression Refrigerating Systems (Dry Expansion with and without high pressure receiver, liquid suction line and liquid overfeed) , using a reasonable computational resource. The simulation of these systems include refrigerant, secondrary coolands and solids parts.
The thesis is divided in six chapters. The first one is devoted to an introduction of the refrigeration, history types of refrigerating systems and an overview of the technical literature. The second one presents the mathematical formulation and the numerical methodology adopted to simulate the components and the whole refrigerating systems. The third is focused on verify the simulation code. The fourth is devoted to the validation of the different components, the dry expansion and the liquid overfeed refrigerating systems modelization. The fifth shows the parametric studies carried out (influence of secondary inlet temperatures in the heat exchangers). And the last one is focused on the concluding remarks and the future actions.

Contents

Chapter 1

General Overview of Refrigerating Systems and Research Objectives

1.1 Introduction

Since the beginning of civilization, the need to preserve the food has been a topic of worry. The first step to conserve meal with cold was using ice or snow. The Hebrews, Greeks, and Romans stored the ice and the snow inside the pits dug into the ground insulated with wood and straw.
In India an evaporative cooling method was employed. A liquid was rapidly vaporized and quickly expanded. This method abruptly increased the energy of the molecules of the liquid (causing the phase change from liquid to vapour), and this increase was drawn from the immediate surroundings of the vapour. These surroundings were therefore cooled.
The next step to preserve and condition the food and drinks, was to add chemicals, like sodium nitrate or potassium nitrate, into the water causing the temperature to fall down. Cooling wine via this method was recorded in 1550, as were the words "to refrigerate".
The first known artificial refrigeration was proved by William Cullen at the University of Glasgow in 1748, boiling ethyl ether into a partial vacuum. Cullen did not use the result to any practical purpose [1]. In 1805 Oliver Evans [2], an American inventor, designed the first refrigeration machine that used vapour instead of liquid. Evans never constructed his machine, but a similar one was built by John Gorrie, an American physician, in 1842. The basic principle of this machine was: compressing a gas, cooling it by sending through radiating coils, and then expanding the gas to lower temperature. The first U.S patent for mechanical refrigeration was granted to

Gorrie in 1851.
In 1859 Ferdinand Carré [3] from France developed a more complex system. Carre's equipment used ammonia because at the atmospheric pressure ammonia liquefies at much lower temperature than water, allowing more heat absorption. Unfortunately, their weak points, (i.e., general cost, size, complexity of the refrigeration systems at that time, and toxicity) excluded their general use. Therefore, the refrigeration in food and drink industry was still carried out by natural ice until the 1900. At the beginning of the 20th century, this situation changed and the Carre's refrigerators start to be used. Consequently, we could say that the early 1900's were when the refrigerating industry, as we currently know, born.
The world of refrigeration has grown parallel with the needs of the industrial processes. In the refrigeration industry two basic refrigeration techniques are used: vapour absorption and vapour-compression systems, which eventually became the standard for the refrigeration systems. Most of the work from the last century was carried out to improve the details of the system, seeking the most efficient refrigerant, developing better compressors, and working out the most efficient arrangement of components and pressures for the desired operating temperatures.
The increasing of the energy consumption in developed societies, as a consequence of the continuous industry growing, due to among other important electricity consumption of refrigeration equipment and air conditioning.Fig. 1.1 shows the evolution of the primary energy consumption to generate electricity, which is increasing due to the growing demand of energy [4]. The sustainable development, allowing to satisfy the present needs without putting at risk the future generations, is challenging the refrigeration and air-conditioning industries. They have to increase the energy efficiency (the primary fossil energy sources are finite) and to develop alternatives for the "classical" refrigerants, which have being used for years (they have an important impact to the environment). Then, the study of new possible cycles that reduce power consumption, the optimization of refrigerating components, the analysis of new refrigerants and its improvements are an important issue from an academic, industrial, economical, social and environmental point of view.

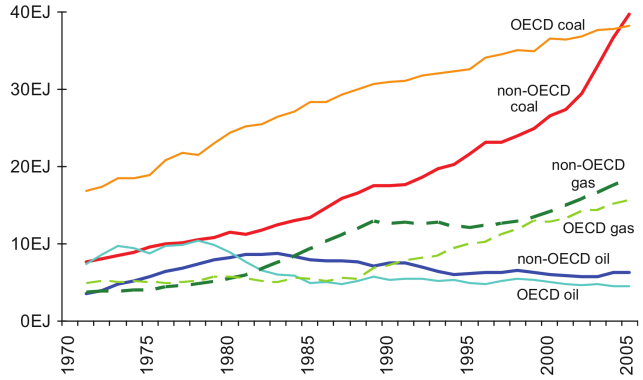

Figure 1.1: Primary fossil energy consumption for electricity generation [4].

1.1.1 Refrigerating systems

As was mentioned above, there are two basic refrigeration systems: absorption systems and vapour compression systems. Absorption systems were widely used at the beginning of the 20th century in the brewing industry. However, when the production and use of the electricity increased, these systems felt down in disuse in favour of vapour compression systems. Nowadays, the use of these systems is growing up, because vapour absorption systems can use low quality of energy such us waste heat, or solar heat from flat plate collectors, and their power electrical consumption is much lower than vapour compression systems.
Vapour compression refrigerating systems are still the most used refrigerating systems. There are two main families of vapour compression refrigerating systems [5]: single-stage cycles and multi-stage cycles (multi-stage compression and expansion, cascade, etc.). The single-stage works with one evaporation temperature and one condensation temperature, therefore, having only two levels of pressure (see Fig. 1.2 (a)). The multi-stage refrigerating systems have two or more evaporation temperatures, and two or more condensation temperatures, therefore, having three or more levels of pressure (see Fig. 1.2 (b)).
From the point of view of components, the multi-stage have two or more compressors and two or more expansion devices, while the single-stage has only one compressor and one expansion device. Regarding the refrigerant circuitry, the cascade systems have two or more different circuits allowing to work with different refrigerants using the optimal one depending on the cycle conditions.

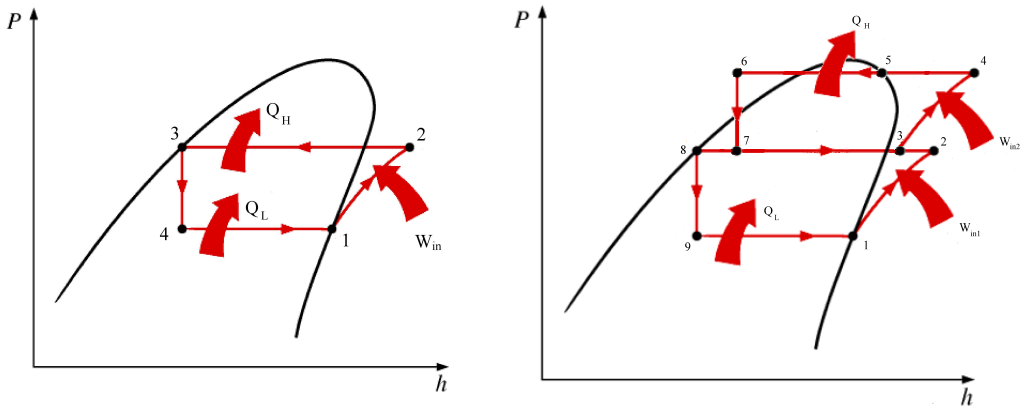

Figure 1.2: a) Single-stage cycle. b)Multi-stage cycle.

Both single-stage and multi-stage refrigeration families can follow a subcritical thermodynamic cycle ($p_{high} < p_{cr}$) or a transcritical thermodynamic cycle ($p_{high} > p_{cr}$), where p_{cr} indicates critical pressure. Multi-stage refrigerating systems can also follow a combination of subcritical and transcritical thermodynamic cycles.
Fig. 1.3 shows a subcritical single stage refrigeration cycle. In this type of cycles the heat exchanger in the high pressure branch is called condenser, due to the refrigerant enters as superheated vapour, condenses in a two-phase liquid-vapour process, and leaves as subcooled liquid. Fig. 1.4 shows a transcritical single-stage cycle. The high pressure heat exchanger is called gas cooler, due to the refrigerant goes from gas to liquid without a two-phase region.

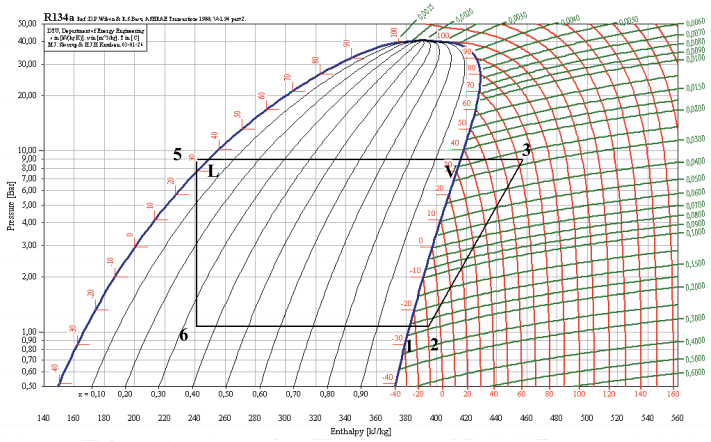

Figure 1.3: The subcritical refrigeration cycle for R-134a [5].

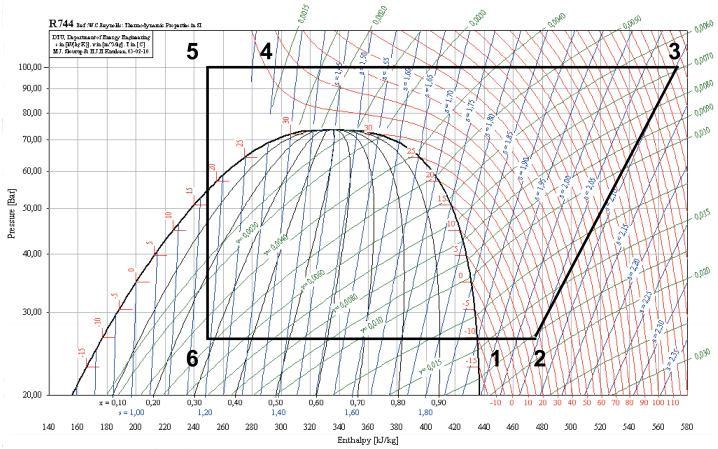

Figure 1.4: The transcritical refrigeration cycle for CO_2 (R-744) [5].

Single-stage and multi-stage cycles can also be classified depending on the heat exchangers and receivers used: i) dry expansion systems (standard dry expansion, dry expansion with high pressure receiver, etc.), ii) liquid recirculation systems (overfeed and gravity fed).
Nowadays, single-stage and subcritical refrigerating systems are very common in domestic, commercial and industrial applications. However, when the evaporator temperature drops below -10 °C the multi-stage cycles begin to be considered by the designers. The energy savings in multi-stage cycles increase when the evaporator temperature drops, and these energy savings compensate the higher cost of the multi-stage system.

1.1.2 Components (heat exchangers, expansion devices, compressors, etc.)

Heat exchangers are key elements in refrigeration and air-conditioning systems. There are many designs and applications of heat exchangers (condensers, evaporators, gas-coolers, intermediate accumulators, etc.) that have been developed for years.
Evaporators can be divided depending on the way the refrigerant is fed into the equipment: direct expansion, flooded evaporators and liquid overfeed evaporators. Direct expansion evaporators are widely used with moderate refrigerating temperatures with HFCs, HCs (isobutane, propane) and natural refrigerants (carbon dioxide, ammonia), etc. In these type of evaporators, the refrigerant begins the evaporation process with some quality until is completely evaporated. In these cases the surface of the evaporators is not used in its most efficient form. When the evaporating temperature

decreases, these kind of evaporators are not recommended, due to the big size and the inherent super-heating of the refrigerant near the end of the evaporator imposes progressively severe penalty in capacity and operating efficiency. Therefore, it is advisable to use other kind of evaporators like flooded and overfeed evaporators for low and very low temperature applications.
In flooded evaporators the refrigerant in liquid state covers the pipes which circulates the secondary flow. In liquid overfeed evaporators, a liquid refrigerant flow above the evaporating rate is supplied by means of a pump or by gravity. Therefore, the refrigerant at the outlet is a liquid-vapour mixture. Flooded and overfeed evaporators do not work by super-heating the refrigerant, which means that the evaporating surface is used more efficiently due to heat transfer coefficients are higher than in the dry expansion evaporators.
There are three families of condensers: air-cooled condensers (with air as secondary coolant), water-cooled condensers (with water as secondary coolant) and evaporative condensers (where a portion of secondary coolant is evaporated).
Due to the poor performance of the air as a coolant, the air-cooled condenser is constructed using fins to increase the surface heat transfer. The air-cooled condensers are commonly combined with fans to force the air through the heat exchangers, in order to increase the superficial heat transfer coefficients.
Water-cooled condensers can be constructed using shell-and-tube, shell-and-coil, tube-in-tube or brazed plate configurations. The size of the cooling load, the refrigerant used, the quality and the temperature of the available cooling water, etc. determine the optimal selection of the condenser type.
An evaporative condenser operates on the principle that heat can be removed from condensing coils by spraying them with water or letting water drip onto them and then forcing air through the coils by a fan. This evaporation of water intensifies the cooling effect and refrigerant condensation.
There are different types of expansion devices, that have been developed through the years, which can be principally divided into expansion valves, capillary tubes, expanders and ejectors. They are key components of any refrigerating cycle. As for the heat exchangers, the application (costs, operating temperatures, etc.) determines which type of expansion device is used.
The compressors are a fundamental element for vapour compression systems. They are divided into positive displacement machines and centrifugal machines. The four basic types of positive displacement compressors are reciprocating, rotary with sliding vanes, screw, and scroll. These are further classified by the number of compression stages, the cooling method (air, water, or oil), the motor integration (open, semi-hermetic, hermetic, ...), etc.
Others elements which are used in the refrigerating systems are pumps. Pumps can be divided in centrifugal and positive displacement pumps.

The centrifugal or roto-dynamic pump produces a head and a flow by increasing the velocity of the liquid through the machine with the help of a rotating vane impeller. Centrifugal pumps include radial, axial and mixed flow units. The positive displacement pump operates by alternating of filling a cavity and then displacing a given volume of liquid. These type of pumps deliver a constant volume of liquid for each cycle against varying discharge pressure or head.

1.1.3 Refrigerants

At the beginning of the vapour compression machines, the refrigerants used were sulphur dioxide, methyl chloride, ammonia, carbon dioxide and some hydrocarbons. Almost all of them were toxic or flammable, and therefore their use was mainly limited to the industry sector. Carbon dioxide was used in marine market; unfortunately, the poor qualities in front of others refrigerants explains the decline and fall of carbon dioxide as a refrigerant [6]. In 1928, a new class of synthetic refrigerants based on chlorofluorocarbons combinations (CFCs), where "Freon" was the trade name and how they were commonly known. With them, the problems of toxicity and flammability were solved. The introduction of the CFCs and the later development of new synthetic compounds as HCFCs (hydro-chlorofluorocarbons) and HFCs (hydro-fluorocarbons) gave a strong push of the refrigeration industry into the household market and the comfort air-conditioning.
Unfortunately, these refrigerants have other problems. Sherwood et al. predicted in their article published in 1974 [7] that the chlorofluorocarbon gases would reach the high stratosphere and damage the protective mantel of ozone. The "ozone hole" over the Antarctic was discovered later in 1985.
United Nations designed an environmental program (UNEP) in 1972. The aim of UNEP [8] is to obtain an environmental management tools, cleaner production, sustainable consumption, multilateral environmental agreements and sustainable product design. In order to improve environmental management tools, UNEP established the global resource information database GRID in 1985. GRID'S main objective is to provide up-to-date, reliable and easily understandable environmental information.
During the recent decades, the concern for the environment has driven to international agreements to forbid the use of some refrigerants widely used in the world of the refrigeration, which are specially aggressive with the ozone layer and the increase of global warming. In 1987, the Montreal Protocol [9] was born with the objective to protect the stratospheric ozone layer and to condemn the HCFCs and the CFCs to phase out as compounds depleting the ozone layer. After the Montreal Protocol the group of allowed refrigerants were reduced to naturals refrigerants and hydrofluorocarbons (HFCs). The Kyoto Protocol [10] in 1997 determinates "to achieve stabilization of atmospheric concentrations of greenhouse gases at levels that would prevent dangerous anthropogenic (human-induced) interference with the climate sys-

tem..." and encourage to promote policies and measures to sustainable development. Since the HFC's have a high global warming potential (GWP), it obliges to regulate these kind of refrigerants, in order to protect the environment. The Rio Summit (The United Nations Conference on Environment and Development UNCED) in 1992, changed the international community's way of thinking. After Rio Summit, environmental issues associated with production start to receive more attention than those linked to consumption. The Johannesburg Summit (WSSD) in 2002 recommended developing and promoting a ten-year framework of regional and national initiatives on sustainable consumption and production.
In 2007, the 19th Meeting of the Parties in Montreal the HCFC Adjustment of Montreal Protocol is being decided for developing countries. Since 2007 these countries are now required to freeze HCFC consumption in the year 2013 and gradually phase-out by the year 2030. This implies that HCFCs should be replaced by substances with a substantially lower GWP. The UNFCCC COP-13 in Bali decided upon the Bali Action Plan, under which the Parties would work towards a conference two years later, with the objective of deciding at that meeting on a second Kyoto period.
At the end of 2009, the Climate Conference in Copenhagen started with many issues on the table. The developed countries want a long-term shared vision of the process with the participation of the USA. Unfortunately the conference presidency was not able to steer all initiatives into a convergence direction.
In 2010, the Climate Conference COP-16 in Cancun failed to progress the climate issue as a whole and Kyoto Amendment for a second period seems further away than ever.
In 2011, the Montreal Protocol Multilateral Fund took more strategic decisions on modalities for dealing the HCFC phase-down via the HPMPs [11].
Therefore, the 'natural refrigerants' (air, water, carbon dioxide, ammonia and hydrocarbons) together with new synthetic refrigerants with low GWP (eg. R1234yf, R1234ze) seems to take leading role in the present and future of the refrigeration (see Fig. 1.5).

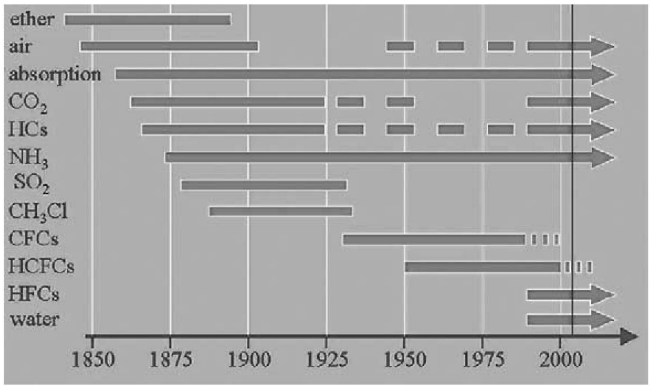

Figure 1.5: Timeline of refrigerants development [6].

1.2 Vapour-Compression Refrigerating System: Different Characteristics and Applications

Since the beginning of the refrigeration industry, the vapour-compression refrigeration (VCR) systems were widely employed. The increased concern for energy savings, makes very important the study and optimization of the different systems of refrigeration and their components. The different VCR systems can be classified as: dry expansion, overfeed, and gravity fed. Every system has its own advantages and disadvantages , which determine its application in one or another situation.

1.2.1 Dry Expansion Refrigerating System

Dry expansion systems are based on the dry expansion cycle , where the refrigerant is compressed from a low pressure state (1) to a higher pressure and temperature state (2). Then the refrigerant leaves its energy to the ambient or by means of another coolant which is at lower temperature than the refrigerant. The next step is to take the refrigerant from state (3) at the high pressure side to the low pressure side (4). At this point, the refrigerant is in liquid-vapour mixture with low temperature and low pressure. The refrigerant is then used to refrigerate a chamber, other fluid, etc., within evaporating process. Figs. 1.6 (a) and (b) show the ideal pressure-enthalpy (in this case there is not subcooled region) and temperature-entropy diagram of a standard dry expansion cycle.

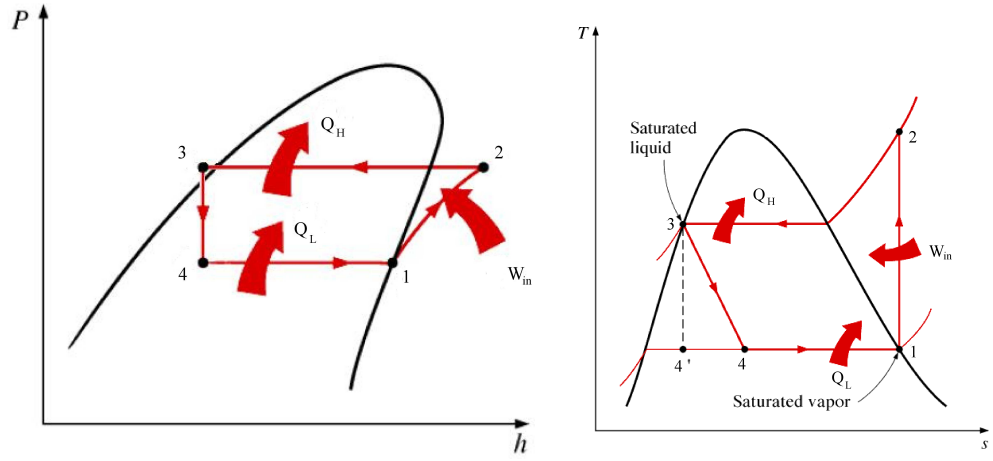

Figure 1.6: a) Diagram p-h. (left) b) Diagram T-s (right).

In a real dry expansion system the pressure-enthalpy diagram shows some differences. The first one is that neither the pressure is constant during the condensation process (from 2 to 3) nor during the evaporation process (from 4 to 1). The second one is that the compression process (from 1 to 2) is not isentropic, because the compression is neither adiabatic nor reversible. Other differences can arise from the expansion process (from 3 to 4), which is not always adiabatic, together with the heat exchange and pressure drops in connecting pipes.
Dry expansion systems presents several advantages and disadvantages.
Advantages:

- Low refrigerant charge.
- Simplicity of the circuit, which means low cost of construction.

Disadvantages:

- Inefficiency at low and very low temperatures, where inlet evaporator point has a too high vapour fraction and the evaporator size needed is too big.
- Reliability. The expansion device has to guarantee that all refrigerant is evaporated to protect the compressor from liquid. It means that the mass flow needs to be regulated in some applications in order to obtain superheated vapour at the compressor inlet.

Fig. 1.7 shows a standard dry expansion system. This system is composed by four main elements and their connecting pipes. The refrigerant is compressed by the

compressor, is liquefied and subcooled in the condenser, expanded in the expansion device and evaporated and superheated in the evaporator.

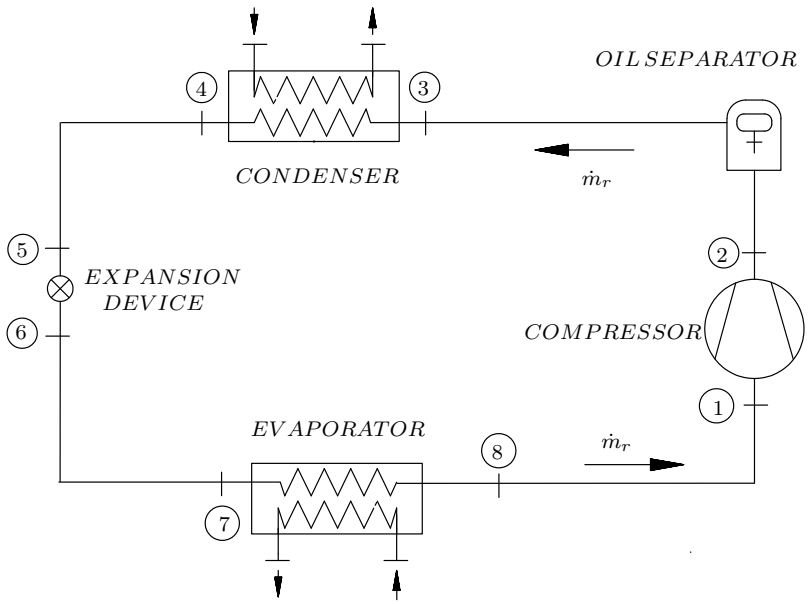

Figure 1.7: Scheme of the Dry Expansion Refrigerating System.

Fig. 1.8 shows a variant of standard dry expansion system. This system has a high pressure receiver after the condenser. The purpose of this high pressure receiver is to:

- Provide the storage capacity of the excess refrigerant when another part of the system must be serviced or the system must be shut down for an extended time.
- Accommodate a fluctuating charge due to the changes in the operating conditions of the condenser and evaporator.
- Hold the full charge of the idle circuit on systems with multi-circuit evaporators that shut off liquid supply to one or more circuits during reduced load and pump out the idle circuit.

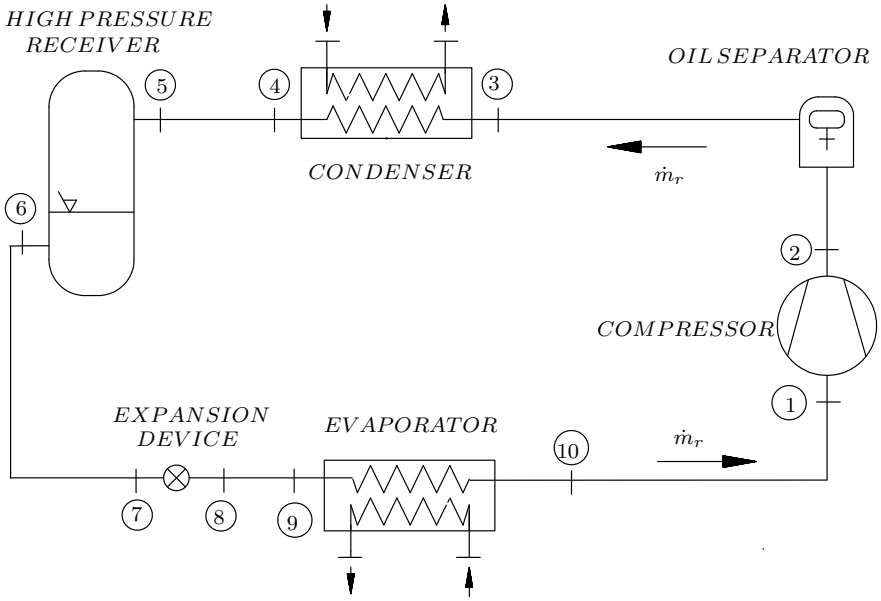

Figure 1.8: Scheme of the Dry Expansion Refrigerating System with high pressure receiver.

Fig. 1.9 shows other variant of standard dry expansion system with a low pressure receiver. This system has a low pressure receiver after the evaporator. The purpose of the low pressure receiver is to:

- Provide the storage capacity of the excess refrigerant when another part of the system must be serviced or the system must be shut down for an extended time.

- Use the heat obtained from the extra subcooling to heat the refrigerant in the low pressure receiver, which provides the mass flow at saturation conditions to the compressor.

- Accommodate a fluctuating charge due to the changes in the operating conditions of the condenser and evaporator.

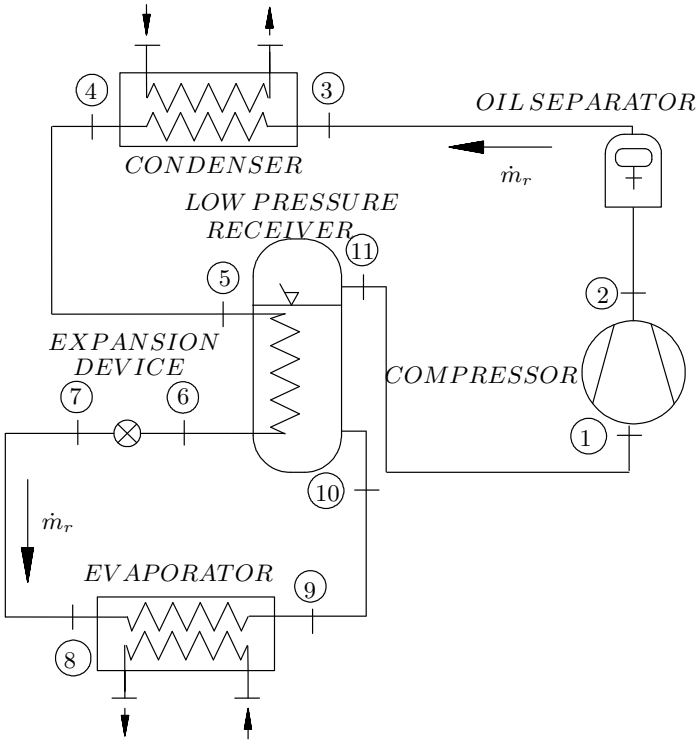

Figure 1.9: Scheme of a single-stage Liquid Suction Refrigerating System, with an intermediate heat accumulator. (IHA)

There is another possible cycle with an intermediate heat exchanger (IHE), placed in the same position as the intermediate heat accumulator presented in Fig. 1.9.

1.2.2 Overfeed Refrigerating System

Overfeed systems are based on the overfeed cycle , where the refrigerant is compressed from a low pressure state (1) to a higher pressure and temperature state (2). Then the refrigerant leaves its energy to the ambient or by means of another coolant which is at lower temperature than the refrigerant. The next step is to take the refrigerant from state (3) at the high pressure side to the low pressure side (4). At this point, the refrigerant is in liquid-vapour mixture with low temperature and low pressure. The refrigerant goes into the low pressure receiver and it leaves at point (5) as saturated

liquid state. The refrigerant is then used to refrigerate a chamber, other fluid, etc., within evaporating process. The refrigerant goes into the low pressure receiver again as liquid-vapour mixture (6). Finally the refrigerant leaves the low pressure receiver as saturated vapour (1). Figs. 1.10 (a) and (b) show the ideal pressure-enthalpy (in this case there is not subcooled region) and temperature-entropy diagram of an overfeed cycle.

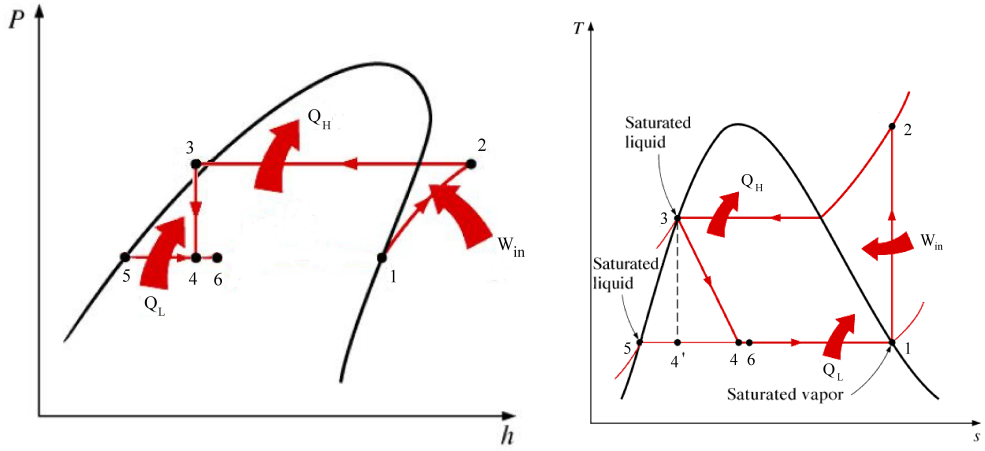

Figure 1.10: a) Diagram p-h. (left) b) Diagram T-s (right).

Overfeed systems are characterized by delivering liquid refrigerant to the evaporator at a higher mass flow rate than it is evaporating. The liquid recirculation is able to be forced by mechanical pumps, by gas-pressure pumping. In Fig. 1.11 an schematic representation of an overfeed refrigerating system is depicted. In these systems, there are two circuits: the first one is composed by the compressor, condenser, high pressure receiver (optional), expansion device, and the low pressure receiver.

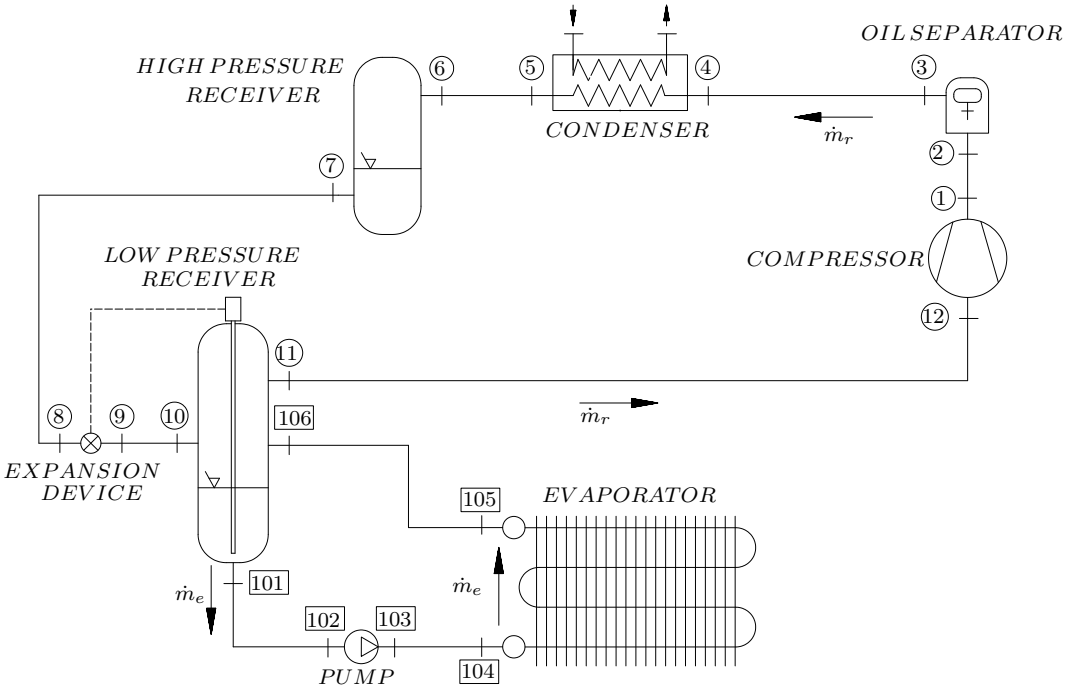

Figure 1.11: Scheme of the Overfeed Refrigerating System.

The refrigerant in vapour state is suctioned by the compressor from the low pressure receiver. The compressor increases the refrigerant pressure to the high pressure side of the system. Then the refrigerant is cooled and led to the high pressure receiver. From the high pressure receiver, the refrigerant goes to the expansion device where the pressure falls down to the low pressure side, and after, the refrigerant is led to the low pressure receiver. The second circuit is composed by the low pressure receiver, the pumping element (pump, gas-pressure pumping), and the evaporator. In this circuit, the refrigerant mass flow, which is higher than the evaporated mass flow, is suctioned by the pumping element and led to the evaporator. In the evaporator, the refrigerant mass flow is partially evaporated and then returned to the low pressure receiver. Usually these systems work with more than one evaporator fed from a common receiver.
The main advantages of liquid overfeed systems [12] are their high efficiency and their reduced operating cost. The energy cost is lower and the operating hours are lower, because:

- The evaporator surface is more efficiently used through good refrigerant distribution completely wetting the internal tube surface (higher local heat transfer coefficients are obtained).
- Some fluctuating loads or malfunctioning controls (depending on the period of the fluctuations and malfunctioning controls) do not affect the state of the refrigerant which is suctioned by compressors, because the low pressure receiver controls these problems.
- Minimum discharge temperature, which prevents lubrication breakdown, minimizes condenser fouling and lengthens the life of the compressor. For this reason the distance between the low pressure receiver and the compressor is the minimum possible. Therefore the suction lines are short, and the refrigerant suctioned is closer to the saturated vapour than in the direct expansion systems.
- Evaporators can be defrosted with little disturbance to the system.

The main disadvantages are:

- Greater charge of refrigerant than in the dry expansion systems.
- The cost of construction is high, because these systems have more components (low pressure receiver, pump and more tube lines). It is also necessary to insulate longer pipes (specially liquid feed lines) and the maintenance of the pumping units also increases the cost of the system.

The advantages of liquid overfeed systems become dominant in low temperature installations and where there are multiple evaporators [13]. In low temperature applications, achieving good heat transfer in evaporators is crucial for the system efficiency. The plants operate with high compression ratios and appreciable quantities of flash gas, and therefore the high suction super-heat could be a problem. Liquid overfeed systems may have advantages also in higher temperature systems used for air conditioning, where improved heat transfer coefficients and positive feeding of multiple evaporators may be achieved. When halocarbon refrigerants miscible with oil are used, oil is conveyed to the low pressure side, and a central oil return line should be provided in the low pressure receiver, rather than running the risk of oil accumulation in the low pressure side.

1.2.3 Gravity-fed Refrigerating System

Gravity-fed systems are also characterized by the excess of liquid through the evaporator, but unlike the overfeed systems, it is forced by gravity. Like in overfeed systems,

there are two circuits: the first one is composed by the compressor, the condenser, the high pressure receiver (optional), the expansion device, and the low pressure receiver.

The refrigerant in vapour state is suctioned by the compressor from the low pressure receiver. The compressor increases the pressure of the refrigerant to the high pressure side of the cycle. Then, the refrigerant is cooled and led to the high pressure receiver. From the high pressure receiver the refrigerant goes to the expansion device where the pressure falls down to the suction pressure, and after this the refrigerant is led to the low pressure receiver. The second circuit is composed by the low pressure receiver, and the evaporator. In this circuit, the refrigerant mass flow which is higher than the mass flow that has been evaporated by the evaporator, is partially evaporated and returned to the low pressure receiver . The circulation of the refrigerant is produced by the buoyancy forces caused by differences of density.

The main advantages and disadvantages are similar to the overfeed systems, although in these systems pumping units are not needed. The limitation of these systems are imposed by the minimal height where the low pressure receiver must be positioned.
When the number of evaporators is small, flooded evaporators can be used with the same effectiveness as liquid overfeed evaporators. In flooded evaporators systems lines for oil return must be made for each coil. When the number of coils exceed 3 or 4 is usually more beneficial to choose liquid overfeed system since the oil is removed at one single point (the low pressure receiver) with one oil return line.

1.3 State-of-the art / bibliography review

In the development of refrigerating system simulation models, it has been important both the study and development of simulation models for the different elements and the integration and global resolution of them. Different research works are presented in the scientific literature, focusing their attention on modelling vapour compression systems, their components, the overall refrigeration cycle, and the comparison of numerical against experimental results.
Chi and Didion [14], and Rajendran and Pate [15] modelized a transient performance of refrigeration system. They based their models on zonal balances inside the condenser, the evaporator and accumulator (Chi and Didion's model distinguishes liquid, vapour, two-phase flow, walls and external air), and parametric models based on non-dimensional correlations for the compressor and the thermostatic expansion valve.
In Chi and Didion's model, the states of the different components are described by a set of first-order differential equations and the numerical solution is obtained by the first order Euler method. Furthermore, this model considers the dynamic responses

of electric motors, compressor, shaft, electric fans, heat exchangers, accumulators and thermostatic expansion valves.
In Rajendran and Pate's model, the transient pressure term for the refrigerant inside each component is considered . The overall refrigeration system is a set of differential and ordinary algebraic equations. These equations are solved numerically using an explicit finite-difference method.
Mc Arthur [16] and Yuan and O'Neal [17] modelized a transient simulation of a refrigeration system using one-dimensional analysis of the governing equations. Mc Arthur solved the heat exchangers using finite difference method. The compressor is solved considering different processes: the heat transfer in the suction and discharge ducts, the pressure drop in the suction valve, in the compressor chamber and in the discharge valve. The mass flow rate in the compressor and the thermostatic expansion valve were simulated using parametric models based on non-dimensional correlations. Yuan and O'Neal solved the elements using an implicit finite difference method.The compressor is modelled as a whole, the compression process is considered polytropic, and the suction and discharge valves are considered adiabatic and isoenthalpic.
Murphy and Goldsmith [18] [19] modelized the start-up and shut-down transient performance of a residential air-conditioner. All the elements were simulated using parametric models based on empirical non-dimensional correlations, except the capillary tube. The compressor was modelled by its steady-state equations. The capillary tube model was based on zonal balances distinguishing sub-cooled liquid and two-phase flow, integrating numerically the different terms and using average friction factors.
Jung and Radermacher [20] modelized the steady state regime for a single evaporator domestic refrigerator. Heat exchangers models are based on zonal balances. The compressor is considered a non-ideal isentropic compressor. The steady state simulation has been done using a successive substitution method and a simultaneous solution Newton-Raphson method.
Paliwoda [21] presented a method for calculating the basic parameters for gravity-fed evaporators, based on the calculation of the pressure drop of two-phase flow of refrigerant over pipes and pipe components.
Khan and Zubair [22] evaluated the performance of a vapour compression refrigerating system, on the basis of different empirical parametric studies, considering the cooling capacity as a lineal function of the evaporator and condenser temperatures. Several results are shown considering different working conditions, a variable-speed system, and sub-cooling and super-heating effects.
Koury et al. [23] presented a numerical simulation model considering a variable speed refrigeration system. The compressor and expansion device are considered under steady state experimental data due to their very small thermal inertia, while heat exchangers are evaluated considering the distributed model for evaporators and condensers, respectively. The numerical resolution is based on an iterative process, where

some specific variables are determined from the Newton-Raphson method.
M.W. Browne and P.K. Bansal [24] presented a steady-state model for predicting the performance of a vapour-compression liquid chillers. The model employs an elemental ϵ-NTU methodology.
M.W. Browne and P.K. Bansal [25] presented a transient simulation model for predicting the dynamic performance of a vapour-compression liquid chillers. The model employs a thermal capacitance approach for specific state variables and only requires a select few initial conditions (eg. the chilled water and condenser water temperatures). A simple compressor model based on empirical regression has been employed in the simulation.
Nutter and O'Neal [26] modelized the transient outlet pressure and mass flow in a small non-adiabatic vessel. The model was derived from basic thermodynamic principles to describe the rate of de-pressurization within the small vessel. The main assumptions in the model were: negligible kinetic and potential energy terms, saturated conditions within the vessel, and equal phase velocities through the exiting orifice.
S. Estrada-Flores et al [27] presented four models of different degrees of complexity to simulate transient behaviour of pressure vessels.
Bendapudi et al. [28] presented a validated system model of a centrifugal chiller system using the finite volume formulation to predict transient performance including start-up. Winkler et al. [29], described three algorithms used to simulate a component-based vapour compression system in steady-state regime. Each component can be individually modelled using a set of mathematical equations that describe the corresponding thermodynamic process occurring within the components.
There are a lot of works in the scientific literature focused on the numerical simulation of the heat exchangers, compressors, and capillary tubes. These elements are simulated from the point of view of global balances analysis, but also from the point of view of the distributed analysis. However there is an element (receivers), that has not been widely studied. The found works develop a general modelitzation and then they focus the simulation on an hermetic receiver, therefore this element should be studied more (numerically and empirically) if it must be included in the simulation of vapour compression refrigerating systems like overfeed systems, low pressure systems, etc.
In the simulation of vapour compression refrigerating systems, the works found in the scientific literature are mainly focused on the standard dry expansion system. The steady and unsteady state regimes of these systems have been modelized. The overfeed systems and others are less studied, although their use is mainly adopted in the industrial application.

1.4 Research at CTTC

The CTTC [1] started its academic activities in the 1970's. Their research activities are focussed on two main lines. The first one is related to the mathematical formulation, numerical resolution and experimental validation of heat and mass transfer phenomena. In this line, the CTTC activities are oriented to natural and forced convection, turbulence modelling (DNS and LES, RANS, etc.), combustion, multiphase flows (free surface flow, two-phase flow, solid-liquid phase change, etc.), radiation, porous media, numerical algorithms and solvers, moving and non-structured grids, high performance computing (parallelisation), verification and validation, etc. The second line is focused on the thermal and fluid dynamic optimization of thermal system and equipment. With the aim of applying the acquired know-how from the basic studies mentioned above, the second line is working on refrigeration (vapour compression refrigerating systems, hermetic reciprocating compressors, absorption refrigerating systems, etc.), HVAC (ventilation, diffusion of contaminants in buildings, etc.), active and passive solar systems (solar collectors using transparent insulation materials, building facades with transparent layers, ventilation and integrated vegetation, etc.), heat exchangers (gas liquid compact heat exchangers for automobile radiators, evaporators and condensers, etc.), heat storage (by liquids and using phase change materials, etc.), numerical simulation of gaseous contaminant transport, etc.
Focusing on the refrigeration field, Escanes et al. [30] and Rigola et al. [31], [32] developed a numerical simulation of the thermal and fluid dynamic behaviour of a single stage dry expansion vapour compression refrigerating system under steady state conditions and working against double pipe condenser and evaporator. On the same line a first experimental unit was initially carried out for validation purpose working under R134a. A second experimental unit [33] [34] was carried out to be used with carbon dioxide. The modelization consists of a main program that sequentially calls different subroutines until the convergence is reached. The heat exchangers and the capillary tube are solved on the basis of a control volume formulation of the governing equations (continuity, momentum and energy), considering transient and one-dimensional flow. The generation of entropy is considered in the capillary tube in order to detect the limitation of the physical process produced under critical flow conditions. The compressor has been modelized by means of global balances between its inlet and outlet cross-section.
Oliet [35] performed a numerical simulation and experimental validation of fin-and-tube heat exchangers. Oliet developed different models for the simulation (detailed / distributed heat exchanger model, semi-analytical heat exchanger model and modelling of multi-heat exchanger systems).
Oliet et al. [36] performed a numerical simulation of dehumidifying fin-and-tube heat

[1] Heat and Mass Transfer Technological Center

exchangers, based on a semi-analytical modelling, and experimental comparison. Oliet et al. [37],[38] developed modelling of fin-and-tube evaporators considering tube-fin heat conduction in detail and non-uniform in-tube heat transfer.
Castro [39] performed a simulation of heat and mass transfer phenomena in the critical elements of $H_2O - LiBr$ absorption cooling machines, with the aim of apply to design absorption machines. The validation process was made using empirical data obtained from an experimental absorption unit developed in the CTTC.
Rigola et al. [40] performed a comparative analysis of R134a sub-critical cycle vs. CO_2 transcritical cycle and carried out numerical studies and experimental comparison. Rigola et al.[41], [42], [43] developed numerical studies and analysis of transcritical carbon dioxide refrigerating cycle.
Ablanque [44] developed a numerical simulation for a main vapour compression refrigeration system (dry expansion system) with a special emphasis on natural refrigerants García-Valladares et al. [45] performed a numerical simulation of a liquid overfeed system working with pure refrigerants in steady state conditions. The global algorithm is based on the sequential resolution of the different elements of the system. For each element, a simplified mathematical model based on global balances of mass, momentum and energy is used.
Danov [46] [47] developed an experimental and numerical infrastructure to study compact heat exchangers and liquid overfeed refrigeration systems.
Following the activities above exposed this thesi is framed in the refrigeration line focused in vapour compression refrigerating systems and their elements. It is focussed on the development of algorithms to solve the vapour compression refrigerating systems, and the implement a detailed model to simulate the refrigerant receivers.

1.5 About this thesis

The current concern for the environment and the economy in the refrigeration sector has motivated both experimental and numerical studies of the most widely used refrigerating systems, i.e. the vapour-compression refrigerating systems.
Within this thesis, two different lines are treated. The first one, has been focused on numerical studies that include the numerical simulation of the elements found in the vapour compression refrigerating systems, solving all the elements at different levels (from global balances to detailed numerical analysis) and covering wide range of types in one code (single-stage dry expansion system, single-stage dry expansion system with high pressure receiver, single-stage with intermediate heat accumulator and single-stage overfeed refrigerating system). The second line, has been devoted to experimental studies that includes the work of adaptation and improvement of the refrigeration cycle facilities in the CTTC and the experimental tests carried out for the validation and comparison purposes.

1.5.1 Numerical studies

Focusing on the numerical simulation, different type of models have been developed depending on the level of simulation considered. The first one is based on global balances, while the second one is based on detailed balances. The global algorithm is based on the sequential resolution of the different elements for each system. Looking at the previously exposed topics involved in the solution of the vapour-compression refrigerating systems, it has been decided to start the work of simulation of the different refrigeration systems, departing from an analysis by means of global balances, and following with an analysis focused on detailed balances.

Analysis by Global Balances

The elements of the system are modelized on a basis of global balances of mass, momentum and energy for steady state conditions: i) using information from high level simulations to be used for overall heat transfer coefficients, and pressure loss in heat exchangers, and ii) manufacturer data for characterising the compressor and the expansion device (thermo expansion valve or electronical operated valve). The treatment of the heat exchangers has been done using a semi-analytical method ($\epsilon - NTU$). The heat losses or gains in the connecting pipes of the system are calculated using a global heat transfer coefficient. The overall heat transfer coefficient in the tubes is calculated on the basis of the inner heat transfer coefficient (single-phase or two-phase), the heat conduction properties of the tubes, the insulation, and the outside heat transfer coefficient. Empirical information for the local pressure losses in singularities are used. The pressure losses are evaluated using correlations for the single-phase and two-phase friction factor.

Analysis by Detailed Balances (finite volume methodology)

In order to simulate unsteady regime and to obtain more details from heat exchanger, and insulated pipes, a numerical code based on detailed balances analysis using a finite volume methodology has been developed.
In this analysis, it has been developed subroutines to simulate both one dimensional transient and steady state regimes in pipes and heat exchangers using the conservation equations of mass, momentum and energy over every control volume. Those subroutines split the element in as many control volumes as needed. The modelization of this elements require some empirical information to evaluate the superficial heat transfer coefficient, the void fraction and the frictional factors.

1.5.2 Experimental studies

The first step has been to adapt and improve the first experimental dry expansion CTTC facility, which operated with R134a, to work with isobutane (R600a).
With the aim to acquire the experimental know-how for validation and comparison purposes, different experimental tests with R600a have been carried out. A detailed revision of these results indicated some deficiencies. In order to refine the quality of experimental data, these deficiencies were solved (improving the insulation of the dry expansion facility, secondary fluid heat exchanger distribution, as well as the conditions to obtain a right evaluation of temperature points of the system (correct mixed secondary flow at the outlet of the double-pipe heat exchangers,avoid premature condensation of the refrigerant at inlet of the condenser, etc.)) and also some sensors improvements (more sensors, sensors upgrades and displacement of sensors,etc), and experimental studies with added components taking into account its influences have been made.
The second step has been the adaptation of the dry expansion with intermediate heat exchanger facility for CO_2 and R134a to refrigerating cycle with low pressure receiver (intermediate heat accumulator).

1.5.3 Objectives

The main objectives of this thesis have been: i) the development of a detailed numerical infrastructure intended to simulate a wide range of vapour-compression refrigerating system types (dry expansion systems and overfeed systems), ii) the verification and validation of the developed numerical tools by means scientific literature reference data and CTTC experimental facility tests carried out during this thesis and previously obtained within the frame of other works, iii) the study of the refrigerating systems and pressured receivers in different operating points, to increase the knowledge of the vapour-compression refrigerating systems and pressured receivers used in some refrigerating systems, iv) the increase of the knowledge of experimental facility and the phenomenology, v) the adaptation and improvement of the experimental facility of the CTTC.

1.5.4 Thesis structure

This thesis has been divided in four main chapters: Mathematical Formulation and Numerical Methodology, Verification Studies and Illustrative Results, Validation Studies and Parametric Studies, among the Introduction and the Conclusions.
The Mathematical Formulation and Numerical Methodology is devoted to present the modelization of all elements involved in the vapour-compression refrigerating systems, as well as the numerical methodology to simulate the elements and the whole

refrigerating systems (dry expansion systems and overfeed refrigerating systems).
In Verification Studies and Illustrative Results, the work carried out to verify the subroutines and the global algorithm for dry expansion and overfeed systems has been presented, as well as some Illustrative results to show the capability of the numerical tool developed.
The Validation studies chapter shows the studies done to compare numerical vs. experimental results for each element and the whole systems, using the available experimental data (from CTTC's facilities and from technical literature).
Finally Parametric Studies chapter is devoted to present some parametric analysis for the studied VCR systems and for the pressure receivers.

1.6 Conclusions

This chapter presents a brief historical perspective and needs of refrigeration introduction, as well as different related topics (refrigerants, phenomenology, refrigeration systems and their components). Furthermore, vapour-compression refrigerating systems, which have been studied and simulated in this PhD thesis, have also been briefly explained.
To complete this chapter, and provide consistency and quality, a review of previous work from the scientific community which treat different topics necessary for conducting this thesis has been presented. It is shown a look at the scientific production and the work carried out in the Heat and Mass Transfer Technological Center (CTTC) within this topic, where this thesis has been developed.
Finally, the main aim of this PhD thesis and the motivation that led us to make this work and the goals we have set are presented. An explanation about the structure in which the thesis has been organized has been provided, in order to facilitate their understanding.

References

[1] James M. Calm. "The next generation of refrigerants : Historical review, considerations, and outlook". In: *International Journal of Refrigeration* 31 (2008), pp. 1123–1133.

[2] Jr Coleman Sellers. "Oliver Evans and his inventions". In: *Journal of the Franklin Institute* 122.1 (1886), pp. 1–16.

[3] Srikhirin Pongsid, Aphornratana Satha, and Chungpaibulpatana Supachart. "A review of absorption refrigeration technologies". In: *Renewable and Sustainable Energy Reviews* 5.4 (2001), pp. 343–372.

[4] N. Murayama and M. J. Eckelman. "Long-term trends of electric efficiencies in electricity generation in developing countries." In: *Energy policy* 37 (2009), pp. 1678–1686.

[5] A. Pilatte. *Refrigeration Fundamentals*. IIR, 2006.

[6] A. Pearson. "Carbone dioxide - new uses for an old refrigerant". In: *International Journal of Heat and Fluid Flow* 28.8 (2005), pp. 1140–1148.

[7] F. S. Rowland and M. R. Molina. "Stratospheric Sink for Chlorofluoromethanes: Chlorine Atom Catalyzed Destruction of Ozone." In: *Nature* 249 (1974), pp. 810–812.

[8] G. Clark. "Evolution of the global sustainable consumption and production policy and the United Nations Environment Programme (UNEP) supporting activities". In: *Journal of Cleaner Production* 15.6 (2007), pp. 492–498.

[9] *United Nations Environmental Programme (UNEP). Montreal protocol on substances that deplete the ozone layer*. 1987.

[10] *United Nations Framework Convention on Climate Change (UNFCCC). Kyoto protocol*. 1997.

[11] L. J. M. Kuijpers. "Refrigeration within a climate regulatory framework". In: *Proceedings of the XXIIIth International Congress of Refrigeration*. 2011.

[12] Inc. ASHRAE. *ASHRAE HANDBOOK - Refrigeration*. ASHRAE, 1998.

[13] W. F. Stoecker. *Industrial Refrigeration Handbook*. McGraw-Hill, 1998.

[14] J. Chi and D. Didion. "A Simulation Model of he Transient Performance of a Heat Pump". In: *International Journal of Refrigeration* 5.3 (1982), pp. 176–184.

[15] N. Rajendran and B. Pate. "A Computer Model of Start-up Transient in a Vapor Compression Refrigeration System". In: (1986).

[16] J.W. MacArthur. "Transient Heat Pump Behaviour". In: *International Journal of Refrigeration* 7.2 (1984), pp. 123–132.

[17] X. Yuan and D. L. ONeal. "Development of a transient simulation model of a freezer. Part I: Model development". In: *Proceedings of the 1994 International Refrigeration Engineering Conference at Purdue*. 1994, pp. 213–224.

[18] W.E. Murphy and V.W. Goldschmidt. "Cyclic Characteristic of a Residential Air Conditioner. Modeling of Sart-up Transient". In: *ASHRAE Transactions* 91.2 (1985), pp. 427–444.

[19] W.E. Murphy and V.W. Goldschmidt. "Cyclic Characteristic of a Residential Air Conditioner. Modeling of Shut-down Transient". In: *ASHRAE Transactions* 92.1 (1986), pp. 186–202.

[20] D. S. Jung and R. Radermacher. "Performance simulation of a single-evaporator domestic refrigerator charged with pure and mixed refrigerants." In: *International Journal of Refrigeration* 14 (1991), pp. 223–232.

[21] A. Paliwoda. "Calculation of basic parameters for gravity-fed evporators for refrigeration and heat pump systems". In: *International Journal of Refrigeration* 15.1 (1992), pp. 41–47.

[22] J. Khan and S. M. Zubair. "Design and performance evluation of reciprocating refrigeration system." In: *International Journal of Refrigeration* 22 (1999), pp. 235–243.

[23] R. N. N. Koury, L. Machado, and K. A. R. Ismail. "Numerical simulation of a variable speed refrigeration system." In: *International Journal of Refrigeration* 24 (2001), pp. 192–200.

[24] M. W. Browne and P. K. Bansal. "An elemental NTU- model for vapour-compression liquid chillers". In: *International Journal of Refrigeration* 24.7 (2001), pp. 612–627.

[25] M. W. Browne and P. K. Bansal. "Transient simulation of vapour-compression packaged liquid chillers." In: *International Journal of Refrigeration* 25 (2001), pp. 597–610.

[26] DW Nutter and DL ONeal. "Modeling the Transient Outlet Pressure and Mass During Flashing of HCFC-22 in a Small Nonadiabatic Vessel." In: *Mathematical and Computer Modelling* 29 (1999), pp. 105–116.

[27] S. Estrada-Flores et al. "Simulation of transient behaviour in refrigeration plant pressure vessels: mathematical models and experimental validation". In: *International Journal of Refrigeration* 26.2 (2003), pp. 170–179.

[28] S. Bendapudi, J. E. Braun, and E. A. Groll. "Dynamic model of a centrifugal chiller system - Model development, numerical study, and validation". In: *ASHRAE Transactions* 111.1 (2005), pp. 132–148.

[29] Jonathan. Winkler, Vikrant. Aute, and Reinhard. Radermacher. "Comprehensive investigation of numerical methods in simulating a steady-state vapor compression system". In: *International Journal of Refrigeration* 31 (2008), pp. 930–942.

[30] F. Escanes et al. "Numerical simulation of a single stage vapour compression refrigerating unit". In: *Proceedings of the 1994 International Compressor Engineering Conference at Purdue*. 1994, pp. 139–144.

[31] J. Rigola et al. "Numerical study of a single stage vapour compression refrigerant unit using non-contaminant refrigerants". In: *Proceedings of the 1996 International Compressor Engineering Conference at Purdue*. 1996, pp. 77–82.

[32] J. Rigola et al. "Numerical study and experimental validation of a complete vapour compression refrigeration cycle". In: *Proceedings of the 1998 International Compressor Engineering Conference at Purdue*. 1998, pp. 201–206.

[33] J. Rigola et al. "Numerical simulation and experimental validation of vapour compression refrigerating systems. Special emphasis on CO2 trans-critical cycles". In: *International Journal of Refrigeration* 28.special issue (2005), pp. 1225–1237.

[34] J. Rigola et al. "Numerical simulation and experimental validation of internal heat exchanger influence on CO2 trans-critical performance". In: *International Journal of Refrigeration* 33.2 (2010), pp. 664–674.

[35] C. Oliet. "Numerical Simulation and Experimental Validation of Fin-and-Tube Heat Exchangers". PhD thesis. Universitat Politècnica de Catalunya, 2006.

[36] C. Oliet et al. "Numerical Simulation of Dehumidifying Fin-and-Tube Heat Exchangers. Semi-Analytical Modelling and Experimental Comparison." In: *International Journal of Refrigeration* 30.7 (2007), pp. 1266–1277.

[37] C. Oliet et al. "Multidimensional and Unsteady Simulation of Fin-and-Tube Heat Exchangers". In: *Numerical Heat Transfer, Part A* 56.3 (2009), pp. 193–210.

[38] C. Oliet et al. "Modelling of fin-and-tube evaporators considering non-uniform in-tube heat transfer". In: *International Journal of Thermal Sciences* 49.4 (2010), pp. 692–701.

[39] J. Castro. "Simulation of Heat and Mass Transfer Phenomena in the Critical Elements of H_2O-LiBr Absorption Cooling Machines. Experimental Validation and Application to Design." PhD thesis. Universitat Politècnica de Catalunya, 2005.

[40] J. Rigola et al. "Comparative analysis of R134a sub-critical cycle vs. CO_2 trans-critical cycle. Numerical study and experimental comparison". In: *Proceedings of the 6th IIR Gustav Lorentzen Natural Working Fluids Conference*. 2004, pp. 1–8.

[41] J. Rigola et al. "Numerical study and experimental validation of a transcritical carbon dioxide refigerating cycle". In: *Proceedings of the 2004 International Refrigeration and Air Conditioning Conference at Purdue*. 2004, pp. 1–8.

[42] J. Rigola et al. "Numerical Analysis and Experimental Validation of Trans-Critical CO_2 Cycles for Small Cooling Capacities. CO_2 Reciprocating Compressor Comparison". In: *Proceedings of the 7th IIR Gustav Lorentzen Natural Working Fluids Conference*. 2006, pp. 455–458.

[43] J. Rigola et al. "Numerical Analysis of CO_2 trans-critical cycles using semi-hermetic reciprocating compressors for small cooling applications. Study of the internal heat exchanger influence under real working conditions." In: *Proceedings of the 22th International Congress of Refrigeration*. 2007, pp. 1–8.

[44] N. Ablanque. "Numerical Simulation and Experimental Validation of Vapor Compression Refrigerating Systems. Special Emphasis on Natural Refrigerants." PhD thesis. Universitat Politècnica de Catalunya, 2010.

[45] O. García-Valladares et al. "Numerical studies of refrigerating liquid overfeed systems working with ammonia and R134a". In: *Proceedings of the 2000 International Compressor Engineering Conference at Purdue*. 2000, pp. 327–334.

[46] S. Danov. "Development of experimental and numerical infrastructures for the study of compact heat exchangers and liquid overfeed refrigeration systems". PhD thesis. Universitat Politècnica de Catalunya, 2005.

[47] S. Danov et al. "Experimental facility for the study of liquid overfeed fin-and-tube evaporators. Validation of numerical models." In: *International Journal of Heat Ventilation Air Conditioning and Refrigeration Research* 14.2 (2008), pp. 221–239.

Chapter 2

Mathematical Formulation and Numerical Methodology

2.1 Introduction

The Simulation of the Vapour Compression Refrigerating Systems implies the thermal and fluid-dynamic behaviour study of the main refrigerant, the secondary coolants and the thermal behaviour of the solids.
The governing equations involved in the simulation of the elements in the Refrigerating Systems are the conservation of mass, momentum and energy for refrigerant and secondary coolants, while the conservation of energy equation joined with the Fourier's law is applied for the solids. The equations mentioned above, are presented in their integral form (equations (2.1)-(2.3)).

$$\frac{\partial}{\partial t}\int_{Vc}\rho\ dV + \int_{Sc}\rho\vec{v}\cdot\ d\vec{S} = 0 \tag{2.1}$$

$$\frac{\partial}{\partial t}\int_{Vc}\vec{v}\rho\ dV + \int_{Sc}\vec{v}\rho\vec{v}\cdot\ d\vec{S} = \sum\vec{F}_{sup} + \sum\vec{F}_{mass} \tag{2.2}$$

$$\frac{\partial}{\partial t}\int_{Vc}(e-\frac{p}{\rho})\rho\ dV + \int_{Sc}e\rho\vec{v}\cdot\ d\vec{S} = \dot{Q} - \dot{W}_s \tag{2.3}$$

Two different levels of discretization have been applied over the resolution equations for each element of the Vapour-Compression Refrigerating Systems (VCRS): the first one is based on global balances, while the second one is based on detailed balances (finite-volume approach).

2.2 Compressor

The compressor is modelled by means of empirical information provided by the supplier, or by a numerical characterisation previously made with software developed in the CTTC group.
The modelization of this element inside the whole cycle has been carried out on the bases of global energy balances between the inlet and outlet cross section. The mass (2.1) and the energy (2.3) conservation equations are evaluated using the compressor as a macro control volume of discretization, neglecting the kinetic and potential energy changes. Both the following mass and energy equations for the compressor are obtained:

$$\dot{m}_{out} - \dot{m}_{in} = 0 \tag{2.4}$$

$$\dot{m}(h_{out} - h_{in}) = \dot{Q}_{loss} - \dot{W}_e \tag{2.5}$$

When the information from the supplier has been used, the compression is assumed as an adiabatic process.
The information used in the simulation of the compressor is integrated in the developed software as data matrices, generated with different discharge and suction pressures. When a value between the calculated matrix points is required, it is obtained by bilinear interpolation.

2.2.1 Empirical modelization

The compressor information is provided by the manufacturer from an empirical modelization. This information is grouped in a set of working curves, obtained as a function of the condensation and the evaporation temperatures (see Figs. 2.1 and 2.2). Those curves consider the suction temperature equal to the evaporation temperature. The mass flow is corrected depending on the suction temperature with a correction factor provided by the supplier.

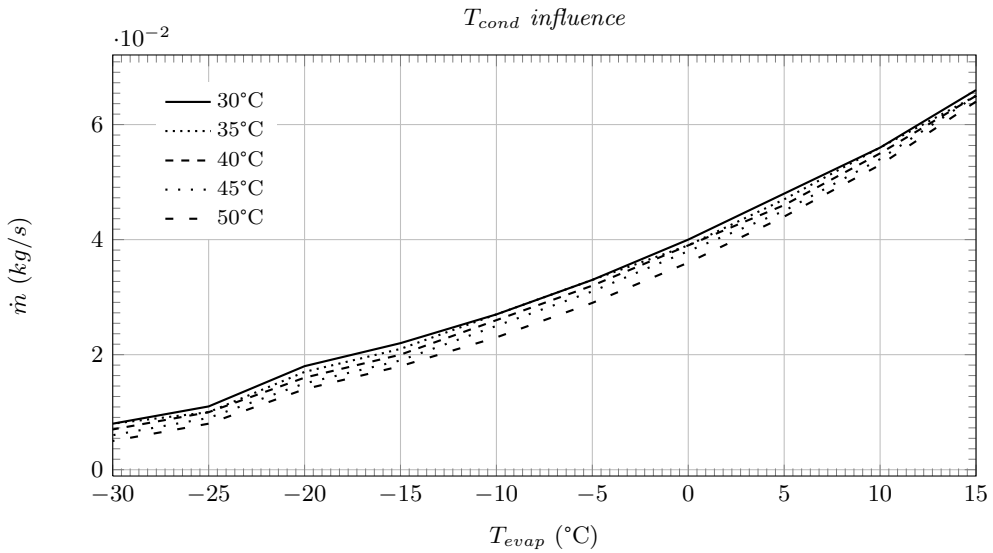

Figure 2.1: Characteristic mass flow curves for compressors for different T_{cond}.

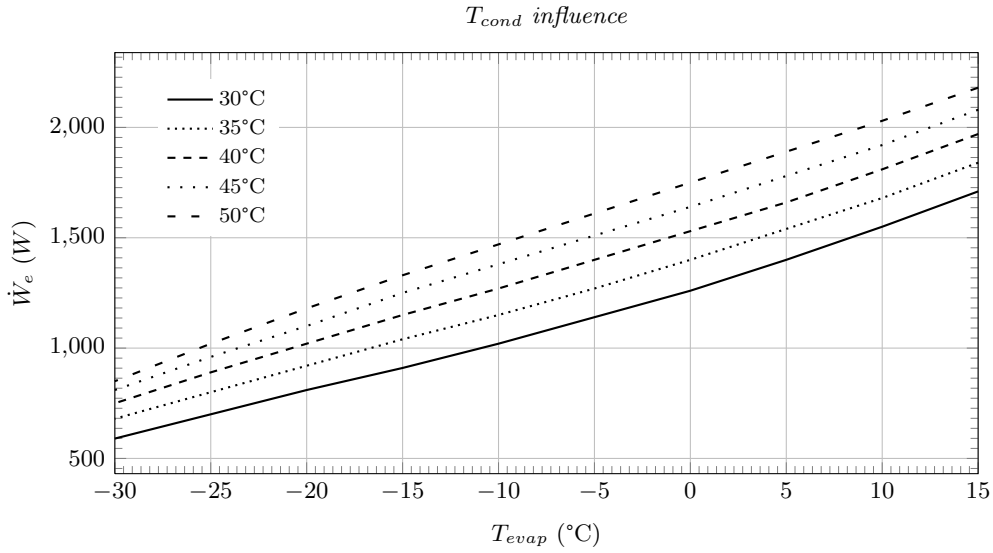

Figure 2.2: Characteristic electrical work curves for compressors for different T_{cond}.

Two matrices have been generated with the information provided by the supplier, one containing the mass flow information, and the other the electrical power consumption.

$$\dot{m} = f(T_c, T_e, \Delta T_{sh}) \tag{2.6}$$

$$\dot{W}_e = f(T_c, T_e) \tag{2.7}$$

$$\dot{Q}_{loss} = (1 - \eta_{me})\dot{W}_e \tag{2.8}$$

2.2.2 Advanced modelization and empirical modelization from CTTC tests

The CTTC's software is based on an advanced simulation model Escanes et al.[1], Rigola et al.[2], which solves the thermal and fluid-dynamic behaviour of hermetic reciprocating compressors in the whole domain (suction line, compression chamber and discharge line) (see Figs. 2.3 and 2.4). An implicit control-volume formulation and a SIMPLE-like algorithm has been used to discretize the one-dimensional and transient governing equations of the fluid flow.

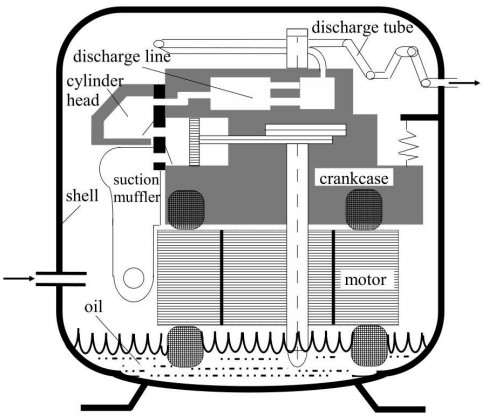

Figure 2.3: General hermetic reciprocating scheme.

Effective flow areas are evaluated considering a multidimensional approach based on modal analysis of fluid interaction in the valve. A direct method TDMA (tri-diagonal matrix algorithm) has been used to solve the complete set of discretised momentum, energy and pressure correction equations. Parallel circuits and extra elements (double orifices, resonators, etc.) are also considered in the formulation.

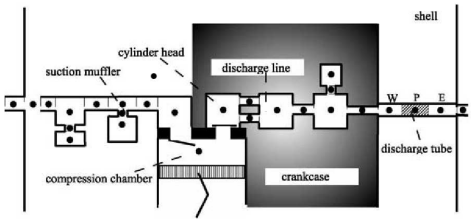

Figure 2.4: Schematic representation of the compressor flow domain.

$$\frac{\partial m}{\partial t} + \Sigma \dot{m}_o - \Sigma \dot{m}_i = 0 \tag{2.9}$$

$$\frac{\partial m\bar{v}}{\partial t} + \Sigma \dot{m}_o v_o - \Sigma \dot{m}_i v_i = F_s \tag{2.10}$$

$$\frac{\partial m(\bar{h} - \bar{e_c})}{\partial t} + \Sigma \dot{m}_o (h_o - e_{co}) - \Sigma \dot{m}_i (h_i - e_{ci}) = V \frac{\delta \tilde{p}}{\delta t} + \dot{Q}_w \tag{2.11}$$

Equations (2.9)-(2.11) show the continuity, momentum and energy governing conservation equations. Applying particular assumptions depending on uniform cross area, sudden enlargements/contractions or compressible flow through valves, the equation (2.10) has been obtained.
The motor torque equation system is linearly independent, and it is solved by means of the inverse matrix system LU resolution.
The solid thermal analysis is based on global energy balances for each one of the macro-control-volumes considered, which has been solved in the same way as motor torque. Equation (2.12) shows the discrete energy equation applied. The discretization is fully implicit and considers convection between solid and fluid control volumes ("k" vs. "i") and both conduction and radiation between each solid element and its neighbours ("k" vs. "j").

$$\frac{\rho_k^{n-1} c_{pk} (T_k^n - T_k^{n-1}) V_k}{\Delta t} = \Sigma_j \frac{T_k^n - T_j^n}{R_{kj}} A_{kj} + \Sigma_i \dot{Q}_{ki}^{conv,n} + \Sigma_j \dot{Q}_{kj}^{rad,n} \qquad (2.12)$$

For an extended view of the theoretical basis of the numerical simulation model see Pérez-Segarra et al.[3], while detailed experimental validation of the model is referred in Rigola et al.[4, 5].
The numerical results obtained from this software are: local instantaneous pressure, temperature and mass flow rate at each fluid flow control volume, instantaneous piston position, angular velocity and acceleration, solid temperatures, etc.

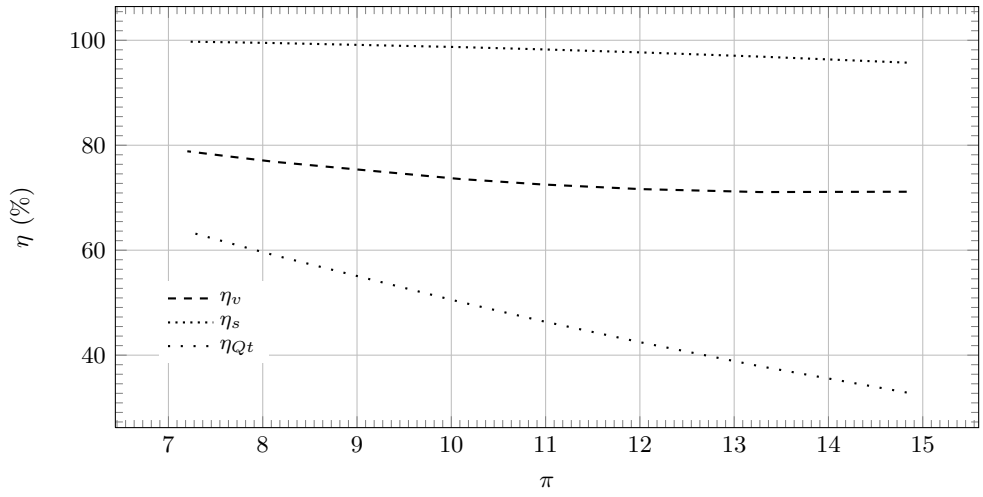

Figure 2.5: Volumetric, isentropic efficiencies and heat transfer losses ratio.

The CPU time to obtain a periodical solution of the compressor is typically 1800 s, while the global resolution time cycle is typically lower than 60 s. Therefore, the inclusion of the numerical simulation model of the compressor in the whole cycle resolution is not advised, in order to maintain reasonable computational time.
A second option to obtain the compressor information is to carried out compressor tests. From compressor tests we extract the typical information mass flow (condensing in the volumetric efficiency curve) and the electrical consumption (condensing in the isentropic efficiency and heat losses ratio).
From the CTTC's software or from empirical tests three matrices are generated. The first one is generated with the volumetric efficiency curve, the second one is generated with the isentropic efficiency curve, while the third one is obtained with the heat

transfer ratio curve (Fig. 2.5). Other option to obtain the

$$\dot{m} = \eta_v \rho_i V_{cil} f_n \tag{2.13}$$

$$\dot{W}_e = \frac{\dot{m}}{\eta_s \eta_m \eta_e} R T_i \frac{\gamma}{\gamma - 1} [(\frac{p_o}{p_i})^{\frac{\gamma-1}{\gamma}} - 1] \tag{2.14}$$

(2.15)

$$\dot{Q}_{loss} = (1 - \eta_{Qt}) \dot{W}_e \tag{2.16}$$

$$\eta_v = f(p_{suc}, p_{disc}) \tag{2.17}$$

$$\eta_s = f(p_{suc}, p_{disc}) \tag{2.18}$$

$$\eta_{Qt} = f(p_{suc}, p_{disc}) \tag{2.19}$$

2.3 Expansion Device

There are different type of expansion devices (capillary tubes, valves, expanders and ejectors). Capillary tubes and valves have been analysed in this thesis, and have been modelled as the compressor. It is simulated by means of information provided by the supplier from an empirical modelization, or by a previously simulation made with a software developed in the CTTC group.
The modelization of this element inside the whole cycle has been carried out on the bases of global energy balances between the inlet and outlet cross section. The mass equation (2.1) and the energy equation (2.3) are considered and applied under the assumptions: i) mass accumulation neglected, and ii) isoenthalpic process. Therefore the inlet mass flow is equal to the outlet mass flow and the inlet enthalpy is equal to the outlet enthalpy.

2.3.1 Thermostatic Expansion Valve (TEV)

The thermostatic expansion valve information is provided by the supplier. This information is grouped in a family of working curves, which determine the mass flow passing through the valve. The working curves of each TEV have been generated by the supplier as a function of the evaporation temperature and the super-heating at the evaporator outlet at a specific inlet temperature and pressure drop. Correction

factors for the temperature at the entry and the pressure drop have also been supplied by the manufacturer. Fig. 2.6 shows a typical supplier information.

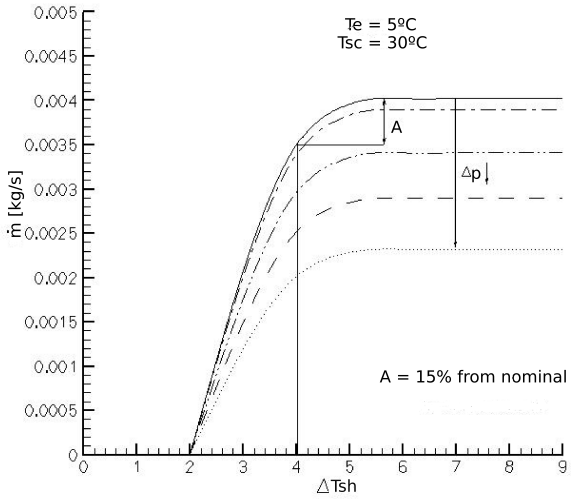

Figure 2.6: TEV curves from supplier.

From the information of the supplier three matrices are generated, for mass flow, inlet temperature correction factor and pressure drop correction factor.

$$\dot{m} = f(T_e, T_{sc}, \Delta T_{sh}, K_{sc}, K_{\Delta p}) \tag{2.20}$$

$$K_{sc} = f(T_{sc}) \tag{2.21}$$

$$K_{\Delta p} = f(\Delta p) \tag{2.22}$$

2.3.2 Electronically Operated Valve (EOV)

The information of mass flow through the valve is grouped in a set of working curves and correction factors curves (the inlet subcooling degree and the evaporation temperature). These set of curves has been generated by the supplier as functions of the pressure drop at a specific inlet sub-cooling temperature ($\Delta T_{sc} = 4K$) and evaporation temperature ($T_{evap} = 5$ °C). Fig. 2.7 shows a typical supplier information.

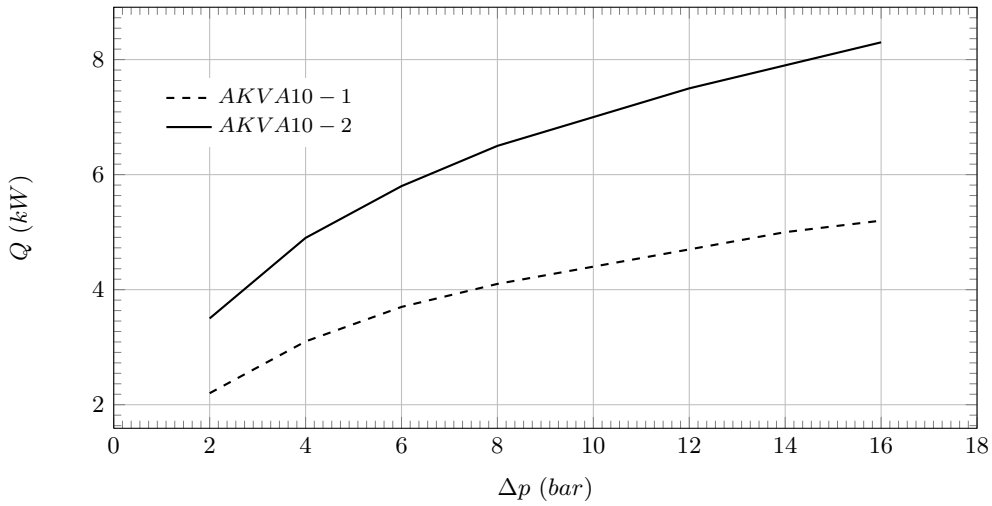

Figure 2.7: EOV curves from manufacture.

From the information of the supplier three matrices are developed. The first one is generated by the information of EOV capacity. The second one is obtained with the information of correction factor for the inlet subcooling temperature. The last one is mounted with the correction factor for the evaporation temperature.
Applying the correction factors of inlet subcooling degree and the evaporation temperature, the correct cooling capacity is obtained. The mass flow is found dividing the capacity by the difference between the compressor inlet enthalpy and the EOV outlet enthalpy.

$$\dot{Q} = f(T_e, T_{sc}, \delta p, K_{sc}, K_{T_e}) \tag{2.23}$$

$$K_{sc} = f(T_{sc}) \tag{2.24}$$

$$K_{T_e} = f(T_e) \tag{2.25}$$

2.3.3 Capillary tubes

Modelling of capillary tubes is divided into two levels. The first one is based on an empirical model (ASHRAE Handbook [6]), while the second one is based on an in-tube two-phase model developed in the CTTC group.

First model

The information used, is grouped in a set of working curves generated for capillary tubes with an specific geometry (L =3.3 m and d=0.86 mm) as a function of the inlet subcooling degree, the inlet pressure and the refrigerant. Correction factors for geometry of the capillary tube have also been provided by ASHRAE literature. The critical mass flow is given by the family of working curves (Fig. 2.8).

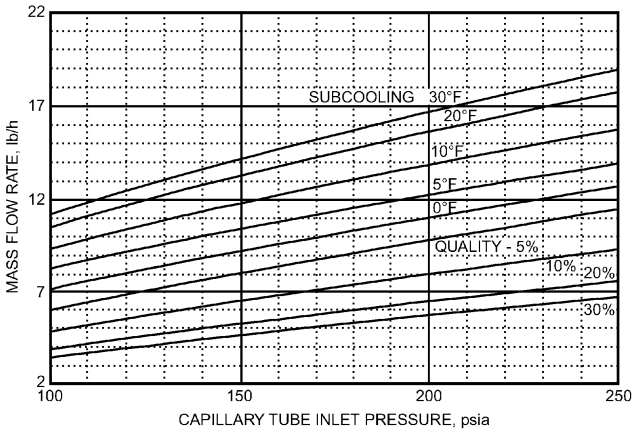

Figure 2.8: Mass flow curves (ASHRAE).

Fig. 2.9 shows the curve to correct the mass flow value for a different geometry of the standard capillary tube from ASHRAE.

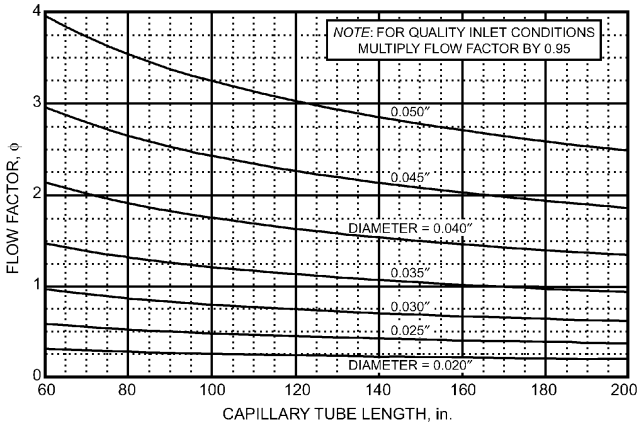

Figure 2.9: Geometry correction factor (ASHRAE).

From the ASHRAE information two matrices have been generated. The first one is obtained with the information of critical mass flow. The second one is developed with the information of correction factor for the capillary tube geometry.
Applying the correction factors of the capillary tube geometry the correct critical mass flow is found.

Second model

The information used in the second model, is obtained from the numerical tool available in the CTTC software infrastructure. The method to simulate capillary tubes is based on an in-tube two-phase flow model where the specific flow characteristics of the expansion process are considered. The main details of the two-phase flow model together with the specific flow regions considered and the whole numerical resolution are presented in this section.

In-tube two-phase model: the numerical in-tube two-phase flow model is obtained from the fluid governing equations discretized along the whole flow domain (the flow domain is divided into a number of finite control volumes, see Fig. 2.10). Considering a steady-state quasi-homogeneous fully-implicit one dimensional model, the discretized governing equations show the following form:

$$\dot{m}_i - \dot{m}_{i-1} = 0 \tag{2.26}$$

$$\dot{m}_i v_i - \dot{m}_{i-1} v_{i-1} = (p_{i-1} - p_i)S - \bar{\tau}_i \pi D \Delta z_i - \bar{\rho}_i g sin\theta S \Delta z_i \tag{2.27}$$

$$\dot{m}_i (h_i + e_{c,i} + e_{p,i}) - \dot{m}_{i-1}(h_{i-1} + e_{c,i-1} + e_{p,i-1}) = \bar{q}_i \pi D \Delta z_i \tag{2.28}$$

$$\dot{m}_i s_i - \dot{m}_{i-1} s_{i-1} = \dot{s}_{gen,i} + \frac{\bar{q}_i}{T_{wall}} \pi D \Delta z_i \tag{2.29}$$

A step-by-step numerical implicit scheme is used to solve the whole flow domain. The main equations (2.26)-(2.29) are rearranged and solved for the i position. Appropriate empirical correlations have been used to evaluate three specific parameters: the void fraction [7], the shear stress [8, 9], and the convective heat transfer coefficient [10–12].

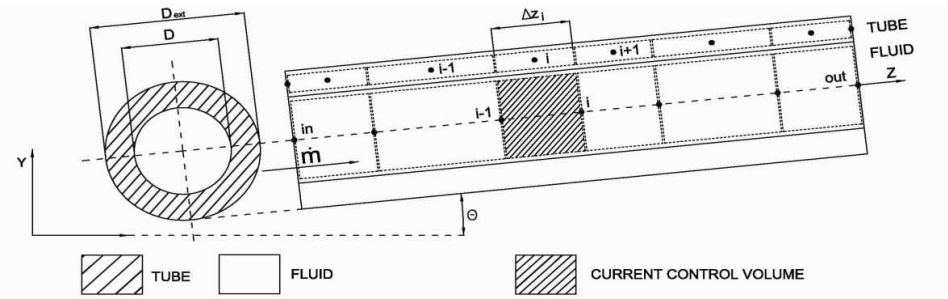

Figure 2.10: Two-Phase flow discretization.

In addition, the solid part is also evaluated by means of an energy balance. Fig. 2.10 shows the discretization of the solid domain. The corresponding set of algebraic equations are solved by an iterative method (Gauss-Seidel) or a direct method (TDMA).

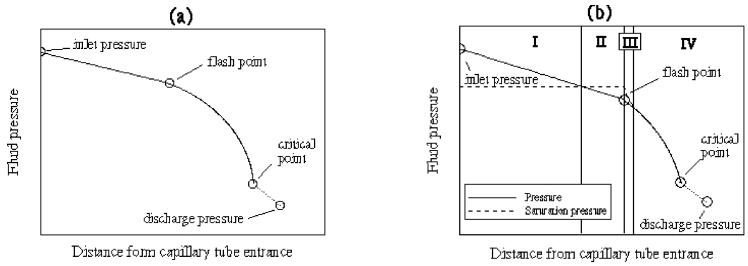

Figure 2.11: Capillary tube: pressure drop (a), phenomena occurring (b).

The expansion process: the refrigerant flow through the capillary tube changes from single phase state to two-phase state. Four states appear during the whole process (Fig. 2.11(b)):

- *Single-phase.* In this region $p \geq p_{sat}$ and $x_g = 0$, where p_{sat} is the saturation pressure at $h_b ub = h$. The heat transfer coefficient and the friction factor are calculated from single-phase empirical correlation.

- *Metastable liquid.* This region is defined by $p_{sat} > p \geq p_v$ and $x_g = 0$. The pressure of vaporization (p_v) is estimated with the correlation proposed by Chen et al. [13]. The fluid properties are evaluated at the liquid saturation conditions

(at the present fluid pressure). The friction factor and the heat transfer coefficient are determined with single-phase flow correlations.

- *Metastable two-phase.* This region includes $p_v > p$, $0 < x_g \leq x_{g,equi}$ and $0 \leq y \leq 1$. The heat transfer coefficient and the friction factor are evaluated with two-phase flow correlations. Feburie et al. [14] define the variable $y = (m_l + m_g)/(m_g + m_l + m_m)$ where m_m corresponds to the superheated liquid.

$$h = (1 - y)h_m + (y - x_g)h_l + x_g h_v \tag{2.30}$$

  $x_{g,equi}$ is calculated from the equation 2.30, where $y = 1$ and h_m is the superheated liquid enthalpy.

- *Two-phase in thermodynamic equilibrium.* In this region $p_v > p$ and $x_{g,equi} < x_g < 1$. Heat transfer coefficient and friction factor are evaluated with appropriate correlations of two-phase flow.

Capillary Tube Numerical Resolution: the simulation of the capillary tube is carried out in two steps:

- *Calculation of critical point:* this condition occurs when the mass flow remains constant even when the evaporating temperature decreases (lower discharge pressure). This critical limit is used to determine the capillary tube working conditions (critical or non-critical); the critical limit occurs when the entropy generation equation is not accomplished ($s_{gen,i} < 0$). In the numerical model the critical limit is reached when the entropy generation equation is accomplished along the whole tube except at the outlet position. It can be alternatively calculated when dp/dz approaches to infinity at the capillary tube end or $dz/dp < \epsilon$. The critical limit values of $\dot{m}_{cr}$ and p_{cr} define the critical conditions.

- *Determination of actual capillary condition:* if the flow is non-critical ($p_{dis} > p_{cr}$) new iterations are carried out in order to obtain the refrigerant thermal and fluid-dynamic behaviour (the mass flow rate is obtained when the discharge pressure is equal to the calculated capillary tube outlet pressure). However, with critical flow ($p_{dis} < p_{cr}$) an additional control volume at the capillary tube outlet end is considered. In this additional control volume the inlet section corresponds to the capillary tube inner diameter while the outlet section corresponds to the discharge tube inner diameter. At this control volume the pressure is considered constant and the heat transfer and transient terms are

neglected in the energy equation, in order to calculate the new enthalpy at the discharge of the capillary tube.

The boundary conditions considered are the fluid inlet and discharge pressures respectively.
For an extended view of the model on the numerical simulation see [15–17].

2.3.4 Micro-metric expansion valves

The micro-metric expansion valves have been simulated with numerical model based on considering the flow through the valves as an isoenthalpic sudden contraction. Mass flow rate is evaluated using the following equation:

$$\dot{m}_r = A_D C_D \sqrt{2\rho_i(p_i - p_o)} \tag{2.31}$$

where A_D is the flow area and C_D is the flow coefficient.
The flow area is evaluated from the geometrical characteristics of the selected valve and the opening level, which is function of the number of turns needed to open the valve. The equation (2.32) is the correlation [18] of the flow coefficient C_D with valve inlet and valve outlet refrigerant density, based on accurate study on the mass flow characteristic of thermal expansion valve.

$$C_D = 0.02005\sqrt{\rho_i} + \frac{0.634}{\rho_o} \tag{2.32}$$

2.4 Pump

As in the compressor and the expansion devices, the pump is simulated by means of the information provided by the supplier from an empirical modelization. The working curves of the pump (volumetric flow and torque) have been generated for each type of pump as a function of the pressure drop and maximum speed (rpm) considering reference inlet viscosities (1 cP and 100 cP). Correction factor for the inlet viscosity has been supplied to obtain the correct torque. Figs. 2.12-2.14 show the typical working curves.

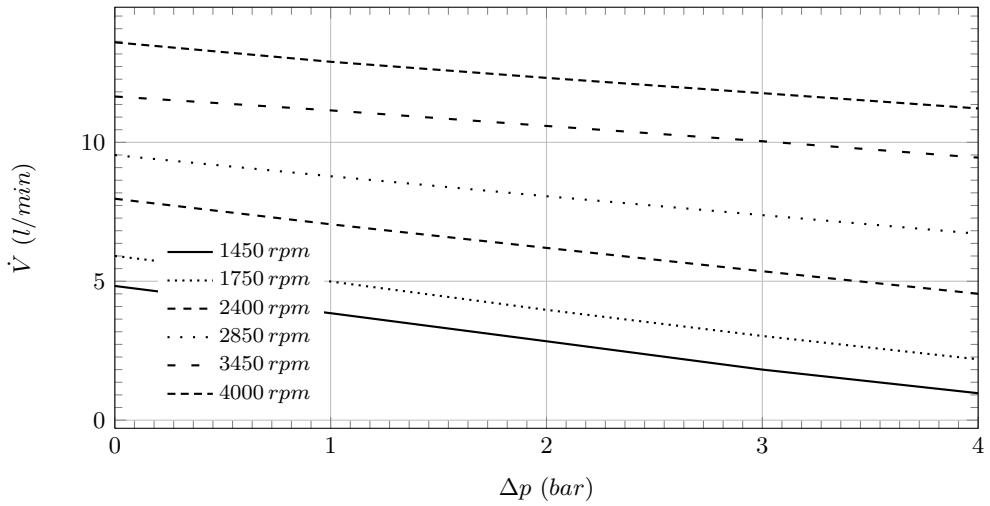

Figure 2.12: Volumetric flow. ($\mu = 1\,cP$)

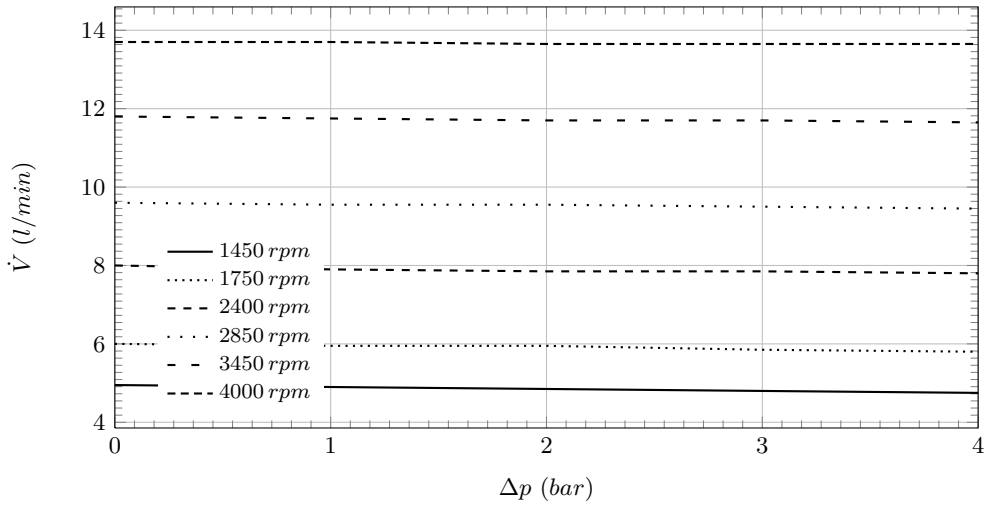

Figure 2.13: Volumetric flow. ($\mu = 100\,cP$)

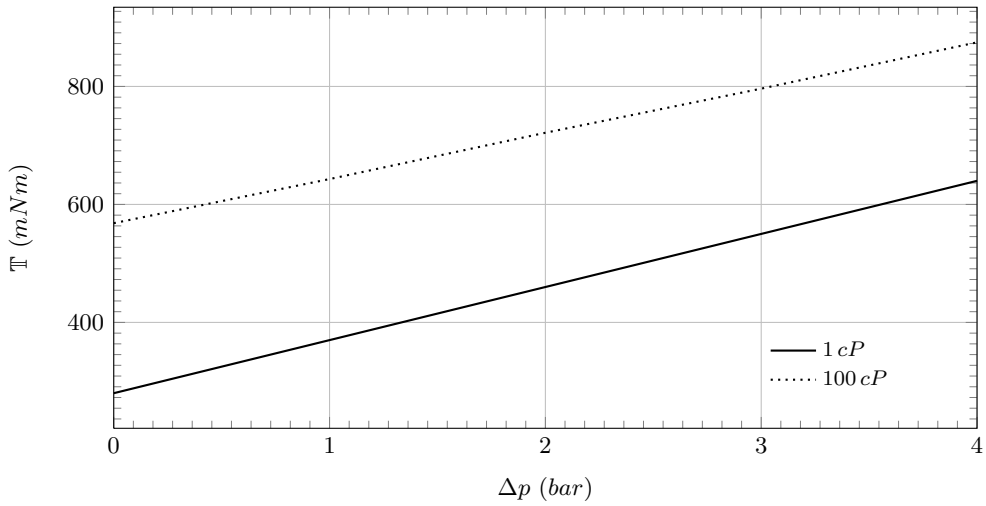

Figure 2.14: Torque.

$$\dot{V} = f(\Delta p, rpm, \mu) \tag{2.33}$$

(2.34)

$$\mathbb{T} = f(\Delta p, rpm, \mu) \tag{2.35}$$

With the supplier information, two matrices have been generated. The first one gave us information about volumetric flow, the second one information about torque. The matrices are used to calculate the value of the mass flow and the pump work in the global simulation of the refrigerating system. When a value between the calculated matrix points is required, it is obtained by bilinear interpolation.
From the mass equation (2.1) and the energy equation (2.3) and using the pump as a macro control volume of discretization, the following mass and energy equation for the pump are obtained.

$$\dot{m}_o - \dot{m}_i = 0 \tag{2.36}$$

$$\dot{m}(h_o - h_i) = \dot{Q}_{pump} - \dot{W}_p \tag{2.37}$$

where $\dot{W}_p$ is the work applied to the refrigerant, obtained with motor torque and speed. In this element an adiabatic process is assumed, while the kinetic and potential energy are considered negligible.

2.5 Receivers

Receiver is a specially important component in the overfeed refrigerating systems, although it is also possible to find this element in other refrigerating systems. In this section, the mathematical formulation and numerical algorithm used to simulate this element is presented in detail. The model implemented for receivers is based on a full energy balance, where the following hypothesis have been assumed: i) refrigerant inside the receiver is divided into perfectly mixed liquid and vapour zones; ii) the internal energy is equal to the enthalpy in liquid zone; iii) the kinetic and potential energy effects are neglected; iv) when mixed flow enters in the receiver, it is separated instantaneously. Therefore, liquid flow enters the liquid zone and vapour flow enters the vapour zone and a net exchange of compression/expansion work between zones to change the liquid level is possible. The model presented for a general receiver (Fig. 2.15) is mainly based on the model proposed by Estrada-Flores [19].The treatment of the solid parts has been improved, and their resolution take into account the heat capacity of the insulation.

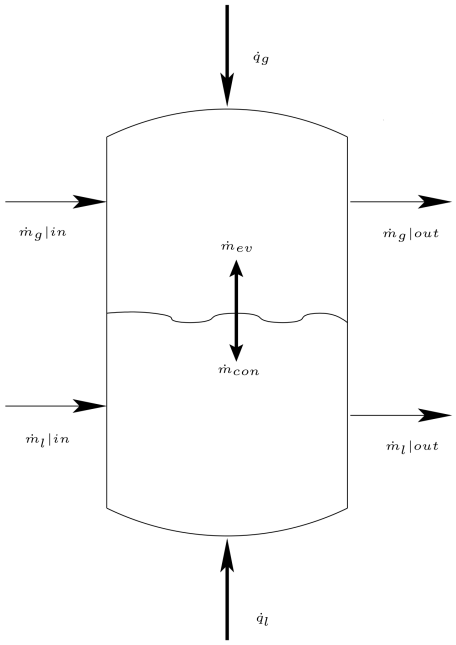

Figure 2.15: Conceptual model for receivers.

2.5.1 Refrigerant mathematical formulation

The equations (2.38) and (2.39) show the mass conservation equation with the addition of explicit terms of evaporation and condensation, applied to the liquid zone and to the vapour zone respectively.

$$\frac{dm_l}{dt} + \Sigma\dot{m}_{l,o} + \dot{m}_{ev} - \Sigma\dot{m}_{l,i} - \dot{m}_{con} = 0 \tag{2.38}$$

$$\frac{dm_g}{dt} + \Sigma\dot{m}_{g,o} + \dot{m}_{con} - \Sigma\dot{m}_{g,i} - \dot{m}_{ev} = 0 \tag{2.39}$$

The continuity equation within the liquid zone has been applied under the following considerations:

- The definition of the liquid refrigerant mass inside the receiver, $m_l = \rho_l V_l = \rho_l A z_l$.
- The variation of the liquid density is neglected.

In this case the differential equation of liquid level is:

$$\frac{dz_l}{dt} = \frac{\Sigma\dot{m}_{l,i} - \Sigma\dot{m}_{l,o} - \dot{m}_{ev} + \dot{m}_{con}}{A\rho_l} \tag{2.40}$$

The following considerations are taken into account for the governing equations of the vapour zone:

- The definition of the vapour refrigerant mass inside the receiver, $m_g = \rho_g V_g = \rho_g A z_g$.
- The relation $z = z_g + z_l$.
- z is constant so $\frac{dz_g}{dt} = \frac{d(z-z_l)}{dt} = -\frac{dz_l}{dt}$

In this case the differential equation of vapour density is:

$$\frac{d\rho_g}{dt} = \left(\frac{\frac{\rho_g}{\rho_l}(\Sigma\dot{m}_{l,i} - \Sigma\dot{m}_{l,o}) + (\dot{m}_{ev} - \dot{m}_{con})(1 - \frac{\rho_g}{\rho_l}) + \Sigma\dot{m}_{g,i} - \Sigma\dot{m}_{g,o}}{A(z_T - z_l)} \right) \tag{2.41}$$

Equations (2.42) and (2.43) show the energy equation applied on liquid zone and vapour zone respectively:

$$\frac{d(m_l u_l)}{dt} + \Sigma\dot{m}_{l,o}h_{l,o} - \Sigma\dot{m}_{l,i}h_{l,i} + \dot{m}_{ev}h_{g,sat} - \dot{m}_{con}h_{l,sat} = \Sigma\dot{Q}_l - \dot{W}_s \quad (2.42)$$

$$\frac{d(m_g u_g)}{dt} + \Sigma\dot{m}_{g,o}h_{g,o} - \Sigma\dot{m}_{g,i}h_{g,i} + \dot{m}_{con}h_{l,sat} - \dot{m}_{ev}h_{g,sat} = \Sigma\dot{Q}_g + \dot{W}_s \quad (2.43)$$

considering equations (2.40) and (2.41), and $\frac{d(m_l u_l)}{dt} = m_l\frac{du_l}{dt} + u_l\frac{dm_l}{dt}$, $\frac{d(m_g u_g)}{dt} = m_g\frac{du_g}{dt} + u_g\frac{dm_g}{dt}$; and approximating $u_l \approx h_l$ and $\frac{du_l}{dt} \approx \frac{dh_l}{dt}$:

$$\frac{dh_l}{dt} = \Sigma\dot{q}_l - \dot{\omega}_s + \frac{\Sigma\dot{m}_{l,in}(h_{l,in} - h_l) - \dot{m}_{ev}(h_{g,sat} - h_l) + \dot{m}_{con}(h_{l,sat} - h_l)}{m_l} \quad (2.44)$$

$$\frac{dh_g}{dt} = \Sigma\dot{q}_g + \dot{\omega}_s + \frac{1}{\rho_g}\frac{dp_g}{dt} + p_g\frac{d\frac{1}{\rho_g}}{dt} + \frac{\Sigma\dot{m}_{g,i}h_{g,i} - \Sigma\dot{m}_{g,o}h_{g,o} - (\Sigma\dot{m}_{g,i} - \Sigma\dot{m}_{g,o} + \dot{m}_{ev} - \dot{m}_{con})(h_g - \frac{p_g}{\rho_g}) + \dot{m}_{ev}h_{g,sat} - \dot{m}_{con}h_{l,sat}}{m_g} \quad (2.45)$$

The equations (2.46) and (2.47) show the mass conservation equations for steady state conditions for liquid zone and vapour zone respectively.

$$\Sigma\dot{m}_{l,i} - \Sigma\dot{m}_{l,o} - \dot{m}_{ev} + \dot{m}_{con} = 0 \quad (2.46)$$

$$\Sigma\dot{m}_{g,i} - \Sigma\dot{m}_{g,o} + \dot{m}_{ev} - \dot{m}_{con} = 0 \quad (2.47)$$

where:
$\Sigma\dot{m}_{g,i} = \Sigma\dot{m}_{y,i}x_{g,y,i}$ and $\Sigma\dot{m}_{g,o} = \Sigma\dot{m}_{y,o}x_{g,y,o}$, for y = 1 to n.

The equation (2.47) can be rewritten as a function of mass fractions at the entrance, therefore the equations becomes:

$$x_{g,n,i} = \frac{\Sigma\dot{m}_{g,o} - \dot{m}_{ev} + \dot{m}_{con} - \Sigma\dot{m}_{y,i}x_{g,y,i}}{\dot{m}_{n,i}} \quad (2.48)$$

where:
$x_{g,y,i} = \frac{h_{i,y} - h_{l,sat}}{h_{g,sat} - h_{l,sat}}$ for y = 1 to n-1

The equations (2.49) and (2.50) show the energy conservation equations for steady state conditions for liquid zone and vapour zone respectively.

$$\frac{\Sigma \dot{m}_{l,i}(h_{l,i} - h_l) - \dot{m}_{ev}(h_{g,sat} - h_l) + \dot{m}_{con}(h_{l,sat} - h_l)}{m_l} = -\Sigma \dot{q}_l + \dot{\omega}_s \qquad (2.49)$$

$$\frac{\Sigma \dot{m}_{g,i} h_{g,i} - \Sigma \dot{m}_{g,o} h_g - (\Sigma \dot{m}_{g,o} - \Sigma \dot{m}_{g,i} + \dot{m}_{ev} - \dot{m}_{con})(h_g - \frac{p_g}{\rho_g})}{m_g} + \frac{\dot{m}_{ev} h_{g,sat} - \dot{m}_{con} h_{l,sat}}{m_g} = -\Sigma \dot{q}_g - \dot{\omega}_s \qquad (2.50)$$

An iterative procedure is used to obtain the pressure inside the receiver.
Using the relation ($h_{n,i} = (1 - x_{g,n,i})h_{l,sat} + x_{g,r} h_{g,sat}$) between the enthalpy of the point (inlet the receiver $h_{n,i}$) in two-phase state, the liquid saturation and vapour saturation enthalpy ($h_{l,sat}$, $h_{g,sat}$ at pressure in the receiver),we obtain the pressure inside the receiver.
Therefore the p_g is a function of the gas enthalpy inside the receiver and also of the inlet enthalpies.

2.5.2 Evaporated-Condensed flow analysis

From the energy conservation equation applied to liquid (2.44) and to gas (2.45), mass flow evaporated and condensed are obtained respectively when the phenomena happens (condensation only if vapour is saturated, evaporation only if liquid is saturated). The criteria used to define the state were:

- when $h_l < h_{l,sat}$ at p_g the liquid state was sub-cooled.
- when $h_g - \frac{p_g}{\rho_g} > h_{g,sat} - \frac{p_g}{\rho_{g,sat}}$ at p_g the vapour state was superheated.
- in any other cases, liquid or vapour were assumed saturated.

The last criterion implies that in cases in which the zone (g/l) properties define a mixture, instantaneous separation of liquid and vapour occurs and the zone affected would adopt saturated properties. The adequate evaporated-condensed flow is calculated in order to fulfill the energy equation in the zone (g/l).
If the zone (g/l) properties define a mixture in a saturated zone, the evaporated-condensed flow must be such that the saturation conditions continue and fulfill the energy equation in the zone (g/l).

Rearranging equations (2.44) and (2.45) with the values of saturation ($h_l = h_{l,sat}$ and $h_g = h_{g,sat}$) respectively, the equations of evaporated mass flow (2.51) and condensed mass flow (2.52) are obtained.

$$\dot{m}_{ev} = \frac{\Sigma \dot{q}_l - m_l(\frac{dh_l}{dt}) - \dot{\omega}_s}{h_{g,sat} - h_{l,sat}} \tag{2.51}$$

$$\begin{aligned} \dot{m}_{con} = & \frac{m_g[\frac{dh_g}{dt} - \frac{dp_g}{\rho_g dt} - \frac{p_g d(\frac{1}{\rho_g})}{dt}] - (\Sigma \dot{m}_{g,i} h_{g,i} - \Sigma \dot{m}_{g,o} h_{g,sat})}{h_{g,sat} - \frac{p_g}{\rho_{g,sat}} - h_{l,sat}} \\ & + \frac{(\Sigma \dot{m}_{g,i} - \Sigma \dot{m}_{g,o} + \dot{m}_{ev})(h_{g,sat} - \frac{p_g}{\rho_{g,sat}}) - \dot{m}_{ev} h_{g,sat} + \Sigma \dot{q}_g + \dot{\omega}_s}{h_{g,sat} - \frac{p_g}{\rho_{g,sat}} - h_{l,sat}} \end{aligned} \tag{2.52}$$

With the steady state conditions the transient terms of the energy conservation equation applied to liquid (2.51) and applied to gas (2.52) disappear.
The criteria used to define the state in transient regime is also valid for steady state regime.

2.5.3 Solid elements analysis

A one-dimensional temperature distribution is assumed in each receiver wall (shell + insulation) for each internal state zone (l/g), (Fig. 2.16). Internal/external convection heat transfer and energy accumulation have been considered. The following equations (2.53)-(2.56) show the set of heat conduction discretized equations, which are solved using the TDMA algorithm [20].

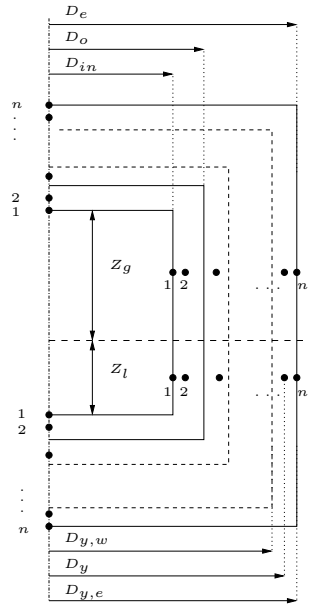

Figure 2.16: Discretization of solid part.

- Lateral wall:

$$a_P T_{wall,P} = a_W T_{wall,W} + a_E T_{wall,E} + b \tag{2.53}$$

Table 2.1 shows the definition of the equation coefficients for lateral walls. $\lambda_{h,k}$ k = e, w is the harmonic mean for λ in each node [20]. And i=l for liquid zone and i=g for vapour zone;

Table 2.1: Energy equation coefficients,lateral walls.

Node	a_P	a_W	a_E	b
1	$a_E + a_W + \alpha_{int,i} A_{int,i}$	0.0	$\frac{\lambda_{h,e} A_e}{\Delta x_E}$	$\alpha_{int,i} A_{int,i} T_{ref,i}$
y	$a_E + a_W + \frac{(\rho c_p V_y)_i}{\Delta t}$	$\frac{\lambda_{h,w} A_w}{\Delta x_W}$	$\frac{\lambda_{h,e} A_e}{\Delta x_E}$	$\frac{(\rho c_p V_y)_i T^o_{wall,P}}{\Delta t}$
n	$a_E + a_W + \alpha_{ext,i} A_{ext,i}$	$\frac{\lambda_{h,w} A_w}{\Delta x_W}$	0.0	$\alpha_{ext,i} A_{ext,i} T_{amb}$

where:
$V_y = \frac{\pi}{4}(D^2_{y,e} - D^2_{y,w}) z_i$

$$\dot{Q}_{int,i} = \alpha_{int,i} A_{int,i} (T_{wall,1} - T_{ref,i}) \tag{2.54}$$

$$\dot{Q}_{ext,i} = \alpha_{ext,i} A_{ext,i} (T_{amb} - T_{wall,n}) \tag{2.55}$$

where:
$A_{int,i} = \pi D_{in} Z_i$ and $A_{ext,i} = \pi D_e Z_i$

- Top or bottom wall:

$$a_P T_{wall} = a_S T_{wall,S} + a_N T_{wall,N} + b \tag{2.56}$$

Table 2.2 shows the definition of the equation coefficients for top and bottom walls.

Table 2.2: Energy equation coefficients, top and bottom walls.

Node	a_P	a_S	a_N	b
1	$a_N + a_S + \alpha_{int,i} A_{int,i}$	0.0	$\frac{\lambda_{h,n} A_n}{\Delta x_N}$	$\alpha_{int} A_{int,i} T_{ref,i}$
y	$a_S + a_N + \frac{(\rho c_p V_y)_i}{\Delta t}$	$\frac{\lambda_{h,s} A_s}{\Delta x_S}$	$\frac{\lambda_{h,n} A_n}{\Delta x_N}$	$\frac{(\rho c_p V_y)_i T^o_{wall,P}}{\Delta t}$
n	$a_S + a_N + \alpha_{ext,i} A_{ext,i}$	$\frac{\lambda_{h,s} A_s}{\Delta x_S}$	0.0	$\alpha_{ext,i} A_{ext,i} T_{amb}$

where:
$V_y = \frac{\pi}{4}(D_y^2) e_y$

$$\dot{Q}_{int,i} = \alpha_{int,i} A_{int,i} (T_{wall,1} - T_{ref,i}) \tag{2.57}$$

$$\dot{Q}_{ext,i} = \alpha_{ext,i} A_{ext,i} (T_{amb} - T_{wall,n}) \tag{2.58}$$

where:
$A_{int,i} = \frac{\pi}{4} D_{in}^2$ and $A_{ext,i} = \frac{\pi}{4} D_e^2$
i=l, t=bottom for liquid zone and i=g, t=top for vapour zone;

The previous equations are also used for the steady state regime, where the transient terms become zero.

2.5.4 Numerical methodology

In this section, the characteristic numerical aspects for transient and steady state regime simulation will be presented.
The algorithm to simulate the transient behaviour of the receiver uses a 4th order Runge-Kutta procedure (Fig. 2.17). Its implementation demands the evaluation and updating of the values of equations (2.40), (2.41), (2.44), (2.45), (2.51), such as pressure and enthalpies.
The relaxation factor (f_r) value depends on the variable and on the number of iterations carried out. For $\dot{m}_{ev},\ \dot{m}_{con}$ *and* $\dot{\omega}_s$ is taken as 0.3, when number of iterations are lower than 20. For the others variables f_r=1.0 is imposed . If the number of iteration is higher than 20 $f_r = 0.2$ for $\dot{m}_{ev},\ \dot{m}_{con}$ *and* w_s and 0.5 for the other variables is recommended.

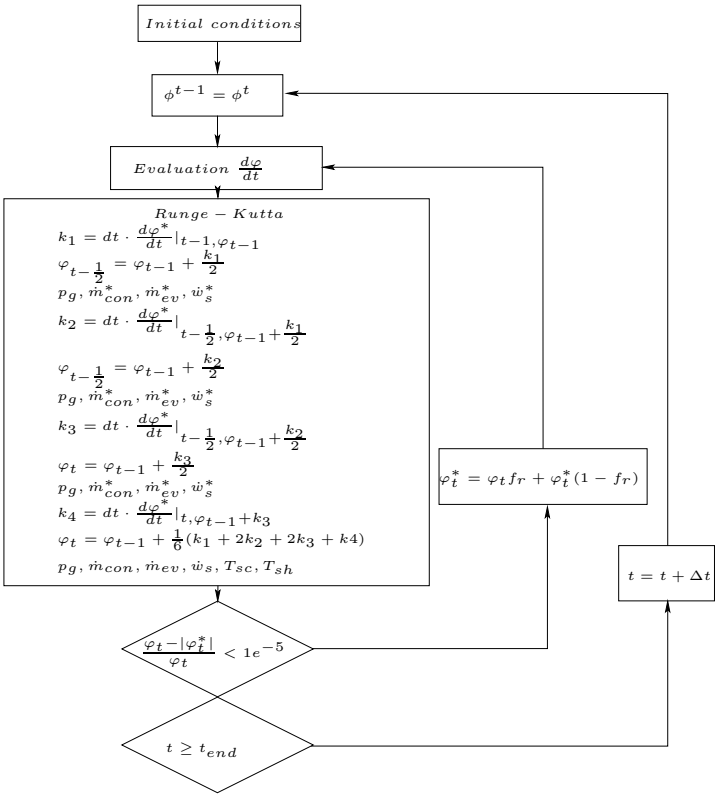

Figure 2.17: Algorithm for transient regime.

Evaporation and condensation flux calculations

To evaluate these two fluxes five derivative terms are used: liquid enthalpy, vapour enthalpy, vapour pressure, vapour mass and vapour density. These five derivative terms are not the same as those used to calculate the variables of the receiver. These terms are evaluated using a combination of values of the previous time step and the values of current time step (equation (2.59)).

$$\frac{d\varphi}{dt} = \frac{\varphi^{t} - \varphi^{t-dt}}{dt} \tag{2.59}$$

where φ is h_l, h_g, p_g, m_g or ρ_g. Table 2.3 resumes the with four possible states and the equations used to solve the variables, in unsteady state.

Table 2.3: Models for transient regime.

	Saturated liquid	Subcooled liquid
Saturated vapour	$\dot{m}_{ev}$ equation (2.51) $\dot{m}_{con}$ equation (2.52) z_l equation (2.40) ρ_g equation (2.41) $h_l = h_{liq,sat}(p_g)$ $h_g = h_{vap,sat}(p_g)$ $\Delta T_{sc} = 0.0$ $\Delta T_{sh} = 0.0$ $p_g = f(h_g, \rho_g)$	$\dot{m}_{ev} = 0.0$ $\dot{m}_{con}$ equation (2.52) z_l equation (2.40) ρ_g equation (2.41) h_l equation (2.44) $h_g = h_{vap,sat}(p_g)$ $\Delta T_{sc} > 0.0$ $\Delta T_{sh} = 0.0$ $p_g = f(h_g, \rho_g)$
Superheated vapour	$\dot{m}_{ev}$ equation (2.51) $\dot{m}_{con} = 0.0$ z_l equation (2.40) ρ_g equation (2.41) $h_l = h_{liq,sat}(p_g)$ h_g equation (2.45) $\Delta T_{sc} = 0.0$ $\Delta T_{sh} > 0.0$ $p_g = f(h_g, \rho_g)$	$\dot{m}_{ev} = 0.0$ $\dot{m}_{con} = 0.0$ z_l equation (2.40) ρ_g equation (2.41) h_l equation (2.44) h_g equation (2.45) $\Delta T_{sc} > 0.0$ $\Delta T_{sh} > 0.0$ $p_g = f(h_g, \rho_g)$

Table 2.4 shows the equations used to solve the variables in steady state for the four possible states in the receiver.

Table 2.4: Models for steady state regime.

	Saturated liquid	Subcooled liquid
Saturated vapour	$\dot{m}_{ev}$ equation (2.51) $\dot{m}_{con}$ equation (2.52) $z_l = cte$ $\rho_g = f(h_g, p_g)$ $h_l = h_{liq,sat}(p_g)$ $h_g = h_{vap,sat}(p_g)$ $\Delta T_{sc} = 0.0$ $\Delta T_{sh} = 0.0$ $p_g = f(h_g, h_{in}, hine)$	$\dot{m}_{ev} = 0.0$ $\dot{m}_{con}$ equation (2.52) $z_l = cte$ $\rho_g = f(h_g, p_g)$ h_l equation (2.44) $h_g = h_{vap,sat}(p_g)$ $\Delta T_{sc} > 0.0$ $\Delta T_{sh} = 0.0$ $p_g = f(h_g, h_{in}, hine)$
Superheated vapour	$\dot{m}_{ev}$ equation (2.51) $\dot{m}_{con} = 0.0$ $z_l = cte$ $\rho_g = f(h_g, p_g)$ $h_l = h_{liq,sat}(p_g)$ h_g equation (2.45) $\Delta T_{sc} = 0.0$ $\Delta T_{sh} > 0.0$ $p_g = f(h_{in}, hine, \dot{m}_{ev}, \dot{m}_{con})$	$\dot{m}_{ev} = 0.0$ $\dot{m}_{con} = 0.0$ $z_l = cte$ $\rho_g = f(h_g, p_g)$ h_l equation (2.44) h_g equation (2.45) $\Delta T_{sc} > 0.0$ $\Delta T_{sh} > 0.0$ $p_g = f(h_{in}, hine, \dot{m}_{ev}, \dot{m}_{con})$

Fig. 2.18 shows the algorithm used to solve the receivers in steady state.

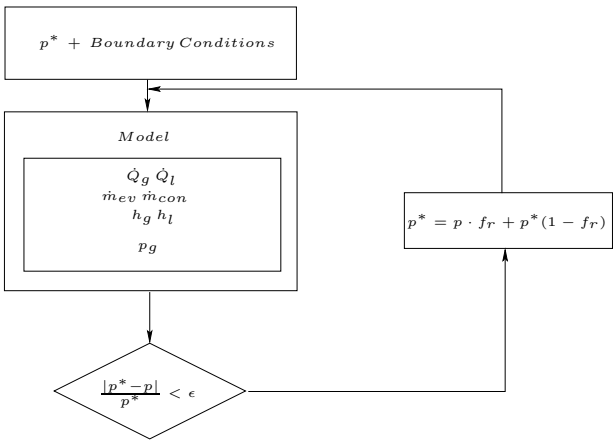

Figure 2.18: Algorithm for steady state regime.

2.5.5 Transition criteria

The criteria used to evaluate the state of the zones are discussed below. The criteria are valid for both transient and steady state regime.

Liquid zone (Steady state / Transient regime)

- *Transition from sub-cooled liquid to saturated liquid.* The transition occurs when the value of liquid enthalpy obtained from the derivative equations (equation (2.44) in transient regime and equation (2.49) in steady state regime) is greater than the saturated liquid enthalpy at vapour pressure. This implies that the scheme of calculation of the liquid enthalpy fails at time t, and the enthalpy must be evaluated as the saturated liquid enthalpy at vapour pressure.
  $h_l^t \geq h_{l,sat}^t$; *transition detected* $\longrightarrow h_l^t = h_{l,sat}^t$

- *Transition from saturated liquid to sub-cooled liquid.* This transition occurs when the evaporation flux (equation (2.51)) calculated is negative. It implies that the liquid enthalpy is less than the saturated liquid enthalpy at the vapour pressure.
  $\dot{m}_{ev} < 0.0$ *transition detected* $\longrightarrow \dot{m}_{ev} = 0.0$

Vapour zone (Steady state / Transient regime)

- *Transition from superheated vapour to saturated vapour.* The transition occurs when the value of vapour internal energy obtained from the derivative equations (equations (2.45), (2.41) in transient regime and equation (2.50) in steady state regime) and vapour pressure is less than the saturated vapour internal energy. This implies that the scheme of calculation of the vapour enthalpy fails at time t, and the enthalpy must be evaluated as the saturated vapour enthalpy at vapour pressure.
  $h_g - \frac{p_g}{\rho_g} \leq h_{g,sat} - \frac{p_g}{\rho_{g,sat}}$; *transition detected* $\longrightarrow h_g^t = h_{g,sat}^t$

- *Transition from saturated vapour to superheated vapour.* This transition occurs when the condensation flux (equation (2.52)) calculated is negative. It implies that the vapour enthalpy is greater than the saturated vapour enthalpy at the vapour pressure.
  $\dot{m}_{con} < 0.0$ *transition detected* $\longrightarrow \dot{m}_{con} = 0.0$

2.6 Heat Exchangers and Insulated Pipes

In this section the mathematical formulation for different type of heat exchangers (double pipe heat exchangers and fin-and-tube heat exchangers) is presented, as well as the connecting insulated pipes. The simulation of this elements have been established with two levels (global balances, and detailed balances).
The range of heat exchangers can be extended to other types with the appropriate parametrization of their efficiencies in the first level of simulation. In the second level of simulation is focused on double pipe heat exchangers since the CTTC laboratory has more experience on it, however we are working on the implementation of the new type of heat exchangers as fin-and-tube heat exchangers.

2.6.1 Global balances Model

Heat exchangers: The first level of simulation considers the whole heat exchanger as a single control volume in steady state. Over this macro control volume the integral conservation equations of mass (2.1), momentum (2.2) and energy (2.3) have been applied. The discretized form of the governing equations is shown in equations (2.60)-(2.62) for heat exchangers and (2.68)-(2.70) for the insulated pipes. Potential and kinetic energy increments are considered not relevant. Both radiative and convective heat transfer to or from the ambient are also considered not relevant.

$$\dot{m}_o - \dot{m}_i = 0 \tag{2.60}$$

$$p_o - p_i = -k\frac{\rho v^2}{2} \tag{2.61}$$

$$\dot{m}(h_o - h_i) = \epsilon(\dot{m}c_p)_{min}\,(T_{s,i} - T_i) = \dot{m}_s c_p\,(T_{s,i} - T_{s,o}) = \dot{Q} \tag{2.62}$$

A semi-analytical method ($\epsilon - NTU$) is used to solve the thermal behaviour of the heat exchangers. Their efficiencies have been integrated with a parametrization of the heat exchangers obtained with a high level simulation software developed in the CTTC group (CHESS, Compact Heat Exchanger Simulation Software).

2.6.2 Advanced Modelization of Compact Heat Exchanger from CTTC

The CTTC's software is based on an advanced simulation model (Oliet et al.[21–24]), which solves the thermal and fluid-dynamic behaviour of compact heat exchangers. The developed resolution strategy is based on a discretisation around the tubes as small heat exchangers (Fig. 2.19). Over these macro-control volumes, the governing

equations have been applied for both fluids (refrigerant and secondary coolant) under the following assumptions: unsteady, unidimensional and radiative heat transfer and viscous dissipation negligible. The energy equation has been applied for the solids elements. The fluid-solid interaction is represented with friction factors, heat transfer coefficients and local pressure loss coefficients, which are evaluated with empirical information (correlations published in the open literature).

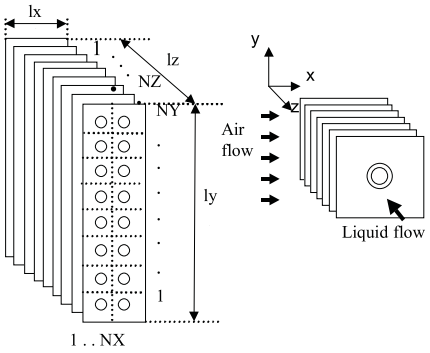

Figure 2.19: Heat exchanger schematic of the discretization

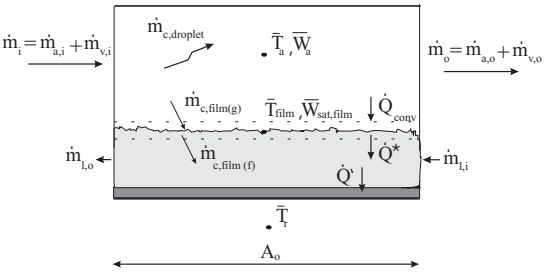

Figure 2.20: Wet heat exchanger analysis - main terms

The internal flow is solved integrating the governing equations (mass, momentum and energy) over the interior of the tube section corresponding to the macro control volume of the heat exchanger. The formulation is developed in general form considering two-phase fluid (see section 2.6.2).
In the air side of heat exchanger the heat transfer and pressure drop at each macro-control volume are calculated by the resolution of the governing equations (mass, momentum and energy), assuming a uniform velocity distribution across the flow control volume section (unidimensional treatment). The global airflow is divided depending on the flow resistance of each zone of the heat exchanger, to get a uniform outlet pressure value.
Related to heat transfer, a local calculation of the psychrometric parameters (dew-point temperature) permits a determination of the dry/wet zones on the airside surfaces, and consequently of the sensible/latent heat ratios and vapour condensation rates at each macro-control volume (Fig. 2.20). In compact evaporators and aircoolers it is of great importance. In wet conditions and surface temperatures below the freezing point, frost formation is analysed, calculating the changes in frost thickness and frost density. Thus, a dry heat exchanger becomes a particular case of this analysis.

The moist airflow mathematical formulation is presented in detail in equations (2.63)-(2.67). Droplet formation in super-saturated air is taken into account. The sensible and latent energies are taken into consideration in a global air energy equation.
Dry air, water vapour, liquid film mass balance:

$$\frac{d}{dt}\left(\bar{\rho}_a V\right) + \dot{m}_{a,o} - \dot{m}_{a,i} = 0 \tag{2.63}$$

$$\frac{d}{dt}\left(\bar{\rho}_v V\right) + \dot{m}_{v,o} - \dot{m}_{v,i} = -\dot{m}_{c,film} - \dot{m}_{c,droplet} \tag{2.64}$$

$$\frac{d}{dt}\left(\bar{\rho}_w V_{film}\right) + \dot{m}_{l,o} - \dot{m}_{l,i} = \dot{m}_{c,film} \tag{2.65}$$

Energy balance over the air control volume, including liquid film interface:

$$\frac{d}{dt}\left(\overline{\rho\left(h - \frac{p}{\rho}\right)}V\right) + \dot{m}_{a,o}h_o - \dot{m}_{a,i}h_i + \dot{m}_{c,film}h_{f|_{film}} + \dot{m}_{c,droplet}h_{w|_{air,o}} = -\dot{Q}^* \tag{2.66}$$

Energy balance over the liquid film:

$$\frac{d}{dt}\left(\overline{\rho\left(h - \frac{p}{\rho}\right)}V\right)_w + \dot{m}_{l,o}h_{w|_{l,o}} - \dot{m}_{l,i}h_{w|_{l,i}} - \dot{m}_{c,film}h_{f|_{film}} = \dot{Q}^* - \dot{Q}' \tag{2.67}$$

Referring to the air fluid-dynamic behaviour, it must be underlined that the code predicts the inlet/outlet pressure drop effects, the changes in kinetic energy (and consequently an acceleration term in the momentum equations), in steady or unsteady analysis. The volume by volume analysis is finally post-processed to obtain the air global time-dependent increments in enthalpy, kinetic energy and vapour mass condensation (or frost formation).
Provided that the tube base temperatures are not always similar between contiguous tubes, transversal and longitudinal heat conduction along the fins can be of great importance. Therefore, the usual hypothesis of adiabatic boundary for the fin efficiency calculation is no longer adequate if tube wall temperatures differ between adjacent tubes. The code integrates a multidimensional simulation of the continuous fins, where the tube-fin and fin-air heats are calculated for the fin zone corresponding to the macro-control volumes, and then real fin efficiencies determined for each one of them. A cutting-cell discretization has been implemented for the fins in order to adapt to the tubes shape, allowing for a rigorous calculation of heat transfer at fin-tube joint (Fig. 2.21).

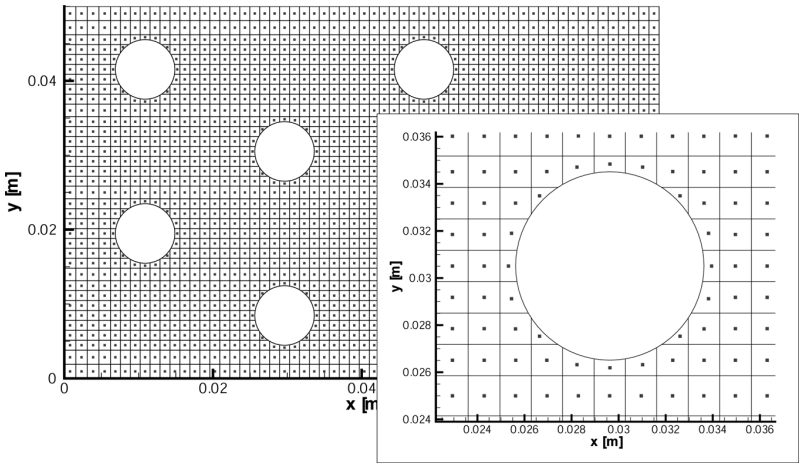

Figure 2.21: Cutting-cell discretisation of the continuous fins.

The numerical resolution of the internal fluid flow is coupled with the resolution of the air-flow and the heat conduction in the solid elements in a segregated way within a global fully implicit transient resolution algorithm.

Insulated pipes: They have been solved in the global balances model using an analytical method with a global heat transfer coefficient to simulate the heat transferred with the environment. The following equations present the discretized equations of mass, momentum and energy.

$$\dot{m}(h_o - h_i) = \dot{Q} \tag{2.68}$$

$$p_o - p_i = -k\frac{\rho v^2}{2} \tag{2.69}$$

$$\dot{Q} = (UA)\Delta T_m \tag{2.70}$$

2.6.3 Detailed Model: Mass, Momentum and Energy Equations. Heat Conduction in the Wall and Insulation Layer

In the second level of simulation the heat exchanger (double pipe heat exchangers) is divided in several control volumes. Over each control volume the integral conservation equations of mass (2.1), momentum (2.2) and energy (2.3) have been applied.
This level considers three different domains namely, the refrigerant fluid, the solid part and the secondary coolant. The resolution algorithm solves both domains iteratively until the convergence is reached. The main aspects of this level of simulation are detailed in the following lines.

To simulate the fluid flow in double pipe heat exchangers and single insulated pipes a quasi-homogeneous two-phase flow model has been used [25], [26]. It neglects the temperature difference between the liquid and vapour phases in both sub-cooled boiling and post-dry-out regimes for evaporating flows. The flow regime is obtained by means of a flow pattern map while the fluid behaviour on each regime is predicted from appropriate empirical correlations found in the technical literature. These correlations allow to predict the void fraction, the shear stress and the convective heat transfer coefficients.

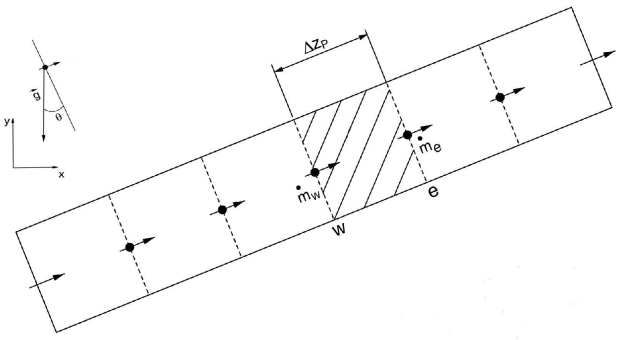

Figure 2.22: Schematic of the discretization meshes used for the fluid flow.

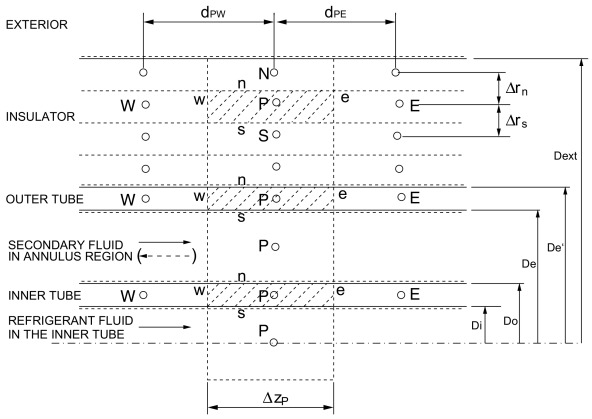

Figure 2.23: Dicretization of solids and fluids in double pipe heat exchanger.

Fig. 2.22 shows the mesh of control volumes for the fluid domain. Fig. 2.23 shows the discretization of a whole double pipe heat exchanger (solid elements and fluid domains). The main nodes assigned to the selected CVs are identified by P, while W,

E, N, S indicate their neighbours. The CVs faces are identified by lower-case letters (w, e, n, s).
Considering the characteristic geometry of ducts, the governing equations (2.1 - 2.3) have been integrated assuming the following assumptions: one-dimensional flow, non-participant radiation medium, negligible radiant heat exchange between surfaces, and negligible fluid axial heat conduction. The continuity equation is discretized as follows:

$$\frac{\overline{\rho}_{tp} - \overline{\rho}^o_{tp}}{\Delta t} S \Delta z_p + \dot{m}_e - \dot{m}_w = 0 \tag{2.71}$$

where the two-phase flow density (ρ_{tp}) is a function of the refrigerant void fraction and liquid and vapour densities. Two-phase flow density is evaluated as follows: $\rho_{tp} = \rho_g \epsilon_g + \rho_l (1 - \epsilon_g)$
The momentum equation is discretized as follows:

$$\frac{\overline{\dot{m}} - \overline{\dot{m}}^o}{\Delta t} \Delta z_p + \dot{m}_e v_e - \dot{m}_w v_w = (p_w - p_e) S - \overline{\tau} P \Delta z_p - mgsin\theta \tag{2.72}$$

where $\overline{\dot{m}} = \overline{v\rho}_{tp} S$ and $\overline{\dot{m}}^o = \overline{v}^o \overline{\rho}^o_{tp} S$. The mean mass flow rate at each control volume face is calculated using the vapour mass fraction: $\dot{m} = \dot{m}_g + \dot{m}_l = \dot{m} x_g + \dot{m}(1 - x_g)$ and the gas and liquid velocities are calculated by means of both the vapour mass fraction (x_g) and the void fraction (ϵ_g): $v_g = \frac{\dot{m} x_g}{\rho_g \epsilon_g S}$, $v_l = \frac{\dot{m}(1-x_g)}{\rho_l (1-\epsilon_g) S}$.
Rearranging in function of vapour mass fraction and void fraction, the momentum equation is written as follows:

$$\frac{\overline{\dot{m}} - \overline{\dot{m}}^o}{\Delta t} \Delta z_p + \frac{\dot{m}_e^2}{S} \left[\frac{x_{g,e}^2}{\rho_{g,e} \epsilon_{g,e}} + \frac{(1 - x_{g,e})^2}{\rho_{l,e} (1 - \epsilon_{g,e})} \right]$$
$$- \frac{\dot{m}_w^2}{S} \left[\frac{x_{g,w}^2}{\rho_{g,w} \epsilon_{g,w}} + \frac{(1 - x_{g,w})^2}{\rho_{l,w} (1 - \epsilon_{g,w})} \right] = (p_w - p_e) S - \overline{\tau} P \Delta z_p - \overline{\rho}_{tp} S \Delta z_p g sin\theta \tag{2.73}$$

The energy equation, discretized and expressed as a function of the vapour mass fraction (x_g) and the void fraction (ϵ_g), is written as:

$$\dot{Q} = \frac{\overline{\rho}_{tp} \overline{h} + \overline{\dot{m}}^2 \left(\frac{\overline{x}_g^2}{2 \overline{\rho}_g^2 \overline{\epsilon}_g^2 S^2} + \frac{(1 - \overline{x}_g)^2}{2 \overline{\rho}_l^2 (1 - \overline{\epsilon}_g)^2 S^2} \right) - \overline{p} - \overline{\rho}^o_{tp} \overline{h}^o - \overline{\dot{m}}^{o2} \left(\frac{\overline{x}_g^{o2}}{2 \overline{\rho}_g^{o2} \overline{\epsilon}_g^{o2} S^2} - \frac{(1 - \overline{x}_g)^{o2}}{2 \overline{\rho}_l^{o2} (1 - \overline{\epsilon}_g^o)^2 S^2} \right) + \overline{p}^o}{\Delta t} S \Delta z_p$$
$$\dot{m}_e \left(h_e + \frac{x_{g,e}^3}{2 \rho_{g,e}^2 \epsilon_{g,e}^2 S^2} + \frac{(1 - x_{g,e})^3}{2 \rho_{l,e}^2 (1 - \epsilon_{g,e})^2 S^2} + g y_e \right) - \dot{m}_w \left(h_w + \frac{x_{g,w}^3}{2 \rho_{g,w}^2 \epsilon_{g,w}^2 S^2} + \frac{(1 - x_{g,w})^3}{2 \rho_{l,w}^2 (1 - \epsilon_{g,w})^2 S^2} + g y_w \right) \tag{2.74}$$

where $\dot{Q} = \alpha (T_{wall,P} - \overline{T}) A$.

The solution of the fluid domain is carried out moving forward step-by-step in the flow direction. The values of the flow variables at the outlet section of each control volume are obtained by solving iteratively the resulting set of algebraic equations (continuity,momentum and energy equations) from both the known values at the inlet section and the boundary conditions.
At each CV appropriate empirical correlations are used to evaluate the shear stress, the convective heat transfer coefficient and the void fraction. The transitory solution is iteratively performed at each time step.

In the solid analysis the heat diffusion equation has been written under the following hypotheses: one dimensional transient temperature distribution (bi-dimensional for insulation layer) and heat exchanged by radiation neglected. From the integration of the energy equation over each CV we obtain the following equation [25]:

$$\rho c_p \frac{T_P - T_P^o}{\Delta t} V_P = \dot{Q}_w + \dot{Q}_e + \dot{Q}_n + \dot{Q}_s \tag{2.75}$$

where $\dot{Q}_s$, $\dot{Q}_n$, $\dot{Q}_e$ and $\dot{Q}_w$ are evaluated from the Fourier law (equation 2.76).

$$\dot{Q}_i = \lambda_i (\frac{T_j - T_P}{d_{Pj}}) A_i \tag{2.76}$$

where i = e, w, n, s and j = E, W, N, S and A_i represents the heat flux cross sectional area.
In every insulated pipe, the following equation has been obtained for each node of the grid:

$$a_P T_P = a_E T_E + a_W T_W + d \tag{2.77}$$

where the value of the coefficients at the border nodes in axial direction depend on the boundary conditions, which can be heat flux or temperature. For border nodes in radial direction forced convection is considered in the surfaces in contact with the fluid (refrigerant and secondary coolant) and for the internal faces the tube thermal conduction is considered.
The set of equations 2.77-2.81 are referred to the tube placed between the fluid domains in double pipe heat exchangers.

$$a_P = \frac{\lambda_w A}{\Delta z} + \frac{\lambda_e A}{\Delta z} + (\alpha_s P_s + \alpha_n P_n)\Delta z + \frac{A \Delta z}{\Delta t} \rho c_p \tag{2.78}$$

$$a_E = \frac{\lambda_e A}{\Delta z} \tag{2.79}$$

$$a_W = \frac{\lambda_w A}{\Delta z} \tag{2.80}$$

$$d = (\alpha_s P_s \overline{T}_S^f + \alpha_n P_n \overline{T}_N^s)\Delta z + \frac{A\Delta z}{\Delta t}\rho c_p T_P^{t,o} \tag{2.81}$$

The equation 2.82 is referred to the external tube and the insulation.

$$a_P T_P = a_E T_E + a_W T_W + a_N T_N + a_S T_S + d \tag{2.82}$$

Forced convection is considered in the surface in contact with secondary coolant, heat conduction is considered in west and east faces, and natural convection in the faces in contact with the environment. Table 2.5 shows the TDMA coefficients for internal nodes and the border TDMA coefficients in radial direction.

Table 2.5: Internal nodes coefficients, for x=2 ... x=$n_x - 1$.

Node	a_P	a_E	a_W	a_N	a_S	d
1	$a_E + a_W + a_N + a_S$	$\frac{\lambda_e A}{\Delta z}$	$\frac{\lambda_w A}{\Delta z}$	$\frac{\lambda_n P_n \Delta z}{\Delta r}$	$\alpha_s P_s$	$\frac{A\Delta z}{\Delta t}\rho c_p T_P^{t,o}$
2...$n_y - 1$	$a_E + a_W + a_N + a_S$	$\frac{\lambda_e A}{\Delta z}$	$\frac{\lambda_w A}{\Delta z}$	$\frac{\lambda_n P_n \Delta z}{\Delta r}$	$\frac{\lambda_s P_s \Delta z}{\Delta r}$	$\frac{A\Delta z}{\Delta t}\rho c_p T_P^{t,o}$
n_y	$a_E + a_W + a_N + a_S$	$\frac{\lambda_e A}{\Delta z}$	$\frac{\lambda_w A}{\Delta z}$	$\alpha_n P_n$	$\frac{\lambda_s P_s \Delta z}{\Delta r}$	$\frac{A\Delta z}{\Delta t}\rho c_p T_P^{t,o}$

Table 2.6 presents the border TDMA coefficients in the axial direction.

Table 2.6: Border nodes coefficients, for x= 1 and x=n_x.

Node x	Node y	a_P	a_E	a_W	a_N	a_S	d
1	1...n_y	1.0	0.0	0.0 *or* 1.0	0.0	0.0	T_{border} *or* 0.0
n_x	1...n_y	1.0	0.0 *or* 1.0	0.0	0.0	0.0	T_{border} *or* 0.0

The set of heat conduction equations is solved using the algorithm Gauss Seidel + TDMA. For extended view of the model and the resolution see [26]

2.7 Vapour Compression Refrigerating Systems

The formulation in the elements have been done considering the unsteady regime, in order to obtain a general formulation. The numerical strategy studied in this chapter is focused in the steady state regime of the refrigerating systems as whole. The first step in the simulations of refrigerating systems, essential to obtain the knowledge to simulate the unstaedy regime.
The proposed numerical strategy to solve the vapour compression refrigerating systems studied in this Thesis (dry expansion system with and without high pressure receiver, liquid suction systems, overfeed refrigerating system and gravity fed refrigerating system) is based on element by element methodology. Both levels of simulations presented in previous sections for each component are applied: i) the model based on global balances and ii) the model based on detailed balances. The objective of this chapter is to present the specific difficulties as well as the numerical strategy adopted to solve all the studied systems.

2.7.1 Dry Expansion Refrigerating Systems

In this section both the basic dry expansion system and a variation of it with a high pressure receiver are presented. Two levels of simulation have been developed. The first simulation model is based on global balances. This model considers the elements of the system as a macro control volumes with their particular formulation (see sections 2.1 to 2.6). The second simulation model split the elements (heat exchangers and connection tubes) in a number of finite control volumes and add an advanced model for the receivers (see sections 2.1 to 2.6). Dry expansion refrigerating systems have been thought to allow the possibility of using thermostatic expansion valves (TEV), capillary tube or micro-metric valves as expansion device. It is important to remark that the use of TEV drives to a simulation strategy different from models proposed to solve dry expansions systems with capillary or micro-metric valves developed at CTTC's group ([17, 27, 28]). The thermostatic expansion valve (TEV) is a component that needs information from the evaporator to be solved. This is the reason why the evaporator is solved together with the TEV. An alternative strategy using the superheating temperature from the previous iteration has also been tried, although does not work correctly (the convergence expected had never been reached).

Standard Dry Expansion System
The numerical resolution consists of a main program composed of different subroutines. These subroutines have been developed to solve: the refrigerant inside the ducts, inside the double pipe heat exchangers and the compression and the expansion process; the secondary coolant in the annular pipe; heat transfer in a tube with insulation, and in tube wall between refrigerant and secondary coolant. The algorithm

is organised in such a way that, at each time step, the subroutines that solve all the different components are called sequentially until the convergence is reached (see Fig. 2.24). In a constant mass prediction simulation, the discharge pressure is recalculated as a function of the refrigerating system mass.

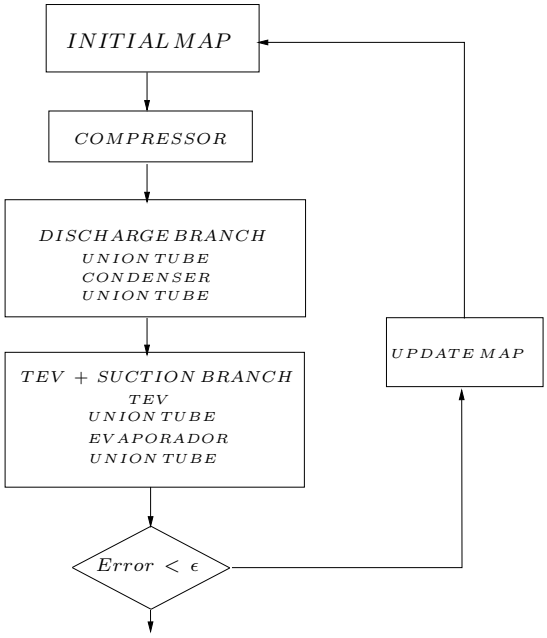

Figure 2.24: Global algorithm for standard dry expansion systems.

The strategy used to solve the couple of TEV and Evaporator consist of finding the point where the operating curve of the TEV and the operating curve of the evaporator cross (see Fig. 2.25). The secant method was implemented to solve the mass flow.

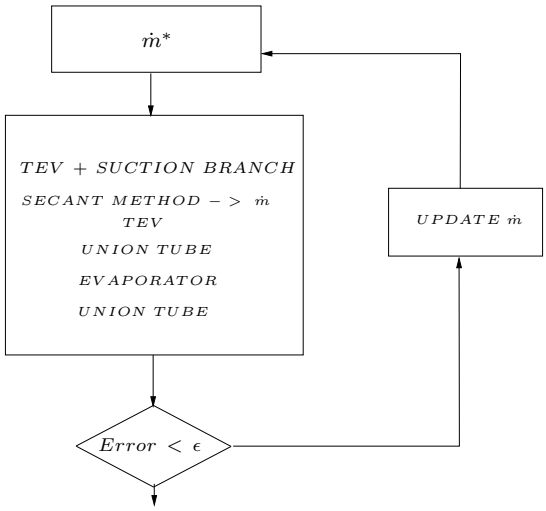

Figure 2.25: Algorithm for subroutine of couple TEV evaporator.

When a capillary tube is used as expansion device, the strategy used to solve expansion device and evaporator coupled, has been simplified. The capillary tube is independent from the super-heating temperature at the outlet of the evaporator. Therefore, the mass flow is obtained with only one iteration.
In steady state simulation, mass flow rate is constant in the whole system. Thus, the continuity equation applied over each control volume gives one independent equation less than we need. Therefore, the set of discretized equations is not determined and an additional equation is needed. The easiest way is to fix one variable.In our model the outlet compressor pressure is fixed. The table 2.7 shows the information transfer scheme for the steady state.

Table 2.7: Information transfer scheme for steady state algorithm in dry expansion refrigerating system.

Components	Inputs	Outputs
Compressor	$\dot{m}_r, p_o, h_i$	p_i, h_o
Condenser	$\dot{m}_r, p_o, h_i$	p_i, h_o
TEV	$p_i, p_o, h_i, \Delta T_{sh}$	$\dot{m}_r, h_o$
Evaporator	$\dot{m}_r, p_o, h_i$	p_i, h_o

Dry Expansion System with High Pressure Receiver
The global algorithm for standard dry expansion system also is applicable for dry expansion system with high pressure receiver (see Fig. 2.24).
Like in the standard dry expansion system, an extra condition to determine the set of discretized equations must be added. In this system the level of liquid in the

high pressure receiver is fixed. Therefore, the strategy and the subroutines used to solve this part of the system are a little bit different. In the high pressure receiver is calculated the pressure of the high pressure branch, and with one loop the pressure at the outlet of the compressor is corrected.
Table 2.8 shows the information transfer scheme for the steady state.

Table 2.8: Information transfer scheme for steady state algorithm in dry expansion refrigerating system with high pressure receiver.

Components	Inputs	Outputs
Compressor	$\dot{m}_r, p_o, h_i$	p_i, h_o
Condenser	$\dot{m}_r, p_o, h_i$	p_i, h_o
High pressure receiver	$\dot{m}_r, h_i$	h_o, p_i, p_o
TEV	$p_i, p_o, h_i, \Delta T_{sh}$	$\dot{m}_r, h_o$
Evaporator	$\dot{m}_r, p_o, h_i$	p_i, h_o

2.7.2 Liquid Suction Refrigerating System

In this section the liquid suction refrigerating system (see Fig. 1.9) numerical simulation is presented.
The global algorithm for standard dry expansion system also is applicable for this system (see Fig. 2.24).
Like in the standard dry expansion system, an extra condition to determine the set of discretized equations must be added. In this system the level of liquid in the intermediate heat accumulator is fixed. Therefore, the strategy and the subroutines used to solve this part of the system are a little bit different. In the intermediate heat accumulator is calculated the pressure of the low pressure branch, and the pressure at the high pressure branch is evaluated by the compressor. Table 2.9 shows the information transfer scheme for the steady state.

Table 2.9: Information transfer scheme for steady state algorithm in dry expansion refrigerating system with high pressure receiver.

Components	Inputs	Outputs
Compressor	$\dot{m}_r, p_i, h_i$	p_o, h_o
Condenser	$\dot{m}_r, p_i, h_i$	p_o, h_o
Coil	$\dot{m}_r, p_i, h_i$	p_o, h_o
ED	$p_i, p_o, h_i, \Delta T_{sc}$	$\dot{m}_r, h_o$
Evaporator	$\dot{m}_r, p_o, h_i$	p_i, h_o
IHA	$\dot{m}_r, h_i$	h_o, p_i, p_o

2.7.3 Overfeed Refrigerating System

In this section, it is presented the numerical strategy used to solve the overfeed refrigerating systems [29], using a step-by-step methodology and the formulation presented in the previous sections. Two models of simulation have also been developed: the first one is based on global balances while the second one is based on detailed balances.
In this refrigerating system, two strategies to solve the simulation using a model based on global balances have been developed. The first strategy is based on a element-by-element methodology to solve the discharge branch (connection tubes, condenser and high pressure receiver) and the suction side (connection tubes, low pressure receiver, evaporator and pump). This methodology calls sequentially the subroutines that solve each element until the convergence is reached for discharge branch and suction side.
The second strategy is based on resolution of one equation, which join all the elements of the discharge branch (connection tubes, condenser and high pressure receiver) and all the elements of suction side (connection tubes, low pressure receiver, evaporator and pump). These two equations (one to solve the discharge branch and another to solve the suction side) can be solved by Newton-Raphson method or by Bisection method.
The global balances model is based on the mathematical formulation presented in the sections 2.2-2.6, considering macro control volumes for each element.
A more accurate model based on detailed balances (see sections 2.2-2.6) where the heat exchangers and the connection tubes are splited in a number of finite control volumes and the advanced simulation model for receivers is used, has been developed.
The simulation resolution implemented is a step-by-step methodology that solve sequentially each element for discharge branch and suction side.
The global algorithm (Fig. 2.26) is organised in such a way that the subroutines which solve all different parts (compressor, discharge branch, expansion device and suction side) are called sequentially until the convergence is reached.

Table 2.10: Information transfer scheme for steady state algorithm in overfeed refrigerating system.

Components	Inputs	Outputs
Compressor	p_i, p_o, h_i	$\dot{m}_r, h_o$
Condenser	$\dot{m}_r, p_o, h_i$	p_i, h_o
High pressure receiver	$\dot{m}_r, h_i$	h_o, p_i, p_o
EV	$\dot{m}_r p_i, p_o, h_i$	h_o
Low pressure receiver	$\dot{m}_r, \dot{m}_e, h_{r,i}, h_{e,i}$	$h_{r,o}, h_{e,o}, p_{low-rec}$
Pump	p_i, p_o, h_i	h_o
Evaporator	$\dot{m}_e, p_o, h_i$	p_i, h_o

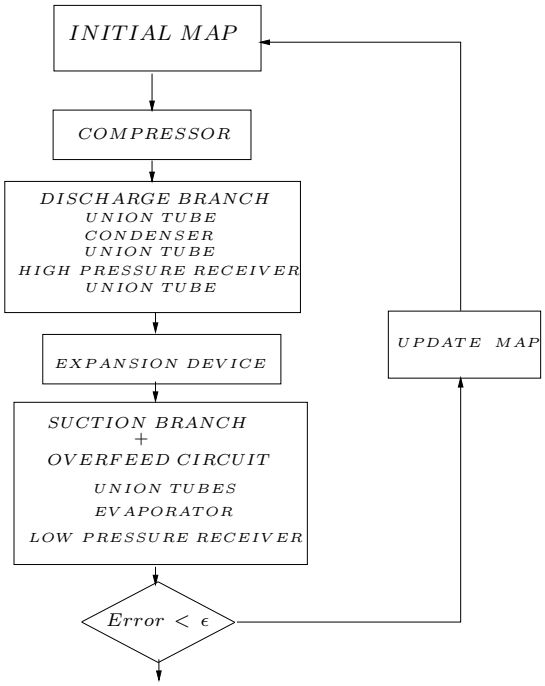

Figure 2.26: Global algorithm for overfeed refrigerating systems.

2.8 Conclusions

The aim oh this chapter is to show:

- The development and the implementation of different levels of simulation for each VCRS components under both transient and steady state conditions.
- The different coupling strategies for VCRS resolution depending on VCRS under steady state conditions.

In this chapter the conservation governing equations (continuity, momentum and energy) are presented in their integral form for the resolution of each VCRS components. Both the compressor and the expansion devices (capillary tube and micrometric valve) have been simulated with two different approaches. The first one is based on empirical data provided by the manufacturer and the second one is based on detailed methods developed at the CTTC. The others elements, pumps, thermostatic valves and electronical valves have been simulated from the manufacturer empirical data.

This chapter also presents the implementation of the information provided by the manufacturer in our code, as well as the main points of the detailed models of the compressor, the capillary tube and the micrometric valves. The isolated pipes and the double-pipe heat exchangers have been simulated with a two-phase flow model (quasi-homogeneous model). Both the equations in their discretized form and the methodology of resolution of those elements have been described. In addition, a detailed model for the simulation of the pressure receivers has been presented. Finally, the methodology for the whole refrigeration systems simulation has also been presented in detail.
In dry expansion systems with TEV has been detected the difficulty of reach the global cycle convergence with the typical element by element methodology. The solution adopted has been the resolution coupled of TEV and low pressure branch.
The simulation of the VCRS under steady sate conditions has been developed as the first approach of the VCRS simulation. The next step must be the extension to the simulation under transient conditions.

2.9 Nomenclature

A	heat transfer area $[m^2]$
D	diameter $[m]$
F	force $[N]$
L	length $[m]$
P	perimeter $[m]$
$\dot{Q}$	heat flux $[W]$
S	transversal area $[m^2]$
T	temperature $[K]$
U	overall heat transfer coefficient$[W/m^2K]$
V	volume $[m^3]$
$\dot{V}$	volumetric flux $[l/min]$
$\dot{W}$	work $[W]$
c_p	specific heat capacity at constant pressure $[J/kgK]$
e	specific energy $[J/kg]$
f	friction factor
g	gravity $[m/s^2]$
h	enthalpy $[J/kg]$
k	local loss coefficient
m	mass $[kg]$
$\dot{m}$	mass flow rate $[kg/s]$
p	pressure $[Pa]$
$\dot{q}$	specific heat flux $[W/kg]$

t	time $[s]$
v	velocity $[m/s]$
$\dot{w}$	specific work $[W/kg]$
x_g	vapour mass fraction
y	height $[m]$
z	height $[m]$

Greek symbols

α	convective heat transfer coefficient $[W/m^2K]$
Δp	pressure drop $[Pa]$
Δt	time step $[s]$
Δz	control volume length or height difference $[m]$
ε_g	void fraction
η	efficiency or ratio
λ	thermal conductivity $[W/mK]$
ρ	density $[kg/m^3]$
τ	shear stress $[N/m^2]$
θ	inclination angle

Subscripts

E	electrical
Q	heat transfer losses
aux	auxiliary
cd	condenser
cp	compressor
e	evaporator
ext	external
me	electrical-mechanical
f	fluid
fr	friction
g	gas or vapour
i	inlet or inner
ins	insulation
l	liquid
lm	logarithmic mean
loc	local
lpr	low-pressure receiver
o	outlet or outer
p	pump
s	secondary fluid

s, i	secondary inlet
s, o	secondary outlet
sat	saturated
$tube$	tube
w	wall, water
$wall$	wall

References

[1] F. Escanes et al. "Numerical simulation of hermetic reciprocating compressors. recent improvements and experimental validation". In: *Proceedings of the 1996 International Compressor Engineering Conference at Purdue*. 1996, pp. 193–198.

[2] J. Rigola et al. "Parametric study and experimental validation of small hermetic refrigeration compressors using an advanced numerical simulation model". In: *Proceedings of the 1998 International Compressor Engineering Conference at Purdue*. 1998, pp. 737–742.

[3] C.D. Pérez-Segarra, J. Rigola, and A. Oliva. "Modeling and numerical simulation of the thermal and fluid dynamics behavior of hermetic reciprocating compressors.Part I: Theoretical basis". In: *International Journal of Heat Ventilation Air Conditioning and Refrigeration Research* 9.2 (2003), pp. 215–236.

[4] J. Rigola, C.D. Pérez-Segarra, and A. Oliva. "Modeling and numerical simulation of the thermal and fluid dynamics behavior of hermetic reciprocating compressors. Part II: Experimental investigation". In: *International Journal of Heat Ventilation Air Conditioning and Refrigeration Research* 9.2 (2003), pp. 237–250.

[5] J. Rigola et al. "Detailed experimental validation of the thermal and fluid dynamic behavior of hermetic reciprocating compressors". In: *International Journal of Heat Ventilation Air Conditioning and Refrigeration Research* 10.3 (2004), pp. 291–306.

[6] Inc. ASHRAE. *ASHRAE HANDBOOK - Refrigeration*. ASHRAE, 2010.

[7] Francesco D. Premoli A. and A. Prima. *An Empirical Correlation for Evaluating Two-Phase Mixture Density Under Adiabatic Conditions. Proc. European Two-Phase Flow Group Meeting, Ispra, Milan, Italy.* 1970.

[8] S. W. Churchill. "Friction-factor equation spans all fluid-flow regimes". In: *Chemical Engineering* 84.24 (1977), pp. 91–92.

[9] L. Friedel. *Improved Friction Pressure Drop Correlation for Horizontal and Vertical Two-Phase Pipe Flow. European Two-Phase Flow Group Meeting, Ispra, Italy. Paper E2.* 1979.

[10] W.H. McAdams. *Heat Transmissions, McGraw-Hill, New York.* 1954.

[11] V. Gnielinski. "New equations for heat and mass transfer in turbulent pipe and channel flow." In: *International Chemical Engineering* 16.2 (1976), pp. 359–368.

[12] M. M. Shah. "A General Correlation for Heat Transfer during Film Condensation inside Pipes". In: *International Journal of Heat and Mass Transfer* 22.4 (1979), pp. 547–556.

[13] Z. H. Chen et al. "A Correlation for Metastable Flow of Refrigerant 12 Through Capillary Tubes." In: *ASHRAE Transactions* 96.1 (1990), pp. 550–554.

[14] V. Feburie et al. "A Model for Chocked Flow Through Cracks with Inlet Subcooling". In: *International Journal of Multiphase Flow* 19.4 (2001), pp. 541–562.

[15] O. García-Valladares, C.D. Pérez-Segarra, and A. Oliva. "Numerical simulation of of capillary-tube expansion devices behaviour with pure and mixed refrigerants considering metastable region. Part I: Mathematical formulation and numerical model". In: *Applied Thermal Engineering* 22.2 (2002), pp. 173–182.

[16] O. García-Valladares. "Numerical Simulation of Non-Adiabatic Capillary Tubes Considering Metastable Region.PArt I: Mathematical Formulation and Numerical Model". In: *International Journal of Refrigeration* 30.4 (2007), pp. 642–653.

[17] N. Ablanque. "Numerical Simulation and Experimental Validation of Vapor Compression Refrigerating Systems. Special Emphasis on Natural Refrigerants." PhD thesis. Universitat Politècnica de Catalunya, 2010.

[18] D. D. Wile. "The measurement of expansion valve capacity." In: *Refrigerating Engineering* 8 (2005).

[19] S. Estrada-Flores et al. "Simulation of transient behaviour in refrigeration plant pressure vessels: mathematical models and experimental validation". In: *International Journal of Refrigeration* 26.2 (2003), pp. 170–179.

[20] S. V. Patankar. *Numerical Heat Transfer and Fluid Flow*. Hemisphere Publishing Corporation, 1980.

[21] C. Oliet et al. "Diseño termo-fluídico de intercambiadores compactos gas-líquido. Aplicación a radiadores de automoción y evaporadores". In: *Anales de Ingeniería Mecánica (Revista de la Asociación Española de Ingeniería Mecánica, Año 10)*. 1998, pp. 581–587.

[22] C. Oliet et al. "Advanced numerical simulation of compact heat exchangers. Application to automotive, refrigeration and air conditioning industries". In: *Proceedings of the Third European Congress on Computational Methods in Applied Sciences and Engineering (ECCOMAS)*. 2000, pp. 1–19.

[23] C. Oliet et al. "Numerical simulation of dehumidifying fin-and-tube heat exchangers. model strategies and experimental comparisons". In: *Proceedings of the 2002 International Refrigeration Engineering Conference at Purdue*. 2002, pp. 1–8.

[24] C. Oliet. "Numerical Simulation and Experimental Validation of Fin-and-Tube Heat Exchangers". PhD thesis. Universitat Politècnica de Catalunya, 2006.

[25] S. Morales-Ruiz et al. "Numerical analysis of two-phase flow in condensers and evaporators with special emphasis on single-phase / two-phase transition zones." In: *Applied Thermal Engineering* 29.5-6 (2009), pp. 1032–1042.

[26] S. Morales Ruiz. "Numerical Simulation of the Thermal and Fluid Dynamics Behaviour of Liquid-Vapour Two-Phase Flow in Evaporators and Condensers." PhD thesis. Universitat Politècnica de Catalunya, 2009.

[27] J. Rigola et al. "Numerical study of a single stage vapour compression refrigerant unit using non-contaminant refrigerants". In: *Proceedings of the 1996 International Compressor Engineering Conference at Purdue*. 1996, pp. 77–82.

[28] J. Rigola et al. "Numerical study and experimental validation of a complete vapour compression refrigeration cycle". In: *Proceedings of the 1998 International Compressor Engineering Conference at Purdue*. 1998, pp. 201–206.

[29] O. García-Valladares et al. "Numerical studies of refrigerating liquid overfeed systems working with ammonia and R134a". In: *Proceedings of the 2000 International Compressor Engineering Conference at Purdue*. 2000, pp. 327–334.

Chapter 3

Verification Studies and Illustrative Results

3.1 Introduction

To provide confidence and robustness to the developed numerical simulation tools, it is necessary to carry out verification studies focused on the quality of the numerical solution by means of a critical analysis of the numerical sources of computational errors: convergence errors, discretization errors, and programming errors. The accuracy of the developed model (modelling errors) for validation purposes is presented in the chapter 4.
In the following sections, the verification studies of the different elements (receiver, double pipe heat exchanger and insulated pipe) are presented, as well as the verification studies of dry expansion, low pressure receiver and overfeed vapour compression refrigerating systems analysed in this PhD Thesis.

3.2 Receivers

In this section, verification studies of the receiver model previously explained are presented. Fig. 3.1 shows a general scheme of a receiver taking into account different inlet and outlet sections, and the heat transferred with the ambient.

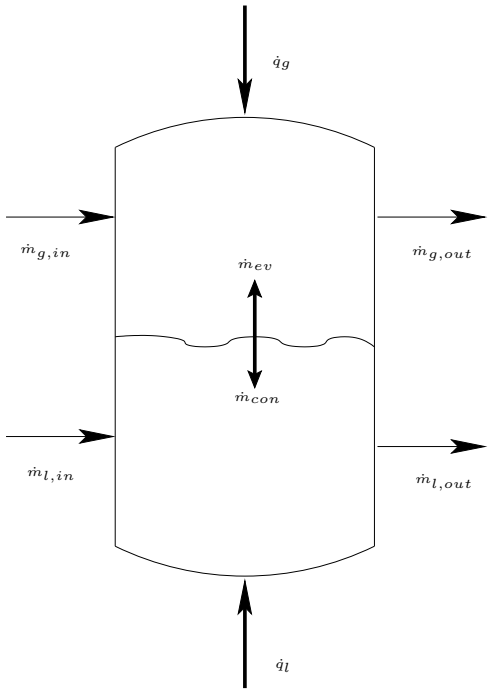

Figure 3.1: Scheme of a general receiver.

3.2.1 Steady state verification study over High Pressure Receiver (HPR)

The HPR studied in this section has one inlet placed on the top of receiver and one outlet situated on the bottom of the receiver. It is a cylindrical vessel with internal diameter of 0.3 m, external diameter of 0.306 m, insulation thickness of 20 mm, and internal height of 0.6 m.
Table 3.1 shows the boundary conditions used in the test cases carried out. For superficial heat transfer coefficients have been set reference values obtained from previous studies on this topic [1]. All numerical tests have been conducted using an environmental temperature of 25 °C.

Table 3.1: HPR: Boundary conditions.

$\dot{m}_{in}\,[kg/s]$	$\dot{m}_{out}\,[kg/s]$	$h_{in}\,[kJ/kg]$	$z_l\,[m]$	$\alpha_l\,[W/m^2K]$	$\alpha_g\,[W/m^2K]$	$\alpha_{ext}\,[W/m^2K]$
$4.4 \cdot 10^{-3}$	$4.4 \cdot 10^{-3}$	370.80	0.3	500	10	10

Table 3.2 shows the results obtained from a study of convergence criterion over a HPR.

Table 3.2: Convergence criterion influence study over a HPR.

N°Iter	ϵ	EB $[W]$	Q_l $[W]$	Q_g $[W]$
23	$1 \cdot 10^{-3}$	$5.31 \cdot 10^{-5}$	-6.1076	-5.3831
83	$1 \cdot 10^{-4}$	$5.94 \cdot 10^{-6}$	-6.1052	-5.3936
102	$1 \cdot 10^{-5}$	$5.77 \cdot 10^{-7}$	-6.1049	-5.3948
121	$1 \cdot 10^{-6}$	$5.61 \cdot 10^{-8}$	-6.1049	-5.3949
140	$1 \cdot 10^{-7}$	$5.45 \cdot 10^{-9}$	-6.1049	-5.3949

It is important to highlight that all energy balances are fulfilled, and they improve when the convergence criterion is getting more restrictive. Heat flows tend to asymptotic values.
Based on the developed studies of convergence criterion, where an important increase of CPU time was observed to obtain a small improvement in the energy balances, the strategy of using a criterion to get precision in energy balances of $1 \cdot 10^{-5}$ has been adopted for the simulation over high pressure receivers.
Illustrative results from the output values of simulation HPR test under steady state regime and using an accuracy of $\epsilon = 1 \cdot 10^{-4}$ are presented in Table 3.3, where the level of detail provided by the simulation code can be seen.

Table 3.3: Steady state results of verification case over a HPR.

	liquid	vapour
p [bar]	13.80	13.78
h [kJ/kg]	368.19	1488.60
T_{ref} [°C]	35.43	35.71
$T_{w,lat}$ [°C]	35.39	34.21
$T_{w,bot/top}$ [°C]	35.39	34.10
$\dot{m}_{evap}$ [kg/s]	-	-
$\dot{m}_{cond}$ [kg/s]	-	$4.82 \cdot 10^{-6}$
z [m]	0.30	0.30
ΔT_{sc} [°C]	0.28	-
ΔT_{sh} [°C]	-	-
$\dot{Q}_{loss}$ [W]	6.10	5.39

3.2.2 Steady state verification study over Low Pressure Receiver (LPR)

A LPR with two inlets and two outlets, with an internal diameter of 0.3 m, an external diameter of 0.306 m, an insulation thickness of 20 mm, and an internal height of 1.0 m is used for the verification tests.
The verification tests have been carried out using 25 °C as environmental temperature and using a fixed reference values for the superficial heat transfer coefficients obtained

from previous works on this topic. Table 3.4 shows the implemented boundary conditions, while Table 3.5 shows the numerical results based on convergence criterion.

Table 3.4: Boundary conditions.

$\dot{m}_r$ $[kg/s]$	$\dot{m}_e$ $[kg/s]$	$h_{in,r}$ $[kJ/kg]$	$h_{in,e}$ $[kJ/kg]$	z_l $[m]$	α_l $[W/m^2K]$	α_g $[W/m^2K]$	α_{ext} $[W/m^2K]$
$4.6 \cdot 10^{-3}$	$1.17 \cdot 10^{-2}$	369.76	578.87	0.5	500	10	10

Table 3.5: Resume convergence criterion influence over a LPR.

N°Iter	ϵ	EB $[W]$	Q_l $[W]$	Q_g $[W]$
49	$1 \cdot 10^{-4}$	$1.23 \cdot 10^{-6}$	35.4458	27.7910
70	$1 \cdot 10^{-5}$	$1.37 \cdot 10^{-8}$	35.4479	27.7918
92	$1 \cdot 10^{-6}$	$1.22 \cdot 10^{-10}$	35.4481	27.7919
113	$1 \cdot 10^{-7}$	$1.61 \cdot 10^{-12}$	35.4482	27.7919
135	$1 \cdot 10^{-8}$	$4.82 \cdot 10^{-13}$	35.4482	27.7919

As should be desirable all the energy balances are fulfilled and the imbalances decreasing with the accuracy. When accuracy desired is more restricted, energy balances are more accurate, increasing CPU time and assuring heat transferred tends to an asymptotic value. Thus, a criterion to get precision of balances of $1 \cdot 10^{-5}$ has been adopted for simulation over low pressure receivers as a compromise between CPU time consumption necessary to assure reasonable energy balance agreement and asymptotic heat transferred values.
Illustrative results from the test case (presented above) using an accuracy $1 \cdot 10^{-4}$ are shown in Table 3.6, where the values of the main parameters obtained from the simulation over a LPR in steady state regime are indicated.

Table 3.6: Steady state results of verification case over a LPR.

	liquid	vapour
p [bar]	3.01	2.96
h [kJ/kg]	156.64	1457.45
T_{ref} [°C]	-9.42	-7.57
$T_{w,lat}$ [°C]	-9.30	-2.04
$T_{w,bot/top}$ [°C]	-9.27	-1.06
$\dot{m}_{evap}$ [kg/s]	$2.74 \cdot 10^{-5}$	-
$\dot{m}_{cond}$ [kg/s]	-	-
z [m]	0.50	0.50
ΔT_{sc} [°C]	-	-
ΔT_{sh} [°C]	-	1.85
$\dot{Q}_{loss}$ [W]	35.45	27.79

3.2.3 Unsteady verification study over HPR

Table 3.7 shows the initial conditions of the receiver for test cases (HPR).The geometry is the same that the one indicated in 3.2.1 section. The receiver initial state is subcooled liquid and saturated vapour (SC-SV). The simulation time is 8.33 h.

Table 3.7: Initial conditions.

Model	h_l $[kJ/kg]$	h_g $[kJ/kg]$	$\dot{m}_{cond}$ $[kg/s]$	$T_{lat,l}$ [°C]	$T_{bottom,l}$ [°C]	$T_{lat,l}$ [°C]	$T_{top,l}$ [°C]	p $[bar]$	$\dot{m}_i, \dot{m}_o$ $[kg/s]$
$SC-SV$	367.80	1488.59	$5.47 \cdot 10^{-6}$	35.32	35.31	34.02	33.69	13.77	$4.4 \cdot 10^{-4}$

The final values of pressure and liquid level as well as the heat losses for a transient simulation of a high pressure receiver when the inlet enthalpy change abruptly from 370.80 to 400.80 $[kJ/kg]$ are resumed in Table 3.8. The mass imbalance is lower than $1.0 \cdot 10^{-11}$ $[kg]$, and the energy imbalance is lower than $1.0 \cdot 10^{-6}$ $[W]$.

Table 3.8: Time step accuracy influence.

Δt $[s]$	p_{end} $[bar]$	$z_{l,end}$ $[cm]$	Q_{losses} $[W]$
0.01	16.15	29.90382677	22.76
0.05	16.15	29.90382677	22.76
0.1	16.15	29.90382677	22.76
1.0	13.71	29.90382665	22.76
10.0	16.15	29.90382554	22.76
20.0	16.15	29.90382432	22.76
30.0	16.15	29.90382232	22.76
40.0	16.15	29.90382194	22.76

Figs. 3.2-3.3 show the transient evolution of the pressure and the liquid level inside the receiver respectively, using different time steps (0.1 s to 40 s). Almost all time step simulations follow the same transient evolution. The highest differences are obtained with the time step of 40 s.

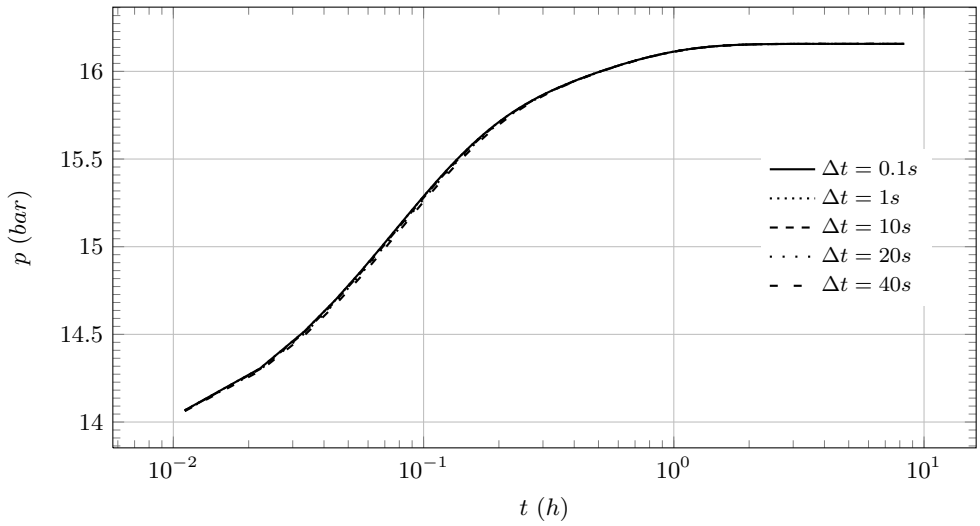

Figure 3.2: Evolution of pressure inside the high pressure receiver.

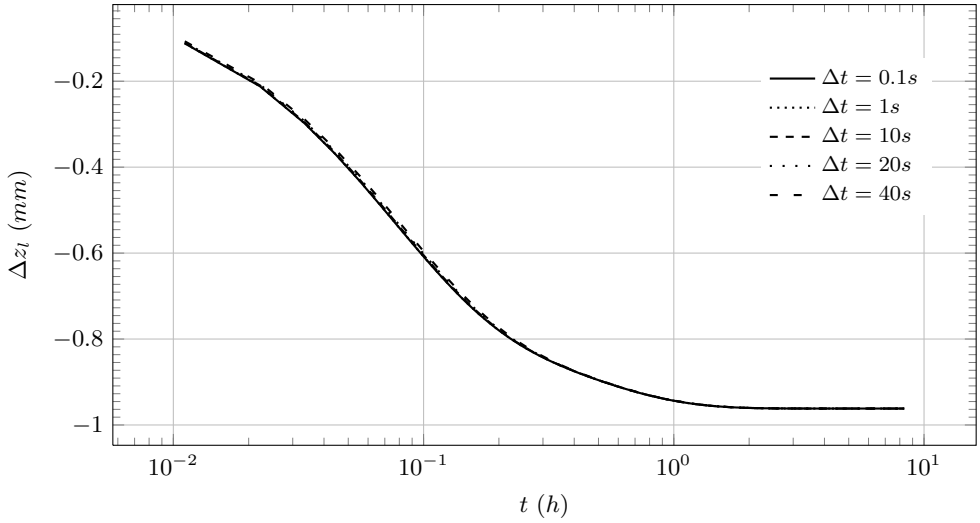

Figure 3.3: Evolution of liquid level inside the high pressure receiver.

In Figs. 3.4 and 3.5 the evolution of the condensed mass flow and the evolution of the differences between the saturated enthalpy and the enthalpy of the phase can be observed. Like in the pressure and liquid level graphs, the transient evolution of the different time steps for these variables follow a similar progress.

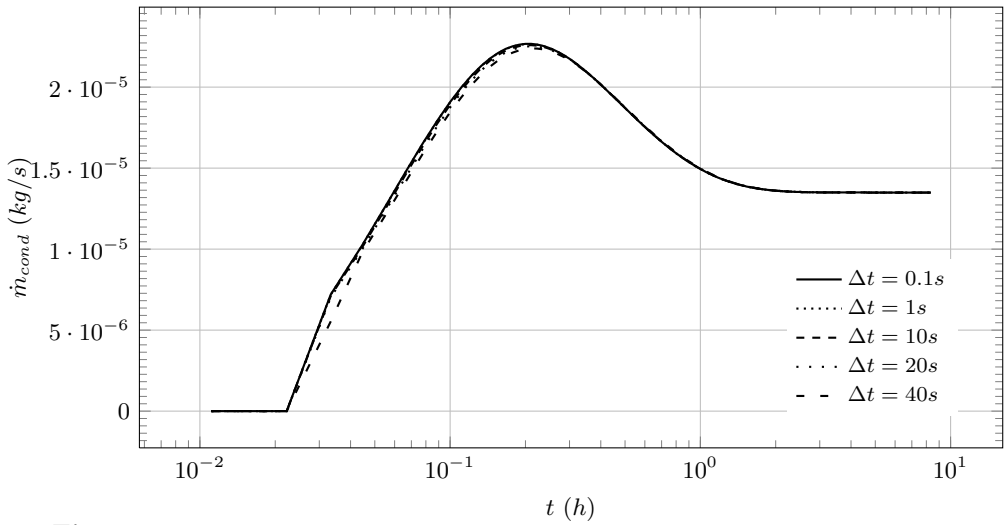

Figure 3.4: Evolution of condensed mass flow inside the high pressure receiver.

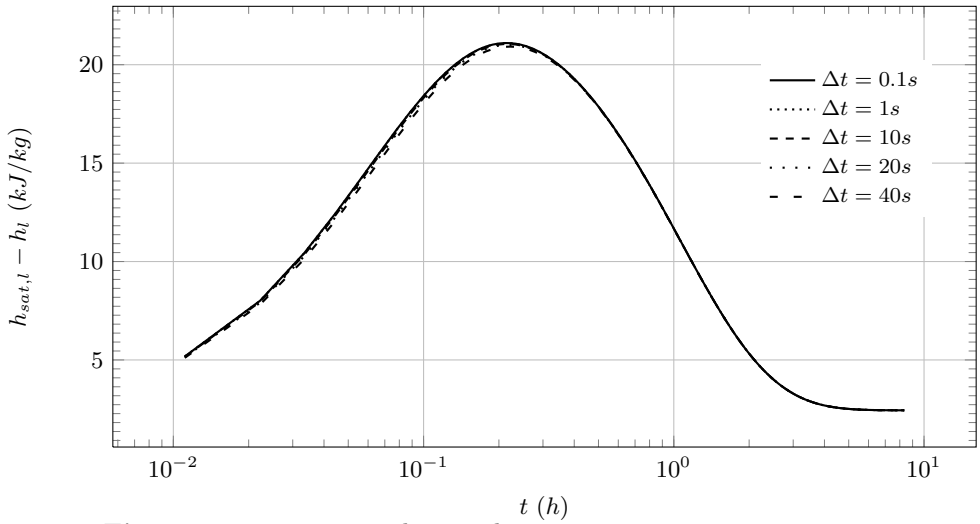

Figure 3.5: Evolution of $h_{sat,l} - h_l$ inside the high pressure receiver.

The conclusion from Figs 3.2-3.5 is that all time steps can predict the transient response of the variables in the receiver with good accuracy. It has been decided to use a $\Delta t = 20s$ as a reasonable simulation time step, which gives us a good compromise between accuracy and CPU time.

3.2.4 Unsteady verification study over LPR

Table 3.9 indicates the initial conditions of the receiver for test cases (LPR). The geometry of the simulated receiver is the same used in section 3.2.2. The receiver initial state is saturated liquid and superheated vapour (LS-SH). The simulation time is $5.55h$.

Table 3.9: Initial conditions.

Model	h_l $[kJ/kg]$	h_g $[kJ/kg]$	$\dot{m}_{evap}$ $[kg/s]$	$T_{lat,l}$ [°C]	$T_{bottom,l}$ [°C]	$T_{lat,l}$ [°C]	$T_{top,l}$ [°C]	p $[bar]$	$\dot{m}_i, \dot{m}_o$ $[kg/s]$
$SL-SH$	156.64	1457.45	$2.74 \cdot 10^{-5}$	−9.30	−9.27	−2.04	−1.06	2.98	$4.4 \cdot 10^{-4}$

Table 3.10 shows the end simulation values of pressure, liquid level, heat gains for an unsteady simulation over the low pressure receiver when the enthalpy at the main circuit inlet ($h_{in,r}$) changes abruptly from 369.76 to 389.76 $[kJ/kg]$ and the overfeed circuit inlet enthalpy ($h_{in,e}$) changes from 578.87 to 638.87 $[kJ/kg]$. The imbalance of mass is lower than $1.0 \cdot 10^{-10}$ $[kg]$ and the energy imbalance is lower than $1.0 \cdot 10^{-8}$ $[W]$.

Table 3.10: Time step accuracy influence.

$\Delta t\,[s]$	$p_{end}\,[bar]$	$z_{l,end}\,[cm]$	$Q_{gains}\,[W]$
0.01	4.92700969	49.88316842	25.2
0.05	4.92700969	49.88316842	25.2
0.1	4.92700969	49.95761419	25.2
1.0	4.92700782	49.88316812	25.2
10.0	4.92698902	49.88316518	25.2
20.0	4.92696896	49.88316209	25.3
40.0	4.92694152	49.88315613	25.3

Illustrative results from the unsteady low pressure receiver test case are presented in Figs. 3.6-3.11. Fig. 3.6 shows the transient evolution of the pressure considering different time steps. The pressure (Fig. 3.6) rapidly grows up at the begining of the simulation, due to the effect of the inlet enthalpies change is at the begining and then it remains constant. The variation of liquid level (Fig. 3.7) follows the same evolution as the pressure.

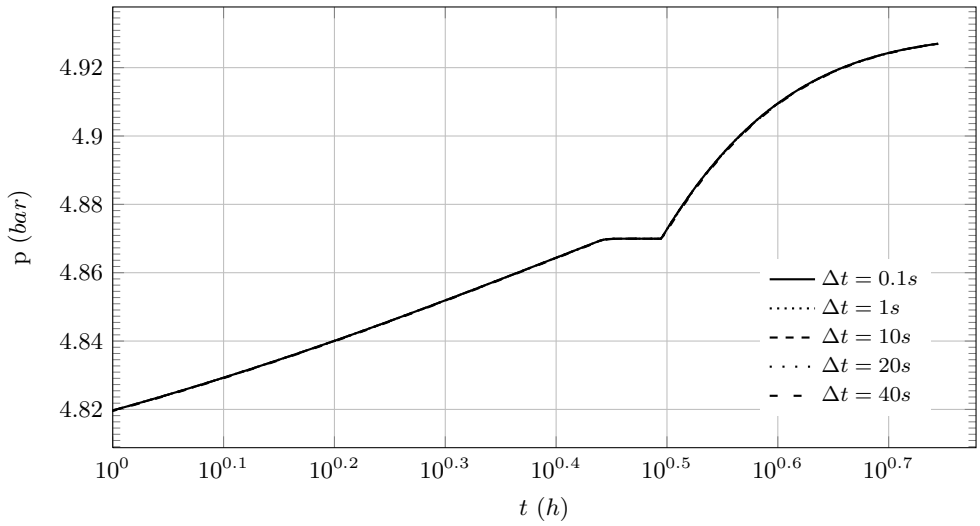

Figure 3.6: Evolution of pressure inside the low pressure receiver.

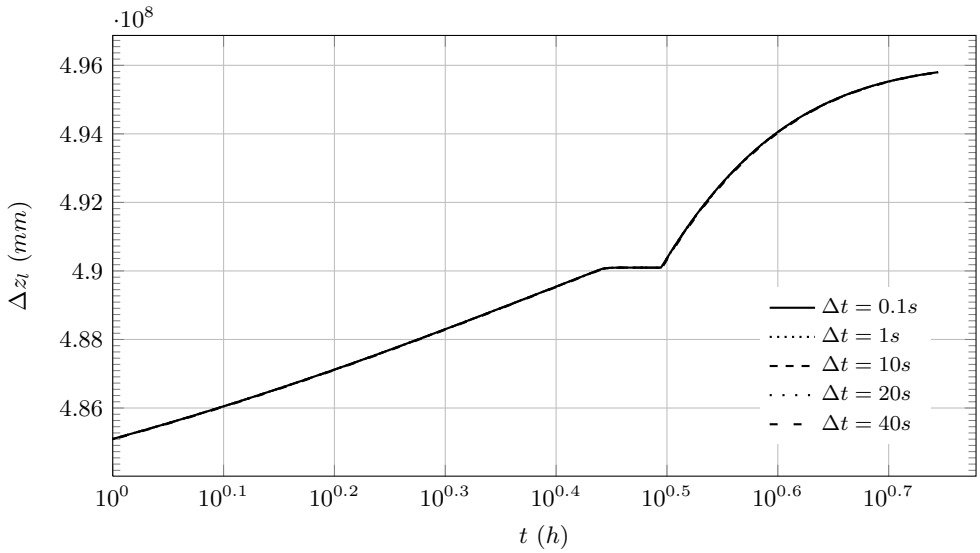

Figure 3.7: Evolution of liquid level inside the low pressure receiver.

In Figs. 3.8, 3.9,3.10 and 3.11 the evolution of the evaporated mass flow, the condensed mass flow and the evolution of the differences between the saturated enthalpy (liquid and vapour) and the enthalpy of the phase (liquid and vapour) can be observed.
Figures show the exact moment when the model inside the receiver change. At the begining the fast increase of the pressure produces the change to subcooled liquid and superheated vapour (SC-SH, $h_{sat,l} - h_l > 0$ and $h_{sat,g} - h_g < 0$), where there aren't condensation neither evaporation. The liquid phase temperature raises more slowly than the liquid saturation temperature. Then the model inside the receiver changes to subcooled liquid and saturated vapour (SC-VS, $h_{sat,l} - h_l > 0$ and $h_{sat,g} - h_g = 0$) and the condensed mass flow starts. The vapour phase temperature increases and as happens with the liquid phase temperature the vapour saturation temperature raise faster than the vapour phase temperature, consequently the vapour phase becomes a saturated vapour. Finally the liquid phase temperature increases till liquid saturation temperature (saturated liquid, SL and $h_{sat,l} - h_l = 0$) and the vapour phase temperature raises more than vapour saturation temperature (superheated vapour, SH and $h_{sat,g} - h_g < 0$), and condensed mass flow disappear and evaporated mass flow starts.

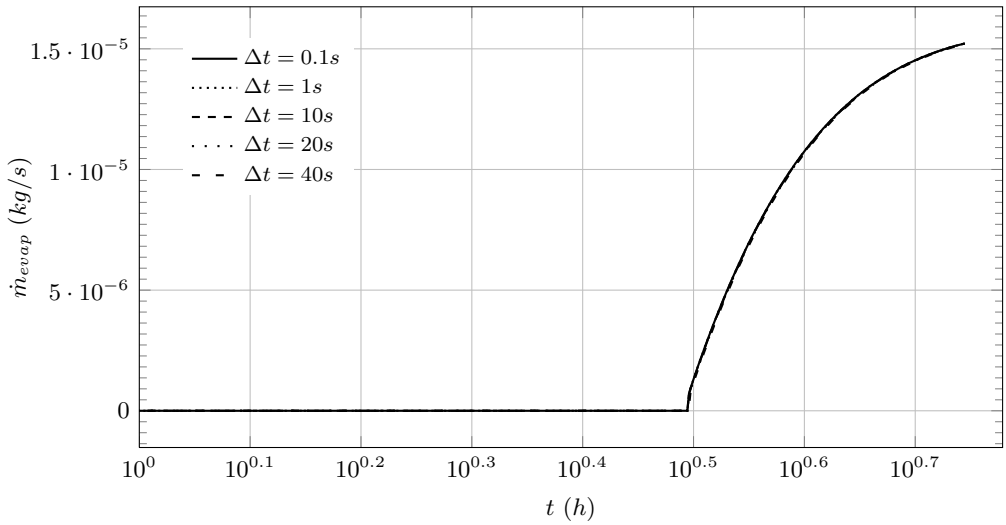

Figure 3.8: Evolution of evaporated mass flow inside the low pressure receiver.

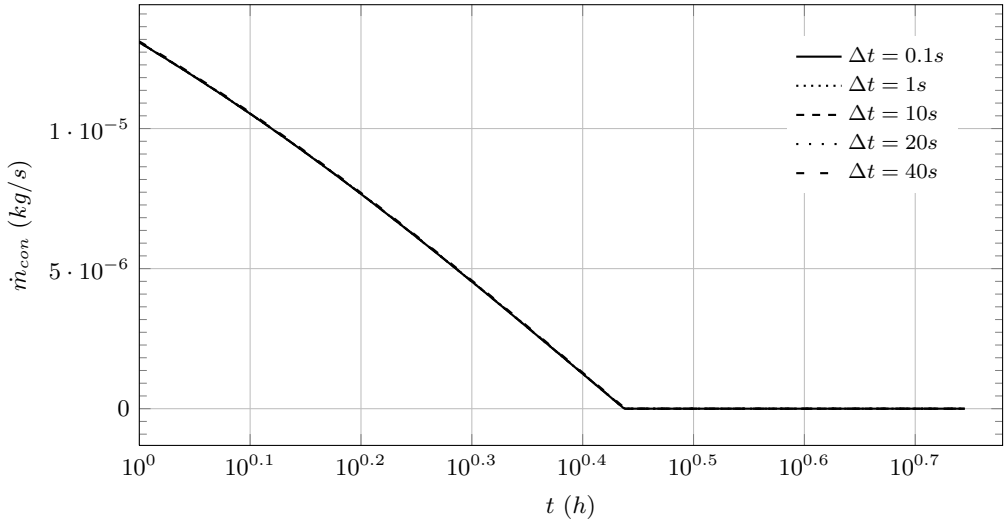

Figure 3.9: Evolution of condensed mass flow inside the low pressure receiver.

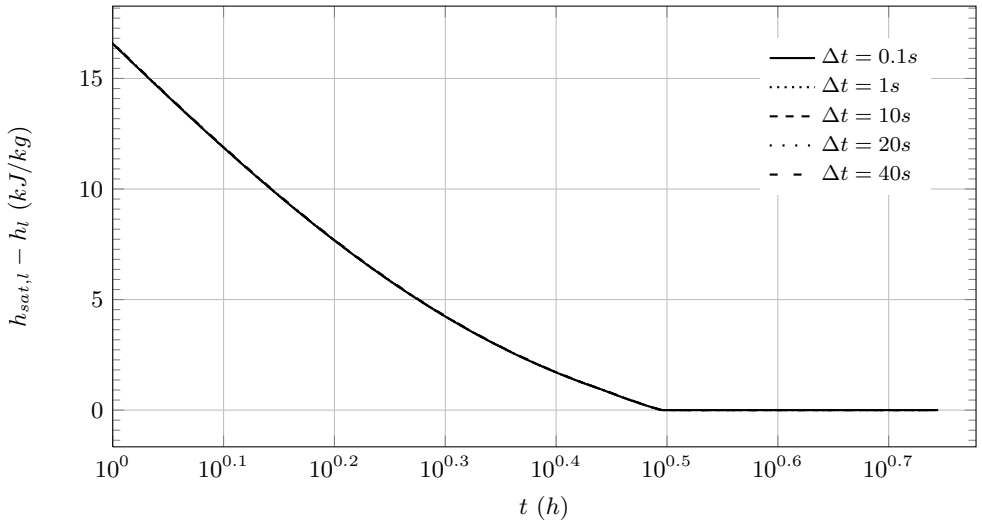

Figure 3.10: Evolution of $h_{sat,l} - h_l$ inside the low pressure receiver.

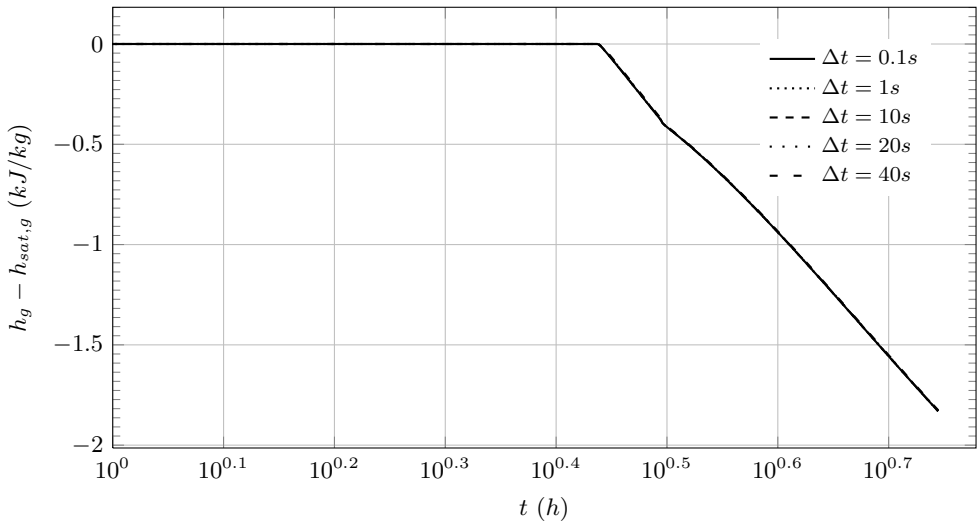

Figure 3.11: Evolution of $h_{sat,g} - h_g$ inside the low pressure receiver.

A $\Delta t = 20s$ have been observed as reasonable time step to satisfy the compromise between accuracy and CPU time consumption.

3.2.5 Illustrative Results

The presented model allows to simulate different kind of transient situations. This is important in order to get the unsteady simulation of refrigerating systems, which use receivers like liquid overfeed, gravity fed, or even dry expansion refrigerating systems with high pressure receiver, etc.
The following test case shows the possibilities of this simulation tool. The geometrical characteristics of the simulated receiver are the same as the high pressure receiver used for the steady state and unsteady studies presented on Table 3.4. Table 3.11 shows the initial conditions and the reference values of superficial heat transfer coefficients used in the simulation, where ammonia has been used as refrigerant. Simulation ended time is 12 h.

Table 3.11: Test case initial conditions.

p_{in} $[bar]$	h_{in} $[kJ/kg]$	$\dot{m}$ $[kg/s]$	h_{liq} $[kJ/kg]$	h_{vap} $[kJ/kg]$	$\dot{m}_{cond}$ $[kg/s]$	$T_{lat,l}$ [°C]	$T_{bottom,l}$ [°C]	$T_{lat,v}$ [°C]	$T_{top,v}$ [°C]
13.77	370.80	$4.4 \cdot 10^{-3}$	367.80	1488.59	$5.47 \cdot 10^{-6}$	35.32	35.31	34.02	33.69

Fig. 3.12, 3.13 and 3.14 present the transient evolution of the boundary conditions

(environmental temperature, enthalpy at the entry and the mass flow entering in the receiver). Fig. 3.12 shows the first step in the transient simulation where the environmental temperature increases linearly from 20.0 [°C] to 25.0 [°C].

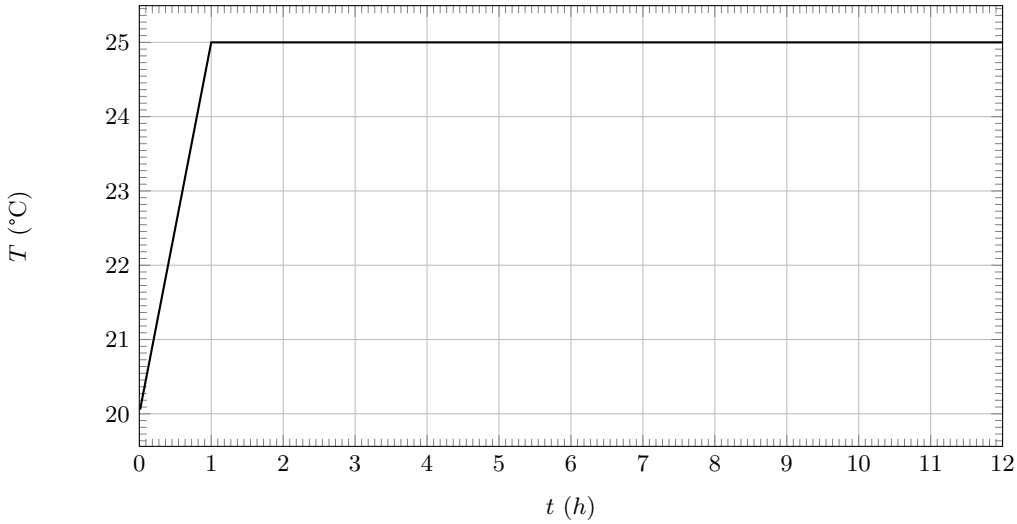

Figure 3.12: Transient evolution of boundary conditions: T_{amb}.

Fig. 3.13 shows the second step of the simulation, where the enthalpy at the entrance changes linearly from 370.80 $[kJ/kg]$ to 400.80 $[kJ/kg]$.

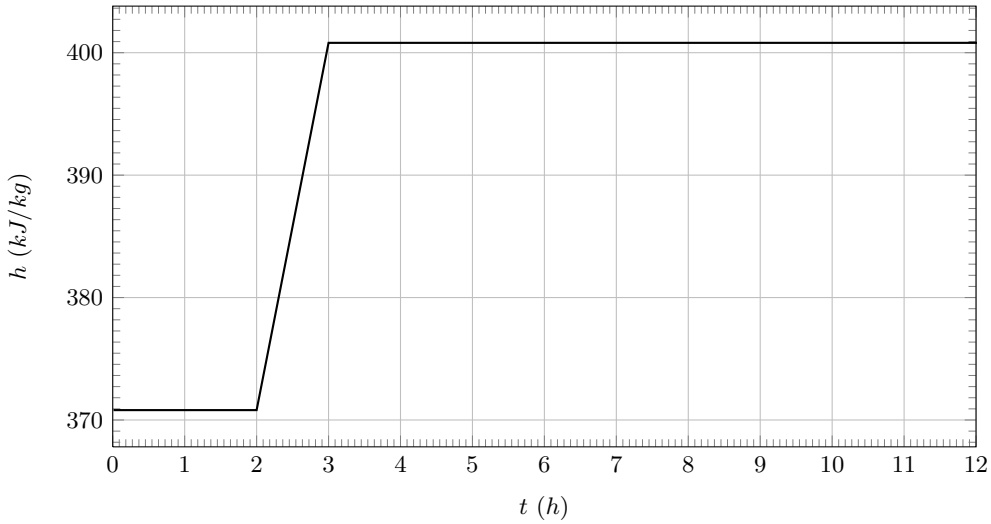

Figure 3.13: Transient evolution of boundary conditions: h_{in}.

Fig. 3.14 shows the third step, where the receiver inlet mass flow decreases linearly from $4.6 \cdot 10^{-3}\,[kg/s]$ to $4.4 \cdot 10^{-3}\,[kg/s]$ and then the outlet mass flow falls down linearly from $4.6{\cdot}10^{-3}\,[kg/s]$ to $4.4{\cdot}10^{-3}\,[kg/s]$, in order to avoid the complet emptying of the receiver.

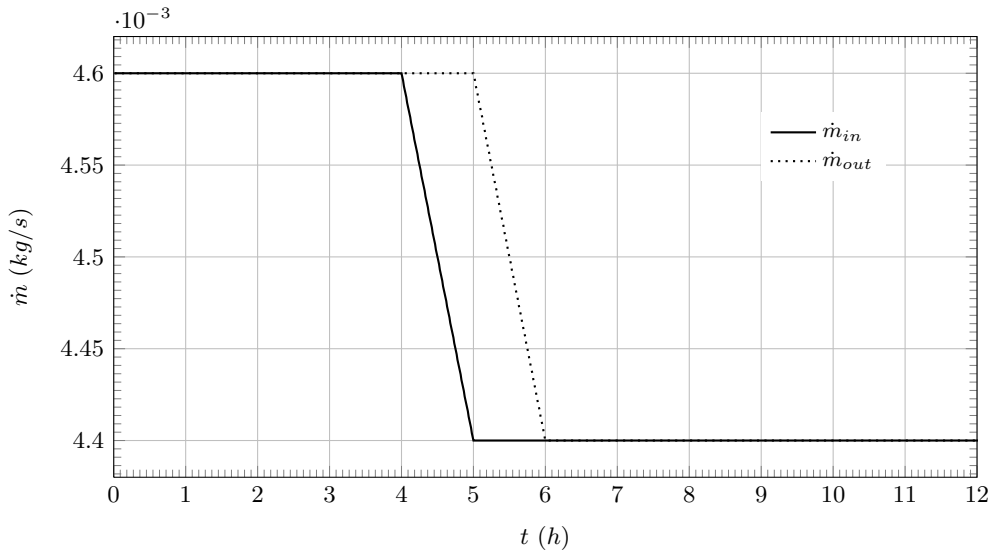

Figure 3.14: Transient evolution of boundary conditions: $\dot{m}_{in}$ and $\dot{m}_{out}$.

Figs. 3.15, 3.16 and 3.17 show the transient evolution of liquid level, pressure and the temperature of the phases inside the receiver respectively. Evaluating the influence of the changes in the studied variables (T_{amb}, h_{in} and $\dot{m}_{in}$), it is interesting to highlight that the influence in the liquid level, the pressure, and the temperatures of the phases inside the receiver from the variation of the environmental temperature is small compared to the changes in the inlet enthalpy and the changes in the inlet mass flow.

The changes in the mass flow entering in the receiver produce the most important change of liquid level from $\Delta Z_l = -0.5$ to $\Delta Z_l = -18$ [mm] (see Fig. 3.15). The changes in the environmental temperature and in the inlet enthalpy imply changes in liquid level lower than 1 [mm].

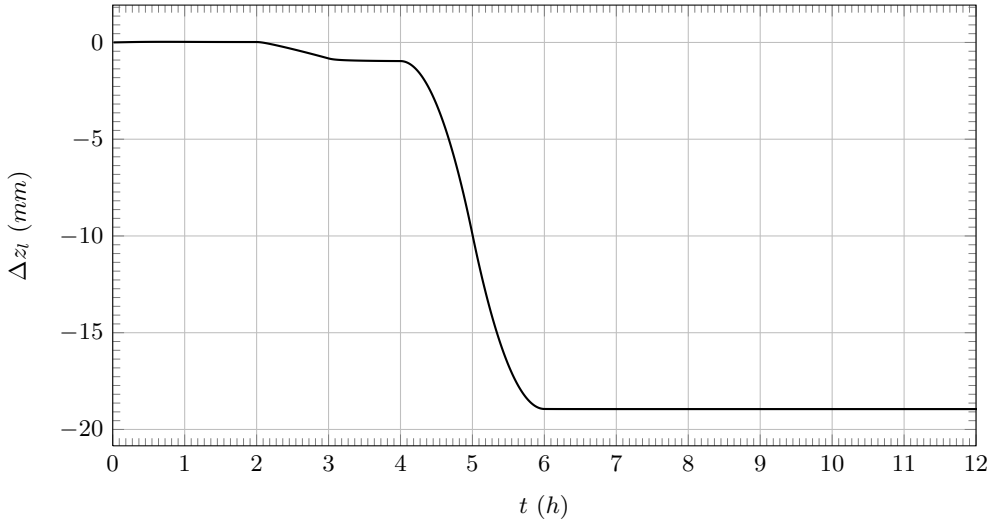

Figure 3.15: Transient evolution of liquid level inside the HPR.

In Fig. 3.16 it is possible to observe that the pressure is going down when the environmental temperature decreases. The pressure drop is expected, since the decrease of the environmental temperature implies that the heat losses are higher than the initials.

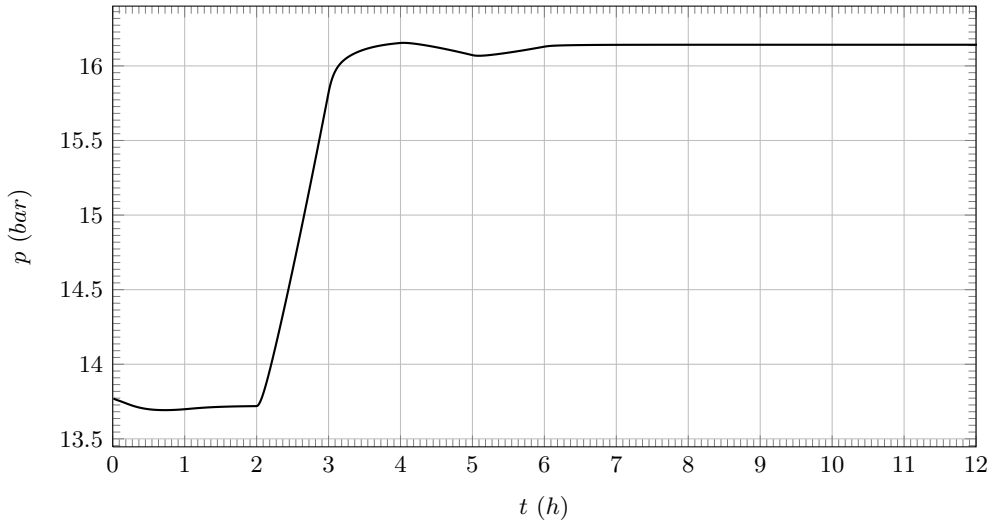

Figure 3.16: Transient evolution of pressure inside the HPR.

When the inlet enthalpy raises, the pressure also increases because the acumulated energy ($\dot{m}_{in}h_{in} - \dot{m}_{out}h_{out} - \dot{Q}_{losses}$) grows up, therefore the pressure must increase. Finally observing the last changes (decrease of inlet mass flow), we could observe that the pressure drops, as should be expected. Then when the outlet mass flow decrease and the pressure raises again till the stabilized final value. The final simulation state is not the initial because, during the unsteady process the total mass in the receiver decreases.
Fig. 3.17 depicts how the temperatures of both phases decrease and then increase following the evolution of the environmental temperature.

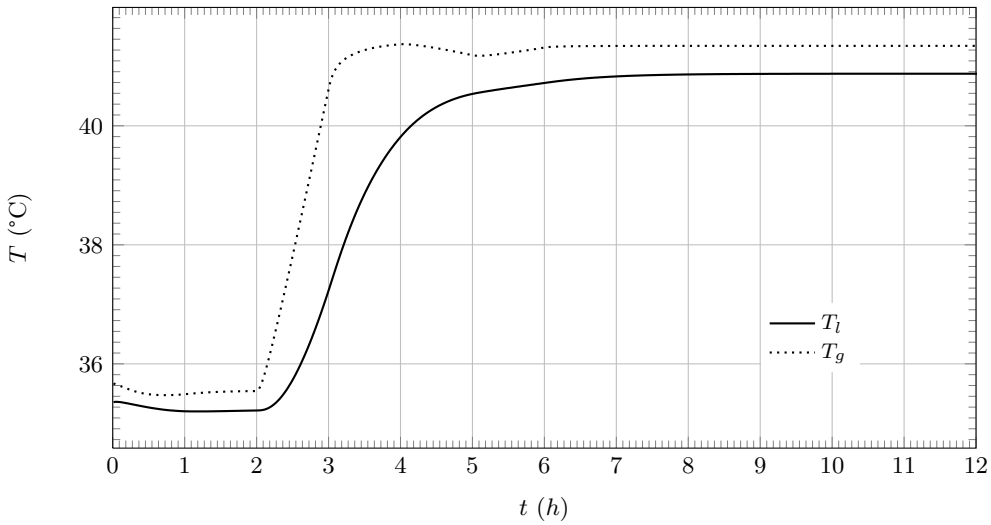

Figure 3.17: Transient evolution of temperatures phases inside the HPR.

When the inlet enthalpy changes, the phases temperature change as the net receiver inlet energy changes. Finally when the mass flow entering decreases, the phases temperature fall down and they raise once again till the final values for the steady state conditions with the new liquid level. The energy acumulated during the second transient step (increase of inlet enthalpy) implies a new and different steady state than the initial, and this new steady state have a higher level of pressure and consequently high phases temperatures. Fig. 3.18 shows the evolution of the condensed mass flow during the transient regime.

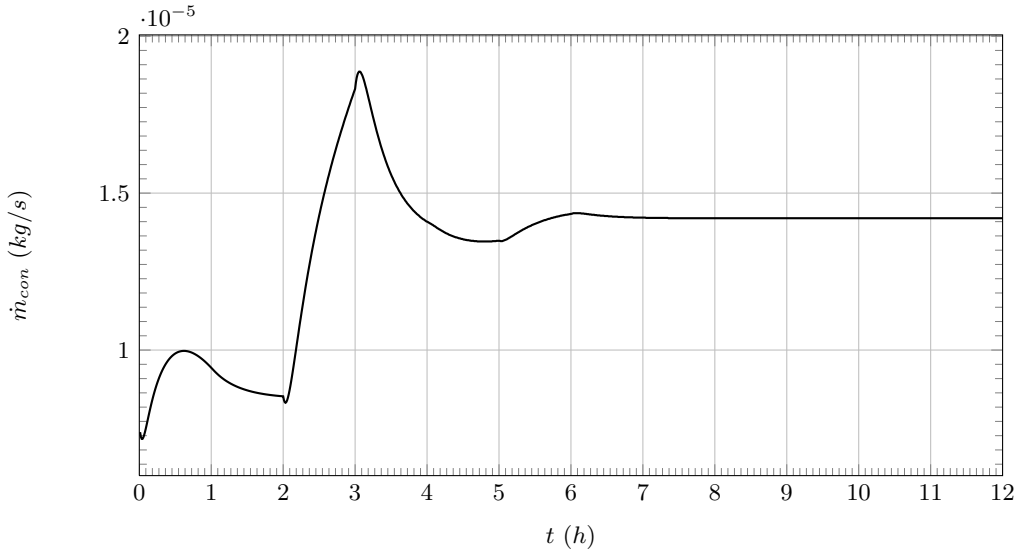

Figure 3.18: Transient evolution of condensed mass flow inside the HPR.

3.3 Heat Exchangers and Insulated pipes

In this section some grid density verification studies for insulated pipes and heat exchangers are presented. The verification studies are focused on the intensification of the grid density on both axial and radial direction.

3.3.1 Insulated pipes

Tested insulated (polyurethane foam) copper pipe has an internal diameter of 4.9 mm, external diameter of 6.4 mm, external insulation diameter of 44.4 mm, and length of 2.0 m.
Table 3.12 shows the boundary conditions used in this verification study.

Table 3.12: Boundary conditions for the verification test cases.

Refrigerant	$\dot{m}_{s,c}$ $[kg/h]$	p_{in} [bar]	T_{in} [°C]	T_{env} [°C]
$R134a$	6.33	13.87	98.00	25.00

Figs. 3.19 and 3.20 show the evolution of the heat losses as function of the grid density in the radial direction and axial direction respectively. It is interesting to highlight that it is important to use an appropriate grid density criterion to obtain good results. The grid density study indicates that the number of control volumes in axial direction and in radial direction which give us a reasonable compromise between

accuracy and CPU time consumtion are N_x=800 in axial direction (Δx = 2.5 mm) and N_y=57 in radial direction (Δy = 0.33 mm).

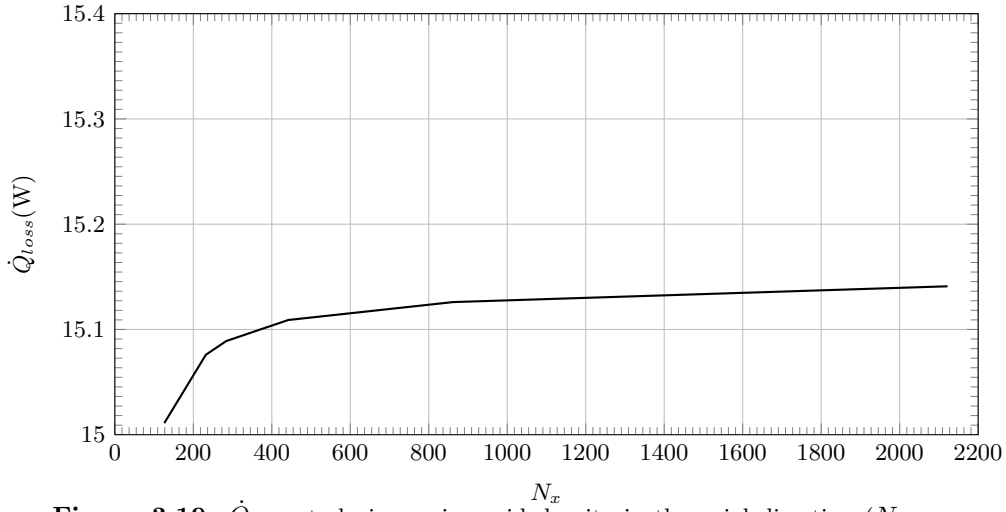

Figure 3.19: $\dot{Q}_{loss}$ study increasing grid density in the axial direction (N_y = 57).

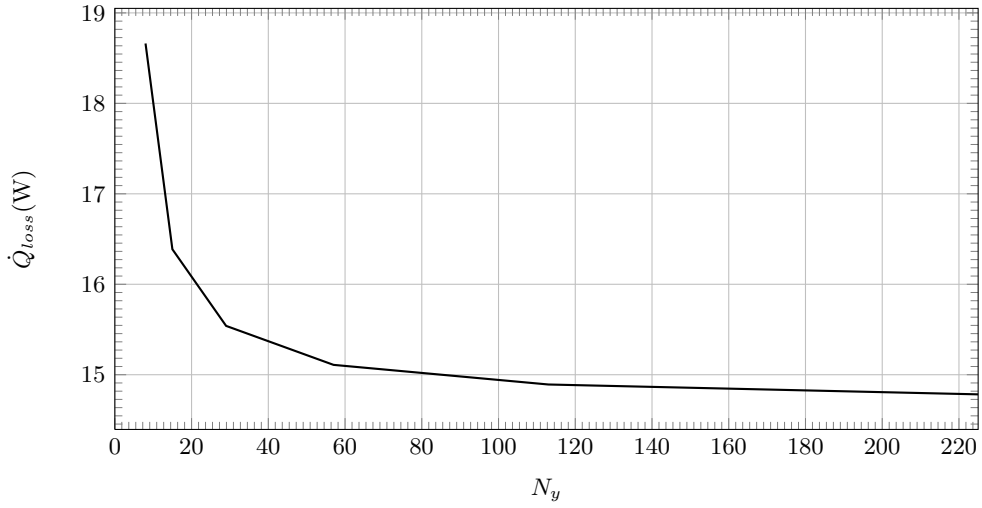

Figure 3.20: $\dot{Q}_{loss}$ study increasing grid density in the radial direction (N_x = 443).

3.3.2 Double pipe heat exchangers

Double copper pipe heat exchanger tested insulated with polyurethane foam has an internal diameter of 6.0 mm, external diameter of 8.0 mm, internal annular diameter of 16.0 mm, external annular diameter of 20.0 mm, external insulation diameter of 58.0 mm, and length of 2.0 m.
Table 3.13 presents the boundary conditions used in this verification study for condensing case. For all test cases water is used as secondary coolant and the environment was at 25.00 °C.

Table 3.13: Boundary conditions for the verification test cases.

Refrigerant	$\dot{m}_r\,[kg/h]$	p_{in} [bar]	T_{in} [°C]	$\dot{m}_s\,[kg/s]$	$p_{s,in}$ [bar]	$T_{s,in}$ [°C]
$R134a$	6.33	13.87	74.74	$6.60 \cdot 10^{-2}$	1.10	23.07

Figs. 3.21 and 3.22 show the evolution of the heat transfer and heat losses respectively in function of the grid density in the axial direction.

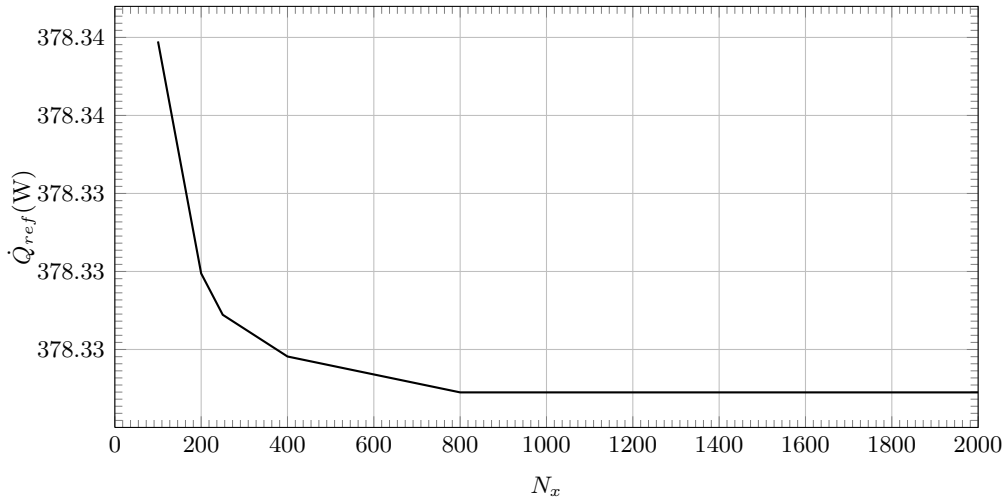

Figure 3.21: Evolution of heat transfer when the grid density in the axial direction increases ($N_y = 70$).

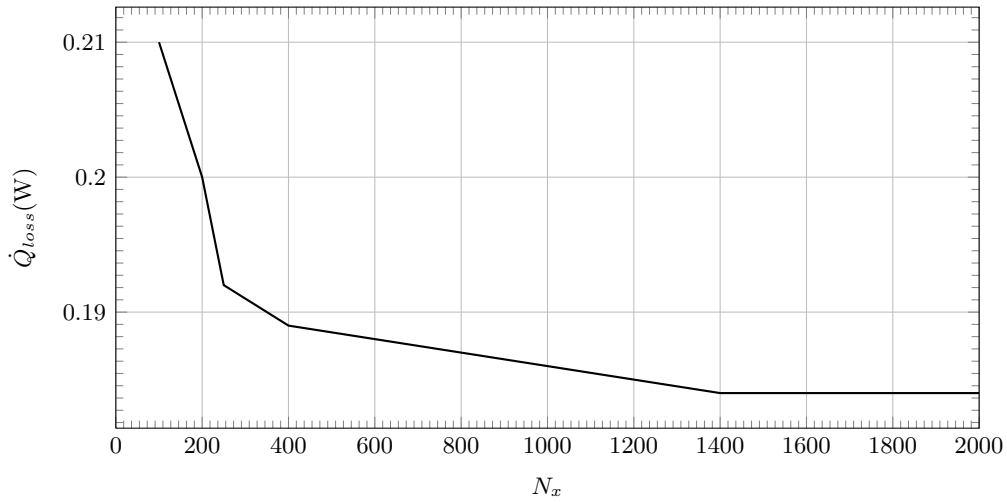

Figure 3.22: Evolution of heat losses when the grid density in the axial direction increases ($N_y = 70$).

The evolution of the heat transferred and heat gains as a function of the grid density in the radial direction (using $N_x = 800$) is detailed in Table 3.14 where it can be seen that the density of the grid in this direction it is not so important in this case. This is because the differences between the environmental temperature and the secondary coolant temperature are not relevant, and the thickness of the internal tube is not so big to need a higher grid density.

Table 3.14: Grid density study in the radial direction: heat transferred and losses.

N_y	$Q_r\,[W]$	$Q_a\,[W]$
10	382.69	−0.23
30	382.69	−0.21
50	382.69	−0.20
70	382.69	−0.20
90	382.69	−0.20
110	382.69	−0.20

3.4 Vapour Compression Refrigerating Systems

3.4.1 Dry Expansion Systems

The steady state verification studies over the dry expansion refrigerating systems code are presented for both global balances model and detailed model.
Fig. 3.23 depicts the standard dry expansion refrigerating system scheme considered.

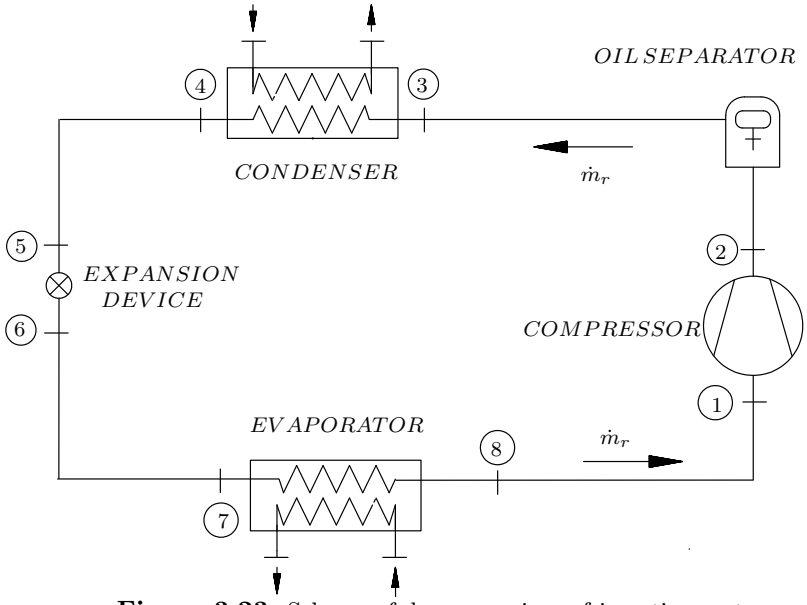

Figure 3.23: Scheme of dry expansion refrigerating system.

Model based on global balances

In order to check possible numerical and programming errors, some tests with different working conditions have been carried out. In this study has been adopted a thermostatic expansion valve as expansion device. In all cases the evaporator secondary coolant is air, and the condenser secondary coolant is water. The condenser secondary inlet temperature considered is 32.0 °C. The environment temperature is 25.0 °C. Table 3.15 shows the verification test conditions used to verify the global balances over the whole system.

Table 3.15: Verification test case.

Test case	1	2	3	4
Refrigerant	*R*134*a*	*R*134*a*	*R*717	*R*717
Evaporator secondary mass flow $\dot{m}_{s,e}$ [kg/s]	1.4199	1.4736	1.4199	1.4736
Evaporator secondary temperature [°C]	0.0	−10.0	0.0	−10.0
Condenser secondary mass flow $\dot{m}_{s,c}$ [kg/s]	0.618	0.618	0.618	0.618
Electromechanic efficiency [%]	80	80	60	50

Table 3.16 presents a brief description of the main elements.

Table 3.16: Geometry of the main elements.

Compressor	BOCK Kältemaschinen: AM2 / 121-4S
Condenser	plate heat exchanger: $\epsilon = 1.0$
TEV	SPORLAN: H, D
Evaporator	fin-and-tube heat exchanger: $\epsilon = 0.3$

For the condenser have used an $\epsilon = 1.0$ because, we have been considered an oversized condenser. Over the test cases presented in the Table 3.15 the thermostatic expansion valve settings have been changed from 4 to 12 [°C] in order to obtain different super-heatings at the outlet of the evaporator.
The numerical results verify that the global energy balance of the refrigerating system tends to zero. Fig. 3.24 shows the typical evolution of the relative error of the main variables and the evolution of the imbalance of the whole system. Both of them present an asymptotic evolution, as should be expected.

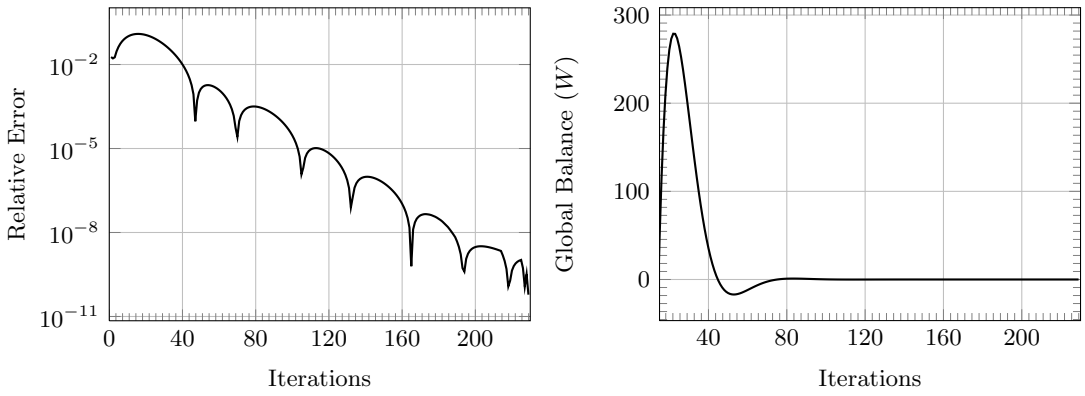

Figure 3.24: Verification Imbalance.

Tables 3.17 and 3.18 show the set of tests carried out in the verification of dry expansion code based on global balances, using respectively R134a and R717 as refrigerant.

Table 3.17: Verification test cases using R134a ($\epsilon = 10^{-10}$).

Case	$\dot{m}_{s,e}$ [kg/s]	ΔT_{sh} [°C]	EB [W]	p_{disc} [bar]	p_{suc} [bar]	$\dot{m}$ [kg/s]	$\dot{Q}_c$ [W]	$\dot{Q}_e$ [W]	$\dot{W}_{cp}$ [W]
1	1.4199	3.96	$3.552 \cdot 10^{-7}$	9.086	1.894	$2.471 \cdot 10^{-2}$	4545.758	3629.949	910.90
1	1.4199	4.94	$3.983 \cdot 10^{-8}$	9.086	1.894	$2.461 \cdot 10^{-2}$	4549.995	3635.662	910.81
1	1.4199	5.92	$-2.727 \cdot 10^{-7}$	9.086	1.893	$2.451 \cdot 10^{-2}$	4554.131	3641.272	910.72
1	1.4199	6.91	$-3.450 \cdot 10^{-8}$	9.087	1.893	$2.441 \cdot 10^{-2}$	4558.170	3646.782	910.64
1	1.4199	8.87	$-2.801 \cdot 10^{-7}$	9.087	1.892	$2.420 \cdot 10^{-2}$	4565.960	3657.508	910.50
1	1.4199	9.85	$4.074 \cdot 10^{-7}$	9.087	1.892	$2.410 \cdot 10^{-2}$	4569.718	3662.730	910.43
1	1.4199	11.80	$-1.831 \cdot 10^{-7}$	9.088	1.891	$2.391 \cdot 10^{-2}$	4576.967	3672.900	910.32
1	1.4199	12.78	$-2.826 \cdot 10^{-7}$	9.088	1.890	$2.381 \cdot 10^{-2}$	4580.459	3677.848	910.27
2	1.4736	4.48	$5.272 \cdot 10^{-6}$	8.967	1.423	$1.791 \cdot 10^{-2}$	3342.007	2557.810	773.60
2	1.4736	5.45	$-4.930 \cdot 10^{-7}$	8.967	1.423	$1.783 \cdot 10^{-2}$	3345.025	2562.246	773.54
2	1.4736	6.42	$3.210 \cdot 10^{-6}$	8.967	1.423	$1.776 \cdot 10^{-2}$	3347.967	2566.605	773.48
2	1.4736	7.39	$-1.032 \cdot 10^{-6}$	8.967	1.423	$1.769 \cdot 10^{-2}$	3350.836	2570.888	773.43
2	1.4736	9.32	$3.283 \cdot 10^{-6}$	8.968	1.422	$1.755 \cdot 10^{-2}$	3356.364	2579.242	773.35
2	1.4736	10.29	$4.736 \cdot 10^{-6}$	8.968	1.422	$1.748 \cdot 10^{-2}$	3359.023	2583.310	773.31
2	1.4736	11.26	$2.330 \cdot 10^{-6}$	8.968	1.422	$1.741 \cdot 10^{-2}$	3361.611	2587.308	773.28
2	1.4736	12.22	$-3.475 \cdot 10^{-7}$	8.968	1.422	$1.734 \cdot 10^{-2}$	3364.132	2591.236	773.25

Table 3.18: Verification test cases using R717 ($\epsilon = 10^{-10}$).

Case	$\dot{m}_{s,e}$ [kg/s]	ΔT_{sh} [°C]	EB [W]	p_{disc} [bar]	p_{suc} [bar]	$\dot{m}$ [kg/s]	$\dot{Q}_c$ [W]	$\dot{Q}_e$ [W]	$\dot{W}_{cp}$ [W]
3	1.4199	2.99	$6.429 \cdot 10^{-5}$	13.758	2.701	$4.526 \cdot 10^{-3}$	6053.654	4918.207	1187.60
3	1.4199	3.95	$-9.039 \cdot 10^{-5}$	13.756	2.705	$4.504 \cdot 10^{-3}$	6039.943	4905.868	1188.22
3	1.4199	4.91	$-8.929 \cdot 10^{-5}$	13.754	2.708	$4.482 \cdot 10^{-3}$	6025.972	4893.292	1188.84
3	1.4199	5.87	$-1.839 \cdot 10^{-5}$	13.752	2.712	$4.460 \cdot 10^{-3}$	6012.063	4880.771	1189.46
3	1.4199	7.78	$-3.691 \cdot 10^{-5}$	13.748	2.719	$4.417 \cdot 10^{-3}$	5984.097	4855.588	1190.71
4	1.4736	4.25	$-8.689 \cdot 10^{-5}$	13.486	2.085	$3.133 \cdot 10^{-3}$	4208.147	3385.419	868.82
4	1.4736	5.19	$-1.338 \cdot 10^{-4}$	13.485	2.087	$3.118 \cdot 10^{-3}$	4198.415	3376.956	869.46
4	1.4736	6.13	$-1.282 \cdot 10^{-4}$	13.484	2.089	$3.103 \cdot 10^{-3}$	4188.663	3368.481	870.10
4	1.4736	7.07	$-8.152 \cdot 10^{-5}$	13.482	2.091	$3.088 \cdot 10^{-3}$	4178.910	3360.006	870.74

Model based on detailed balances

The verification study over the detailed balances model has been carried out in two parts, the first checking the influence of the grid density over the global energy balance in the cycle, and the second checking the influence of the numerical precision over the global energy balance of the cycle.
The following test case has been used for verification purposes, where the dry expansion refrigerating system is composed by a hermetic reciprocating compressor, two double pipe heat exchangers (DPHE, using water as secondary coolant) and a capillary tube as expansion device. Tables 3.19 and 3.20 show the boundary conditions for DPHE and the geometry of the main elements used in the verification test cases respectively.

Table 3.19: Boundary conditions for the verification test cases.

Refrigerant	p_{disc} [bar]	T_{env} [°C]	$\dot{m}_{s,e}\,[kg/s]$	$T_{s,ie}$ [°C]	$\dot{m}_{s,c}\,[kg/s]$	$T_{s,ic}$ [°C]
$R134a$	13.87	22.63	0.05	19.24	0.066	23.07

Table 3.20: Geometry of the main elements.

Compressor	ACC Comp. $V_{cl} = 9\,cm^3$
Condenser	DPHE: $D_i = 6\,mm,\ D_e = 8\,mm,\ D_a = 16\,m$
	$D_{ae} = 20\,mm,\ D_{ins} = 60\,mm,\ L = 2.19\,m$
Capillary tube	$D_i = 0.65\,mm,\ L = 1.96\,m$
Evaporator	DPHE: $D_i = 8\,mm,\ D_e = 9.6\,mm,\ D_a = 16\,m$
	$D_{ae} = 20\,mm,\ D_{ins} = 60\,mm,\ L = 6.15\,m$

Table 3.21 shows the main variables of the system as well as the number of the global iterations needed for each grid to reach the convergence. All energy balances (EB) are fullfiled, and they are lower than $1.0 \cdot 10^{-3}$.

Table 3.21: Verification test cases: Grid density ($\epsilon = 10^{-6}$).

Δx [cm]	p_{suc}[bar]	$\dot{m}_r$ [kg/s]	$\dot{Q}_c$[W]	$\dot{Q}_e$[W]	$\dot{W}_E$[W]
1.0	1.428	$1.733 \cdot 10^{-3}$	−415.979	318.699	−144.22
0.8	1.430	$1.736 \cdot 10^{-3}$	−417.111	319.644	−144.51
0.5	1.436	$1.745 \cdot 10^{-3}$	−420.242	322.217	−145.30
0.25	1.444	$1.758 \cdot 10^{-3}$	−425.327	326.371	−146.58
0.1	1.453	$1.771 \cdot 10^{-3}$	−429.992	330.190	−147.75
0.05	1.455	$1.776 \cdot 10^{-3}$	−431.636	331.603	−148.19
0.01	1.456	$1.779 \cdot 10^{-3}$	−432.096	332.624	−148.37

The changes in the heat transferred values and in the compression work from the $\Delta x = 1.0\,cm$ to $\Delta x = 0.1\,cm$ are near 3.5 % while from $\Delta x = 0.1\,cm$ to $\Delta x = 0.01\,cm$ are near 0.5 %. It has been decided to use a grid density of $\Delta x = 0.1\,cm$, because it gives as a reasonable CPU time consumption with good accuracy.
Convergence study results are indicated in Table 3.22, where the main variables of the system with grid density of $\Delta x = 0.1\,cm$ are shown.

Table 3.22: Verification test cases: Convergence criterion ($\Delta x = 0.1\,cm$).

ϵ	p_{suc} [bar]	m_r [kg/s]	EB [W]	$\dot{Q}_c$[W]	$\dot{Q}_e$[W]	$\dot{W}_E$[W]	Iter
$1.0e^{-3}$	1.453	$1.772 \cdot 10^{-3}$	$1.5 \cdot 10^{-2}$	-429.646	330.282	-147.75	8
$1.0e^{-4}$	1.453	$1.771 \cdot 10^{-3}$	$1.2 \cdot 10^{-2}$	-430.019	330.237	-147.77	10
$1.0e^{-5}$	1.453	$1.771 \cdot 10^{-3}$	$4.8 \cdot 10^{-3}$	-429.986	330.190	-147.75	15
$1.0e^{-6}$	1.453	$1.771 \cdot 10^{-3}$	$4.9 \cdot 10^{-4}$	-429.992	330.190	-147.75	23

As it should be expected, the solution of the system tends to an asymptotic result when the convergence criterion is more accurate.

3.4.2 Dry Expansion Systems with High Pressure Receiver

A set of test cases have also been carried out to verify the numerical simulation code based on detailed balances in a dry expansion refrigerating system with a high pressure receiver (see Fig. 3.25), which is composed by a hermetic reciprocating compressor, two double pipe heat exchangers (condenser and evaporator, using water as secondary coolant), a capillary tube and a high pressure receiver.

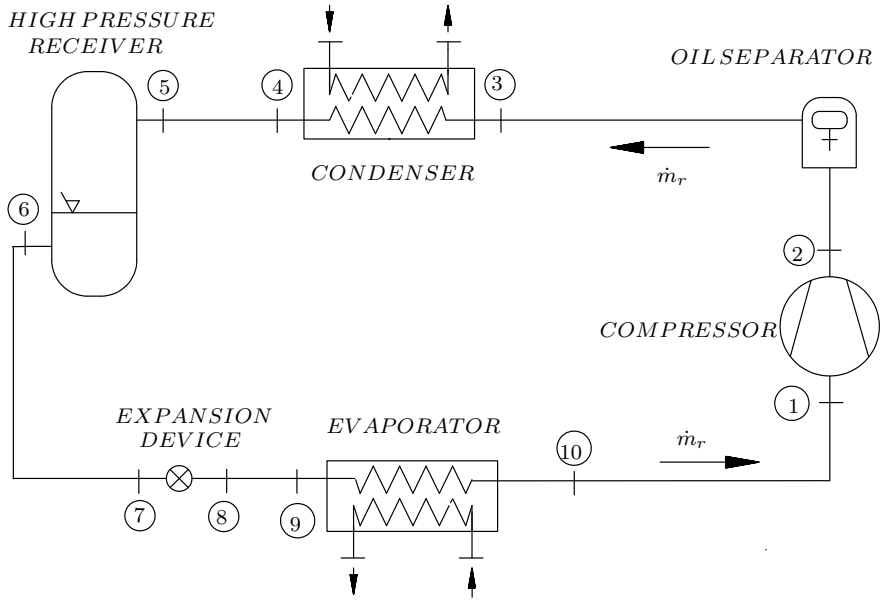

Figure 3.25: Scheme of dry expansion refrigerating system with high pressure receiver.

Table 3.24 show the geometry of the main elements used in the verification test cases. The boundary conditions for the DPHE are indicated in Table 3.23.

Table 3.23: Boundary conditions for the verification test cases.

Refrigerant	T_{env} [°C]	$\dot{m}_{s,e}\,[kg/s]$	$T_{s,ie}$ [°C]	$\dot{m}_{s,c}\,[kg/s]$	$T_{s,ic}$ [°C]
$R134a$	25.00	0.05	19.24	0.026	33.07

Table 3.24: Geometry of the main elements.

Compressor	ACC comp. $V_{cl} = 9\,cm^3$
Condenser	DPHE: $D_i = 6\,mm,\ D_e = 8\,mm,\ D_a = 16\,m$
	$D_{ae} = 20\,mm,\ D_{ins} = 60\,mm,\ L = 2.19\,m$
Capillary tube	$D_i = 0.65\,mm,\ L = 1.96\,m$
HPR	$D_i = 0.07\,m,\ H_t = 0.15\,m,\ H_{liq} = 0.07\,m$
Evaporator	DPHE: $D_i = 8\,mm,\ D_e = 9.6\,mm,\ D_a = 16\,m$
	$D_{ae} = 20\,mm,\ D_{ins} = 60\,mm,\ L = 6.15\,m$

Table 3.25 shows the results obtained from the grid refinement analysis for a dry expansion system with high pressure receiver. All the EB are lower than $1.0 \cdot 10^{-3}$.

Table 3.25: Verification test cases: Grid density ($\epsilon = 10^{-6}$).

Δx [cm]	$\dot{m}$[kg/s]	p_{disc}[bar]	p_{suc}[bar]	$\dot{Q}_c$[W]	$\dot{Q}_e$[W]	$\dot{W}_E$[W]
1.0	$8.986 \cdot 10^{-4}$	12.605	0.844	−186.867	136.670	−64.94
0.8	$8.969 \cdot 10^{-4}$	12.559	0.842	−186.622	136.608	−64.69
0.5	$8.936 \cdot 10^{-4}$	12.471	0.839	−186.141	136.487	−64.22
0.25	$8.897 \cdot 10^{-4}$	12.366	0.834	−185.560	136.339	−63.65
0.1	$8.857 \cdot 10^{-4}$	12.260	0.830	−184.942	136.188	−63.08
0.05	$8.831 \cdot 10^{-4}$	12.189	0.827	−184.322	136.102	−62.71
0.01	$8.821 \cdot 10^{-4}$	12.150	0.825	−184.024	136.064	−62.53

The changes in the heat capacities and in the compression work from the $\Delta x = 1.0\,cm$ to $\Delta x = 0.1\,cm$ is near 1.5 % while the from $\Delta x = 0.1\,cm$ to $\Delta x = 0.01\,cm$ is near 0.5 %. Therefore we decided to use a grid density of $\Delta x = 0.1\,cm$, which gives a reasonable compromise between the CPU time consumption and accuracy. Table 3.26 shows the main variables of the system simulation with grid density of $\Delta x = 0.1\,cm$.

Table 3.26: Verification test cases: Convergence criterion ($\Delta x = 0.1\,cm$).

ϵ	EB [W]	$\dot{m}$[kg/s]	p_{disc}[bar]	p_{suc}[bar]	$\dot{Q}_c$[W]	$\dot{Q}_e$[W]	$\dot{W}_E$[W]
$1.0e^{-3}$	$2.2 \cdot 10^{-2}$	$8.855 \cdot 10^{-4}$	12.253	0.830	−184.797	136.200	−63.04
$1.0e^{-4}$	$1.6 \cdot 10^{-2}$	$8.856 \cdot 10^{-4}$	12.256	0.830	−184.854	136.199	−63.06
$1.0e^{-5}$	$1.1 \cdot 10^{-3}$	$8.857 \cdot 10^{-4}$	12.260	0.830	−184.933	136.191	−63.08
$1.0e^{-6}$	$1.1 \cdot 10^{-4}$	$8.857 \cdot 10^{-4}$	12.260	0.830	−184.942	136.188	−63.08

As it should be expected, the working point of the system tends to asymptotic value with the increase of the required accuracy convergence criterion.

3.4.3 Liquid Suction Line Vapour-Compression System

A set of test cases have also been carried out to verify the numerical simulation code baased on detailed balances with an intermediate heat accumulator vapour-compression refrigerating system (see Fig. 3.26), which is composed by a hermetic reciprocating compressor, two double pipe heat exchangers (condenser and evaporator, using watre solution of 40% propylene glycol as secondary coolant), a micrometric valve and a heat accumulator receiver.

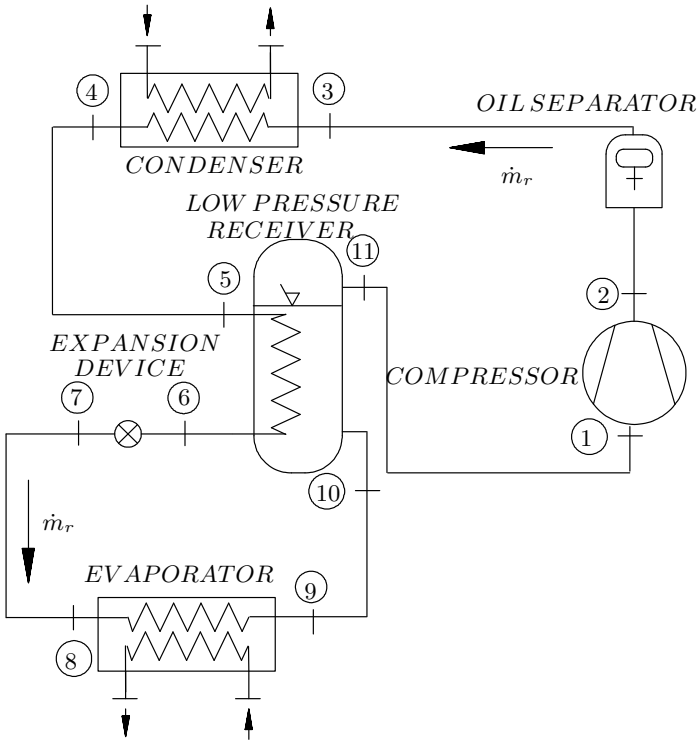

Figure 3.26: Scheme of intermediate heat accumulator vapour-compression refrigerating system.

Table 3.27 shows the boundary conditions adopted for the DPHE, while Table 3.28 describes the geometry of the main elements used in these verification test cases.

Table 3.27: Boundary conditions for the verification test cases.

Refrigerant	T_{env} [°C]	$\dot{m}_{s,e}$ $[kg/h]$	$T_{s,ie}$ [°C]	$\dot{m}_{s,c}$ $[kg/h]$	$T_{s,ic}$ [°C]
$R134a$	25.00	180.0	5.0	169.2	32.0

Table 3.28: Geometry of the main elements.

Compressor	ACC Comp.$V_{cl} = 9\,cm^3$
Condenser	DPHE: $D_i = 8\,mm,\ D_e = 9.6\,mm,\ D_a = 16\,m$
	$D_{ae} = 20\,mm,\ D_{ins} = 60\,mm,\ L = 2.0\,m$
IHA	$D_i = 0.07\,m,\ H_t = 0.15\,m,\ H_{liq} = 0.07\,m$
	$D_i = 6\,mm,\ D_e = 8\,mm,\ L = 0.1\,m$
Evaporator	DPHE: $D_i = 8\,mm,\ D_e = 9.6\,mm,\ D_a = 16\,m$
	$D_{ae} = 20\,mm,\ D_{ins} = 60\,mm,\ L = 0.8\,m$

The table 3.29 presents the results obtained from the grid refinement analysis for a intermidate heat accumulator vapou-compression system. All the EB are lower than $2.4 \cdot 10^{-3}$.

Table 3.29: Verification test cases: Grid density ($\epsilon = 10^{-6}$).

Δx [cm]	$\dot{m}$[kg/s]	p_{disc}[bar]	p_{suc}[bar]	$\dot{Q}_c$[W]	$\dot{Q}_e$[W]	$\dot{W}_E$[W]	$\dot{Q}_{IHA}$[W]
1.0	$2.476 \cdot 10^{-3}$	14.881	1.766	−442.22	280.30	−230.65	−32.71
0.85	$2.482 \cdot 10^{-3}$	14.922	1.771	−444.83	282.35	−231.32	−32.58
0.5	$2.502 \cdot 10^{-3}$	15.064	1.787	−452.60	288.37	−233.54	−32.22
0.25	$2.526 \cdot 10^{-3}$	15.248	1.826	−461.05	294.78	−236.63	−31.89
0.1	$2.552 \cdot 10^{-3}$	15.467	1.829	−469.74	301.25	−239.47	−31.62
0.05	$2.570 \cdot 10^{-3}$	15.599	1.843	−475.08	305.20	−241.83	−31.49
0.01	$2.580 \cdot 10^{-3}$	15.642	1.847	−475.38	306.10	−242.13	−31.32

The changes in the heating/cooling capacities and in the compression work from the $\Delta x = 1.0\,cm$ to $\Delta x = 0.1\,cm$ are near 4.1 % while the from $\Delta x = 0.1\,cm$ to $\Delta x = 0.01\,cm$ are near 1.1 %. The grid density which has been decided to be used, is $\Delta x = 0.1\,cm$. This grid density gives a reasonable compromise between accuracy and CPU time consumption.
Table 3.30 shows the main variables of the system simulation with grid density of $\Delta x = 0.1\,cm$.

Table 3.30: Verification test cases: Convergence criterion ($\Delta x = 0.1\,cm$).

ϵ	EB [W]	$\dot{m}$[kg/s]	p_{disc}[bar]	p_{suc}[bar]	$\dot{Q}_c$[W]	$\dot{Q}_e$[W]	$\dot{W}_E$[W]	$\dot{Q}_{IHA}$[W]
10^{-3}	$7.2 \cdot 10^{-2}$	$2.552 \cdot 10^{-3}$	15.469	1.829	−469.91	301.18	−239.90	−31.62
10^{-4}	$6.2 \cdot 10^{-2}$	$2.553 \cdot 10^{-3}$	15.471	1.828	−469.88	301.29	−239.45	−31.63
10^{-5}	$2.0 \cdot 10^{-3}$	$2.553 \cdot 10^{-3}$	15.469	1.829	−469.82	301.25	−239.47	−31.62
10^{-6}	$2.1 \cdot 10^{-4}$	$2.552 \cdot 10^{-3}$	15.467	1.829	−469.74	301.25	−239.47	−31.62

As it should be expected, the work point of the system tend to be stable when the convergence criterion is more accurate.

3.4.4 Overfeed Refrigerating Systems

In order to verify the code based on global balances and the numerical solution, a set of test cases have been carried out with an overfeed refrigerating system (see Fig.

3.27) which is composed by an hermetic reciprocating compressor, two receivers (high pressure and low pressure), a pump, a fin-and-tube heat exchanger (evaporator), a plate heat exchanger (condenser), and an electronical operated valve (EOV).

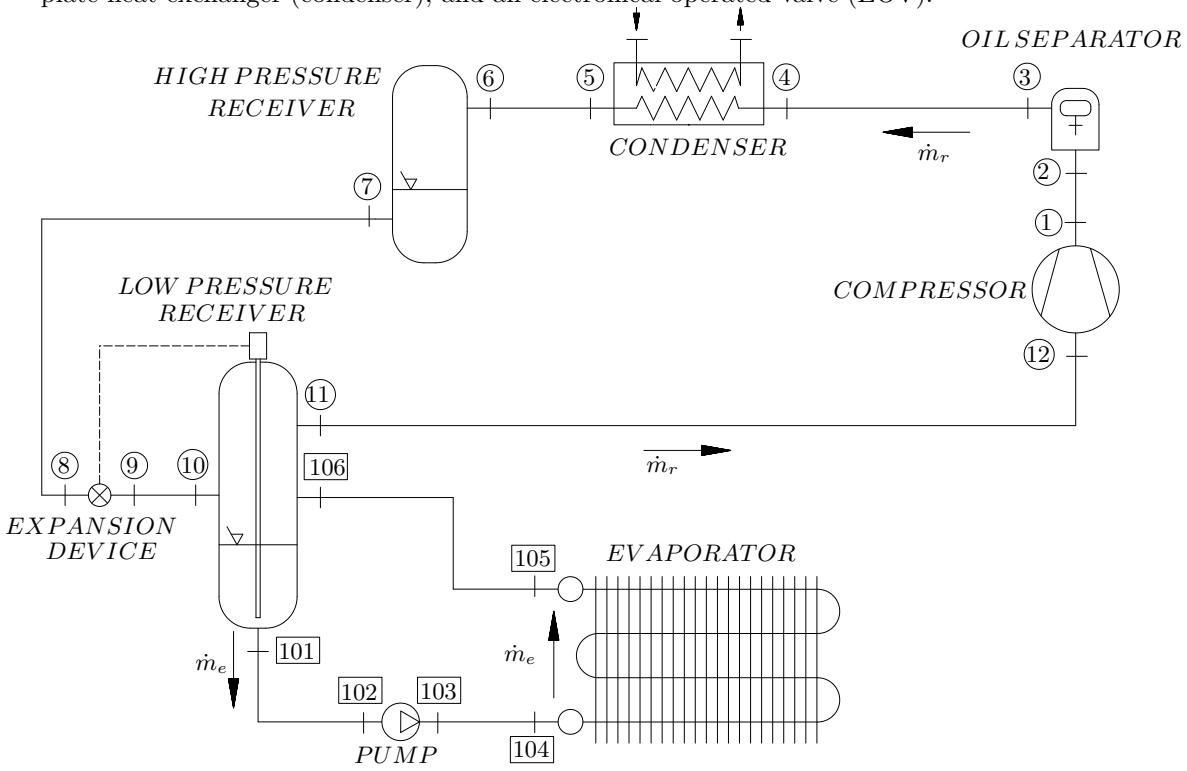

Figure 3.27: Scheme of liquid overfeed refrigerating system.

Table 3.31 describes the geometry of the main element of the liquid overfeed refrigerating system.

Table 3.31: Geometry of the main elements.

Compressor	BOCK Kältemaschinen: AM2 / 121-4S
Condenser	plate heat exchanger: $\epsilon_1 = 0.786$, $\epsilon_2 = 0.781$
High pressure receiver	$D_i = 168.3\,mm$, $H_t = 0.990\,m$
EOV	Alco, Emerson Corp.: EX2
Low pressure receiver	$D_i = 219\,mm$, $H_t = 1.240\,m$
Magnetically coupled gear pump	Micropump Inc.:Model 223
Evaporator	fin-and-tube heat exchanger: $\epsilon_1 = 0.369$, $\epsilon_2 = 0.281$

Table 3.32 shows the boundary conditions used in the verification studies. All

tests are conducted using R134a as working fluid. Air as secondary coolant in the evaporator and water in the condenser. The environment temperature is 25 °C.

Table 3.32: Boundary conditions for the verification test cases. Second step.

Case	$\dot{m}_{s,e}$[kg/s]	$T_{s,e,in}$[°C]	ϵ_e[%]	$\dot{m}_{s,c}$[kg/s]	$T_{s,c,in}$[°C]	ϵ_c[%]
1	0.4713	32.48	36.90	0.338	50.28	78.60
3	0.4727	32.42	35.70	0.343	50.36	78.90
8	0.7213	29.44	28.70	0.344	43.97	78.10
9	0.7200	29.36	28.10	0.344	43.78	78.10
13	0.9678	29.50	24.70	0.344	44.07	78.30
15	0.9620	29.43	24.10	0.344	43.80	78.30
19	0.7082	29.98	28.50	0.343	49.94	78.60
20	0.7094	29.97	28.70	0.343	49.87	78.70

Fig. 3.28 shows the evolution of the energy imbalances as a function of the global iterations, for both solvers (element-by-element and one equation, presented on section **??**). As it should be expected the imbalances tends to zero with iterations.

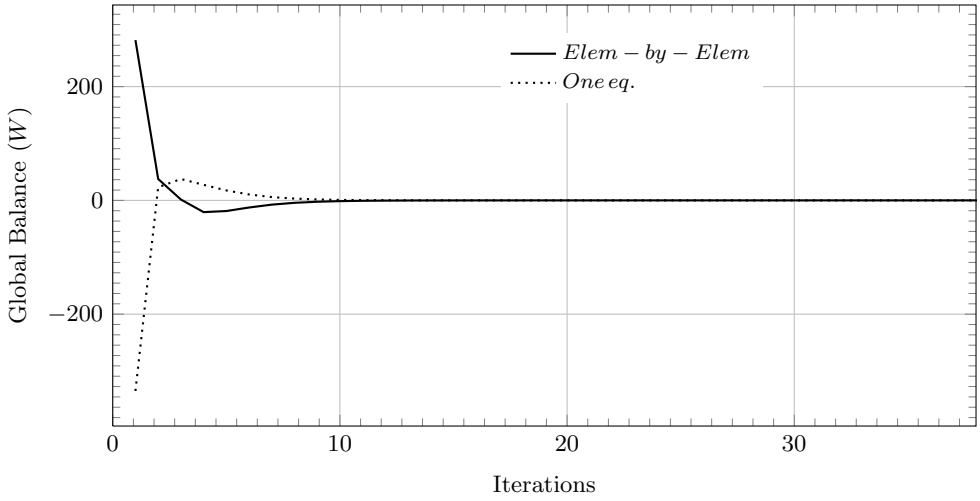

Figure 3.28: Verification Imbalance.

Table 3.33 resumes the results of the test cases. All the energy balances tend to zero, as it should be expected.

Table 3.33: Verification test cases. Ref 134a ($\epsilon = 10^{-10}$).

Case	T_{evap}[°C]	EB [W]	p_{disc} [bar]	p_{suc} [bar]	$\dot{m}_r$ [kg/s]	$\dot{m}_e$ [kg/s]	$\dot{Q}_c$ [W]	$\dot{Q}_e$ [W]	$\dot{W}_{cp}$ [W]
1	5.80	$-2.991 \cdot 10^{-8}$	15.812	3.274	$3.990 \cdot 10^{-2}$	$4.220 \cdot 10^{-2}$	6217.570	4668.361	1499.58
3	5.61	$-2.689 \cdot 10^{-8}$	15.764	3.211	$3.903 \cdot 10^{-2}$	$9.756 \cdot 10^{-2}$	6095.836	4552.026	1486.72
8	5.40	$-2.497 \cdot 10^{-8}$	13.697	3.219	$3.972 \cdot 10^{-2}$	$6.806 \cdot 10^{-2}$	6547.054	5006.585	1465.40
9	5.24	$-2.697 \cdot 10^{-8}$	13.601	3.164	$3.896 \cdot 10^{-2}$	$9.735 \cdot 10^{-2}$	6443.026	4909.095	1453.24
13	7.08	$-2.474 \cdot 10^{-8}$	13.854	3.423	$4.247 \cdot 10^{-2}$	$4.205 \cdot 10^{-2}$	6955.943	5391.877	1506.36
15	6.84	$-2.547 \cdot 10^{-8}$	13.723	3.350	$4.151 \cdot 10^{-2}$	$9.723 \cdot 10^{-2}$	6826.850	5269.528	1490.87
19	6.10	$-3.927 \cdot 10^{-8}$	15.724	3.357	$4.107 \cdot 10^{-2}$	$2.992 \cdot 10^{-2}$	6406.469	4847.974	1514.61
20	6.22	$-3.262 \cdot 10^{-8}$	15.701	3.363	$4.114 \cdot 10^{-2}$	$3.256 \cdot 10^{-2}$	6421.917	4862.739	1515.36

3.5 Conclusions

In this chapter, verification studies for the different simulation subroutines of the refrigeration system elements have been presented. For the insulated pipes and the double pipe heat exchangers, the verification studies have been carried out increasing mesh density and increasing the numerical accuracy. These verification studies allows to obtain an optimum mesh density criterion and a numerical accuracy criterion to assure optimum compromise between acurate results and minimum CPU time.
The verification studies for the receivers and the whole refrigerating systems (dry expansion, overfeed, etc.) have been carried out with the aim of guarantee the energy and mass balances. It has been presented the potential of the software of receiver simulation in different boundary conditions and steady state or unsteady regime.

3.6 Nomenclature

h	enthalpy $[J/kg]$
$\dot{m}$	mass flow rate $[kg/s]$
p	pressure $[Pa]$
t	time $[s]$
x_g	vapour quality
D	diameter $[m]$
H	height $[m]$
L	lengh $[m]$
N	Number of control volums
$\dot{Q}$	heat flux $[W]$
T	temperature $[K]$
$\dot{W}$	work $[W]$
Z	height $[m]$

Greek symbols

α	convective heat transfer coefficient $[W/m^2K]$
Δp	pressure drop $[Pa]$
Δt	time step $[s]$
η	efficiency
λ	thermal conductivity $[W/mK]$

Subscripts

a	insulate external
an	annular
$bottom$	bottom wall

c	condenser
cp	compressor
$cond$	condenser
$disc$	discharge
e	overfeed circuit, external or evaporator
env	environment
$evap$	evaporator
f	fluid
g	gas or vapour
i	inlet or inner
in	inlet
ins	insulation
l	liquid
lat	lateral wall
liq	liquid
$loss$	losses
r	main circuit
rec	receiver
ref	refrigerant
s	secondary fluid
sc	sub-cooling
sh	super-heating
suc	suction
s, in	secondary inlet
s, out	secondary outlet
top	top wall
vap	vapour
w	wall
$wall$	wall

References

[1] S. Estrada-Flores et al. "Simulation of transient behaviour in refrigeration plant pressure vessels: mathematical models and experimental validation". In: *International Journal of Refrigeration* 26.2 (2003), pp. 170–179.

Chapter 4

Validation

4.1 Introduction

In the process of developing a simulation code, it is important to verify that the code has not programming errors as well as to validate the accuracy of the mathematical model (modelling errors). Once verification analysis is given in chapter 3, a comprehensive comparison between numerical simulation results and experimental data is given in this chapter.
The following sections present the validation studies for the elements as well as the refrigerating system models (dry expansion and liquid overfeed) developed in this PhD thesis. The presented studies are based on experimental data obtained in the dry expansion facility and in the overfeed refrigerating facility at CTTC. A description of the experimental units used to obtain experimental data for validation purposes is also presented. During this thesis some adaptations and improvements have been done in dry expansion facility and a new set of experiments have been carried out and post-processed. In the following sections these facilities will be shortly presented.

4.2 Dry expansion Facility at CTTC

The experimental single-stage vapour compression refrigerating unit designed at CTTC research group (Figs. 4.1 and 4.2), was build with two objectives. The first one was to study each one of the elements separately. The test method used to study the compressor, is according to ISO 917 for testing refrigerant compressors. The second one was to study the dry expansion refrigerating systems as a whole, according to UNE-EN 378-1.

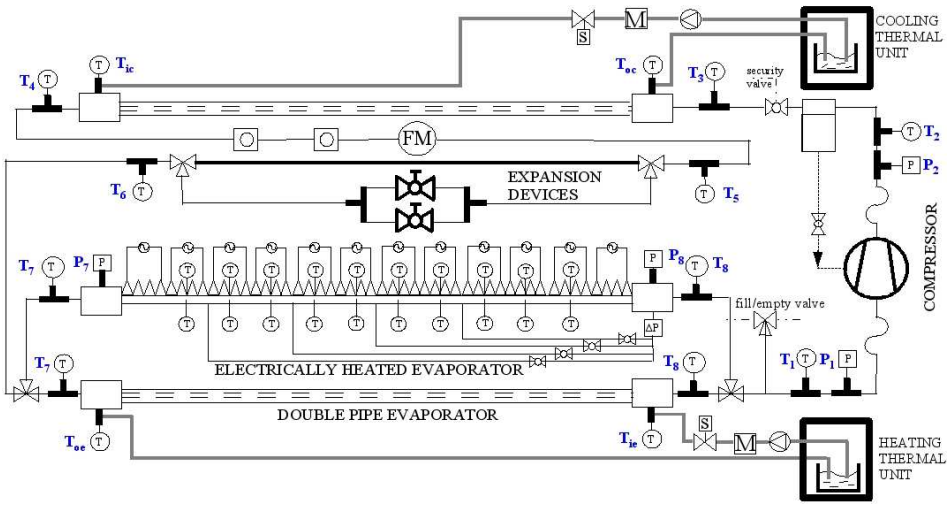

Figure 4.1: Test facility scheme.

The experimental unit is made up of the following elements: i) one hermetic reciprocating compressor, ii) one double-pipe condenser, iii) one capillary tube or one micro-metric valve as expansion device, and iv) one double-pipe evaporator or one electrically heated evaporator.
The fluid flow temperatures inside the tubes and annuli are measured with platinum resistance Pt-100 thermometer sensors (with an accuracy of $\pm 0.15 \pm 0.002\,T$ °C), which are located at the inlet and outlet sections of each element of the primary and secondary circuits. Condenser and evaporator absolute pressure are measured by transducers in ranges of 0-16 bars and 0-6 bars respectively with an accuracy of ±0.1% Full Scale. A Coriolis-type mass flowmeter with an accuracy of ±0.0009 kg/min (for R134a) and 0.2% of reading (for isobutane), is used to measure the refrigerant mass flow rate. The water inlet temperature in the evaporator and the condenser are controlled by two thermostatic heating and cooling units respectively. Variable speed driven gear pumps control the volumetric flow of the auxiliary coolants. Two magnetic flowmeters, with an accuracy of ±0.01 l/min from 0-2.5 l/min, and ±0.5% Full Scale from 2.5-25 l/min are used to measure the volumetric coolant flow. For an extended view of the experimental infrastructure see Rigola [1].
Different aspects have been updated and improved within this thesis: i) the experimental unit has been adapted to work with hydrocarbons like isobutane, ii) some sensors have been replaced and others have been added and calibrated, iii) different insulation aspects over some critical points have been improved, iv) the unit has also been prepared to use variable speed compressors, v) new capillary tube oriented to

household refrigeration capacity has been introduced, vi) better climatic control and vii) software control improved.

Figure 4.2: Dry expansion facility: Views of the whole cycle, compressor, auxiliary heaters.

4.3 Liquid Overfeed refrigerating Facility at CTTC

The test facility consists of liquid overfeed refrigeration system circuit working with R134a, experimental cold-storage room where the compact fin-and-tube heat exchanger (evaporator) is installed, and compensating/regulating chamber provided with electric heaters and vapour injection humidifier that will maintain the set tem-

perature and humidity in the cold-storage room. For an extended view of the experimental infrastructure see Danov [2].

4.3.1 Refrigeration circuit

It is made up of the following elements: one compressor (Bock AM2/121-4S), two plate heat exchangers (condenser and auxiliary heat exchanger for the oil return circuit), one fin-and-tube heat exchanger (evaporator), one electronically operated valve (Alco EX2) and two receivers (high pressure and low pressure). Fig. 4.3 shows the scheme of the refrigeration circuit, while Fig. 4.4 show the experimental overfeed refrigerating facility at CTTC

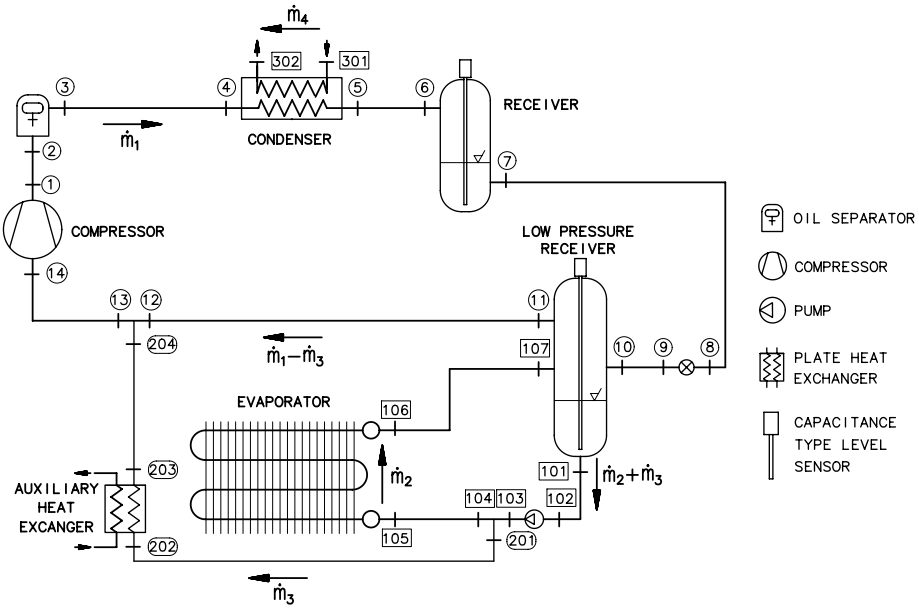

Figure 4.3: Test facility scheme.

Eight RTD Pt100 and two k thermo-couples are used in order to measure refrigerant temperature in several points of the cycle. Two absolute pressure sensors type Roseount 3051 TA normalised range 0 to 25 bars (error ±0.15% of span) are used to measure the high and low pressure. One differential transmitter type Rosemount 3051 CD calibrated in range 0 to 62200 Pa (error ±0.15% of span) is used to measure the

pressure drop through the evaporator. Two Coriolis-effect mass flow meters are used to measure the mass flow of the main circuit and the mass flow of the overfeed circuit, while two capacitance level sensors for receivers close the instrumentation used in the refrigeration circuit.

Figure 4.4: Liquid overfeed facility. Left: overfeef ref. circuit (LPR, comp, pump) Right: details of compressor and evaporator connection.[2]

4.3.2 Environmental chamber

It was constructed with polyurethane panels and their dimensions are 7.78x2.46x2.48 m. The evaporator will be mounted over a platform balance that would permit the measurement of the frost accumulation. A centrifugal fan suctions the chamber air through evaporator section then it drives air to an insulated pipe 18“ ASTM-API,

where airflow is measured by one mass flow meter Flexasster model ST95 with calibration VORTAB model ISFC-A180A1. The air circuit instrumentation consist on two temperature and relative humidity transmitters type THR-370/RS (temperature range from -30 to 70 °C, error ±2% RH), one absolute pressure sensor type TPN12-18V2 to measure the pressure in the cold-storage room, one differential pressure transmitter type 3051Cd calibrated in the range 0 to 6000 Pa, span 0 to 300 Pa (error ±0.15% of the span) to measure the air pressure drop through the evaporator.

4.3.3 Compensating/Regulating chamber.

This chamber has a set of electric resistances (9kW) and a set of humidifiers (9 kg/h). The cold-storage room together with the compensating/regulating chamber form the air circuit.

4.4 Measuring and post-processing experimental data

All the temperature sensors (RTD, Pt100 and thermocouples K type) are calibrated in the CTTC versus precision thermometer with accuracy ±0.03 °C. Pressure sensors, flow-meters, humidity sensors and level sensors are factory calibrated.

The experimental uncertainty of a particular measurement (temperature, pressure, etc.) is directly obtained from the sensor accuracy. However, the experimental uncertainty from a indirect variable (heat transferred, COP, etc.) is obtained using the methodology introduced by Moffat [3] to calculate the computer propagation error. The method is based on the contribution in the global error made by the individual sensor. The resulting uncertainty is calculated as the root sum square of those contributions.

The post-processing used has been mainly based on: applying the calibration curves to the experimental data, and statistical treatment of experimental data for the steady state cases. The average experimental data is compared with the numerical data from the simulation.

4.5 Validation of components

In this section a comparison between numerical results and experimental data is presented for specific components instead of analyse the whole cycle. The experimental data was obtained using the experimental unit described in section 4.2.

4.5.1 Compressor

Validation tests have been done using an isobutane hermetic reciprocating compressor with a capacity of $9\,cm^3$. Many tests for hermetic reciprocating compressors have been carried out in CTTC's facility. The information collected has been used to model the compressors. In this subsection three tests have been presented as an example of the validation of an empirical compressor modelization. Table 4.1 shows the input avlues used to simulate the compressor. The numerical results presented on Table 4.2 have been obtained using the empirical modelization for hermetic reciprocating compressors from compressor tests carried out in the CTTC and presented on Section 2.2.2, where $\Delta\phi_{rel} = 100 \cdot \frac{\phi_{ex}-\phi nu}{\phi_{ex}}$.

Table 4.1: Compressor: Experimental vs Numerical (inputs).

Test	T_i [°C]	p_i [bar]	p_o [bar]
1	32.51	0.89	7.98
2	32.72	0.63	7.68
3	32.77	0.59	7.68

Table 4.2: Compressor: Experimental vs Numerical results.

Test	$T_{o,ex}$ [°C]	$T_{o,nu}$ [°C]	$\dot{m}_{r,ex}$ [kg/h]	$\dot{m}_{r,nu}$ [kg/h]	$\Delta\dot{m}_{rel}$ [%]	$\dot{W}_{e,ex}$ [W]	$\dot{W}_{e,nu}$ [W]	$\Delta\dot{W}_{rel}$ [%]
1	92.77	91.29	2.627	2.655	1.06	119.51	118.34	0.97
2	89.41	89.71	1.767	1.735	1.81	94.92	92.26	2.80
3	89.09	89.32	1.553	1.603	3.21	90.03	88.62	1.56

A good agreement between numerical and experimental results has been obtained for all validation cases, the differences in the mass flow are lower than 3.3 % and the differences in the electrical consumption are lower than 2.9 %. Good agreement in the discharge temperature have been obtained as can be seen with discrepancies lower than 1.5 °C.

4.5.2 Double pipe heat exchangers

The validation study for counterflow double pipe heat exchangers is presented with two different geometries. The first one corresponds to a condenser with an internal diameter of 6.0 mm, an external diameter of 16.0 mm, an internal annular diameter of 8.0 mm, an external annular diameter of 20.0 mm, an external insulation diameter of 60.0 mm, and a length of 2.19 m. The second one is an evaporator with an internal diameter of 8.0 mm, an external diameter of 9.6 mm, an internal annular diameter of 16.0 mm, an external annular diameter of 20.0 mm, an external insulation diameter of 60.0 mm, and a length of 6.15 m. Four different working conditions (see Table 4.3) have been validated.

Table 4.3: Boundary conditions for the validation test cases.

Validation Test	1	2	3	4	5
Refrigerant	*R*600*a*	*R*600*a*	*R*600*a*	*R*600*a*	*R*134*a*
T_{env} [°C]	25.00	25.00	25.00	25.00	25.00
$p_{e,i}$ [bar]	0.66	0.58	0.86	0.76	1.36
$x_{g,e,i}$	0.32	0.33	0.29	0.25	0.27
$\dot{m}_{r,c}$ [kg/h]	1.882	1.631	2.592	2.362	6.336
$p_{c,i}$ [bar]	7.88	7.76	7.69	5.98	13.87
$T_{c,i}$ [°C]	73.50	67.79	74.34	67.31	74.74
Evap. coolant	40% prop	40% prop	40% prop	40% prop	water
$\dot{m}_{s,e}$ $[kg/s]$	118.8	118.8	118.8	118.8	180.0
$T_{s,ie}$ [°C]	31.02	32.42	32.23	32.35	19.24
Cond. coolant	40% prop	40% prop	40% prop	40% prop	water
$\dot{m}_{s,c}$ [kg/h]	169.56	169.56	169.56	169.56	237.60
$T_{s,ic}$ [°C]	32.04	31.00	32.00	20.53	23.07

Tables 4.4 and 4.5 present the comparison of experimental versus numerical results for the simulation of double pipes heat exchangers (condenser and evaporator respectively) using the detailed model presented on Section 2.6, where a good agreement is obtained in the outlet temperatures as well as in the heat transferred (differences lower than 2.9 %).
The discrepancies are lower than 1°C in the refrigerant temperatures, and for the secondary coolant temperatures are lower than 0.4°C.

Table 4.4: Condenser: experimental vs numerical results.

Test	$T_{o,ex}$ [°C]	$T_{o,nu}$ [°C]	$T_{s,oc,ex}$ [°C]	$T_{s,oc,nu}$ [°C]	$\dot{Q}_{ex}$ [W]	$\dot{Q}_{nu}$ [W]	$\Delta\dot{Q}_{rel}$ [%]
1	32.14	32.33	33.18	33.17	203.19	202.94	0.12
2	32.07	31.99	32.94	32.95	171.08	170.96	0.07
3	32.09	31.83	32.54	32.57	281.46	280.39	0.38
4	21.27	20.53	22.05	22.07	268.54	268.75	0.07
5	24.75	25.07	24.72	24.43	369.60	380.04	2.82

Table 4.5: Evaporator: experimental vs numerical results.

Test	$T_{i,ex}$ [°C]	$T_{i,nu}$ [°C]	$T_{o,ex}$ [°C]	$T_{o,nu}$ [°C]	$T_{s,oe,ex}$ [°C]	$T_{s,oe,nu}$ [°C]	$\dot{Q}_{ex}$ [W]	$\dot{Q}_{nu}$ [W]	$\Delta\dot{Q}_{rel}$ [%]
1	−22.53	−22.14	30.99	31.00	29.44	29.48	176.42	176.45	0.01
2	−24.72	−25.09	32.23	32.22	30.91	30.92	155.29	153.97	0.85
3	−15.58	−15.79	32.38	32.40	30.16	30.37	244.51	244.20	0.12
4	−18.80	−18.38	32.26	32.33	30.13	30.47	236.03	236.15	0.05
5	−19.60	−19.49	19.22	19.20	18.28	18.04	299.80	308.14	2.78

Figs. 4.5 and 4.6 show the inlet and outlet evolution temperature for the test case 1, observing the high level of detail obtained from the simulation. It also can be seen

the good agreement of the numerical and experimental values of the inlet and outlet temperatures of the tested double pipe heat exchangers.

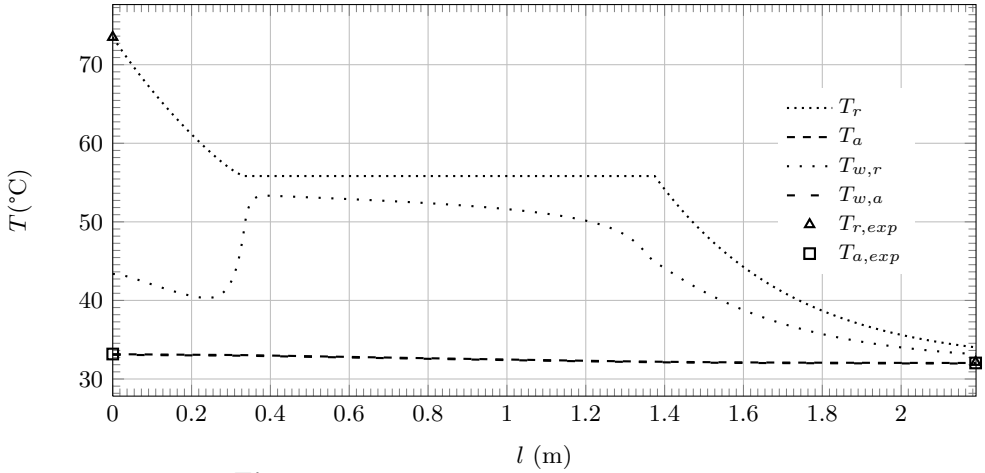

Figure 4.5: Condenser temperature evolution.

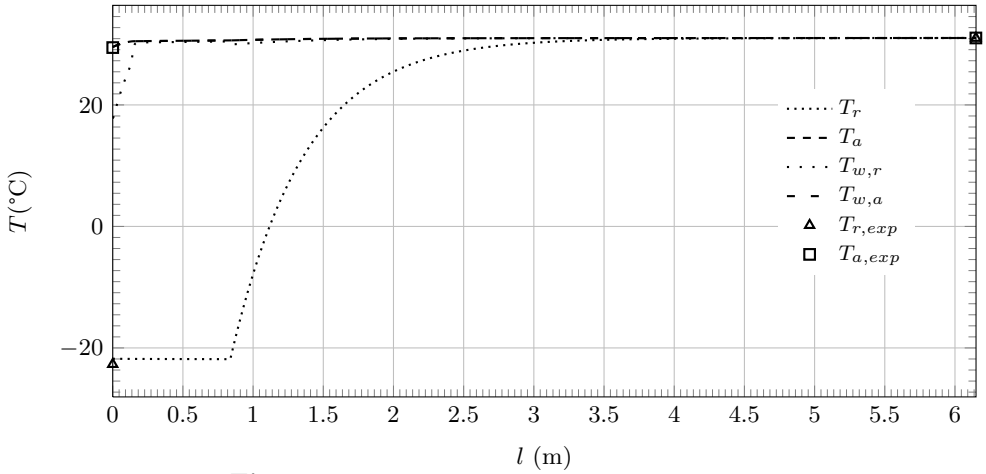

Figure 4.6: Evaporator temperature evolution.

Figs. 4.7 and 4.8 show the evolution of the vapour mass fraction along the double pipe length. As can be seen the double pipe heat exchangers would be oversized under these specific working conditions.

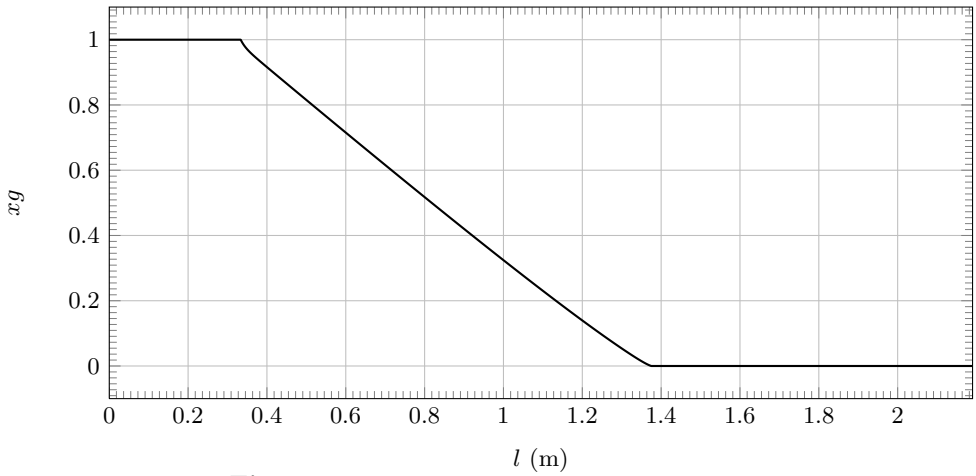

Figure 4.7: Condenser mass fraction evolution.

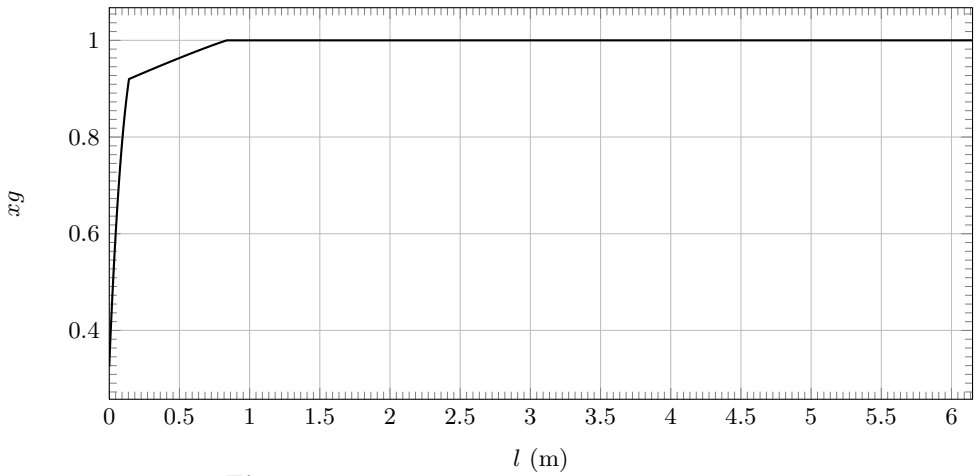

Figure 4.8: Evaporator mass fraction evolution.

4.5.3 Expansion Device

In this section is shown the validation of the expasion device modelizaton for micrometric expansion valve and for capillary tubes. Experiments 1 to 4 were carried out with a micrometric valve, while the last one experiment a capillary tube was used. Table 4.6 shows the comparison between the experimental data and the numerical results obtained from the simulation using the model for micro-metric expansion valves

presented on section 2.3.4, and from the simulation of a capillary tube with the advanced model developed in the CTTC's group presented on section 2.3.3.

Table 4.6: Expansion device: Experimental data vs Numerical results.

Test	T_i [°C]	p_i [bar]	p_o [bar]	$T_{o,ex}$ [°C]	$T_{o,nu}$ [°C]	$\dot{m}_{ex}$ [kg/h]	$\Delta\dot{m}_{rel}$ [kg/h]	%
1	30.41	7.75	0.75	−22.53	−19.12	1.883	1.861	1.17
2	29.22	7.59	0.67	−24.72	−21.78	1.630	1.624	0.36
3	30.20	7.64	0.97	−15.58	−12.79	2.592	2.589	0.11
4	22.11	5.84	0.86	−18.71	−15.79	2.362	2.358	0.17
5	23.45	13.87	1.36	−19.48	−19.49	6.336	6.372	0.57

As can be seen differences are lower than 1.5% for the mass flow and lower than 3.5°C in the outlet temperatures.

4.5.4 Tube connections

This section shows the comparison between numerical results and experimental data for the tube connections between main components. The compressor-condenser connection has been selected since the difference between refrigerant and environment temperatures are higher. Numerical results have been obtained from the simulation based on the advanced twophase flow madelization presented on section 2.6. The Table 4.7 shows the comparison between numerical results and experimental data for the compressor-condenser tube connection. The environmental temperature was 32 °C for all tests.

Table 4.7: Connection tube: Experimental vs Numerical results.

Test	$\dot{m}_r$ [kg/h]	T_i **[°C]**	p_i **[bar]**	$T_{o,ex}$ [°C]	$T_{o,nu}$ [°C]	$\dot{Q}_{ex}$ [W]	$\dot{Q}_{nu}$ [W]
1	2.666	90.76	7.70	80.63	83.54	15.64	11.16
2	1.722	90.16	7.77	76.03	79.63	14.08	10.49
3	1.584	88.81	7.70	74.95	77.73	12.64	10.11

Validation cases present a reasonable agreement showing that the highest discrepancies are in test case 2, even it all of them are lower than 3.6°C and 5 W of heat losses. The imperfection of the experiment (the tube connection which is part of the dry expansion facility, has sensors, valves and the perfect contact between pipe and insulation is difficult to assure) seems that could produces more heat losses than the ideal experiment with a perfect insulation and without sensors. It has been decided that the agreement obtained is reasonable since the discrepances are no so important in the study of the whole cycle.
Fig. 4.9 shows the evolution of the temperature through the insulation in the radial direction in the middle of the tube connection between compressor and condenser, where both refrigerant temperature and environmental temperature are indicated.

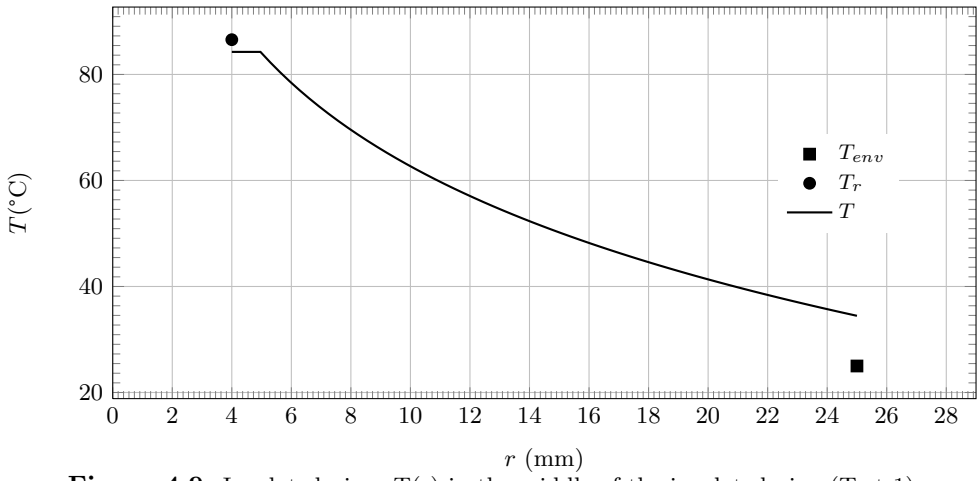

Figure 4.9: Insulated pipe: T(r) in the middle of the insulated pipe (Test 1).

4.5.5 Receivers

In order to validate the receiver numerical model presented on Section 2.5, the numerical results have been compared with the experimental data collected by Estrada-Flores [4] from two calorimeters adapted to the receivers study. These installations consist of a refrigeration system with a compressor, a condenser, an expansion device, and a closed insulated receiver, where the evaporator (an ellipsoidal or a circular coil) is placed together with the heaters. A detailed description of the experimental setup can be found in Estrada-Flores [4].
Table 4.8 shows the characteristics of the main elements of the experimental facility.

Table 4.8: Experimental facility description. [4]

Calorimeter	Star	South Bank
Compressor	Bitzer Type 2 (open type) Motor 1.1 kW	Prestcold K75/0010 (hermetic type) Motor 0.75 kW
Condenser	Water cooled unit (shell and tube)	Water cooled unit (shell and coil type)
EOEV	Danfoss AKV-10	Thermostatic (Danfoss)
Evaporator	Copper tubing (ellipsoidal coil)	Copper tubing (Circular coil)
Calorimeter metallic shell	Material: Steel BS1501 161 430A $h = 675\,mm,\ D_i = 335\,mm$ $e_{shell} = 10\,mm,\ e_{ins} = 100\,mm$ of Armaflex class O	Material: Steel BS1501 161 430A $h = 580\,mm,\ D_i = 180\,mm$ $e_{shell} = 7.5\,mm,\ e_{ins} = 200\,mm$ of glass fiber plus
Heaters	Interchangeable heaters (0.4, 1 and 1.5 kW)	1 variable (0 to 1.5 kW) 1 fixed (1.5 kW)

The experimental data was obtained from five different tests. Table 4.9 presents

the boundary conditions of test cases.

Table 4.9: Test conditions.

Test cases	Calorimeter	T_{ini} (liq, vap) [°C]	T_{amb} [°C]	t_{end} [s]	Heating Power
TRIAL 1	Star	11.1 , 13.3	25	11000	yes
TRIAL 2	Star	28.0 , 28.1	18	11550	no
TRIAL 3	South Bank	-5.4 , -5.1	18	5010	yes
TRIAL 4	South Bank	8.5 , 8.8	16	8810	yes
TRIAL 5	South Bank	8.2 , 8.5	15	7160	yes

Fig. 4.10 shows the temporal functions of heaters and coil placed inside the insulated receiver used as boundary conditions in the numerical simulation of the validation trial 1. In trial 2 the heaters and the coil are switch off.

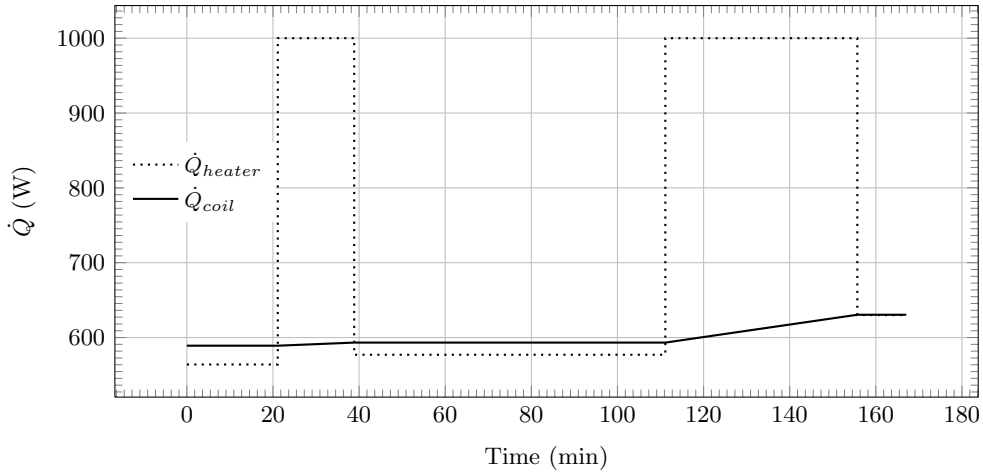

Figure 4.10: Transient boundary conditions for trial 1.

Fig. 4.11 shows a comparative analysis of temperatures inside the receiver between experimental, numerical [4] (with insulate thickness = $100\,mm$), numerical 1 (with insulate thickness = $100\,mm$) and numerical 2 (with insulate thickness = $10\,mm$) for trial 2, (where numerical 1 and numerical 2 are obtained with our simulation).

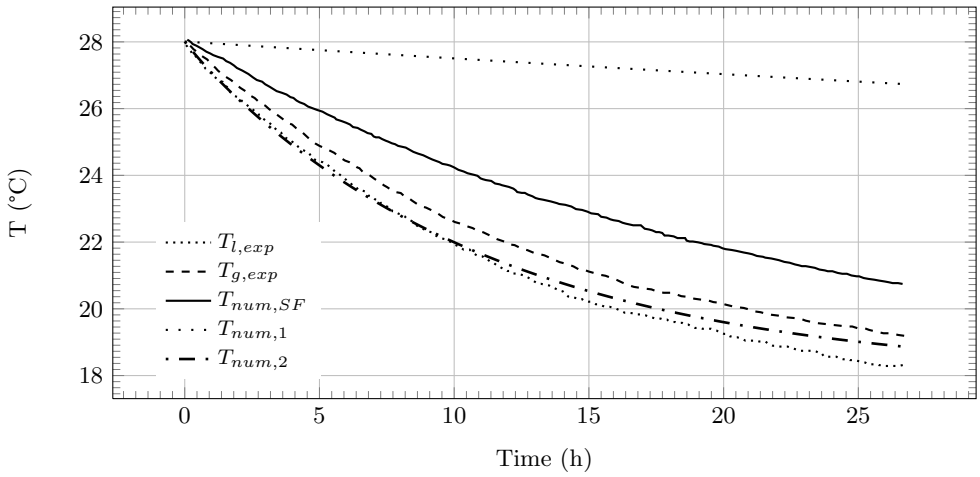

Figure 4.11: Validation (trail 2).

As can be seen in Fig. 4.11 the numerical results obtained with the insulate thickness of the 100 mm present an important deviation (near 9°C) from the experimental data. With the insulation thickness of 10 mm the results obtained are in a good agreement with the experiments (less than 1°C, Fig. 4.11). It has been carried out heat losses study in function of the insulation, in order to evaluate possible inaccuracy in geometrical data.
The first step was to calculate with the analytical formulation (eq. 4.1), the average heat losses of the transient simulation. The second step was to calculate the average heat losses from the experimental data. Table 4.10 presents the results from the two different insulation thickness. It seems that the geometrical information from [4] is not accurate enough.

$$\dot{Q} = UA(T_i - T_o) \tag{4.1}$$

where A is the external surface of the receiver ($A = f(D_o)$).
U is the overall heat transfer coefficient ($U = f(\alpha_i^l, \alpha_i^v, \alpha_o, \lambda_{ins})$).
$\alpha_i^l = 500\,\frac{W}{m^2K}$, $\alpha_i^v = \alpha_o = 10\,\frac{W}{m^2K}$ and $\lambda_{ins} = 0.035\,\frac{W}{mK}$

Table 4.10: Heat losses study.

Insulation thickness [mm]	$\dot{Q}_{in}[W]$	$\dot{Q}_{end}[W]$	$\dot{Q}_{aver} = \frac{\dot{Q}_{in}+\dot{Q}_{end}}{2}[W]$
100	3.627	0.289	1.958
10	18.074	1.444	9.759
Experimental	—	—	9.104

Fig. 4.12 shows the comparison of the numerical temperature obtained with the numerical simulation tool and the temperature obtained with an analytical simulation method (lumped capacitance method, considering one temperature inside the receiver and different zones with their own heat transfer coefficients) with an insulation thickness of 10 mm. A good agreement between both simulations can be seen, therefore it seems that the heat losses have been evaluated correctly.

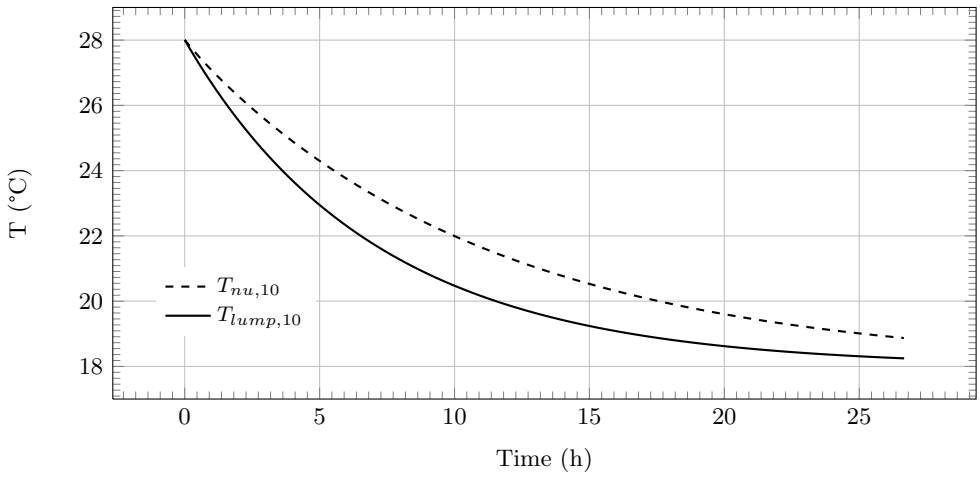

Figure 4.12: Comparision lumped method and numerical simulation

Fig. 4.13 shows the comparison of the temperatures inside the receiver between experimental, $T_{num,SF}$ [4], and T_{num} (from our simulation) for trial 1.

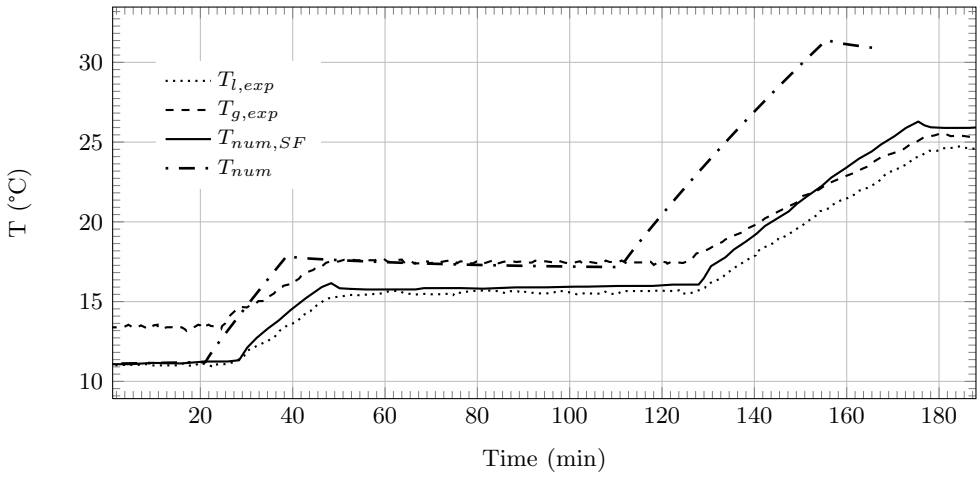

Figure 4.13: Validation. Trail 1

In Fig. 4.13 the numerical results obtained from the simulation are presented. A sensible deviation (near 7°C) from the experimental data and an important delay (of the experimental temperatures from the start time of the increase of the heater power) have been observed. In order to understand this deviation and delay, it has been carried out a study of the transient functions of boundary conditions.

- The first step was to evaluate the experimental increase of heat needed to get the intermediate steady state ($T_l = 16.0$ [°C]).
  $\Delta E_{1-2,exp} = M_{liq}(h_{liq,st2} - h_{liq,st1}) + M_{vap}(h_{vap,st2} - h_{vap,st1}) = 173708.06\,J$
  Where st1 (steady1) $T_l = 11.1$ [°C] and st2 (steady2) $T_l = 16.0$ [°C].

- The second step was to evaluate the numerical increase of heat from the temporal boundary condition functions used in [4].
  $\dot{Q}_{h,tr} = 1000\,W$
  Steady 1 coil: $\dot{Q}_{c1} = \dot{Q}_{h,st1} - \dot{Q}_{l,st1} = 564 - 25.09 = 538.91\,W$
  Steady 2 coil: $\dot{Q}_{c2} = \dot{Q}_{h,st2} - \dot{Q}_{l,st2} = 577 - 16.25 = 560.75\,W$
  $\Delta E_{tr} = \dot{Q}_{h,tr}\Delta t_{tr} - 0.5(\dot{Q}_{c1} + \dot{Q}_{c2})\Delta t_{tr} = 1000 \cdot 960 - 549.83 \cdot 960 = 432163.2\,J$

The comparison between the experimental increase of energy needed and the numerical increase of energy use in the simulation are different. It makes us to think that the information of the temporal boundary condition functions of heaters and coils are not accurate enough. Despite of it, the evolution of our numerical results is similar

as the experimental data.
The studies presented do not demonstrate that our code is valid, since there are no reliable experimental data. As a future action we are considering to conduct our own experiment to validate our numerical code.

4.6 Dry Expansion Refrigerating System

For test cases using R134a and R600a had been carried out in order to validate our simulation code based on detailed balances for dry expansion refrigerating systems. Table 4.11 shows the boundary conditions for the set of validation cases.

Table 4.11: Boundary conditions for the validation test cases.

Validation Test	1	2	3	4
Refrigerant	$R134a$	$R600a$	$R600a$	$R600a$
p_{disch} [bar]	13.87	7.88	7.76	7.69
T_{env} [°C]	25.00	25.00	25.00	25.00
Evap. coolant	water	40% prop	40% prop	40% prop
$\dot{m}_{s,e}\,[kg/h]$	180.00	114.21	114.83	114.83
$T_{s,ie}$ [°C]	19.24	32.62	32.53	32.58
Cond. coolant	water	40% prop	40% prop	40% prop
$\dot{m}_{s,c}\,[kg/h]$	237.60	168.38	167.31	167.76
$T_{s,ic}$ [°C]	23.07	31.99	31.89	31.91

Table 4.12 describes the geometry of the system. The R134a case uses a capillary tube as a expansion device. However, the R600a cases use a micromentric valves as a expansion device.

Table 4.12: Geometry of the system.

Dry System	
Compressor	ACC Comp. $V_{cl} = 9\,cm^3$
Tube connection (cp-cd)	$D_i = 8.0\,mm,\ D_e = 9.6\,mm,\ D_{ins} = 50.0\,mm,\ L = 1.85\,m$
Condenser	double pipe: $D_i = 6\,mm,\ D_e = 8\,mm,\ D_a = 16\,mm$
	counterflow $D_{ae} = 20\,mm,\ D_{ins} = 60\,mm,\ L = 2.19\,m$
Tube connection (cd-ed)	$D_i = 8.0\,mm,\ D_e = 9.6\,mm,\ D_{ins} = 50.0\,mm,\ L = 1.8\,m$
Expansion device	Micrometric valve, Capillary tube
Tube connection (ed-ev)	$D_i = 8.0\,mm,\ D_e = 9.6\,mm,\ D_{ins} = 50.0\,mm,\ L = 3.3\,m$
Evaporator	double pipe: $D_i = 8\,mm,\ D_e = 9.6\,mm,\ D_a = 16\,mm$
	counterflow $D_{ae} = 20\,mm,\ D_{ins} = 60\,mm,\ L = 6.15\,m$
Tube connection (ev-cp)	$D_i = 8.0\,mm,\ D_e = 9.6\,mm,\ D_{ins} = 50.0\,mm,\ L = 2.6\,m$

4.6.1 R134a validation case

The empirical data used to validate the software were obtained from a previous experiments of the update of the experimental facilities to use isobutane. Table 4.13 shows the comparison of experimental temperatures of the inlet-outlet components versus numerical temperatures from the simulation.

Table 4.13: Temperatures: Experimental vs Numerical results.

	T_1 [°C]	T_2 [°C]	T_3 [°C]	T_4 [°C]	T_5 [°C]	T_6 [°C]	T_7 [°C]	T_8 [°C]
ex1	20.11	98.54	74.74	24.71	23.45	−19.48	−19.60	19.22
nu1	19.40	106.45	90.01	25.30	24.74	−17.68	−17.70	19.17

Tables 4.15-4.16 present the comparision of numerical energetical values and experimental energetical values.

Table 4.14: Cycle (1): Experimental vs Numerical results.

	$\dot{Q}_{e,ex}$ [W]	$\dot{Q}_{e,nu}$ [W]	$\Delta\dot{Q}_{e,rel}$ [%]	$\dot{Q}_{c,ex}$ [W]	$\dot{Q}_{c,nu}$ [W]	$\Delta\dot{Q}_{c,rel}$ [%]
1	299.8	310.6	3.60	369.6	380.3	2.89

Table 4.15: Cycle (1): Experimental vs Numerical results.

	$\dot{W}_{e,ex}$ [W]	$\dot{W}_{e,nu}$ [W]	$\Delta\dot{W}_{rel}$ [%]	COP_{ex}	COP_{nu}	Π_{ex}	Π_{nu}
1	191.3	178.9	6.48	1.57	1.73	10.22	9.67

Table 4.16: Cycle (2): Experimental vs Numerical results.

	$\dot{m}_{r,ex}$ [kg/h]	$\dot{m}_{r,nu}$ [kg/h]	$\Delta\dot{m}_{rel}$ [%]
1	6.33	6.27	0.94

The comparison analysis presents a reasonable agreement, except the empirical temperature and numerical temperature at the condenser inlet (T_3), where the difference is almost 15°C. The comparison of energetic values are in a reasonable agreement (all are lower than 10 %). Two weak points to explain it have been detected after an important work of analysis of the comparision between eperimental data and numerical results. The first aspect affects to the numerical results. The evaluation of the heat losses ratio of the compressor is not accurate enough, therefore the discharge temperature is higher than experimental. The second one affects to the experimental infrastructure. The insulation of the compressor-condenser connection tube had deficiencies, the contact between tube and the insulation were not good. This deficiency

were detected and the tube-insulation contact were improved during the execution of the recent experimental cases with R600a.
Fig. 4.14 shows the comparison experimental versus numerical results of the main cycle points in a p-h diagram.

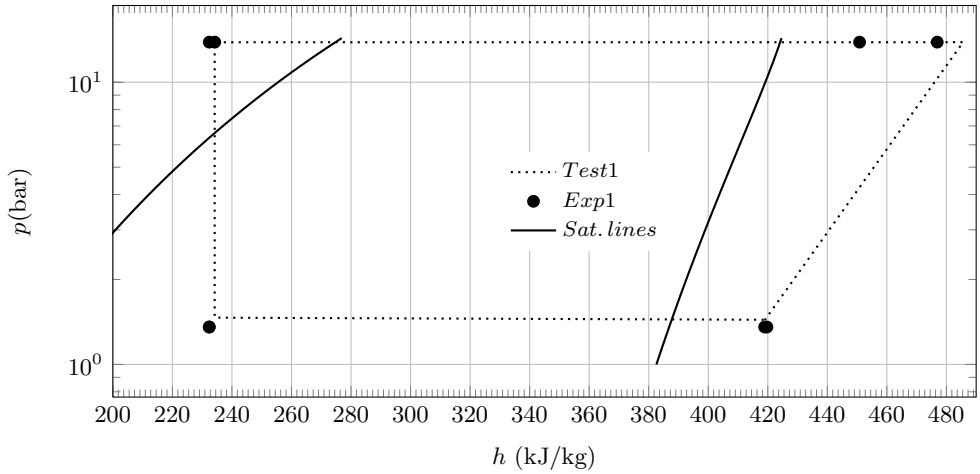

Figure 4.14: Diagram: p-h validation test 1.

4.6.2 R600a validation case

The boundary conditions of validation tests using isobutane are defined in Table 4.11, and the geometry of the cycle is presented in Table 4.12 The temperatures comparison analysis for the set of validation cases carried out, are presented in Table 4.17.
A good agreement between the experimental data and the numerical results has been obtained. The highest difference in the temperatures has been detected on the inlet condenser, and it is lower than 3°C.

Table 4.17: Refrigerating system: Experimental vs Numerical results.

	T_1 [°C]	T_2 [°C]	T_3 [°C]	T_4 [°C]	T_5 [°C]	T_6 [°C]	T_7 [°C]	T_8 [°C]
ex2	32.37	90.76	80.63	33.48	34.10	−14.57	−14.81	32.56
nu2	31.18	89.75	81.83	33.12	32.35	−14.45	−14.57	32.60
ex3	32.70	90.16	76.03	32.10	33.93	−22.97	−23.21	32.47
nu3	30.49	87.59	76.32	32.12	31.11	−22.83	−22.98	32.52
ex4	32.81	88.81	74.95	32.03	33.82	−24.53	−24.74	32.51
nu4	30.39	86.99	74.78	32.07	30.99	−24.43	−24.61	32.57

Tables 4.18-4.20 present the comparision between numerical and experimental energy values of the cycle, the mass flow and the pressure ratio. A reasonable good agreement is observed in all parameters, and all discrepances are lower than 10.0 %.

Table 4.18: Cycle (1): Experimental vs Numerical results.

	$\dot{Q}_{e,ex}$ [W]	$\dot{Q}_{e,nu}$ [W]	$\Delta\dot{Q}_{e,rel}$ [%]	$\dot{Q}_{c,ex}$ [W]	$\dot{Q}_{c,nu}$ [W]	$\Delta\dot{Q}_{c,rel}$ [%]
2	242.15	233.62	3.52	294.01	299.46	1.85
3	157.00	144.76	7.79	186.90	188.99	1.11
4	144.19	131.41	8.86	170.59	172.71	1.24

Table 4.19: Cycle (2): Experimental vs Numerical results.

	$\dot{W}_{e,ex}$ [W]	$\dot{W}_{e,nu}$ [W]	$\Delta\dot{W}_{rel}$ [%]	COP_{ex}	COP_{nu}	Π_{ex}	Π_{nu}
2	116.03	113.37	2.29	2.08	2.06	8.75	8.72
3	92.00	87.73	4.63	1.70	1.65	12.53	12.46
4	87.63	82.13	6.27	1.64	1.60	13.27	13.27

Table 4.20: Cycle (3): Experimental vs Numerical results.

	$\dot{m}_{r,ex}$ [kg/h]	$\dot{m}_{r,nu}$ [kg/h]	$\Delta\dot{m}_{rel}$ %
2	2.640	2.666	1.14
3	1.706	1.722	0.93
4	1.564	1.584	1.27

Fig. 4.15 shows the comparison of experimental data versus numerical results of the main cycle points from the set of validation cases carried out in a diagram p-h.

4.7 Validation of Liquid Overfeed Refrigerating System

Six simulation cases of an overfeed refrigerating system have been carried out. The numerical results have been compared with the experimental data [2] obtained from the CTTC experimental facility, in order to validate the overfeed refrigerating systems model described on Section 2.7.3. The efficiencies used in the simulation were obtained from a parametrization done from a previously high level simulation of the heat exchangers.
Table 4.21 shows the boundary conditions used to simulate the validation cases.

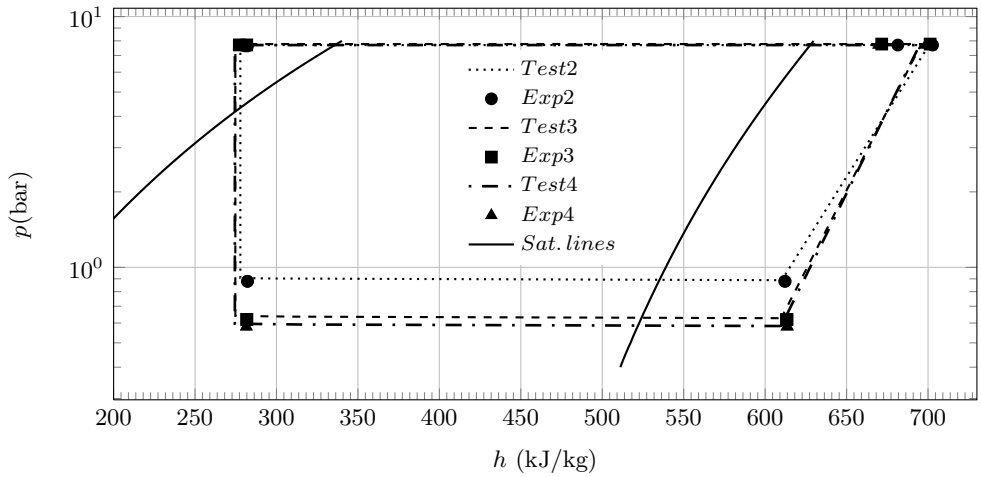

Figure 4.15: Diagram: p-h validation tests 2 to 4.

Table 4.21: Boundary conditions for test cases.

Case	$\dot{m}_e\,[\frac{kg}{h}]$	$\dot{m}_{s,e}\,[\frac{kg}{h}]$	$\epsilon_e\,[\%]$	$T_{s,ie}$ [°C]	$\dot{m}_{s,c}\,[\frac{kg}{h}]$	$\epsilon_c\,[\%]$	$T_{s,ic}[C]$	$\eta_{em}\,[\%]$
1	151.92	1696.68	36.9	32.48	1216.8	78.6	50.28	80.0
2	447.36	1705.32	35.5	32.48	1234.8	79.1	50.53	80.0
3	545.88	1724.40	34.7	29.51	1234.8	79.3	50.55	80.0
4	650.40	1734.48	34.0	29.38	1234.8	79.3	50.59	80.0
5	151.86	2592.72	29.2	29.48	1238.4	77.7	43.86	80.0
6	245.04	2596.68	28.7	29.44	1238.4	78.1	43.97	80.0

Table 4.22 indicates the main geometry of the overfeed refrigerating system simulated.

Table 4.22: Geometry of the system.

Overfeed System	
Compressor	Reciprocating compressor: AM2/121-4S Bock Kältemaschinen.
Tube con. (cp-cd)	$D_i = 17.27\,mm,\ D_e = 19.05\,mm,\ D_{ins} = 21.05\,mm,\ L = 4.69\,m$
Condenser	Brazed plate condenser: NB51 Alfa Laval.
Tube con. (cd-hpr)	$D_i = 10.92\,mm,\ D_e = 12.7\,mm,\ D_{ins} = 14.7\,mm,\ L = 0.56\,m$
High pressure receiver	$D_i = 30.0\,mm,\ D_e = 35.0\,mm,\ D_{ins} = 39.0\,mm,\ H = 0.6\,m,\ Z_l = 0.3\,mm$
Tube con. (hpr-ed)	$D_i = 10.92\,mm,\ D_e = 12.7\,mm,\ D_{ins} = 14.7\,mm,\ L = 1.14\,m$
Expansion device	Electronic expansion valve: EX2 Alco, Emerson Corp.
Tube con. (ed-lpr)	$D_i = 10.92\,mm,\ D_e = 12.7\,mm,\ D_{ins} = 14.7\,mm,\ L = 0.92\,m$
Low pressure receiver	$D_i = 30.0\,mm,\ D_e = 35.0\,mm,\ D_{ins} = 39.0\,mm,\ H = 1.0\,m,\ Z_l = 0.4\,mm$
Tube con. (lpr-cd)	$D_i = 17.27\,mm,\ D_e = 19.05\,mm,\ D_{ins} = 21.05\,mm,\ L = 3.81\,m$
Tube con. (lpr-pu)	$D_i = 22.0\,mm,\ D_e = 25.0\,mm,\ D_{ins} = 27.4\,mm,\ L = 1.61\,m$
Pump	Magnetically coupled gear pump: Model 223 Micropump Inc.
Tube con. (pu-ev)	$D_i = 22.0\,mm,\ D_e = 25.0\,mm,\ D_{ins} = 27.4\,mm,\ L = 3.31\,m$
Evaporator	Fin-and-Tube heat exchanger: (complete geometry description available in [2]).
Tube con. (ev-lpr)	$D_i = 22.0\,mm,\ D_e = 25.0\,mm,\ D_{ins} = 27.4\,mm,\ L = 4.03\,m$

The comparison analysis of the overfeed refrigerating system is presented in the Table 4.23. The maximum differences in the temperatures are lower than 7°C and they are located in the discharge of compressor and in the inlet of the condenser. There are some aspects that can explain it. The first one, the accuracy of the experimental data provided by the compressor supplier could be not good enough, since no information of heat losses in the compressor is given. The second one, the connecting pipes are treated as a macro control volume and there are some connecting pipes quite large. Therefore, the error in this tubes are higher than the desirable. Finally, it is important to highlight that all the other variables errors are under or very close to the 10 % error, which is considered acceptable. Table 4.24 presents the comparison numerical versus experimental values of the cooling capacity and the condenser capacity. As can be seen a reasonable good agreement has been obtained, and all the disrapances are lower than 6 %.

Table 4.24: Overfeed refrierating system: Experimental vs Numerical results 2.

	$\dot{Q}_{e,ex}$ [W]	$\dot{Q}_{e,nu}$ [W]	$\Delta\dot{Q}_{e,rel}$ [%]	$\dot{Q}_{c,ex}$ [W]	$\dot{Q}_{c,nu}$ [W]	$\Delta\dot{Q}_{c,rel}$ [%]
1	4567	4668	2.21	6285	6217	1.08
2	4599	4508	1.98	6294	6050	3.88
3	4291	4158	3.10	5904	5675	3.88
4	4268	4056	4.97	5911	5567	5.82
5	4898	5058	3.27	6555	6600	0.69
6	4964	5006	0.85	6676	6547	1.93

Table 4.23: Overfeed refrigerating system: Experimental vs. Numerical results 1

	$\dot{m}_r\,[\frac{kg}{h}]$	$T_{e,i}$ [°C]	$T_{e,o}$ [°C]	$P_{e,i}\,[kPa]$	$T_{cd,i}$ [°C]	$T_{cd,o}$ [°C]	$P_{cd}\,[kPa]$	$T_{lpr,l}$ [°C]	$\dot{m}_{cp}\,[\frac{kg}{h}]$	$T_{cp,o}$ [°C]
ex1	151.92	8.30	7.61	395.6	71.84	55.30	1528.0	7.69	135.70	74.76
nu1	151.92	6.01	5.59	362.1	65.01	55.86	1523.3	4.89	143.64	68.59
$\Delta\phi_{rel}$ %	0.00			8.48			0.31		5.85	
ex2	447.36	8.02	8.25	417.9	71.87	55.59	1537.0	7.68	136.20	74.84
nu2	447.36	4.59	4.76	372.9	65.19	55.86	1523.0	4.16	139.57	68.85
$\Delta\phi_{rel}$ %	0.00			10.76			0.91		2.47	
ex3	545.88	6.42	6.59	402.2	72.07	55.33	1525.0	6.05	126.40	75.12
nu3	545.88	2.80	3.08	363.6	65.52	55.59	1513.1	2.41	129.96	69.40
$\Delta\phi_{rel}$ %	0.00			2.95			0.78		2.81	
ex4	650.40	6.50	7.12	409.2	72.12	55.36	1527.0	6.10	126.40	75.35
nu4	650.40	2.24	2.65	371.5	65.67	55.48	1509.1	1.92	127.44	69.63
$\Delta\phi_{rel}$ %	0.00			9.21			1.17		0.82	
ex5	151.86	7.68	6.96	387.4	66.32	48.88	1311.0	6.99	135.30	68.97
nu5	151.86	5.78	5.36	359.2	60.58	49.79	1310.0	4.65	145.44	64.08
$\Delta\phi_{rel}$ %	0.00			7.27			0.07		7.49	
ex6	245.04	7.82	7.65	400.7	66.36	49.12	1318.0	7.36	137.70	69.02
nu6	245.04	5.22	4.98	359.6	60.74	49.79	1311.1	4.44	142.92	64.17
$\Delta\phi_{rel}$ %	0.00			10.25			0.52		3.79	

4.8 Conclusions

In this chapter, validation studies for the different elements of the refrigerating systems, for the dry expansion refrigerating systems and for the overfeed systems have been presented. Good agreement between experimental data and numerical results have been shown in almost all studies, therefore the modelitzation of the elements and the refrigerating systems as a whole have been validated. With the aim of improve the quality of the experimental data an extensive analysis of the results has been done, and it has been allowed us to detect weak points in the experimental facilities of the CTTC, and improved them.

4.9 Nomenclature

T	Temperature $[K]$
E	Energy $[J]$
A	Heat transfer area $[K]$
U	Global heat transfer coefficient $[W/m^2K]$
$\dot{Q}$	Heating power $[W]$
D	Diameter $[m]$
L	Length $[m]$
M	Mass $[kg]$
h	Enthalpy $[J/kg]$ or height $[m]$
e	Thickness $[m]$
t	Time $[s]$
p	Pressure $[Pa]$
$\dot{m}$	Mass flow $[kg/s]$
x_g	Mass fraction
$ex1$	Experiment 1
$nu1$	Numerical simulation 1

Greek symbols

α	Convective heat transfer coefficient $[W/m^2K]$
Δ	Relative error [%]
ϕ	Different variables (mass flow, electrical consumption, heat transfer,etc.)
λ	Thermal conductivity $[W/mK]$
η	Efficiency

Subscripts

a	Annular
$aver$	Average

amb, *env*	Environment
c	Condenser, coil
cd	Condenser
cp	Compressor
disch	Discharge inlet condenser
e	Evaporator
ed	Expansion devive
em	Electro-mechanical
ev	Evaporator
exp,*ex*	Experimental
h	Heater
hpr	High pressure receiver
i	Inlet, in
ic	Inlet condenser
ie	Inlet evaporator
ini,*in*	Initial
ins	Insulation
liq, *l*	Liquid
lpr	Low pressure receiver
num,*nu*	Numerical
o	Outlet, out
pu	Pump
r	Refrigerant
s	Secondary
sim	Simulation
st	Steady
tr	Transient
vap, *v*	Vapour

References

[1] J. Rigola. "Numerical simulation and experimental validation of hermetic reciprocating compressors. integration in vapour compression refrigerating systems". PhD thesis. Universitat Politècnica de Catalunya, 2002.

[2] S. Danov. "Development of experimental and numerical infrastructures for the study of compact heat exchangers and liquid overfeed refrigeration systems". PhD thesis. Universitat Politècnica de Catalunya, 2005.

[3] R. J. Moffat. "Describing uncertainties in experimental results". In: *Exp. Thermal and Fluid Science* 1.1 (1988), pp. 3–17.

[4] S. Estrada-Flores et al. "Simulation of transient behaviour in refrigeration plant pressure vessels: mathematical models and experimental validation". In: *International Journal of Refrigeration* 26.2 (2003), pp. 170–179.

Chapter 5

Parametric studies

5.1 Introduction

This chapter is devoted to increase knowledge of the pressured receivers and the vapour compression refrigerating systems under different working conditions.
In the study of the pressured receivers, it has been investigate the influence of the some variables (inlet enthalpy, inlet mass flow, environmental temperature, insulation thickness, heat transfer coefficients and liquid level), which are important to understand their influence in the pressure of the receiver and to understand how receivers affect to the refrigerating systems.
Basic studies changing the heat and cold temperature sources of the refrigerating systems and maintaining the compressor outlet pressure or the liquid level in the receivers have been carried out to understand how the refrigerating systems work under different boundary conditions. For dry expansion systems it has also been studied the evolution of the working point with a constant refrigerant charge in the system.

5.2 Steady State Studies for the Receiver

Receivers are usually found in vapour compression refrigerating systems. They can be divided in low pressure receivers and high pressure receivers. High pressure receivers work as a lung of refrigerant in dry expansion refrigerating system. Low pressure receivers are the join element between two parts of circuit in the liquid overfeed refrigerating system or in the gravity fed refrigerating systems. Besides the exposed differences (Fig. 5.1), the high pressure receivers typically have a single inlet ($\dot{m}_{r,in}$ which can be a mass flow of vapour,liquid or a mixture of vapour and liquid) and a single outlet ($\dot{m}_{r,out}$ which is mass flow of liquid), whereas the low pressure receivers have several inlets ($\dot{m}_{r,in}$ and $\dot{m}_{e,in}$ which can be a mass flow of vapour,liquid or a mixture of vapour and liquid) and outlets ($\dot{m}_{r,out}$ which is mass flow of vapour and $\dot{m}_{e,out}$ which is mass flow of liquid, in a typical low pressure receiver in overfeed

systems). $\dot{m}_r$ is the mass flow which is conducted through the main circuit and $\dot{m}_e$ is the mass flow in the evaporator circuit in liquid overfeed systems.
The studies of the influence of some boundary conditions on this component are interesting to know their response, which are important to understant the evolution of the working point in systems which has this elements under typical variations of temperatures from cold and hot sources, enviromental temperature, etc.
This section present a set of parametric studies performed on a low pressure receiver by means of the detailed simulating model presented on chapter 2. The description of the test cases and some of the results obtained from the parametric studies (boundary conditions, geometry) are showed on the following subsections.

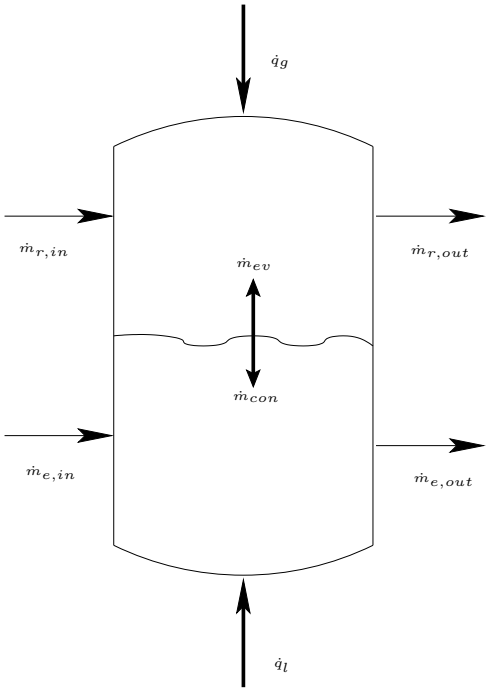

Figure 5.1: Characteristic entries and exits for receivers.

5.2.1 Low Pressure Receiver

A set of parametric studies for a low pressure receiver (thinking in a low pressure receiver for a liquid overfeed refrigerating system) is presented in this section. In this studies, the influence of mass flow (main circuit), enthalpy at the entry (main and overfeed circuit), liquid level, thickness of the insulation and the heat transfer coefficient have been studied. In the next section the standard test case is presented.

Test Case Description

A low pressure receiver (LPR) with two entries and two exits, internal diameter of 0.3 m, external diameter of 0.306 m, insulation thickness is of 0.02 m, and internal height of 1.0 m is used for the verification tests.
The verification tests have been carried out using $1 \cdot 10^{-4}$ as convergence criterion and using 25 °C as environmental temperature. Table 5.1 shows the implemented boundary conditions.

Table 5.1: Boundary conditions.

$\dot{m}_r\ [kg/s]$	$\dot{m}_e\ [kg/s]$	$h_{in,r}\ [kJ/kg]$	$h_{in,e}\ [kJ/kg]$	$z_l\ [m]$	$\alpha_l\ [W/m^2K]$	$\alpha_g\ [W/m^2K]$
$4.6 \cdot 10^{-3}$	$1.17 \cdot 10^{-2}$	369.76	578.87	0.5	500	10

Influence of Enthalpy at the Entry

A total of 16 simulations have been carried out changing the enthalpy at the entry of the main circuit and 13 simulations changing the enthalpy at the entry of the overfeed circuit to study their influence over the main parameters of the receiver. Tables 5.2 and 5.3 show the results obtained.

Table 5.2: Study of low pressure receiver with variable $h_{r,in}$.

Case	$h_{r,in}[kJ/kg]$	$p_g[bar]$	T_g [°C]	T_l [°C]	Model	$Q_{gains}[W]$	$\dot{m}_{evap}[kg/s]$
0	209.764	1.757293	−19.40	−21.75	LS-SH	75.23	$3.12 \cdot 10^{-5}$
1	229.764	1.882035	−17.96	−20.22	LS-SH	72.78	$3.03 \cdot 10^{-5}$
2	249.764	2.013728	−16.52	−18.69	LS-SH	70.33	$2.94 \cdot 10^{-5}$
3	289.764	2.299078	−13.63	−15.63	LS-SH	65.43	$2.75 \cdot 10^{-5}$
4	329.764	2.615901	−10.74	−12.56	LS-SH	60.52	$2.57 \cdot 10^{-5}$
5	349.764	2.786728	−9.30	−11.03	LS-SH	58.06	$2.47 \cdot 10^{-5}$
6	**369.764**	**2.966356**	**−7.85**	**−9.50**	**LS-SH**	**55.61**	$\mathbf{2.38 \cdot 10^{-5}}$
7	389.764	3.154969	−6.40	−7.97	LS-SH	53.15	$2.28 \cdot 10^{-5}$
8	409.764	3.352969	−4.95	−6.43	LS-SH	50.69	$2.18 \cdot 10^{-5}$
9	429.764	3.560685	−3.50	−4.90	LS-SH	48.23	$2.08 \cdot 10^{-5}$
10	469.764	4.006451	−0.60	−1.83	LS-SH	43.30	$1.89 \cdot 10^{-5}$
11	489.764	4.245169	0.85	−0.30	LS-SH	40.83	$1.79 \cdot 10^{-5}$
12	509.764	4.494959	2.30	1.22	LS-SH	38.37	$1.68 \cdot 10^{-5}$

Table 5.3: Study of low pressure receiver with variable $h_{e,in}$.

Case	$h_{e,in}[kJ/kg]$	$p_g[bar]$	T_g [°C]	T_l [°C]	Model	$Q_{gains}[W]$	$\dot{m}_{evap}[kg/s]$	$\dot{m}_{cond}[kg/s]$
0	508.874	1.650477	−20.70	−23.13	LS-SH	77.44	$3.21 \cdot 10^{-5}$	0.0
1	528.874	1.965678	−17.03	−19.24	LS-SH	71.21	$2.97 \cdot 10^{-5}$	0.0
2	548.874	2.327073	−13.36	−15.34	LS-SH	64.97	$2.74 \cdot 10^{-5}$	0.0
3	568.874	2.739433	−9.69	−11.45	LS-SH	58.73	$2.50 \cdot 10^{-5}$	0.0
4	**578.874**	**2.966356**	**−7.85**	**−9.50**	**LS-SH**	**55.61**	$\mathbf{2.38 \cdot 10^{-5}}$	**0.0**
5	588.874	3.207845	−6.01	−7.55	LS-SH	52.48	$2.25 \cdot 10^{-5}$	0.0
6	608.874	3.737369	−2.32	−3.65	LS-SH	46.22	$2.00 \cdot 10^{-5}$	0.0
7	648.874	5.001840	5.07	4.14	LS-SH	33.67	$1.49 \cdot 10^{-5}$	0.0
8	688.874	6.578612	12.51	11.96	LS-SH	21.07	$9.54 \cdot 10^{-6}$	0.0
9	728.874	8.516358	19.99	19.78	LS-SH	8.43	$3.92 \cdot 10^{-6}$	0.0
10	748.874	9.636411	23.75	23.69	LS-SH	2.10	$9.90 \cdot 10^{-7}$	0.0
11	768.874	10.867733	27.61	27.57	SC-VS	−4.30	0.0	$1.74 \cdot 10^{-6}$
12	788.874	12.216411	31.54	31.44	SC-VS	−10.76	0.0	$4.42 \cdot 10^{-6}$

The energy balance ($\Sigma \dot{m}_{i,in} h_{i,in} - \Sigma \dot{m}_{i,out} h_{i,out} + \dot{Q}_{gains} = 0$) determines the behaviour of all the parameters of the receiver and it is possible to group the studies which affect directly the term $\Sigma \dot{m}_{i,in} h_{i,in}$ (and indirectly also affect the heat gains term) and the studies which affect the term $\dot{Q}_{gains}$.
Figs. 5.2 and 5.3 show the evolution of the pressure when the enthalpy rise. The changes in the enthalpy at the entry of the overfeed circuit are more influential than the changes in the enthalpy at the entry of the main circuit. The reason is because the mass flow of the main circuit is lower than the mass flow of the overfeed circuit. If the energetic level of the LPR, where the temperature of the two phases inside the receiver are below the environmental temperature, increases ($\Sigma \dot{m}_{i,in} h_{i,in}$) it means that the receiver is closer to the environment conditions, therefore the pressure increases and $\dot{Q}_{gains}$ are reduced.

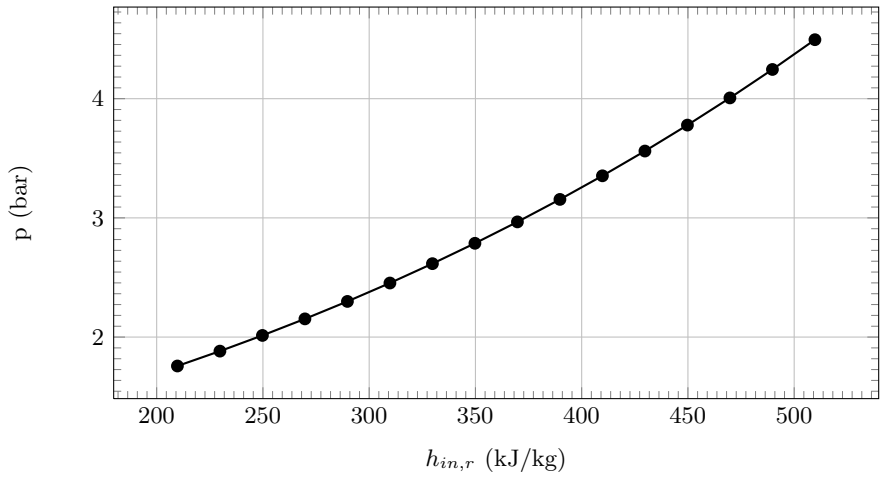

Figure 5.2: Evolution of pressure inside the low pressure receiver.

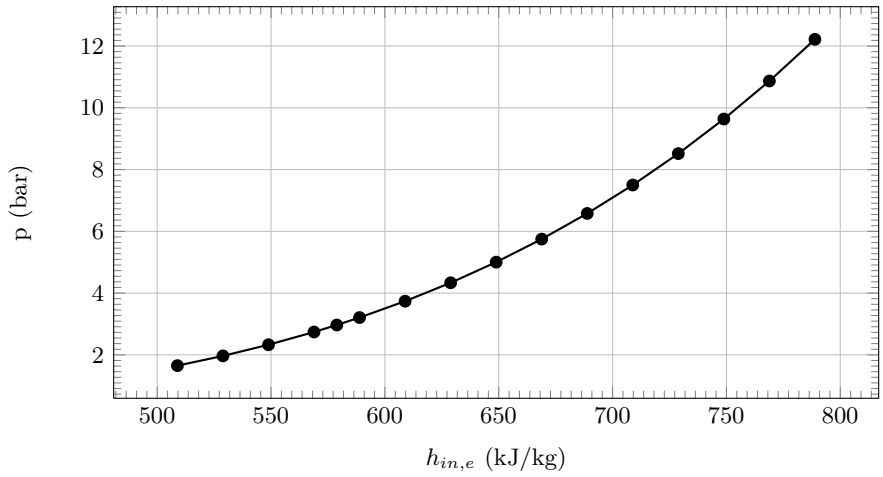

Figure 5.3: Evolution of pressure inside the low pressure receiver.

As it would be expected from the analysis of the energy balances in this study, Figs. 5.4 and 5.5 show the evolution of heat gains in the receiver which tend to zero, and in the extreme case they change to heat losses (the model inside the receiver change from liquid saturated and vapour superheated to subcooled liquid and saturated vapour) when the saturation temperature at the pressure receiver is higher than the environment temperature.

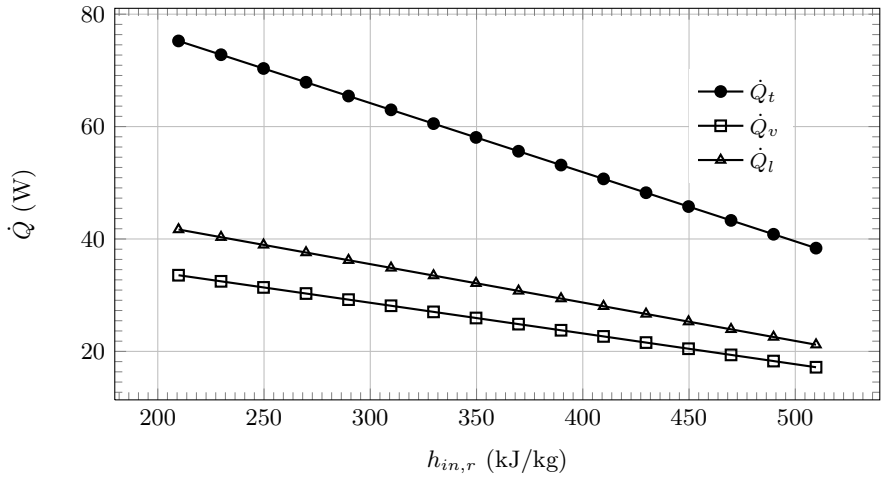

Figure 5.4: Evolution of heat gains inside the low pressure receiver.

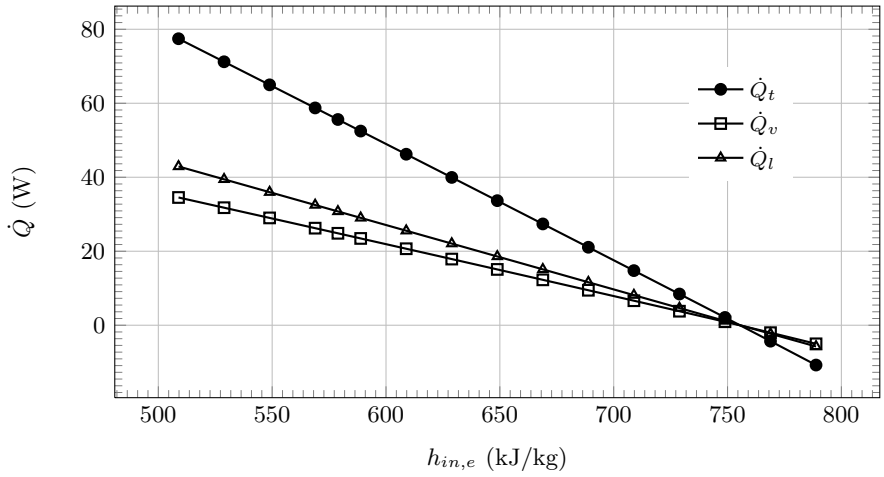

Figure 5.5: Evolution of heat gains inside the low pressure receiver.

Figs. 5.6 and 5.7 show the evolution of the temperatures of the two phases inside the receiver which tend to the saturation temperature at the pressure of the receiver. The last cases of the study where the enthalpy at the entry of the overfeed circuit is high, the liquid tends to be subcooled.

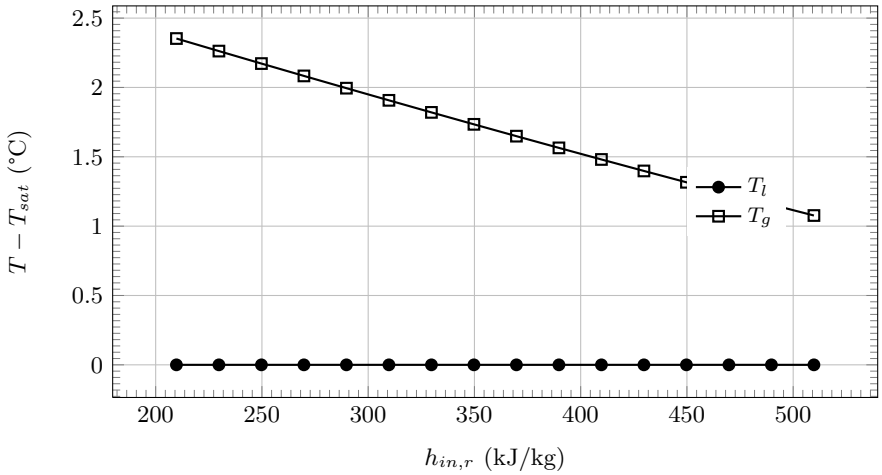

Figure 5.6: Evolution of temperatures inside the low pressure receiver.

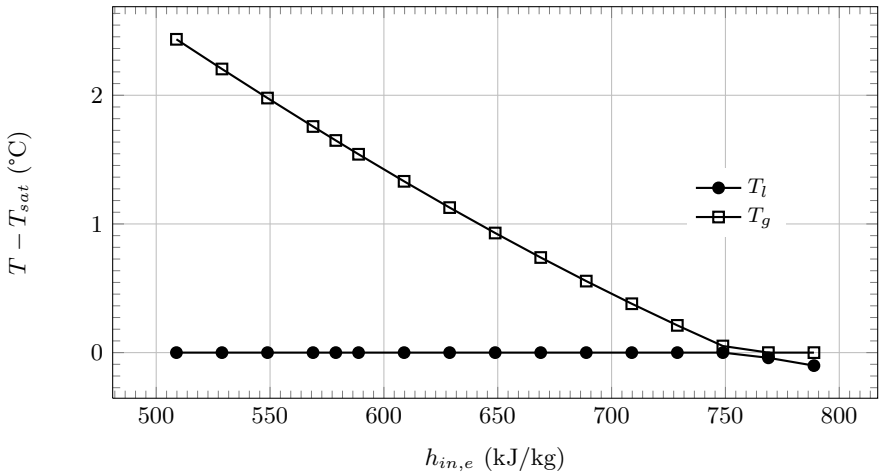

Figure 5.7: Evolution of temperatures inside the low pressure receiver.

In Figs. 5.8 and 5.9 we could observe the evolution of the evaporated mass flow, which is decreasing until zero and then when the model inside the receiver changes, a condensed mass flow appears.

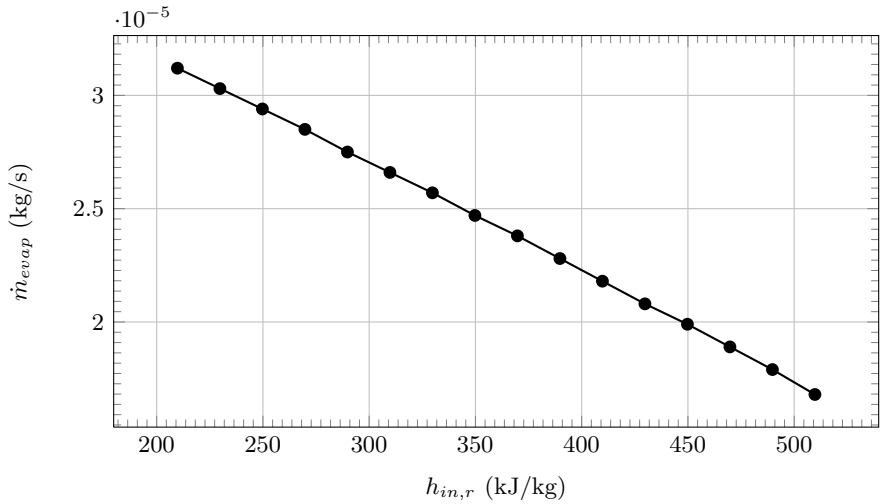

Figure 5.8: Evolution of evaporated mass flow inside the low pressure receiver.

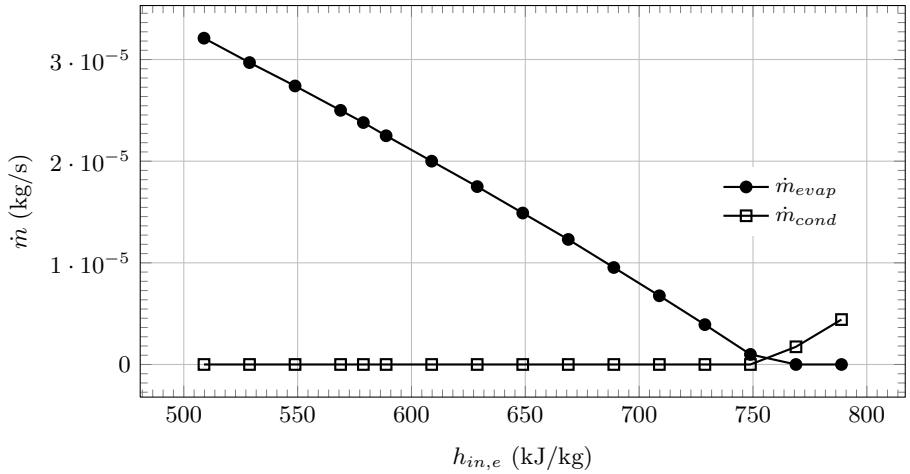

Figure 5.9: Evolution of evaporated mass flow inside the low pressure receiver.

Influence of Mass Flow

The study of the mass flow influence (main circuit) in the main parameters of the low pressure receiver,has been carried out with 16 simulations, whereas the mass flow change between $3.0 \cdot 10^{-3}\, kg/s$ to $5.8 \cdot 10^{-3}\, kg/s$. The results are showed on the Table 5.4 and in some figures which are going to be commented in next lines.

Table 5.4: Study of LPR with variable mass flow ($\dot{m}_r = \dot{m}_{r,in} = \dot{m}_{r,out}$).

Case	$\dot{m}_r[kg/s]$	$p_g[bar]$	T_g [°C]	T_l [°C]	Model	$Q_{gains}[W]$	$\dot{m}_{evap}[kg/s]$
0	$3.0 \cdot 10^{-3}$	8.616251	20.44	20.15	LS-SH	8.81	$3.65 \cdot 10^{-6}$
1	$3.2 \cdot 10^{-3}$	7.623168	16.87	16.37	LS-SH	15.70	$6.41 \cdot 10^{-6}$
2	$3.4 \cdot 10^{-3}$	6.723938	13.30	12.60	LS-SH	22.58	$9.09 \cdot 10^{-6}$
3	$3.6 \cdot 10^{-3}$	5.912591	9.74	8.86	LS-SH	29.44	$1.17 \cdot 10^{-5}$
4	$3.8 \cdot 10^{-3}$	5.183090	6.19	5.13	LS-SH	36.28	$1.42 \cdot 10^{-5}$
5	$4.0 \cdot 10^{-3}$	4.529518	2.65	1.43	LS-SH	43.08	$1.67 \cdot 10^{-5}$
6	$4.2 \cdot 10^{-3}$	3.945932	−0.86	−2.23	LS-SH	49.84	$1.91 \cdot 10^{-5}$
7	$4.4 \cdot 10^{-3}$	3.426754	−4.37	−5.88	LS-SH	56.56	$2.15 \cdot 10^{-5}$
8	$\mathbf{4.6 \cdot 10^{-3}}$	**2.966356**	**−7.85**	**−9.50**	**LS-SH**	**55.61**	$\mathbf{2.38 \cdot 10^{-5}}$
9	$4.8 \cdot 10^{-3}$	2.559490	−11.31	−13.09	LS-SH	69.86	$2.60 \cdot 10^{-5}$
10	$5.0 \cdot 10^{-3}$	2.201148	−14.74	−16.64	LS-SH	76.45	$2.82 \cdot 10^{-5}$
11	$5.2 \cdot 10^{-3}$	1.886739	−18.15	−20.16	LS-SH	82.97	$3.03 \cdot 10^{-5}$
12	$5.4 \cdot 10^{-3}$	1.611752	−21.53	−23.65	LS-SH	89.43	$3.24 \cdot 10^{-5}$
13	$5.6 \cdot 10^{-3}$	1.372110	−24.89	−27.11	LS-SH	95.84	$3.44 \cdot 10^{-5}$
14	$5.8 \cdot 10^{-3}$	1.163935	−28.21	−30.53	LS-SH	102.1	$3.64 \cdot 10^{-5}$
15	$6.0 \cdot 10^{-3}$	1.100000	−29.98	−31.67	LS-SH	102.1	$3.70 \cdot 10^{-5}$

With low mass flow, the net entry energy is low ($\Sigma\dot{m}_{i,in}h_{i,in} - \Sigma\dot{m}_{i,out}h_{i,out}$, $\Sigma\dot{m}_{i,in} = \Sigma\dot{m}_{i,out}$ and $\Sigma h_{i,in}$ lower than $\Sigma h_{i,out}$) which means that the saturation temperature inside the receiver must be closer to the environment to keep the energy balances. When the mass flow increase the pressure decreases (Fig. 5.10) and the energy to keep the refrigerant cooled increase. Therefore the heat gains (Fig. 5.11)and evaporated mass flow (Fig. 5.13) increase, even though the temperatures decrease (Fig. 5.12).

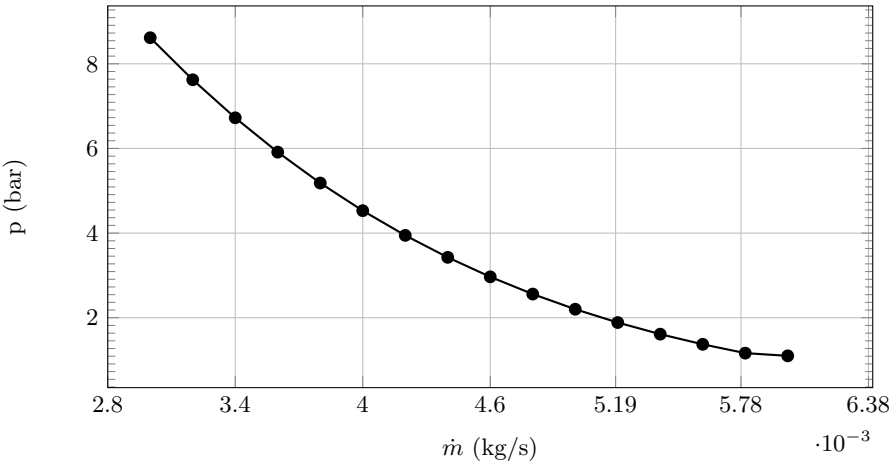

Figure 5.10: Evolution of pressure inside the low pressure receiver.

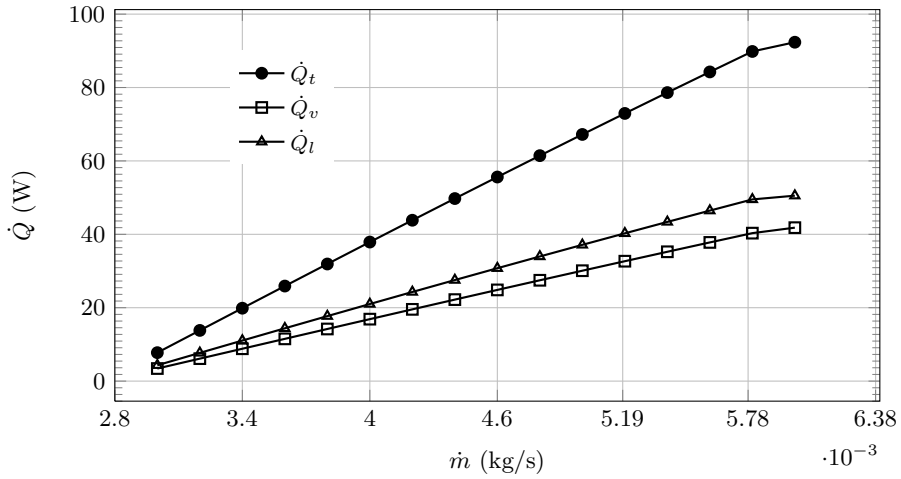

Figure 5.11: Evolution of heat gains inside the low pressure receiver.

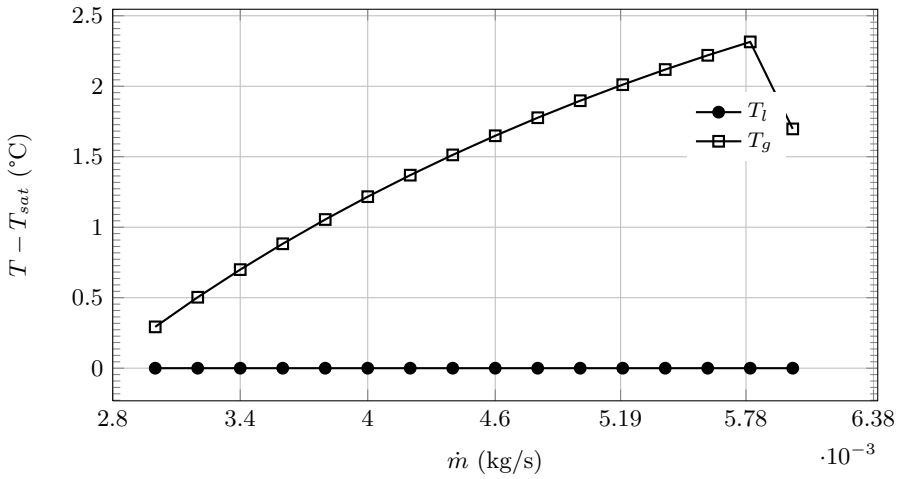

Figure 5.12: Evolution of temperatures inside the low pressure receiver.

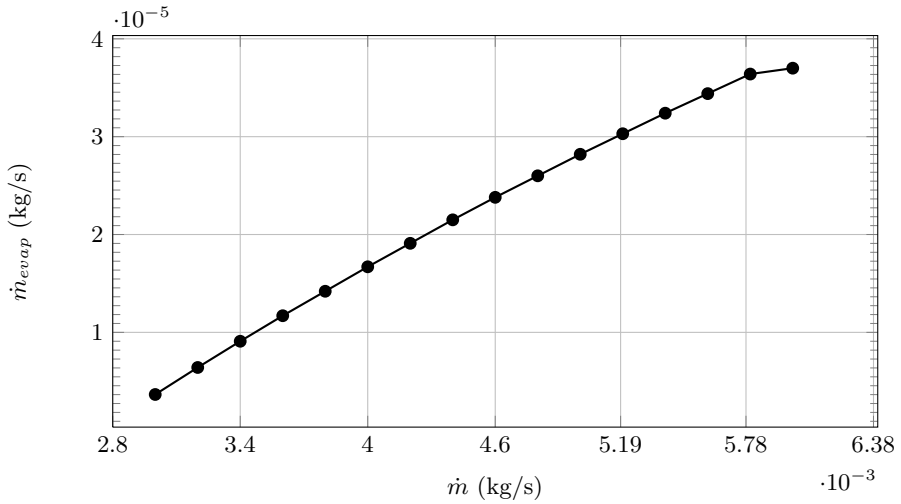

Figure 5.13: Evolution of evaporated mass flow inside the low pressure receiver.

Influence of Heat Transfer Coefficient

It has been carried out a group of simulations changing the heat transfer coefficient and maintaining the $\lambda_{ins} = 0.035\,[W/mK]$ to analyse their influence to all the receiver parameters. Table 5.5 shows the results obtained after the simulation of 15 test cases where the heat transfer coefficient for surface in contact with the environment changes between $1\,[W/m^2K]$ to $500\,[W/m^2K]$.

Table 5.5: Study of low pressure receiver with variable α_{ext}.

Case	$\alpha_{ext}[W/m^2K]$	$p_g[bar]$	T_g [°C]	T_l [°C]	Model	$Q_{gains}[W]$	$\dot{m}_{evap}[kg/s]$
0	1	2.931915	−8.97	−9.79	LS-SH	26.15	$1.06 \cdot 10^{-5}$
1	2	2.944149	−8.54	−9.68	LS-SH	37.03	$1.53 \cdot 10^{-5}$
2	3	2.951140	−8.32	−9.63	LS-SH	43.01	$1.80 \cdot 10^{-5}$
3	4	2.955643	−8.18	−9.59	LS-SH	46.79	$1.97 \cdot 10^{-5}$
4	5	2.958781	−8.08	−9.56	LS-SH	49.40	$2.09 \cdot 10^{-5}$
5	**10**	**2.966356**	**−7.85**	**−9.50**	**LS-SH**	**55.61**	$\mathbf{2.38 \cdot 10^{-5}}$
6	20	2.970984	−7.71	−9.46	LS-SH	59.34	$2.55 \cdot 10^{-5}$
7	30	2.972683	−7.66	−9.45	LS-SH	60.70	$2.62 \cdot 10^{-5}$
8	40	2.973565	−7.64	−9.44	LS-SH	61.41	$2.65 \cdot 10^{-5}$
9	50	2.974105	−7.62	−9.43	LS-SH	61.84	$2.67 \cdot 10^{-5}$
10	100	2.975211	−7.59	−9.43	LS-SH	62.72	$2.71 \cdot 10^{-5}$
11	200	2.975777	−7.58	−9.42	LS-SH	63.17	$2.73 \cdot 10^{-5}$
12	300	2.975968	−7.57	−9.42	LS-SH	63.32	$2.74 \cdot 10^{-5}$
13	400	2.976064	−7.57	−9.42	LS-SH	63.40	$2.74 \cdot 10^{-5}$
14	500	2.976121	−7.57	−9.42	LS-SH	63.44	$2.75 \cdot 10^{-5}$

Table 5.6 shows the results obtained after the simulation of 15 test cases where the superficial heat transfer coefficient for surface in contact with the vapour part of the refrigerant inside the receiver changes between $1\,[W/m^2K]$ to $500\,[W/m^2K]$.

Table 5.6: Study of low pressure receiver with variable α_g.

Case	$\alpha_g[W/m^2K]$	$p_g[bar]$	T_g [°C]	T_l [°C]	Model	$Q_{gains}[W]$	$\dot{m}_{evap}[kg/s]$
0	1	2.966356	−8.75	−9.50	LS-SH	42.07	$2.38 \cdot 10^{-5}$
1	2	2.966356	−8.43	−9.50	LS-SH	46.98	$2.38 \cdot 10^{-5}$
2	3	2.966356	−8.24	−9.50	LS-SH	49.72	$2.38 \cdot 10^{-5}$
3	4	2.966356	−8.13	−9.50	LS-SH	51.48	$2.38 \cdot 10^{-5}$
4	5	2.966356	−8.05	−9.50	LS-SH	52.69	$2.38 \cdot 10^{-5}$
5	**10**	**2.966356**	**−7.85**	**−9.50**	**LS-SH**	**55.61**	$\mathbf{2.38 \cdot 10^{-5}}$
6	20	2.966356	−7.73	−9.50	LS-SH	57.38	$2.38 \cdot 10^{-5}$
7	30	2.966356	−7.69	−9.50	LS-SH	58.02	$2.38 \cdot 10^{-5}$
8	40	2.966356	−7.67	−9.50	LS-SH	58.36	$2.38 \cdot 10^{-5}$
9	50	2.966356	−7.65	−9.50	LS-SH	58.57	$2.38 \cdot 10^{-5}$
10	100	2.966356	−7.62	−9.50	LS-SH	58.99	$2.38 \cdot 10^{-5}$
11	200	2.966356	−7.61	−9.50	LS-SH	59.20	$2.38 \cdot 10^{-5}$
12	300	2.966356	−7.60	−9.50	LS-SH	59.27	$2.38 \cdot 10^{-5}$
13	400	2.966356	−7.60	−9.50	LS-SH	59.31	$2.38 \cdot 10^{-5}$
14	500	2.966356	−7.60	−9.50	LS-SH	59.33	$2.38 \cdot 10^{-5}$

Table 5.7 shows the results obtained after the simulation of 16 test cases where the superficial heat transfer coefficient for surface in contact with the liquid part of the refrigerant inside the receiver changes between $50\,[W/m^2K]$ to $5000\,[W/m^2K]$.

Table 5.7: Study of low pressure receiver with variable α_l.

Case	$\alpha_l[W/m^2K]$	$p_g[bar]$	T_g [°C]	T_l [°C]	Model	$Q_{gains}[W]$	$\dot{m}_{evap}[kg/s]$
0	50	2.964581	−7.86	−9.51	LS-SH	54.75	$2.31 \cdot 10^{-5}$
1	100	2.965554	−7.86	−9.51	LS-SH	55.22	$2.34 \cdot 10^{-5}$
2	200	2.966053	−7.85	−9.50	LS-SH	55.46	$2.36 \cdot 10^{-5}$
3	300	2.966221	−7.85	−9.50	LS-SH	55.54	$2.37 \cdot 10^{-5}$
4	400	2.966305	−7.85	−9.50	LS-SH	55.58	$2.37 \cdot 10^{-5}$
5	**500**	**2.966356**	**−7.85**	**−9.50**	**LS-SH**	**55.61**	$\mathbf{2.38 \cdot 10^{-5}}$
6	700	2.966414	−7.85	−9.50	LS-SH	55.64	$2.38 \cdot 10^{-5}$
7	900	2.966446	−7.85	−9.50	LS-SH	55.65	$2.38 \cdot 10^{-5}$
8	1000	2.966457	−7.85	−9.50	LS-SH	55.66	$2.38 \cdot 10^{-5}$
9	1500	2.966491	−7.85	−9.50	LS-SH	55.67	$2.38 \cdot 10^{-5}$
10	2000	2.966508	−7.85	−9.50	LS-SH	55.68	$2.38 \cdot 10^{-5}$
11	2500	2.966518	−7.85	−9.50	LS-SH	55.69	$2.38 \cdot 10^{-5}$
12	3500	2.966530	−7.85	−9.50	LS-SH	55.69	$2.38 \cdot 10^{-5}$
13	4500	2.966537	−7.85	−9.50	LS-SH	55.70	$2.38 \cdot 10^{-5}$
14	5000	2.966539	−7.85	−9.50	LS-SH	55.70	$2.38 \cdot 10^{-5}$

As it has been seen before, the studies where the heat transfer coefficients, liquid level of the refrigerant, and the thickness of the insulation affect the term $\dot{Q}_{gains}$ from the energy balance ($\Sigma \dot{m}_{i,in} h_{i,in} - \Sigma \dot{m}_{i,out} h_{i,out} + \dot{Q}_{gains} = 0$). If this term decreases and the term $\Sigma \dot{m}_{i,in} h_{i,in}$ is constant, it means that $\Sigma \dot{m}_{i,out} h_{i,out}$ decrease, therefore

the pressure must decrease. Comparing Figs. 5.14-5.16, we could observe that the most influent heat transfer coefficient is the external heat transfer coefficient (α_{ext}). It is because this coefficient affect all the external surface of the receiver, therefore it is important to get a low external heat transfer coefficient to avoid the heat gains.

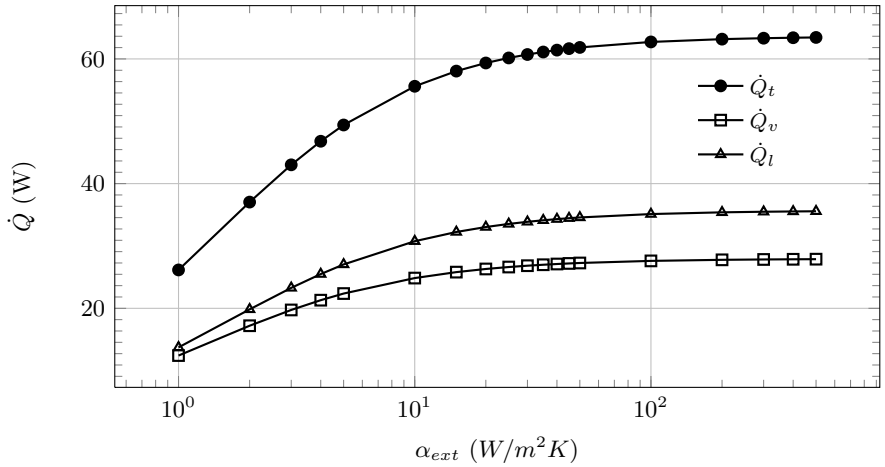

Figure 5.14: Evolution of heat gains inside the low pressure receiver.

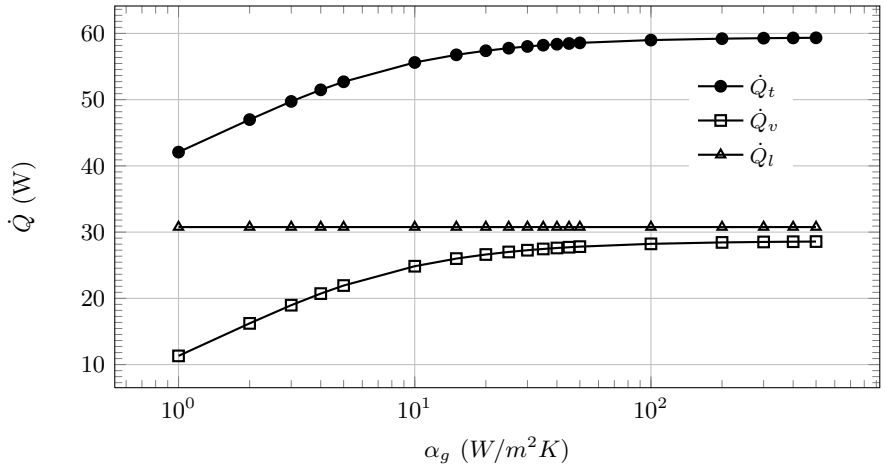

Figure 5.15: Evolution of heat gains inside the low pressure receiver.

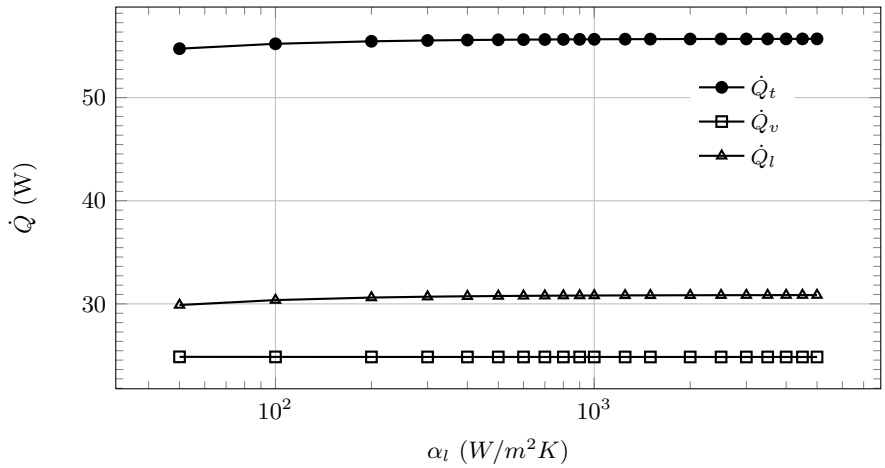

Figure 5.16: Evolution of heat gains inside the low pressure receiver.

Table 5.8 shows the results obtained from the study of the influence of the liquid level in the main parameters of the receiver. The study was done, carrying out a group of 9 simulations, where the liquid level changed between 0.1 m to 0.9 m.

Table 5.8: Study of low pressure receiver with variable liquid level.

Case	$Z_l[m]$	$p_g[bar]$	T_g [°C]	T_l [°C]	Model	$Q_{gains}[W]$	$\dot{m}_{evap}[kg/s]$
0	0.1	2.923863	−7.14	−9.85	LS-SH	50.36	$7.50 \cdot 10^{-6}$
1	0.2	2.934497	−7.31	−9.76	LS-SH	51.80	$1.16 \cdot 10^{-5}$
2	0.3	2.945077	−7.49	−9.68	LS-SH	53.16	$1.57 \cdot 10^{-5}$
3	0.4	2.955742	−7.67	−9.59	LS-SH	54.43	$1.97 \cdot 10^{-5}$
4	**0.5**	**2.966356**	**−7.85**	**−9.50**	**LS-SH**	**55.61**	$\mathbf{2.38 \cdot 10^{-5}}$
5	0.6	2.976915	−8.04	−9.41	LS-SH	56.69	$2.78 \cdot 10^{-5}$
6	0.7	2.987421	−8.23	−9.32	LS-SH	57.69	$3.18 \cdot 10^{-5}$
7	0.8	2.997910	−8.42	−9.24	LS-SH	58.58	$3.57 \cdot 10^{-5}$
8	0.9	3.008447	−8.62	−9.15	LS-SH	59.38	$3.97 \cdot 10^{-5}$

As it would be expected, the liquid area increases when the liquid level increases. Therefore the available volume for vapour decrease. The reduction of this volume and the increase of mass in the vapour area ($\dot{m}_{evap}$ raises) make that pressure inside the receiver increases (Fig. 5.17).

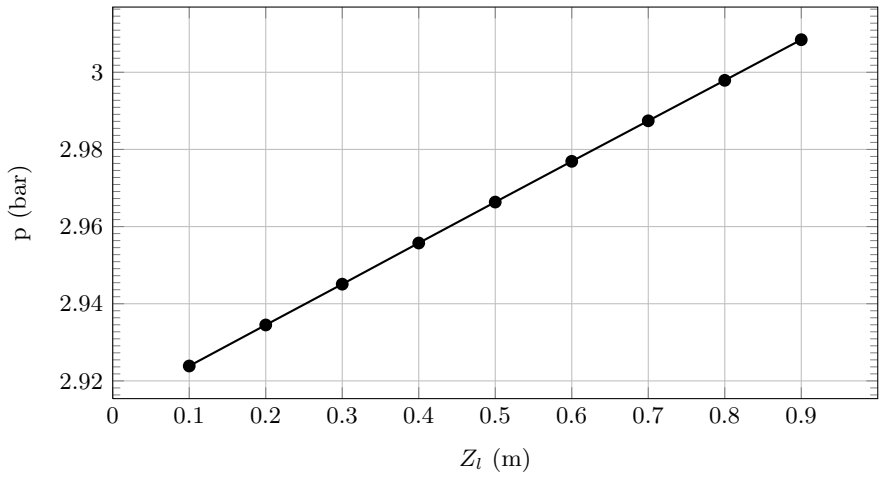

Figure 5.17: Evolution of pressure inside the low pressure receiver.

The increase of liquid level makes the heat gains in vapour area to decrease and to increase in liquid area (Fig. 5.18), the temperatures are becoming closer (Fig. 5.19). The increase of heat gains in liquid area imply that the energy available to evaporate refrigerant is higher, therefore the evaporated mass flow increases (Fig. 5.20).

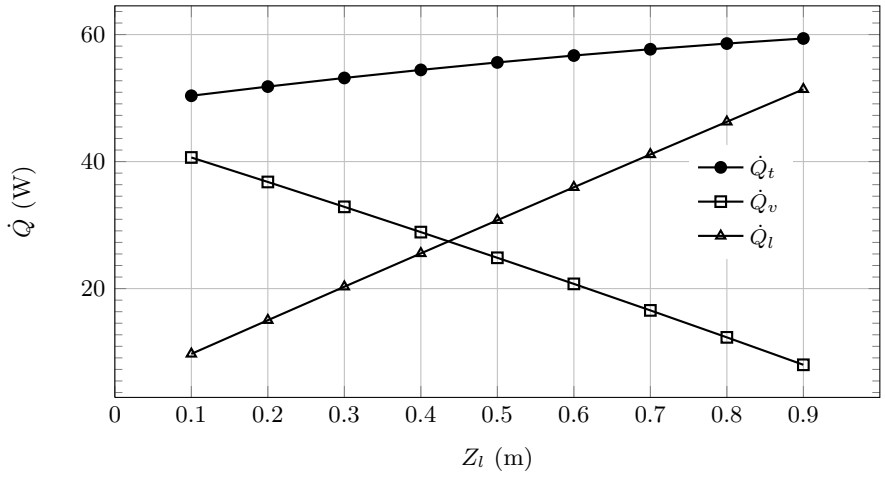

Figure 5.18: Evolution of heat gains inside the low pressure receiver.

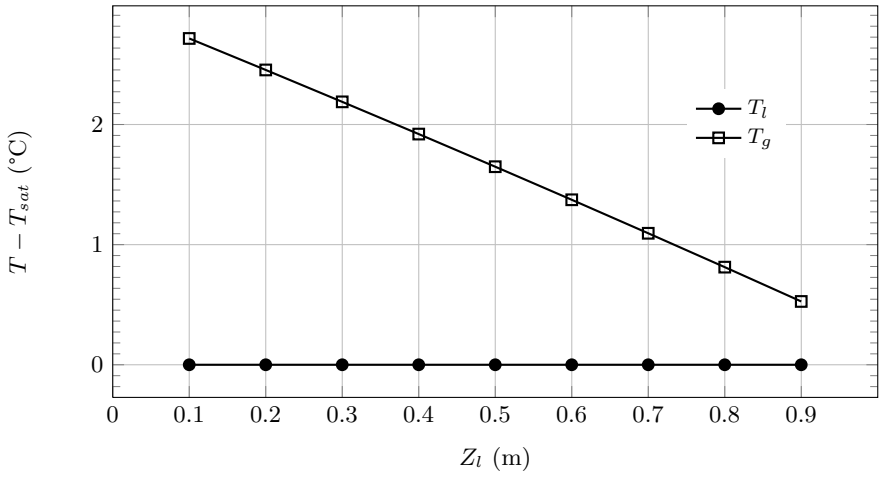

Figure 5.19: Evolution of temperatures inside the low pressure receiver.

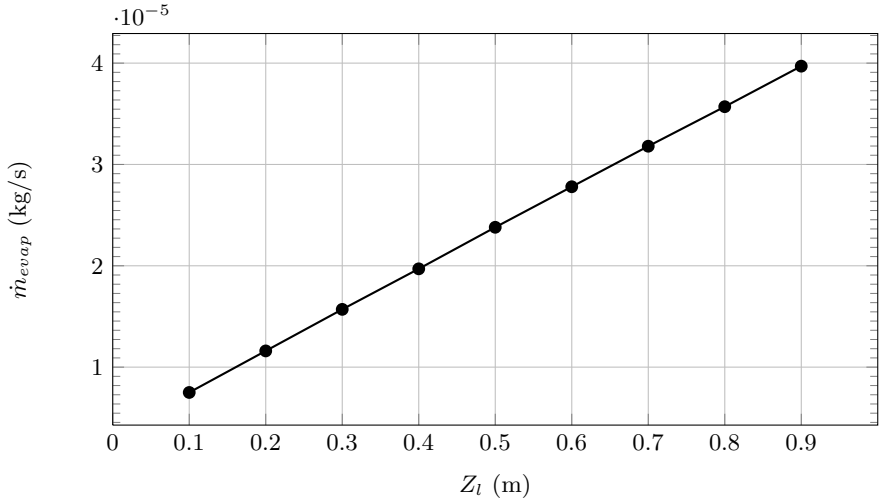

Figure 5.20: Evolution of evaporated mass flow inside the low pressure receiver.

Influence of Insulation Thickness

To finish the parametric studies of the low pressure receiver, the influence of the insulation thickness has been studied, carrying out 14 test cases where the thickness

changes between 10 mm to 200 mm. Table 5.9 shows a resume of the main receiver parameters.

Table 5.9: Study of low pressure receiver with variable insulation thickness.

Case	$\delta_{ins}[mm]$	$p_g[bar]$	T_g [°C]	T_l [°C]	Model	$Q_{gains}[w]$	$\dot{m}_{evap}[kg/s]$
0	10	3.007808	−6.73	−9.16	LS-SH	87.58	$3.95 \cdot 10^{-5}$
1	**20**	**2.966356**	**−7.85**	**−9.50**	**LS-SH**	**55.61**	$\mathbf{2.38 \cdot 10^{-5}}$
2	40	2.940175	−8.68	−9.72	LS-SH	33.54	$1.38 \cdot 10^{-5}$
3	60	2.930440	−9.02	−9.80	LS-SH	24.81	$1.00 \cdot 10^{-6}$
4	80	2.925320	−9.20	−9.84	LS-SH	20.11	$8.06 \cdot 10^{-6}$
5	100	2.922153	−9.32	−9.87	LS-SH	17.16	$6.84 \cdot 10^{-6}$
6	120	2.919996	−9.40	−9.89	LS-SH	15.13	$6.01 \cdot 10^{-6}$
7	140	2.918428	−9.46	−9.90	LS-SH	13.65	$5.41 \cdot 10^{-6}$
8	160	2.917235	−9.51	−9.91	LS-SH	12.52	$4.95 \cdot 10^{-6}$
9	180	2.916296	−9.54	−9.92	LS-SH	11.62	$4.59 \cdot 10^{-6}$
10	200	2.915535	−9.57	−9.92	LS-SH	10.90	$4.29 \cdot 10^{-6}$

Like in previous observations the heat gains determine a level of pressure, the temperatures for each area (liquid area and vapour area) and the evaporated mass flow. As it would be expected, when the thickness of the insulation increases the differences in heat gains tend to zero, and all the parameters tend to stabilise their values. See Figs. 5.21-5.23.

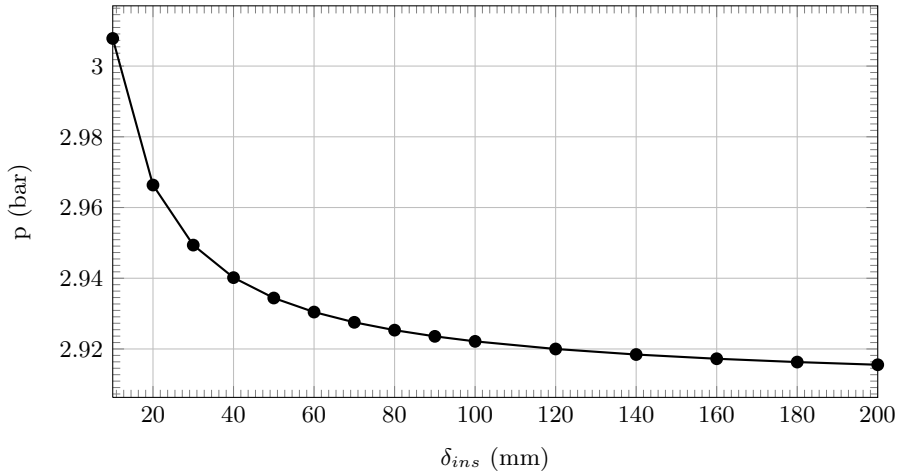

Figure 5.21: Evolution of pressure inside the low pressure receiver.

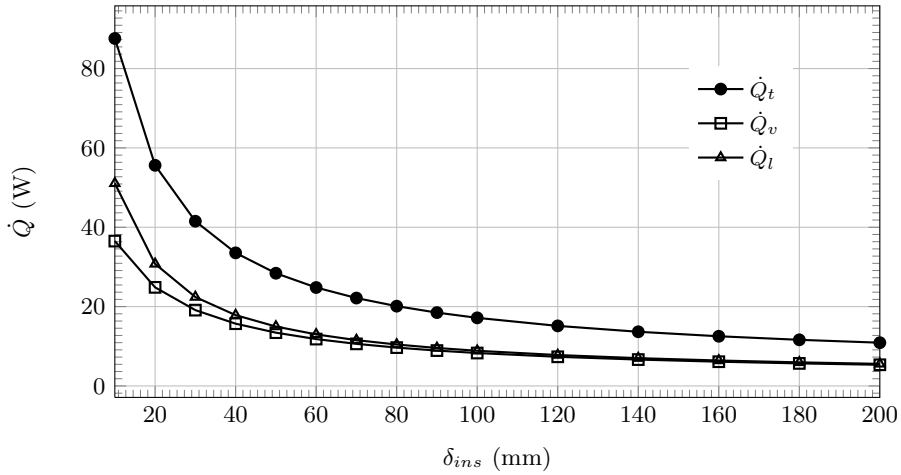

Figure 5.22: Evolution of heat gains inside the low pressure receiver.

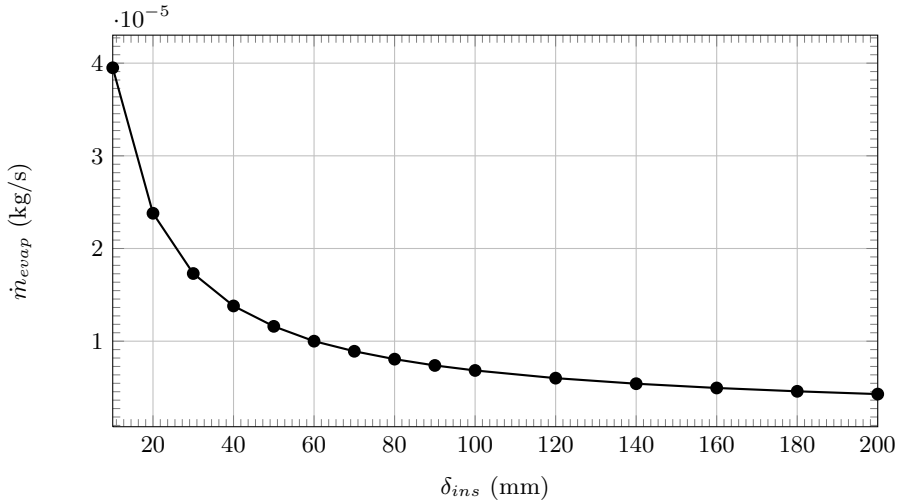

Figure 5.23: Evolution of evaporated mass flow inside the low pressure receiver.

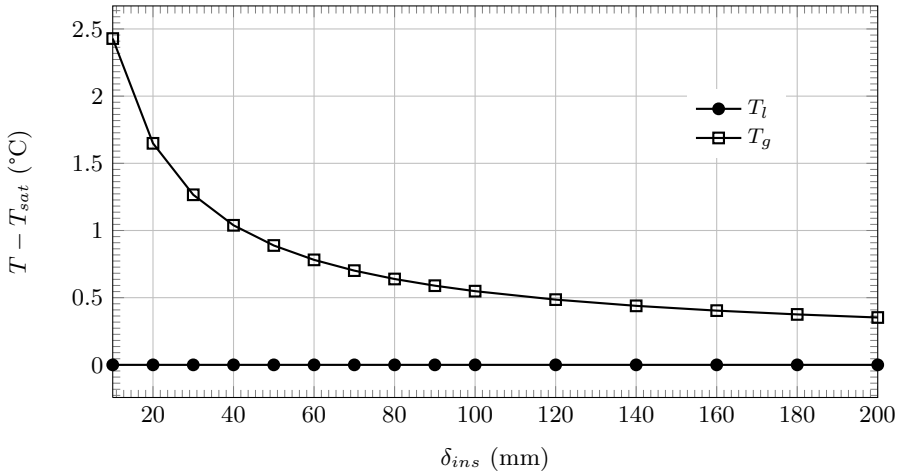

Figure 5.24: Evolution of temperatures inside the low pressure receiver.

5.3 Dry expansion refrigerating system.

This section presents the parametric studies of the dry expansion refrigerating system. The geometry used have been presented in Table 4.12 on section 4.6.
The parametric studies have been divided into two main studies, both analysing the influence of the secondary inlet temperature of the double pipe heat exchangers (condenser and evaporator). The first study maintain constant the outlet compressor pressure and variable the mass in the system. The second study maintain the mass in the system constant by iterating through outlet compressor pressure.

5.3.1 Study with variable system mass

These studies have been done using R134a and R600a, but the evolution observed with these two refrigerants are similar. Therefore in order to avoid repetitions the results presented are obtained with R600a as refrigerant.

Study of influence $T_{s,ci}$

The parametric study of the secondary inlet temperature of the condenser has been done changing the temperature from 22°C to 42°C. The main boundary values are: i) $p_{disc} = 7.72$ [bar], ii) $T_{env} = 22$ °C, iii) $\dot{m}_{s,e} = 118.8$ [kg/h], iv) $\dot{m}_{s,c} = 169.2$

[kg/h] and v) $T_{s,ei} = 32$°C.
Table 5.10 presents all the parameters of the simulated system carried out in the $T_{s,ci}$ parametric study. Subscript a correspond to cases with adiabatic compressor, while subscript b correspond to cases with real compressor (taking into account heat losses in the compressor).
It's interesting to highlight that for both assumptions (real and adiabatic compressor) the cooling capacity as well as the electrical power consumption of the compressor are the same, because the condenser used is oversized and the higher discharge enthalpy of the adiabatic compressor does not affect the subcooling degree at the expansion device inlet. The difference between both assumptions can be seen on the condenser capacity. For the adiabatic compressor the condenser have to be able to evacuate more heat than for the real compressor assumption. The COP decreases as should be expected, due to the inlet evaporator enthalpy falls down when the $T_{s,ci}$ decreases.

Table 5.10: Influence of $T_{s,ci}$ over the parameters of the system.

Case	$T_{s,ci}$ [°C]	Π	COP	$\dot{Q}_e$ [W]	$\dot{Q}_c$ [W]	$\dot{W}_e$ [W]	$\dot{m}$ [kg/s]	T_{disc} [°C]
1_a	22.0	11.79	1.478	174.73	263.00	118.16	$5.296 \cdot 10^{-4}$	129.40
1_b	22.0	11.79	1.478	174.75	218.52	118.16	$5.296 \cdot 10^{-4}$	82.73
2_a	27.0	11.89	1.423	167.27	254.22	117.52	$5.245 \cdot 10^{-4}$	129.73
2_b	27.0	11.89	1.423	167.27	209.77	117.52	$5.245 \cdot 10^{-4}$	82.57
3_a	32.0	11.99	1.368	159.89	245.46	116.87	$5.194 \cdot 10^{-4}$	130.07
3_b	32.0	11.99	1.368	159.89	201.05	116.87	$5.194 \cdot 10^{-4}$	82.40
4_a	37.0	12.10	1.312	152.53	236.69	116.21	$5.141 \cdot 10^{-4}$	130.42
4_b	37.0	12.10	1.312	152.54	192.29	116.21	$5.142 \cdot 10^{-4}$	82.18
5_a	42.0	12.22	1.256	145.15	227.88	115.53	$5.088 \cdot 10^{-4}$	130.79
5_b	42.0	12.22	1.256	145.20	183.51	115.53	$5.088 \cdot 10^{-4}$	81.95

Depending on the compressor considerations (adiabatic or real) the compressor outlet temperature has an important difference (around 50 °C). Fig. 5.25 shows the evolution of the cycle in a p-h diagram. As should be expected the enthalpy drop decreases in the condenser, therefore the cooling capacity falls down.

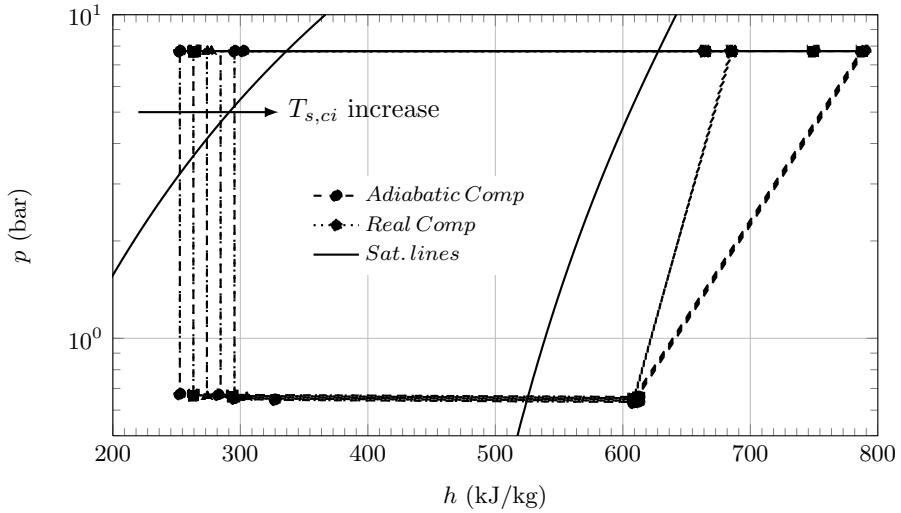

Figure 5.25: Diagram: p-h of parametric cases.

In Fig. 5.26 the evolution of the mass in the system can be observed. The mass decreases in order to maintain the fixed working discharge pressure. The total mass in the system have a difference near 4 g depending on the compressor hypothesis.

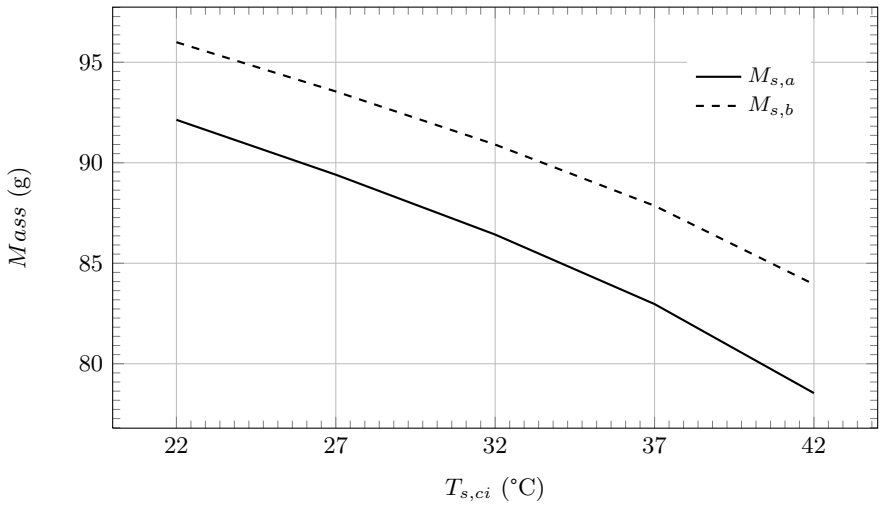

Figure 5.26: Evolution of the system mass.

As the condenser secondary inlet temperature increases, the mass in the system and the condenser capacity fall down. The cooling capacity decreases as well as the

compressor work (Fig.5.27). It is also important to highlight that the hypothesis of adiabatic compressor implies that the available compression work is higher.

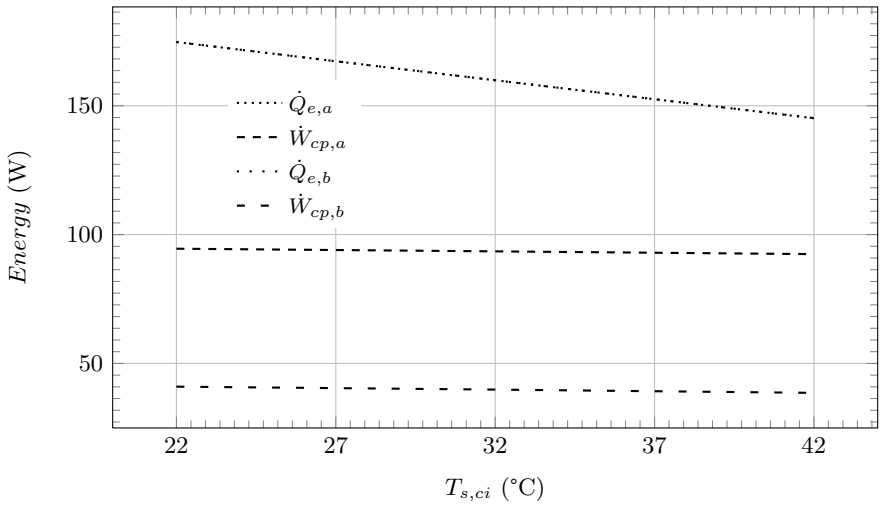

Figure 5.27: Evolution of cooling power and compression work.

From the point of view of the compressor hypothesis, the study shows that the differences between consider an adiabatic compressor or not, mainly affect to the outlet compressor and inlet condenser temperatures and the total mass in the system, while the cooling capacity remains almost unaffected. From the analysis of the secondary inlet temperature, the study shows that the increase of this temperature implies a loos of cooling capacity in these working conditions and a decrease in mass.

Study of influence $T_{s,ei}$

The parametric study of the evaporator secondary inlet temperature has been done changing the temperature from 22°C to 42°C. The main boundary values are: i) $p_{disc} = 7.72$ [bar], ii) $T_{env} = 22$ °C, iii) $\dot{m}_{s,e} = 118.8$ [kg/h], iv) $\dot{m}_{s,c} = 169.2$ [kg/h] and v) $T_{s,ci} = 32$°C.

Table 5.11 shows the main parameters of the system and the mass flow. The behaviour observed on the $T_{s,ci}$ study presented above, has been detected once again in this study. The cooling capacity, the COP, and the electrical consumption are the same for both systems (real compressor and adiabatic compressor). The condenser capacity, the compressor outlet temperature and the condenser inlet temperature have the main differences between the two assumptions.

Table 5.11: Influence of $T_{s,ei}$ over the energetic parameters of the system.

Case	$T_{s,ei}$ [°C]	Π	COP	$\dot{Q}_e$ [W]	$\dot{Q}_c$ [W]	$\dot{W}_e$ [W]	$\dot{m}$ [kg/s]	T_{disc} [°C]
1_a	22.0	12.28	1.306	150.91	239.20	115.50	$5.199 \cdot 10^{-4}$	123.29
1_b	22.0	12.28	1.306	150.92	194.48	115.50	$5.199 \cdot 10^{-4}$	74.85
2_a	27.0	12.14	1.336	155.27	242.28	116.18	$5.197 \cdot 10^{-4}$	126.63
2_b	27.0	12.14	1.336	155.28	197.71	116.18	$5.197 \cdot 10^{-4}$	78.56
3_a	32.0	11.99	1.368	159.89	245.46	116.87	$5.194 \cdot 10^{-4}$	130.07
3_b	32.0	11.99	1.368	159.89	201.05	116.87	$5.194 \cdot 10^{-4}$	82.40
4_a	37.0	11.87	1.397	164.15	248.40	117.50	$5.191 \cdot 10^{-4}$	133.22
4_b	37.0	11.87	1.397	164.16	204.07	117.50	$5.191 \cdot 10^{-4}$	85.86
5_a	42.0	11.75	1.427	168.67	251.50	118.16	$5.189 \cdot 10^{-4}$	136.53
5_b	42.0	11.75	1.427	168.68	207.27	118.16	$5.189 \cdot 10^{-4}$	89.51

From the results shown above, it can be seen that the evolution of the cycle is similar to the evolution of inlet condenser temperature study, therefore the comments and the conclusions from the point of view of adiabatic or real compressor are also valid for this study.
From the point of view of the secondary inlet temperature, it can be observed how the COP and cooling capacity increase when the secondary inlet temperature in the evaporator grows up, while the electrical consumption remains al,ost constant. Fig. 5.28 shows the evolution of the cycle in a p-h diagram.

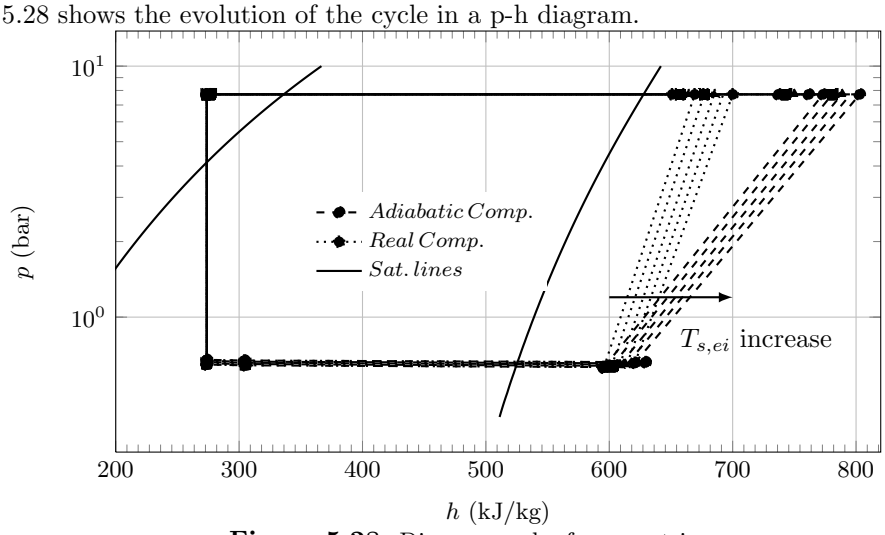

Figure 5.28: Diagram: p-h of parametric cases.

The mass in the system decreases (1.985 g) but the variation is lower than in the secondary inlet condenser temperature study (12.046 g) (see Fig. 5.29), therefore the mass in the system is much more sensible with the secondary inlet condenser temperature than the secondary inlet evaporator temperature when the discharge

pressure is fixed at a specific working point.

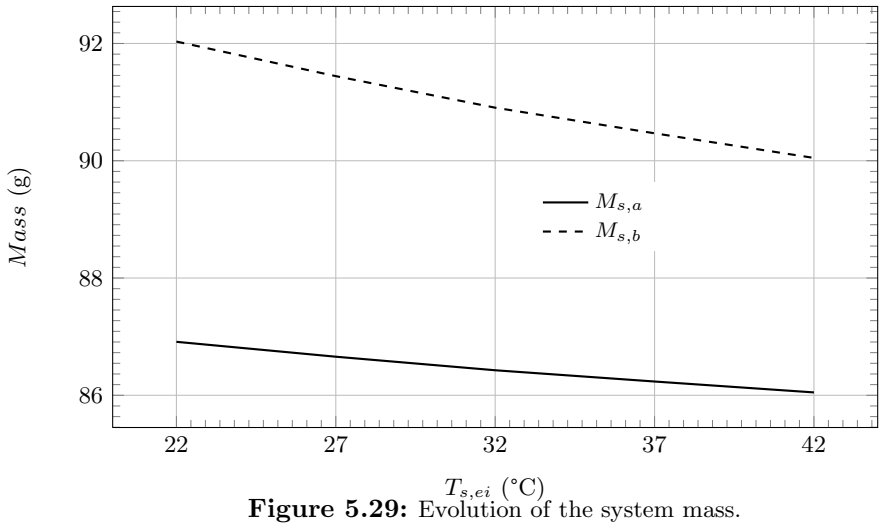

Figure 5.29: Evolution of the system mass.

Fig. 5.30 shows the evolution of cooling capacity and the compression work.

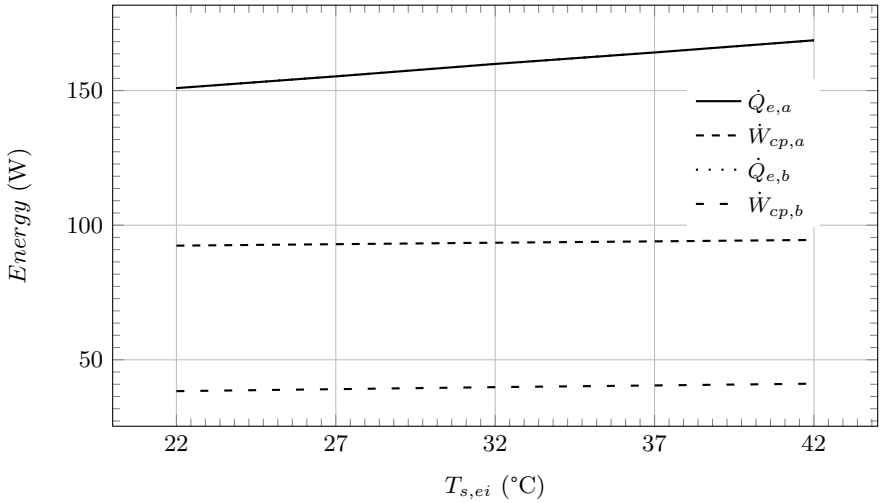

Figure 5.30: Evolution of cooling power and compressor work.

From the analysis of the evaporator secondary inlet temperature, the study shows that the increase of this temperature implies a higher cooling capacity in this working conditions and an increase of outlet compressor temperature.

5.3.2 Study with constant system mass

The studies carried out with constant mass in the system, which are the equivalent to those presented with the variant mass, are focused on evaluate the influence of the heat and cool sources of the refrigerating system. This study have also been done using R134a and R600a, and the evolution observed with these two refrigerants are similar. Therefore in order to avoid repetitions the results presented are obtained with R600a as refrigerant.

Study of influence $T_{s,ci}$

The parametric study of the secondary inlet temperature of the condenser has been done changing the temperature from 22°C to 42°C. The main boundary values are: i) $m_{system} = 90.905$ g, ii) $T_{env} = 22$ °C, iii) $\dot{m}_{s,e} = 118.8$ [kg/h], iv) $\dot{m}_{s,c} = 169.2$ [kg/h] and v) $T_{s,ei} = 32$°C.
Table 5.12 presents the main values of the system considering two different assumptions: subscript a adiabatic compressor and subscript b real compressor. Simulations 4 and 5 using hypothesis of adiabatic compressor works with a discharge pressure higher than the maximum pressure of the available compressor data. In this study it is interesting to highlight that the assumption of adiabatic compressor has a lower COP than the real compressor assumption. It happens because even if the cooling capacity decreases, the electrical consumption for the adiabatic compressor consideration decreases more than for the real compressor consideration

Table 5.12: Influence of $T_{s,ci}$ over the parameters of the system.

Case	$T_{s,ci}$ [°C]	Π	COP	$\dot{Q}_e$ [W]	$\dot{Q}_c$ [W]	$\dot{W}_e$ [W]	$\dot{m}$ [kg/s]	T_{disc} [°C]
1_a	22.0	11.42	1.863	165.93	249.68	89.02	$5.062 \cdot 10^{-4}$	127.63
1_b	22.0	10.48	1.962	145.93	187.91	74.37	$4.530 \cdot 10^{-4}$	82.14
2_a	27.0	12.57	1.751	178.65	272.40	102.00	$5.561 \cdot 10^{-4}$	132.46
2_b	27.0	11.29	1.904	153.66	195.63	80.70	$4.871 \cdot 10^{-4}$	82.47
3_a	32.0	13.95	1.635	191.84	297.85	117.33	$6.115 \cdot 10^{-4}$	137.96
3_b	32.0	11.99	1.851	159.92	201.07	86.38	$5.194 \cdot 10^{-4}$	82.41
4_a	37.0	–	–	–	–	–	–	–
4_b	37.0	13.01	1.741	166.18	207.06	95.41	$5.548 \cdot 10^{-4}$	83.20
5_a	42.0	–	–	–	–	–	–	–
5_b	42.0	13.98	1.677	170.64	210.18	101.71	$5.875 \cdot 10^{-4}$	83.52

Fig. 5.31 shows the evolution of the cycle in a p-h diagram. As should be expected the enthalpy drop decreases in the condenser, therefore the cooling capacity falls down. It is important to highlight that the heat losses in the compressor imply that the outlet compressor enthalpy decreases when the condenser secondary inlet temperature increases. If the compressor is adiabatic the outlet compressor enthalpy don't follow this evolution, and this enthalpy increases as should be expected.

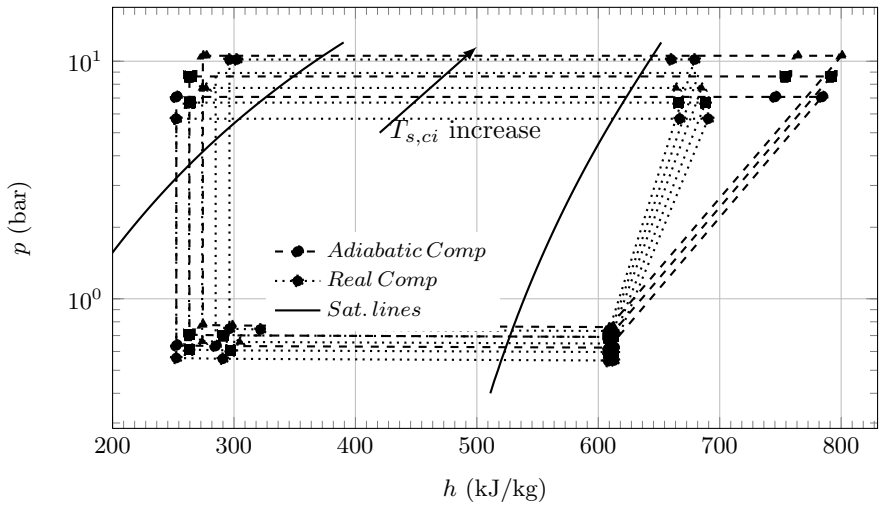

Figure 5.31: Diagram: p-h of parametric cases.

High and low pressures of the system evolution are presented in Fig. 5.32. Both suction and discharge pressures increase, but the discharge pressure increases more than the suction pressure (Table 5.12, Π increases).

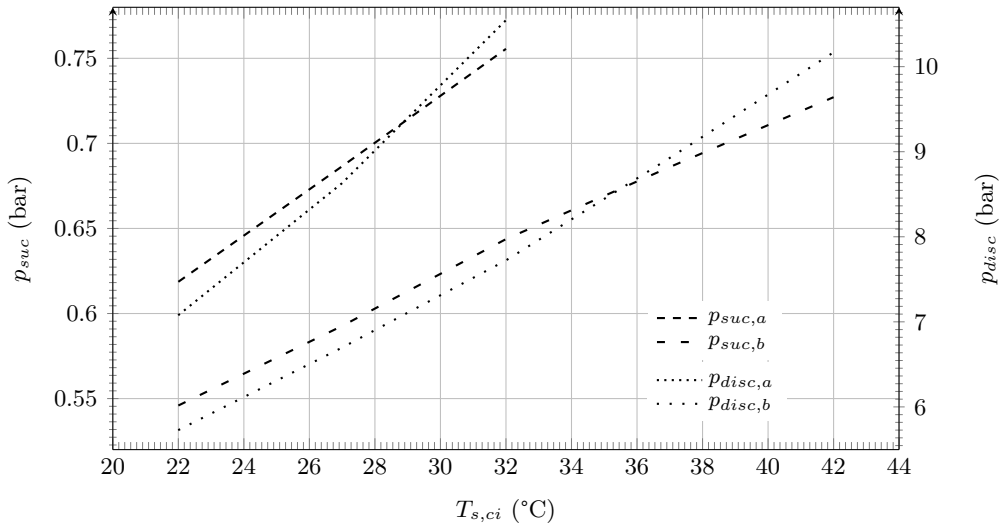

Figure 5.32: Evolution of the system mass.

Fig. 5.33 shows the decreasing evolution of the cooling capacity, when the secondary inlet temperature increases.

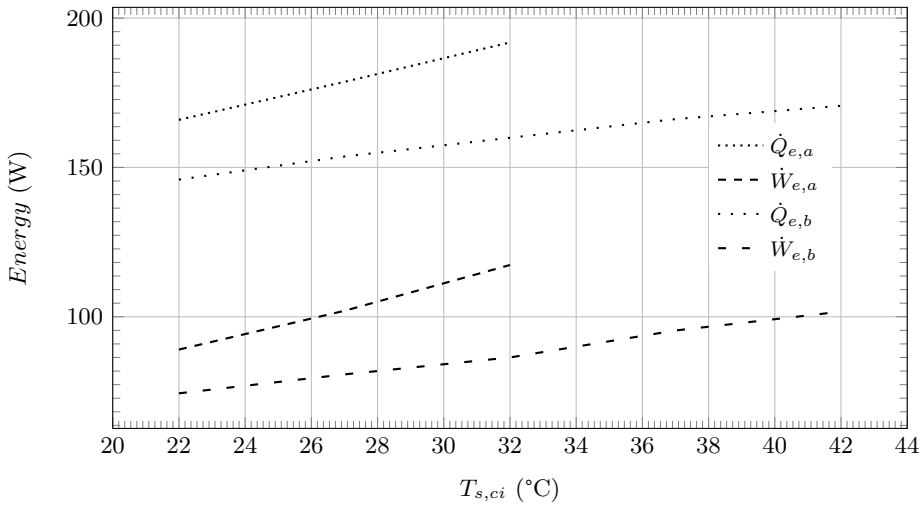

Figure 5.33: Evolution of the cooling capacity.

Study of influence $T_{s,ei}$

The parametric study of the evaporator secondary inlet temperature has been done changing the temperature from 22°C to 42°C. The main boundary values are: i) m_{system} = 90.905 g, ii) T_{env} = 22 °C, iii) $\dot{m}_{s,e}$ = 118.8 [kg/h], iv) $\dot{m}_{s,c}$ = 169.2 [kg/h] and v) $T_{s,ci}$ = 32°C.
The main parameters of the system are presented on Table 5.13. Like in the study presented above, the COP is better for the real compressor assumption than for the adiabatic compressor assumption; the reason is the same as in that study.

Table 5.13: Influence of $T_{s,ei}$ over the energetic parameters of the system.

Case	$T_{s,ei}$ [°C]	II	COP	$\dot{Q}_e$ [W]	$\dot{Q}_c$ [W]	$\dot{W}_e$ [W]	$\dot{m}$ [kg/s]	T_{disc} [°C]
1_a	22.0	14.02	1.575	176.99	282.33	112.32	$5.990 \cdot 10^{-4}$	129.85
1_b	22.0	12.06	1.770	146.31	189.80	82.66	$5.061 \cdot 10^{-4}$	74.86
2_a	27.0	14.00	1.604	184.30	290.16	114.90	$6.056 \cdot 10^{-4}$	133.87
2_b	27.0	12.03	1.810	152.96	195.36	84.50	$5.129 \cdot 10^{-4}$	78.55
3_a	32.0	13.95	1.635	191.84	297.85	117.33	$6.115 \cdot 10^{-4}$	137.96
3_b	32.0	11.99	1.851	159.92	201.07	86.38	$5.194 \cdot 10^{-4}$	82.41
4_a	37.0	13.90	1.663	198.68	304.67	119.45	$6.163 \cdot 10^{-4}$	141.66
4_b	37.0	12.01	1.876	166.52	206.66	88.76	$5.257 \cdot 10^{-4}$	86.06
5_a	42.0	13.83	1.693	205.83	311.72	121.55	$6.209 \cdot 10^{-4}$	145.53
5_b	42.0	12.03	1.902	173.55	212.65	91.24	$5.322 \cdot 10^{-4}$	89.92

Fig. 5.34 show the evolution of the cycle in a p-h diagram. As should be expected the increase of the evaporator outlet enthalpy,due to the increase of inlet secondary temperature, increases the cooling capacity of the system. It is important to highlight

that the heat losses in the compressor implies that the outlet compressor enthalpy decrease when the secondary inlet temperature increases. In this study the heat losses in the compressor remains more or less constant, therefore the evolution of the outlet compressor enthalpy follows a similar way as the system with an adiabatic compressor.

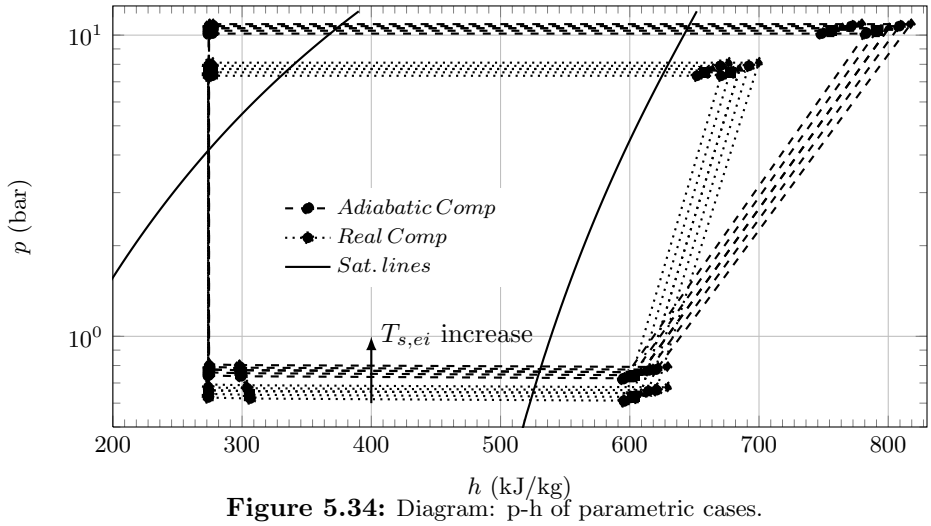

Figure 5.34: Diagram: p-h of parametric cases.

High and low pressures of the system evolution are presented in Fig. 5.35. For adiabatic compressor assumption, both pressures increase, but the compressor inlet pressure increases more than the compressor outlet pressure, therfore the Π decreases. For real compressor assumption the increase of compressor inlet and outlet pressure is almost the same, therefor the Π remains almost constant (Table 5.13).

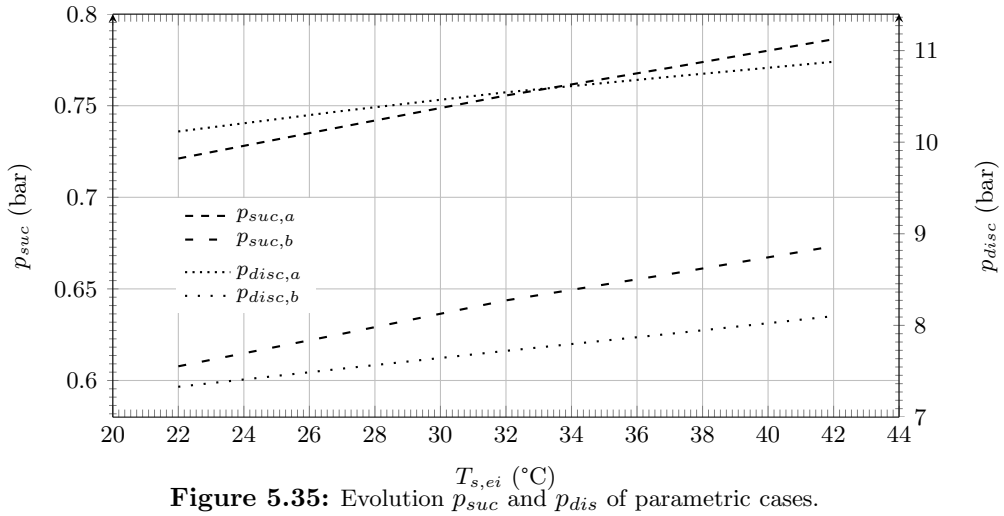

Figure 5.35: Evolution p_{suc} and p_{dis} of parametric cases.

Fig. 5.36 shows the increasing evolution of the cooling capacity, when the secondary inlet temperature increases.

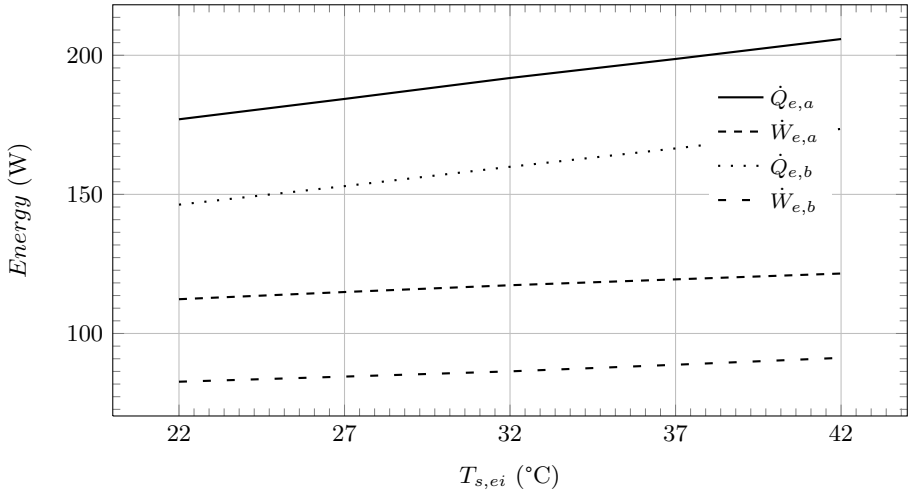

Figure 5.36: Evolution of the cooling capacity.

5.4 Dry expansion refrigerating system with high pressure receiver

This section presents the parametric studies of the dry expansion refrigerating system with a high pressure receiver. The geometry used have been presented in Table 3.24 on section 3.4.2.
The parametric studies have been divided into two main studies, both of them considering the liquid level in the high pressure receiver constant (variable mass in the system). The first one, studying the influence of the inlet temperature in the secondary fluid of the condenser. The second one, also study the influence of the evaporator secondary inlet temperature. Both studies have been carried out considering the liquid level in the high pressure receiver as constant.
These studies have been done using R134a and R600a, but the evolution observed with this two refrigerants are similar. Therefore in order to avoid repetitions the results presented are obtained with R600a as refrigerant.

5.4.1 Study of influence $T_{s,ci}$

The parametric study of the secondary inlet temperature of the condenser has been done changing the temperature from 39°C to 47°C increasing 2°C between tests. The main boundary values are: i) $z_l = 7$ [cm], ii) $T_{env} = 25$°C, iii) $\dot{m}_{s,e} = 118.8$ [kg/h], iv) $\dot{m}_{s,c} = 169.2$ [kg/h] and v) $T_{s,ei} = 32$°C.
In Table 5.14 the main values of the system are shown. Like in the previous studies carried out for the dry expansion system with constant mass, the increase of the $T_{s,ci}$ implies that the pressure ratio and the electrical consumption increase but the cooling capacity of the this system also raises. Despite of it the COP falls down, because the electrical consumption grows up more than the cooling capacity.

Table 5.14: Refrigerating system: COP and Π.

Case	$T_{s,ci}$ [°C]	Π	COP	$\dot{Q}_e$ [W]	$\dot{Q}_c$ [W]	$\dot{W}_e$ [W]	$\dot{m}$ [kg/s]	$T_{cp,o}$ [°C]
1	39.0	11.61	1.546	124.57	139.41	80.56	$4.349 \cdot 10^{-4}$	87.01
2	41.0	11.87	1.503	125.04	138.92	83.17	$4.434 \cdot 10^{-4}$	87.24
3	43.0	12.14	1.461	125.42	138.33	85.83	$4.518 \cdot 10^{-4}$	87.49
4	45.0	12.41	1.419	125.69	137.62	88.55	$4.602 \cdot 10^{-4}$	87.75
5	47.0	12.69	1.378	125.87	136.83	91.34	$4.686 \cdot 10^{-4}$	88.03

Fig. 5.37 shows the p-h diagram, where it is interesting to highlight the inlet of high pressure receiver which is near the liquid saturation curve.

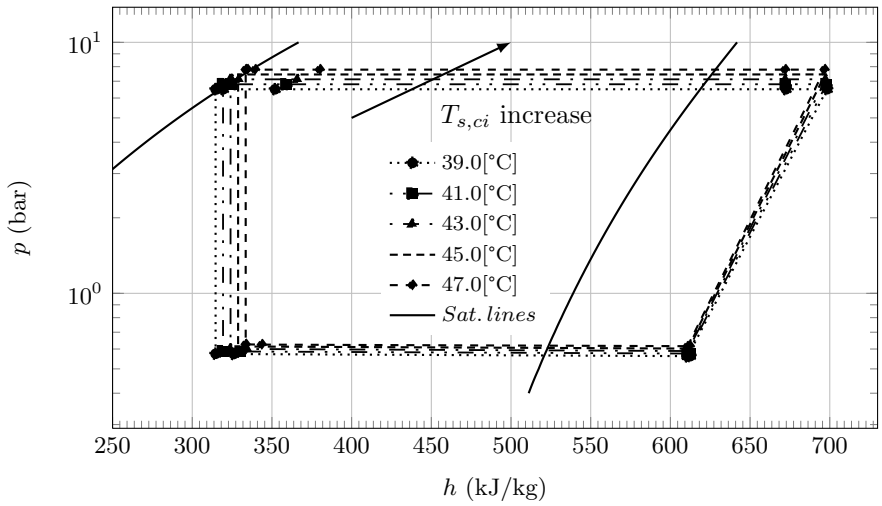

Figure 5.37: Diagram: p-h of parametric cases ($T_{s,ci}$).

Fig. 5.38 presents the evolution of the cooling capacity and the electrical power consumption of the compressor when the $T_{s,ci}$ increases. In this figure can be seen how the increase of the electrical consumption is higher than the raise of the cooling capacity.

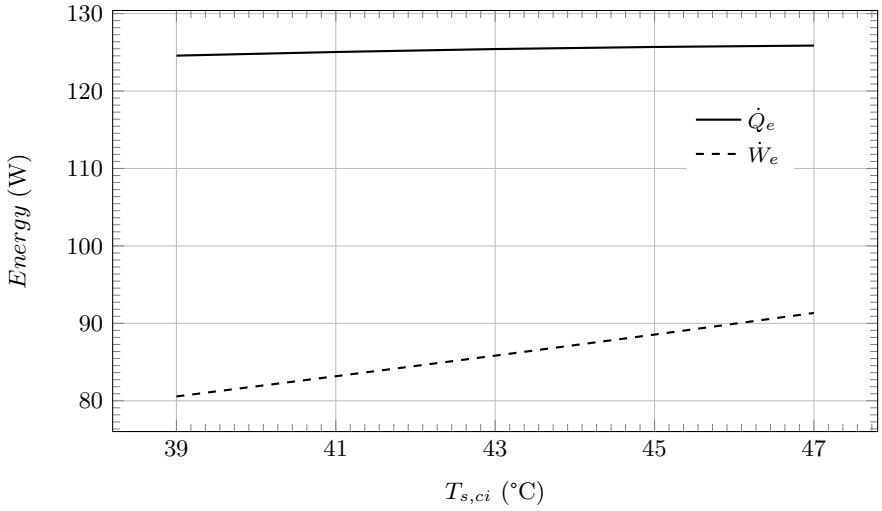

Figure 5.38: Evolution of cooling power and compressor work ($T_{s,ci}$).

Fig. 5.39 depicts the evolution of the total refrigerant mass in the system. The high pressure raises , therefore the gas density inside the receiver increases and the

liquid density decreases. The mass decreases, because the increase of gas density is lower than the decrease of liquid density, therefore it is ecessary to have less refrigerant to maintain the liquid level.

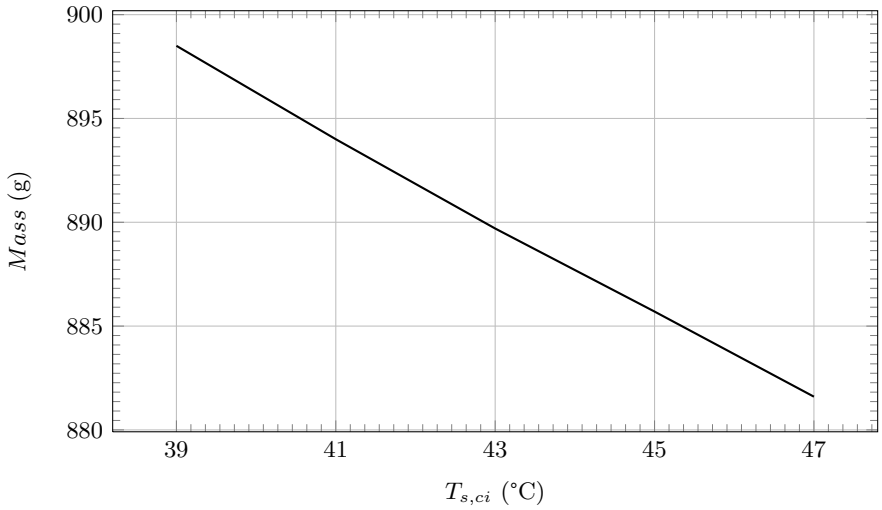

Figure 5.39: Evolution of the mass in the system ($T_{s,ci}$).

5.4.2 Study of influence $T_{s,ei}$

The parametric study of the secondary inlet temperature of the condenser has been done changing the temperature from 17°C to 37°C increasing 5°C between tests. The main boundary values are: i) $z_l = 7$ [cm], ii) $T_{env} = 25$°C, iii) $\dot{m}_{s,e} = 118.8$ [kg/h], iv) $\dot{m}_{s,c} = 169.2$ [kg/h] and v) $T_{s,ci} = 39$°C.
In Table 5.15 the main values of the system are shown. Like in the previous studies carried out for the dry expansion system without HPR, the increase of the $T_{s,ei}$ implies that the COP raises, due to the cooling capacity increase more than the electrical consumption of the compressor.

Table 5.15: Refrigerating system: COP and Π.

Case	$T_{s,ei}$ [°C]	Π	COP	$\dot{Q}_e$ [W]	$\dot{Q}_c$ [W]	$\dot{W}_e$ [W]	$\dot{m}$ [kg/s]	$T_{cp,o}$ [°C]
1	17.0	11.97	1.448	113.72	131.03	78.51	$4.338 \cdot 10^{-4}$	74.56
2	22.0	11.84	1.482	117.27	133.78	79.11	$4.339 \cdot 10^{-4}$	78.65
3	27.0	11.73	1.513	120.89	136.58	79.85	$4.344 \cdot 10^{-4}$	82.84
4	32.0	11.61	1.546	124.57	139.41	80.56	$4.349 \cdot 10^{-4}$	87.01
5	37.0	11.50	1.579	128.31	142.27	81.26	$4.354 \cdot 10^{-4}$	91.18

Fig. 5.40 depicts the p-h diagram and the low influence of the $T_{s,ei}$ in the high pressure.

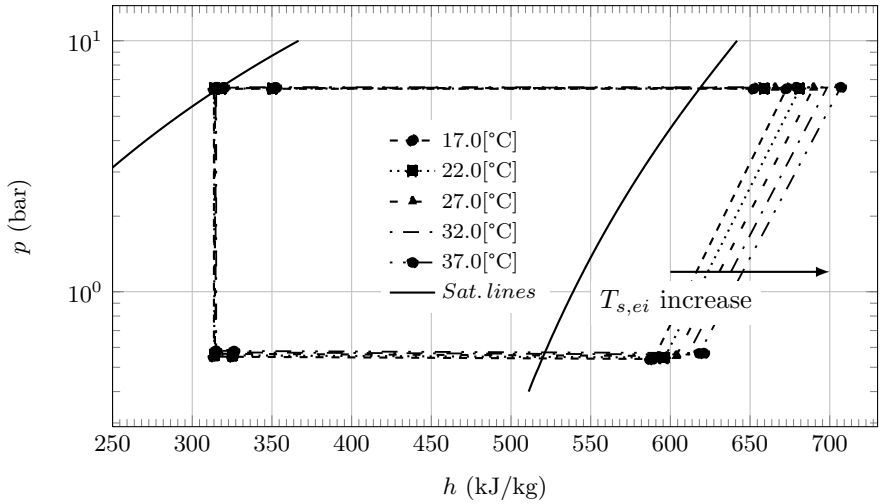

Figure 5.40: Diagram: p-h of parametic cases ($T_{s,ei}$).

Fig. 5.41 presents the evolution of the cooling capacity and the electrical power consumption of the compressor when the $T_{s,ei}$ increases. In this figure can be seen how the increase of the electrical consumption is lower than the raise of the cooling capacity.

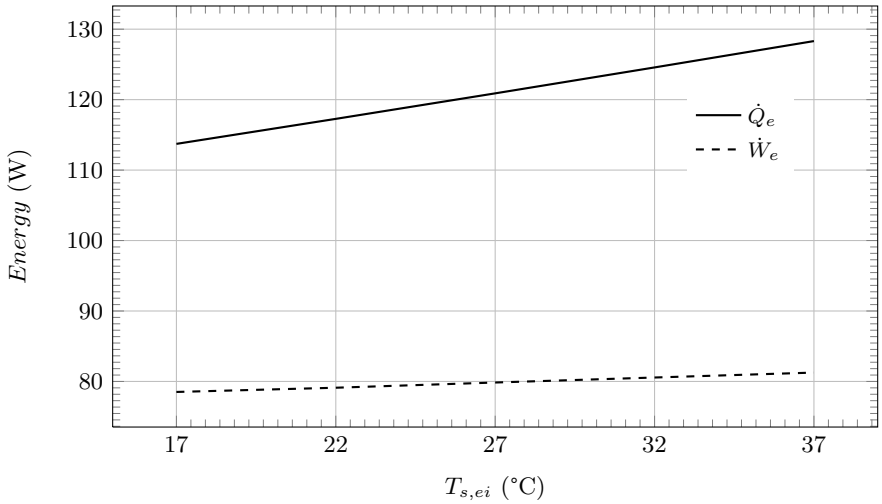

Figure 5.41: Evolution of cooling power and compressor work ($T_{s,ei}$).

Fig. 5.42 shows the evolution of the total refrigerant mass in the system. The mass decreases because the low pressure raises, therefore the mass in the low pressure side of the system to maintain the level in the high pressure receiver is lower. The high pressure is almost the same this is why the total refrigerant mass doesn't change too much.

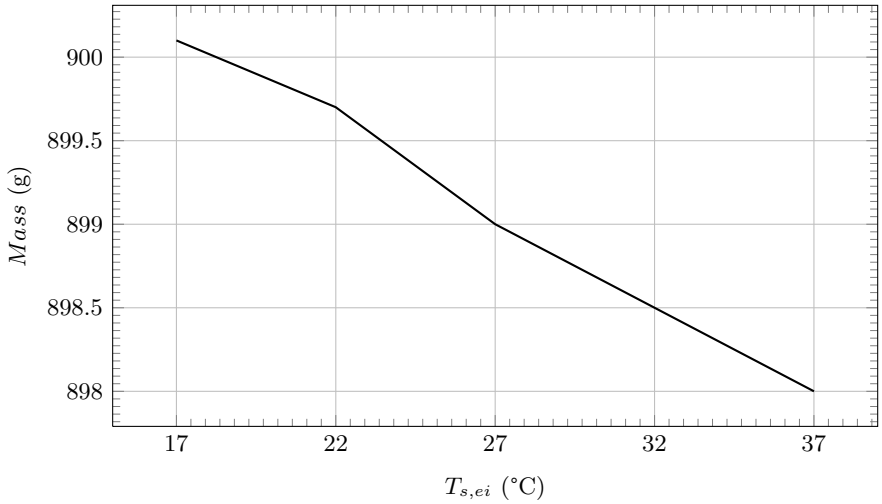

Figure 5.42: Evolution of the mass in the system ($T_{s,ei}$).

5.5 Liquid suction line refrigerating system

This section presents the parametric studies of the liquid suction line refrigerating system. The geometry used have been presented in Table 3.27 on section 3.4.3.

5.5.1 Study of influence $T_{s,ei}$

The parametric study of the secondary inlet temperature of the evaporator has been done changing the temperature from 3°C to 7°C increasing 2°C between tests, considering the mass in the system variable and keeping constant the liquid level in the low pressure receiver. The main boundary values are: i) $z_l = 7$ [cm], ii) $T_{env} = 25$°C, iii) $\dot{m}_{s,e} = 180.0$ [kg/h], iv) $\dot{m}_{s,c} = 169.2$ [kg/h] and v) $T_{s,ci} = 32$°C.
Table 5.16 shows the main values of the system. The electrical consumption and the cooling capacity raise with the increase of the evaporator secondary inlet temperature. It is interesting to highlight that a double pipe heat exchanger of only 0.8 m of lenght produces a cooling capcity of 290-300 W, while for dry expansion system the lenght used was 6 m and the cooling capacity was arround 170-200 W.

Table 5.16: Refrigerating system: COP and Π.

Case	$T_{s,ei}$ [°C]	Π	COP	$\dot{Q}_e$ [W]	$\dot{Q}_c$ [W]	$\dot{Q}_{coil}$ [W]	$\dot{W}_e$ [W]	$\dot{m}$ [kg/s]	$T_{cp,o}$ [°C]
1	3.0	8.31	1.252	290.64	453.30	32.26	232.14	$2.493 \cdot 10^{-3}$	82.83
2	5.0	8.43	1.257	301.25	469.74	31.62	239.47	$2.552 \cdot 10^{-3}$	84.90
3	7.0	8.61	1.246	310.94	487.22	31.32	249.55	$2.625 \cdot 10^{-3}$	87.86

Fig. 5.43 depicts the p-h diagram and the low influence of the $T_{s,ei}$ in the high pressure.

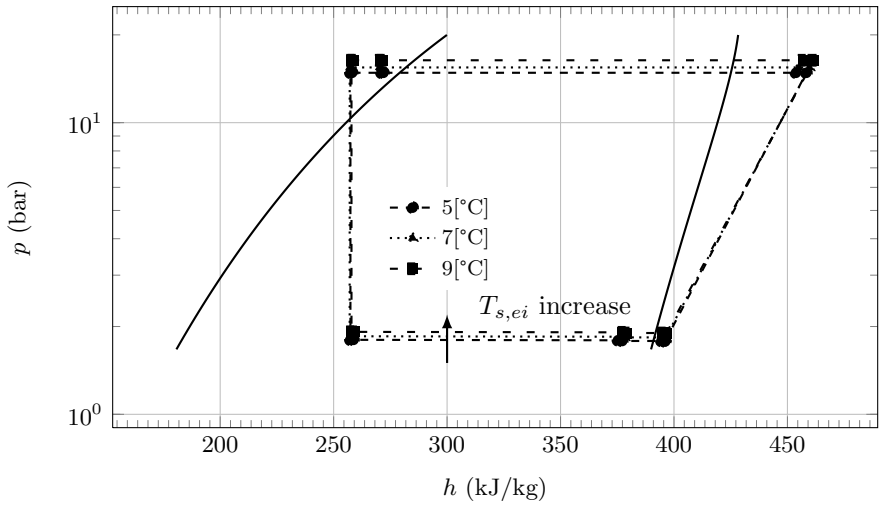

Figure 5.43: Diagram: p-h of parametric cases (z_l= cte).

Fig. 5.44 presents the evolution of the cooling capacity and the electrical power consumption of the compressor when the $T_{s,ei}$ increases. In this figure can be seen how the increase of the electrical consumption and the raise of the cooling capacity are more or less proportional, therefore the COP remains almost constant.

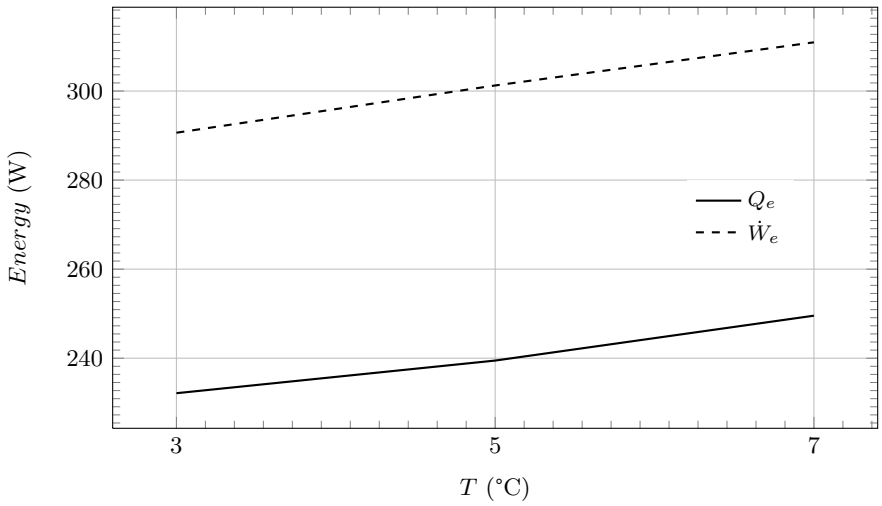

Figure 5.44: Evolution of cooling capacity in the study.

Fig. 5.45 shows the evolution of the total refrigerant mass in the system. The mass decreases because the low pressure raises (gas density increase less than the decrease of liquid density), therefore the mass in the low pressure side of the system to maintain the level in the low pressure receiver is higher. The raise of mass in the system was 3 g.

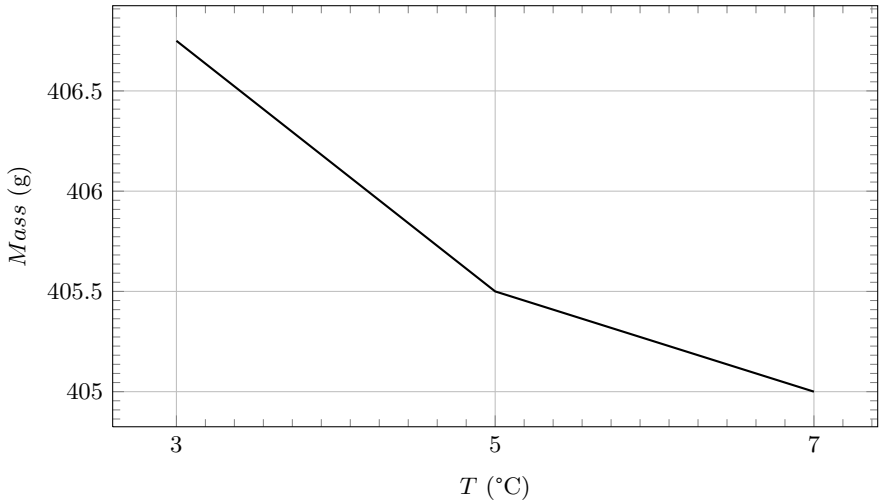

Figure 5.45: Evolution of system mass in the study.

5.5.2 Study of influence $T_{s,ci}$

The parametric study of the secondary inlet temperature of the condenser has been done changing the temperature from 30°C to 34°C increasing 2°C between tests, considering the mass in the system variable and keeping constant the liquid level in the low pressure receiver. The main boundary values are: i) $z_l = 7$ [cm], ii) $T_{env} = 25$°C, iii) $\dot{m}_{s,e} = 180.0$ [kg/h], iv) $\dot{m}_{s,c} = 169.2$ [kg/h] and v) $T_{s,ei} = 5$°C.
Table 5.17 shows the main values of the system. The electrical consumption, while the cooling capacity decreases with the increase of the condenser secondary inlet temperature.

Table 5.17: Refrigerating system: COP and Π.

Case	$T_{s,ci}$ [°C]	Π	COP	$\dot{Q}_e$ [W]	$\dot{Q}_c$ [W]	$\dot{Q}_{coil}$ [W]	$\dot{W}_e$ [W]	$\dot{m}$ [kg/s]	$T_{cp,o}$ [°C]
1	30.0	8.19	1.322	305.96	469.01	30.28	231.38	$2.503 \cdot 10^{-3}$	82.14
2	32.0	8.43	1.257	301.25	469.74	31.62	239.47	$2.552 \cdot 10^{-3}$	84.90
3	34.0	8.71	1.183	295.25	470.34	33.15	249.42	$2.609 \cdot 10^{-3}$	88.25

Fig. 5.46 depicts the p-h diagram and the low influence of the $T_{s,ci}$ in the high pressure.

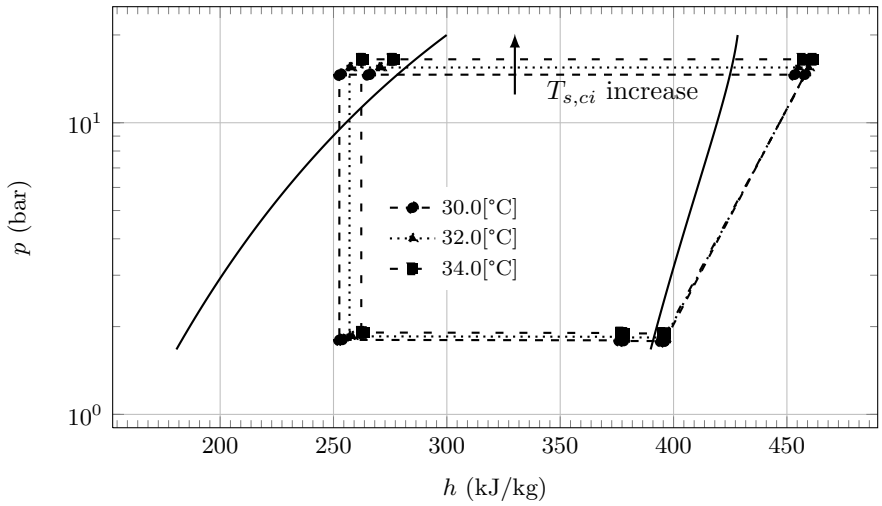

Figure 5.46: Diagram: p-h of parametric cases (z_l= cte).

Fig. 5.47 presents the evolution of the cooling capacity and the electrical power consumption of the compressor when the $T_{s,ci}$ increases. In this figure can be seen how electrical consumption increases while the cooling capacity descreases, therefore the COP drops.

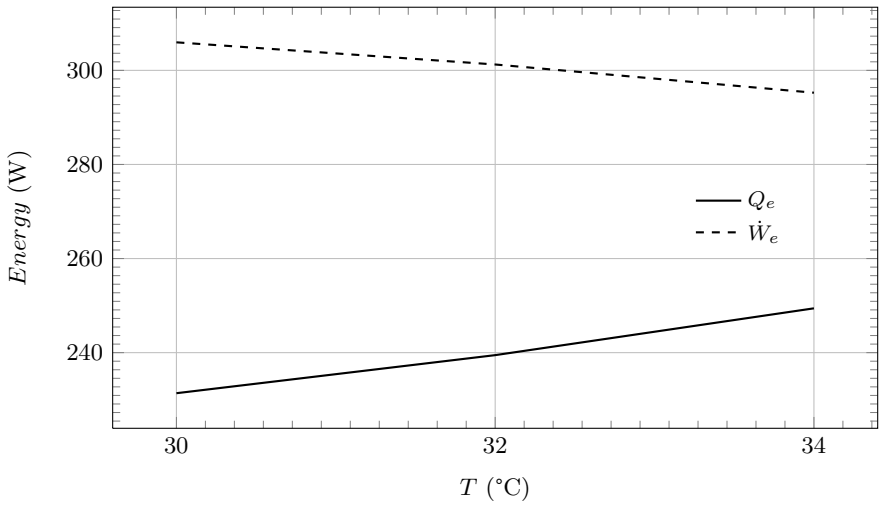

Figure 5.47: Evolution of cooling capacity in the study.

Fig. 5.48 shows the evolution of the total refrigerant mass in the system. The mass decreases because the low pressure raises (gas density increase less than the decrease of liquid density), therefore the mass in the low pressure side of the system to maintain the level in the low pressure receiver is lower. The variation of mass in the system was 2 g.

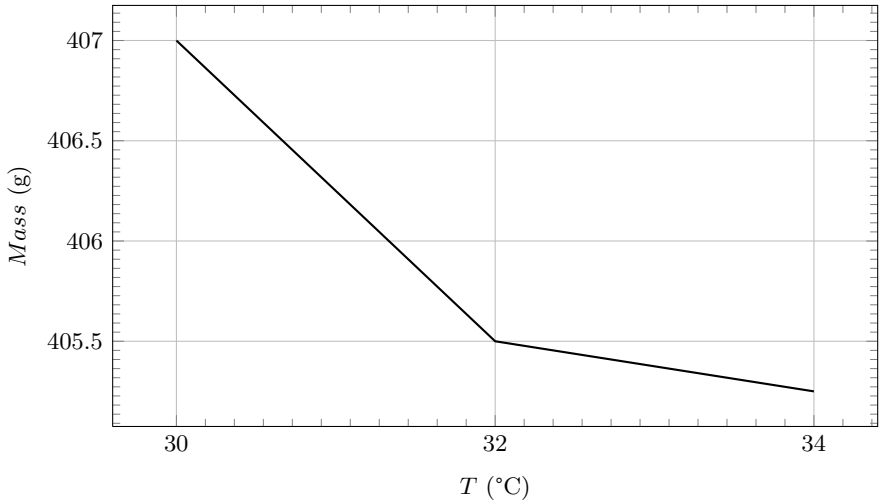

Figure 5.48: Evolution of system mass in the study.

5.6 Liquid overfeed refrigerating system

This section presents the parametric studies of an overfeed refrigerating system, using R717 as working fluid. The geometry used have been presented in Table 4.22 on section 4.7.
The parametric studies have been focused on the study of the influence of the evaporator secondary inlet temperature. For this set of tests the system mass is variable. The main boundary values are: i) $\dot{m}_e = 45.72$ [kg/h], ii) $T_{env} = 25$°C, iii) $\dot{m}_{s,e} = 0.6186$ [kg/s], iv) $\dot{m}_{s,c} = 0.8717$ [kg/s], v) $T_{s,ci} = 20$°C, vi) $z_{l,lp} = 0.4$ [m] and $z_{l,hp} = 0.3$ [m]. In the study the secondary inlet temperature of the evaporator change from 5.5°C to 12.5°C.
Fig. 5.49 shows the results of the parametric study for the overfeed refrigerating system in a diagram pressure-enthalpy. As can be seen the pressures of the system increase when the secondary inlet temperature grows up.

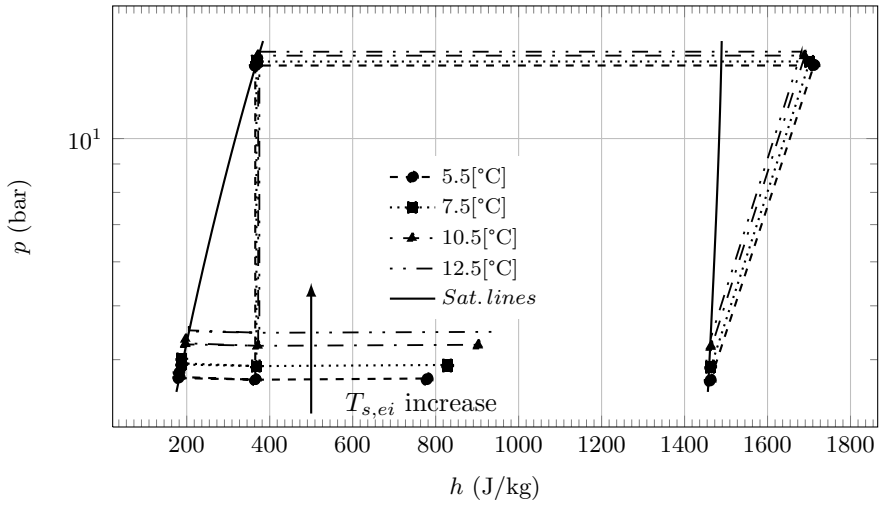

Figure 5.49: Diagram: p-h of overfeed parametric cases.

Table 5.18 shows some interesting values of the refrigerating system. The cooling capacity, the electrical work and the main circuit mass flow increase as should be expected when the secondary inlet evaporator temperature grows. The COP raises even when the electrical consumption increases, due to the cooling capacity grows up more than the electrical consumption. The evaporator outlet mass fraction increase, due to the cooling capacity raises and the evaporator mass flow remains constant. It is interesting to highlight that the increase of pressures together with the condition of liquid level in the receiver constant implies a lower refrigerant charge for the system

when the $T_{s,ei}$ increases (see Fig. 5.50).

Table 5.18: Comparison values from the parametric cases.

Case	Π	COP	$\dot{Q}_e$ [W]	$\dot{Q}_c$ [W]	$\dot{W}_e$ [W]	$\dot{m}$ [kg/s]	$\dot{x}_{g,eo}$
1	3.70	3.484	7595.37	9379.22	2180.07	$6.974 \cdot 10^{-3}$	0.468
2	3.56	3.643	8140.82	9964.73	2234.17	$7.481 \cdot 10^{-3}$	0.504
3	3.35	3.857	8956.81	10845.86	2321.94	$8.240 \cdot 10^{-3}$	0.558
4	3.23	4.020	9544.28	11471.53	2373.90	$8.789 \cdot 10^{-3}$	0.597

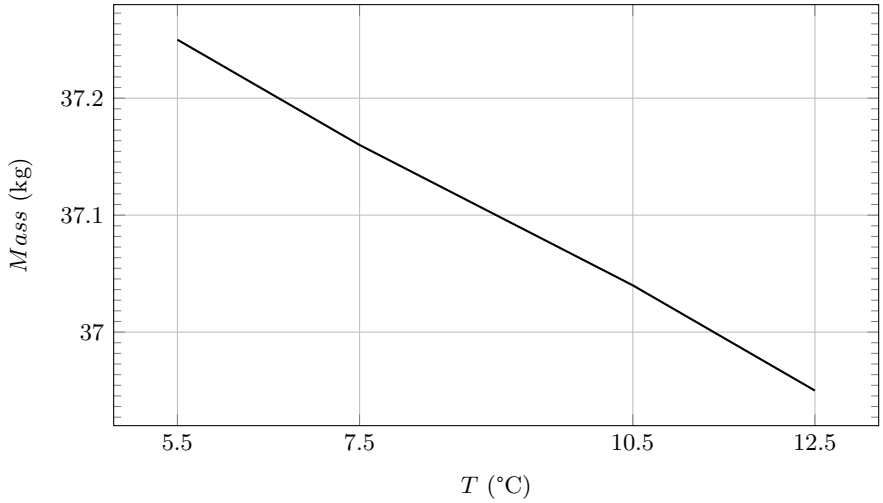

Figure 5.50: Evolution of the mass in the system ($T_{s,ei}$).

5.7 Conclusions

In this chapter, parametric studies of the receiver, dry expansion system and overfeed refrigerating system have been presented. These studies allows as to increase our knowledge about the pressured receivers, as well as the behaviour of the refrigerating systems. For dry expansion systems have been carried out studies with variable mass in the system, as well as studies with a constant mass. From the mass constant study, we are thinking on the possibility of studying the transient regime using a pseudo steady simulation of this system. The evolution of the dry expansion system have been observed in a similar way in the dry expansion system with high pressure receiver, despite it this study shows how works a refrigerating system with a high

pressure receiver and how the high pressure of the system fits to the pressure to obtain the outlet conditions of the condenser near saturation.
The study of the liquid suction line system, shows how the evaporator works without evaporate all the refrigerant (working in a similar way as the evaporator of the liquid overfeed refrigerating system, but with a lower $x_{g,out}$ than in liquid overfeed system).
The study of overfeed refrigerating system have been carried out considering the liquid levels in the receivers fixed. This is the first step to obtain the knowledge to carri out a study with mass constant in these systems.

5.8 Nomenclature

D	Diameter $[m]$
h	Enthalpy $[J/kg]$
L	Length $[m]$
$\dot{m}$	Mass flow rate $[kg/s]$, $[kg/h]$
p	Pressure $[Pa]$, $[kPa]$
$\dot{Q}$	Heat flux $[W]$
T	Temperature $[^oC]$
Z	Height $[m]$

Greek symbols

α	Convective heat transfer coefficient $[W/m^2K]$
δ	Insulation thickness $[m]$

Subscripts

a	Annular, Adiabatic
ae	External annular
b	Real or non adiabatic
c	Condenser
$comp$	Compressor
$cond$	Condensation
cp	Compression
$disc$	Discharge
e	External, Evaporator loop, evaporator, electrical
env	Environment
eo	Evaporator outlet
$evap$	Evaporation
ext	Exterior, environment
g	Vapour

gains	Gains
hp	High pressure receiver
i	Internal
in	Inlet
ins	Insulation
l	Liquid
lp	Low pressure receiver
out	Outlet
r	Main overfeed loop
s	Secondary
suc	Suction
system	System
t	Total

Chapter 6

Conclusions and future actions

6.1 Concluding remarks

The work developed throughout this thesis has concluded with the generation of the numerical simulation tool for the vapour compression refrigerating systems. The work have been focused on dry expansion refrigerating system, dry expansion system with high pressure receiver, liquid suction line system and liquid overfeed refrigerating system.

In the simulation of the whole refrigerating system, it has involved: i) the study of the refrigeration systems as well as their components, ii) the development of a numerical tool to simulate refrigerant pressured receivers, iii) the implementation of numerical tool developed in the CTTC (to simulate: two-phase flow into pipes, double pipe heat exchanger, capillary tube and compressors) and iv) the implementation of the supplier information of compressor, thermostatic expansion valve, electronical operated valve and pump.

The thesis has been divided into several chapters, starting from an overview of the refrigeration world (its beginnings and evolution), passing to the development of the numerical simulation tool for the vapour compression refrigerating systems, and ending with a parametric studies of these systems.

The development of the simulation software have been divided into three chapters. The first one presents the numerical formulation used to simulate all the components of the cycle as well as the numerical strategies developed to solve the refrigerating system as a whole. Some components as compressor, heat exchanger, capillary tube and pipe can be simulated with two different levels. Both levels of simulation are explained in the mathematical formulation an numerical methodology chapter. The second chapter devoted to the development of the numerical tool is focused on verify that the numerical code has not any programming errors. To verify the code, it has

been done several studies as mesh density and accuracy for the components as well as the system as a whole. Finally, in the validation chapter it has been compared the numerical solution against the experimental data for different components (compressor, double pipe heat exchanger, insulated pipe and expansion device), for the dry expansion refrigerating system and liquid overfeed refrigerating system. In this chapter also have been presented some adaptation and improvements in the experimental facilities of the CTTC that have been done during this thesis.
The last chapter has been focused on the study of different refrigerating systems and the pressured receiver under different boundary conditions.

6.1.1 Mathematical formulation, numerical methodology and numerical aspects

Mathematical modelling of vapour compression refrigerating systems has been planned, as explained above,in a multi-element strategy. This strategy allow to use different levels of simulation for the elements. Different algorithms have been investigate to solve the refrigerating system as a whole and has been detected that each refrigerating system need its own algorithm, despide of it, the strategy allows to extent the simulation of different systems easily. This stategy also allows to simulate the systems under different points of view: i) systems with mass constant in the system ii)systems with a specific working point (specific discharge pressure for dry expansion systems or with specific liquid level for refrigerating systems with pressured receivers).
The proposed numerical stategies have been revealed as capable of simulating with a reasonable degree of accuracy different vapour compression refrigerating systems. The numerical simulation methodology has been detected that the CPU time consumption is quite large, therefore a future actions should be interesting to be oriented to reduce the CPU time consumption.

6.1.2 Validation and experimental facilities

The experimental validation studies of the elements and the whole refrigerating system have been an important part of this thesis, although the preparation and runing of the experimental work (liquid overfeed refrigerating system and pressured receiver) have been performed in the framework of others PhD works. The preparation and runing of the experiments and improvements on the dry expansion facility at CTTC has been carried out by the author.
The dry expansion facility has been the experimental data bank to validate the compressor, the connection pipe, the double pipe heat exchanger and the micrometric expansion valve. Some validation results have been presented for almost all the elements of the refrigerating system as well as for two vapour compression refrigerating systems. It is important to obtain empirical dat to ensure the validation of the dry

expansion system with high pressure receiver as well as the liquid suction line system. As a general conclusion, the presented validation results show a reasonable good agreement with the physic behaviour for all the elements and the refrigerating systems. Regarding the pressured receiver, the empirical data have been revealed as unreliable because the geometrical information and the transient boudary conditions information seems that they are not accurate enough, despide of it the temporal evolution has a similar tendency. Therefore it should be important to obtain new experimental data to ensure the validation of this element.

6.1.3 Parametric studies

Once the simulation models have been verify and validate (dry expansion and liquid overfeed), some parametric studies have been carried out in order to evaluate the influence and the behaviour of the studied vapour compression refrigerating systems under different working conditions. The simulation model have shown their potential use to understant the behaviour of this system when the heat source or the cold source change.
The receiver studies carried out have been oriented to understand the behaviour of this component widely used in the refrigeration industry, in order to investigate the weak points of this component.

6.2 Future actions

The work initiated in this thesis can be continued in various directions that can be classified into two main aspects (experimental and numerical). In the experimental aspects can be expanded to:

- Existing experimental facilities: i) improve the insulation in order to obtain better empirical data, ii) complement the experimental measures in order to obtain more experimental data or improve the temperature measures for the transient response.

- Develop new facilities: i) receiver facility in order to obtain our own empirical data to validate the receiver simulation tool, ii) liquid suction line refrigerating system facility, dry expansion systems with high pressure receivers to validate our models and oriented to compare different refrigerating systems.

The numerical aspects can be divided into:

- Improve the annular correlations.

- Optimize the CPU time consumption by investigate new solvers and parallelization schemes for the vapour compression refrigerating systems.

- Extent the high level simulation of double pipe heat exchangers to other type of heat exchangers like fin-and-tube heat exchangers.

- Integrate the refrigeration cycle simulation into a multi-component simulation (refrigerating chambers, buildings building facades, PCM aplications, food, etc.).

- Extend the parametric studies, focused on the comparison of different refrigerating systems.